The Dissertation Committee for Rachel Marie Buchanan Certifies that this is the approved version of the following dissertation:

An integrated computational-experimental approach for the in situ estimation of valve interstitial cell biomechanical state

Committee:

Michael S. Sacks, Supervisor

Aaron B. Baker

Jeanne C. Stachowiak

Tess J. Moon

Farshid Guilak

An integrated computational-experimental approach for the in situ estimation of valve interstitial cell biomechanical state

by

Rachel Marie Buchanan, B.S.; M.S.E.

Dissertation

Presented to the Faculty of the Graduate School of
The University of Texas at Austin
in Partial Fulfillment
of the Requirements
for the Degree of

Doctor of Philosophy

The University of Texas at Austin
May 2016

Dedication

I dedicate this dissertation to my family: Mom, Dad, Melissa, Rebecca and Christopher Buchanan, my husband Matthew and my new family, the Murphys. Thank you for your unconditional love and support and never doubting me.

Acknowledgements

I would first like to thank my advisor, Dr. Michael Sacks for the opportunity to join his laboratory from its very beginning at UT. Thank you for your patience and constant guidance over the years. Also, thank you to my committee members for their support throughout this process. I would also like to thank the Department of Biomedical Engineering at the University of Texas at Austin. It has been an honor to represent this department over the past 6 and a half years and I consider it to be an extension of my family

I would like to recognize and thank Dr. Kristyn Masters, Dr. Jane Grande-Allen and Dr. Giovanni Ferrari for the enjoyable collaborations and advice in the field of heart valves. Thank you for always being forthcoming with your knowledge and experience. Also, a special thanks to Dr. Farshid Guilak who served on my dissertation committee and allowed me to conduct research in his laboratory for several weeks to examine aortic valve cells using microindentation techniques. Thank you specifically to Johannah Sanchez-Adams and Holly Leddy for all of your help during my time at Duke and for making me feel at home during my stay.

I would like to thank my wonderful lab mates and close friends Christine Scheve, Kristen Feaver, Avinash Gadok and Salma Ayoub. You have given me strength and support throughout this long process, lifting me up when I needed it the most. I also have such gratitude for the post-doctoral fellows in my lab, Chung-Hao Lee and Joao Soares in particular for their mentorship and guidance in the field of computational modeling.

Lastly, and most importantly I would like to thank my husband, Matthew Murphy, for all his support from the very beginning. Thank you for believing in me, putting up with me, and always being on my side. I love you always.

An integrated computational-experimental approach for the in situ estimation of valve interstitial cell biomechanical state

Rachel Marie Buchanan, Ph.D.
The University of Texas at Austin, 2016

Supervisor: Michael S. Sacks

Mechanical forces are known to regulate aortic valve interstitial cell (AVIC) functional state by modulating their biosynthetic activity, translating to differences in tissue composition and structure and, potentially, leading to aortic valve (AV) dysfunction. While advances have been made toward the understanding of AVIC behavior *ex-situ*, the AVIC biomechanical state in its native extracellular matrix (ECM) remains largely unknown. Consequently, changes in AVIC behaviors, such as stiffness and contractility, resulting from pathological cues *in-situ* remain unidentified. We hypothesize that improved descriptions of AVIC biomechanical state *in-situ*, obtained using an inverse modeling approach, will provide deeper insight into AVIC interactions with the surrounding ECM, revealing important changes resulting from pathological state, and possibly informing pharmaceutical therapies. To achieve this, a novel integrated numerical-experimental framework to estimate AVIC mechanobiological state *in-situ* was developed. Flexural deformation of intact AV leaflets was used to quantify the effects of AVIC stiffness and contraction at the tissue level. In addition to being a relevant deformation mode of the cardiac cycle, flexure is highly sensitive to layer-specific changes in AVIC biomechanics. As a first step, a tissue-level bilayer model that accurately captures the bidirectional flexural response of AV intact layers in a passive state was developed. Next, tissue micromorphology was incorporated in a macro-micro scale framework to simulate layer-specific AVIC-ECM interactions. The macro-micro AV model enables the estimation of changes in effective AVIC stiffness and contraction *in-situ* that are otherwise grossly inaccessible through experimental approaches alone. Finally, microindentation studies examining AVIC activation were run in parallel with *in-situ* studies to emphasize the necessity of an *in-situ* approach, and the advantage it affords over existing ex-situ methodology. In conclusion, the developed numerical-experimental methodology can be used to obtain AVIC properties *in-situ*. Most importantly, it can lead to further understanding of AVIC-ECM mechanical coupling under various pathophysiological conditions and the investigation of possible treatment strategies targeting the myofibroblast phenotype characteristic of early signs of sclerotic valvular disease.

Table of Contents

List of Tables xiii

List of Figures xv

CHAPTER 1: INTRODUCTION 1

Preface 1
  Heart Valve structure and function 1
    Structure of the AV at multiple length scales 2
      Valve endothelial cells 4
      Valve interstitial cells 6
    Biomechanical function 8
      Time dependent behaviors 9
      Flexural deformation 11
  AV disease and treatment options 13
    AV replacements 15
  Cell-Level Mechanobiology 17
    VIC deformation under physiological loading 18
    Ex-situ methods of measuring cell stiffness 21
      Micropipette Aspiration 21
      Atomic Force Microscopy (AFM) 21
    Measurable AVIC changes in-situ 22
  Computational Modeling Approaches in biomechanics 23
  Integrated Computational-Experimental Approaches in biomechanics 25
  Motivation, Rational, and Specific Aims 27
    Specific Aim 1. Develop a model of the AV leaflet that captures non-viable tissue level behavior 29
    Specific Aim 2. Develop and validate a micro-anatomically realistic macro-micro FE model to estimate i*n situ* AVIC mechanical behavior under activation. 29

Specific Aim 3. Measure the layer dependent contractile response of AVICs *in situ* using the developed macro-micro model in a simulated pathological state and validate measured responses against microindentation experiments. 30

References 42

CHAPTER 2: INTERLAYER MICROMECHANICS OF THE AORTIC HEART VALVE LEAFLET 54

Preface 54

Introduction 55

Methods 56

Initial simulations of AV leaflet tissue flexure 57

Interlayer bonding simulation 58

Transmural strain experimental validation studies 59

Validation of experimental/simulation method 62

Results 62

Initial tissue material model 62

Parametric interlayer bonding model study 63

Transmural strain experimental results 63

Refined leaflet model 64

Model validation 66

Discussion 66

Overview 66

Bimodular material model for leaflet tissue in flexure 67

Implications for AV micromechanical function 68

Limitations and the need for an integrated experimental/simulation approach 69

Conclusions 70

References 80

CHAPTER 3: IN SITU CONTRACTILE BEHAVIOR OF THE AORTIC VALVE INTERSTITIAL CELL 83

Preface....................83

International prize....................84
  Introduction....................84
    Traditional multi-scale methodology....................86
    Limitation for biological materials....................87
  Methods....................89
    Flexural tissue testing....................89
    Macro-model....................91
      Formulation....................91
      Boundary conditions....................92
      Mesh93
      Estimating tissue parameters....................93
      Macro RVE averaged stress....................94
    Micro-model....................94
      RVE geometry and mesh....................94
      Formulation....................95
      Layer-specific connectivity....................96
    Macro-micro coupling....................97
      Micro-model boundary conditions....................97
      Macro-micro matching method....................97
      Systematic error check....................98
      Preliminary micro model parametric studies....................99
      Micro model parametric studies: estimating AVIC stiffness, contractility and connectivity....................101
    Validation of macro-micro methodology....................101
    Immunofluorescence....................102
  Results....................103
    Effective moduli values and fold increase....................103

Parameter estimation of the macro-model 104

Macro RVE averaged stress 104

Micro model estimates of AVIC stiffness, contractility and connectivity 105

Fibrosa and ventricularis under tension: uniform connectivity 105

AVIC layer differences under tension: varied connectivity 106

AVIC-ECM connectivity differences in the native AV 107

Pam gel validation 107

Discussion 108

Conclusions 110

References 126

CHAPTER 4: MEASURING THE EFFECTS OF CONTRACTILE STIMULI ON AVIC BIOMECHANICAL BEHAVIOR IN SITU **131**

Preface 131

Introduction 131

Protocols 132

Tissue preparation and treatment 132

End-loading bending protocol 133

Linearized effective modulus 135

Tissue bulk modulus estimates using the macro-micro model 135

Macro RVE averaged stress 136

AVIC stiffness and contractile force estimates using the macro-micro model 136

Results 136

Linearized effective modulus of AV leaflets 136

Tissue bulk modulus estimates using the macro-micro model 138

Underlying changes in AVIC stiffness and contractile forces 139

Discussion and Conclusions 140

References 152

CHAPTER 5: MEASURING THE EFFECTS OF CONTRACTILE STIMULI ON AVIC MECHANICAL BEHAVIOR USING MICROINDENTATION TECHNIQUES 153

Preface....153
Introduction....154
Protocols....155
AVIC culture....155
Pretreatment....156
Microindentation....157
AVIC elastic modulus analysis....159
Immunofluorescence quantitative analysis....160
Results....161
Observed differences in measured AVIC biomechanical state....161
Discussion....162
References....174

CHAPTER 6: SUMMARY, CONCLUSIONS AND FUTURE DIRECTIONS 176

Summary....176
Conclusions....178
Future Directions....178
References....180

BIBLIOGRAPHY 181

List of Tables

Table 2.1: Silicone material validation study, showing E (MPa). 70

Table 2.2: Predicted and measured neutral axis locations. 71

Table 2.3: Normalized material parameters..71

Table 3.1: List of symbols and nomenclature. 111

Table 3.2: Estimated moduli values for each layer under tension and compression at each activation state: inactive, normal and hypertensive. R^2 goodness of fit values as well as neutral axis locations are also reported for each activation state 112

Table 3.3: Macro homogenized von Mises stress values for each layer under tension and compression for each activation state: inactive, normal and hypertensive. Units in kPa. 113

Table 3.4: Estimated relative ventricularis connectivity (βAVIC) parameter using the estimated uniform AVIC stiffness (μAVIC) of 18kPa and hyper contractility (αAVIC) of 32E-5...113

Table 4.1: List of symbols and nomenclature. 141

Table 4.2: Estimated shear moduli values for the control treatment group at all three activation states. Moduli relations were derived from the in depth analysis presented in **Chapter 3**. Schematic detailing neutral axis location trends during AV bending is provided in **Fig. 2.8**. 142

Table 4.3: Estimated shear moduli values for the TGF-β1 treatment group at all three activation states. Moduli relations were derived from the in depth analysis presented in **Chapter 3**. 143

Table 4.4: Macro homogenized von Mises stress values for the control tissue for each layer under tension and compression for each activation state: inactive, normal and hypertensive. Units in kPa............................144

Table 4.5: Macro homogenized von Mises stress values for the TGF-β1 tissue for each layer under tension and compression for each activation state: inactive, normal and hypertensive. Units in kPa............................144

Table 4.6: Estimated connectivity (βAVIC) parameters for Control tissue using the estimated uniform stiffness of 18kPa (μAVIC), and the uniform estimated hypertensive contraction force of 26E-5 1/K (αAVIC)..145

Table 4.7: Estimated connectivity (βAVIC) parameters for TGF-β1 treated tissue using the estimated uniform stiffness of 18kPa (μAVIC), and the uniform estimated hypertensive contraction force of 35E-5 1/K (αAVIC)..145

Table 5.1: Summary of treatment groups and abbreviated names. Two pre-treatments (control and TGF-β1 tested under 3 different activation states: inactive, normal (5mM) and hypertensive (90mM). CytoD treatment served as a negative control for an inactivated cytoskeletal network.164

List of Figures

Figure 1.1: Schematic depicting the location of the four heart valves (mayoclinic.com). 30

Figure 1.2: A schematic approach to the biomechanics and mechanobiology of heart valve function. Heart valve function can be divided into multiple length scales: organ-, tissue-, cell-, and sub-cell levels. 31

Figure 1.3: Layered architecture of the Aortic Valve illustrated at its attachment [2] to the aorta and a more detailed illustration of the various constituents of the leaflet layers adapted from [161]. 32

Figure 1.4: Blood flow across the aortic valve adapted from [161]. 32

Figure 1.5: (a) Diagram of the AV cusp highlighting the belly, commissures, nodulus, and regions of coaptation. Small angle light scattering results with the orientation index at (b) 0mmHg, (c) 4mmHg, and (d) 90mmHg transvalvular pressure. No further changes in fiber alignment were observed past 4mmHg. These results are consistent with histological-based data that quantifies the percent area of tissue displaying collagen fiber crimp (e). Adapted from Sacks *et al.* [53]. 33

Figure 1.6: (a) Schematic showing the region of tissue used for bending tests in the AV. (b) Schematic showing directions of bending for the AV with respective layers (V: ventricularis, S: spongiosa, and F: fibrosa). M vs. Δκ relations in both the AC and WC directions for (c) specimens tested in 5 mM and 90 mM KCl, and (d) specimens flexed in 5 mM KCl and samples treated in 10 μM thapsigargin overnight and then flexed in 5 mM KCl. While the application of 90 mM KCL induced an increase in stiffness in the AC direction only, both bending directions experienced a loss of stiffness with the addition of thapsigargin to the bathing medium. 34

Figure 1.7: Progression of CAVD (modified from Otto et al. [162] and Rajamannan *et al.* [161]). The spectrum of disease ranges from the 'at risk' patient to the patient with end-stage severe symptomatic aortic stenosis. The light blue line represents the expected event-free survival and the purple line represents the survival curve at the onset of aortic sclerosis, which deviates from the expected survival line. Atherosclerotic risk factors involved in the development of aortic valve disease from aortic sclerosis to calcified aortic valve disease are included...................................35

Figure 1.8: Left: Medtronic Open Pivot Mechanic Valve (www.medtronic.com) Right: St. Jude Medical Epic Stented Valve (www.sjm.com)..........36

Figure 1.9: (a) The relation between AVIC nuclear aspect ratio (NAR) and transvalvular pressure loading, with values reported over normalized leaflet thickness. (b) AVIC NAR vs. the normalized collagen fiber orientation index (NOI) at different transvalvular pressure levels. These results suggest that AVICs are not appreciably loaded until the collagen fibers fully straighten at transvalvular pressures above ~4 mmHg...36

Figure 1.10: (a) A VIC under micropipette aspiration – the vertical bar represents the aspiration length. (b) Functional correlations of effective cell stiffness E vs. transvalvular pressure. (c) Linear correlation between Hsp47 vs. α-SMA, showing a strong correlation between the two proteins (*r* = 0.996) as the one progresses from the right to the left side of the heart. 37

Figure 1.11. Transmural MVIC distribution and deformation in the mitral valve anterior leaflet under controlled biaxial loading. (a) Stack of two-photon excited fluorescence images. Red represents collagen fibers and green represents cell nuclei stained with Cytox Green. Image-stacks were processed and used to quantify cellular deformation by measuring the nuclear aspect ratio (NAR) (b) Measured layer-specific NAR as a function of membrane tension. (A: atrialis, S: spongiosa, F: fibrosa, V: ventricularis). Adapted from Lee *et al.* [163]. 37

Figure 1.12. The macro-micro finite element (FE) model used to investigate MVIC deformation. (a) Schematic diagram of the tissue-level model: the region of interest of the MVAL tissue under equibiaxial tension loading. (b) Diagram of the cell-level microenvironment model, which consists of 37 uniformly distributed MVICs embedded in the layer-specific representative volume element. The tissue-level deformations are used to prescribe boundary displacements. Adapted from Lee *et al.* [163]. 38

Figure 1.13. Comparisons of the experimentally measured and numerically predicted NARs as a function of tissue-level tension: (a) atrialis layer ($r^2 = 0.8403$), (b) spongiosa layer ($r^2 = 0.9166$), (c) fibrosa layer ($r^2 = 0.8906$), and (d) ventricularis layer ($r^2 = 0.9373$). Adapted from Lee *et al.* [163]. 39

Figure 1.14. (a) Schematic of the AFM experiment, showing how the VIC rests on a collagenous surface and expresses α-SMA. (b) Reported effective moduli of AVIC and PVICs, which were ~100 fold larger than the equivalent micropipette results. (c) AFM simulation setup with finite element mesh. The mesh was refined around the indentation region, with typically 10,000~50,000 linear tetrahedron elements. Note that this is a cross-section of the geometry, but we simulated the whole cell. Adapted from Sakamoto *et al.* [157]. 40

Figure 1.15. The step-by-step calibration process. 1. The cytoskeletal shear modulus (μ_{cyto}) and α-SMA fiber shear modulus (μ_{sf}) were calibrated using the micropipette aspiration data for different types of VICs with different expression levels of α-SMA fibers. 2. Using the AFM indentation data on the cell peripheral regions, the fiber active contraction strength (f) was calibrated for AVICs and PVICs. 3. Using the AFM indentation data on the cell central region, the shear modulus of nucleus (μ_{nuc}) was calibrated for AVICs and PVICs. The parameters in red represents the ones that are being calibrated in the step, the parameters in gray represents the ones that are assumed not contribute to the mechanical response of the VICs (hence ignored) in the step, and the parameters in black represents the ones that are already calibrated from the previous steps and integrated into the model. Adapted from Sakamoto *et al.* [157]. 41

Figure 1.16. (a) Contraction strength of the α-SMA fibers in the AVICs and PVICs. About 9:1 ratio in the contraction strength was observed from AVICs to PVICs. (b) Shear moduli of the AVICs and PVICs nuclei, which exhibited no differences. Adapted from Sakamoto *et al.* [157]........42

Figure 2.1: (a) The aortic valve (b) A 1 mm x 1 mm section from the central belly region illustrating the 3D the tri-layered leaflet structure................72

Figure 2.2: (a) A schematic showing the orientation of the tissue strip and leaflet, and the location of the transmural strain measurement, (b) A free body diagram of tissue mounted in the testing device with a force, P, applied to its free end. The orientation of the X_1 and X_2 coordinate system specifies the X_1 axis coincident with the circumferential direction and the X_2 axis to reflect the thickness of the leaflet, (c) Markers used by the macro-imaging system shown on the edge of the tissue strip, (d) Transmural strain images obtained using micro camera, showing the reference and deformed tissue states..73

Figure 2.3: Comparison of the M-Δκ data [13] with the analytical solution of the one-term Ogden model using various α parameter values. Note that the experimental data was normalized to the maximum achieved moment at a Δκ of 0.28 mm^{-1} A value for α of 2.0 approximately captured the shape of the M-Δκ...74

Figure 2.4: Transmural stretch Λ_1 simulation results plotted against the normalized leaflet thickness. For measurable differences to occur in transmural stretch between the fibrosa and ventricularis, simulations indicate the spongiosa must possess a shear modulus less than 1 kPa. The WC bending direction simulation results are shown for sake of clarity, although the same simulation results were observed for the AC bending direction. The cuvature change reported is 0.2mm^{-1} since the reported results demonstrated independence of curvature change.................75

Figure 2.5: The M-Δκ response of a native porcine AV leaflet in the AC and WC directions that has been bent to a Δκ of 0.2 mm^{-1} in either direction. Simulations using a unimodular (dashed line) and bimodular material model (solid line) are superimposed over experimental data. The bimodular model represents the bidirectional bending behavior slightly better than the unimodular material. 76

Figure 2.6: Experimental transmural Λ_1 results plotted against the normalized thickness for (a,c) WC and (b,d) AC samples at Δκ=0.2 mm^{-1}, along with the corresponding unimodular (dashed line) and bimodular (solid line) simulation results. (a)-(b) represent strain matched in the WC direction, showing the resulting discrepancy in the AC fit using a unimodular model. Similarly, (c)-(d) represent strain matched in the AC direction, resulting in a poor WC fit using the unimodular model. Although the M-Δk behavior is captured with unimodular model, the transmural deformation response can only be captured in both the WC and AC directions using the bimodular material model. 77

Figure 2.7: (a) Transmural Green-Lagrange strain distribution (E_{11}) from the simulated flexure model demonstrating a disruption at the edges due to standard warping that occurs during bending. (b) A significant shift (2% stretch) in axial deformation is observed by plotting Λ_1 vs. normalized thickness in both the WC and (c) AC bending directions. It is important to note the associated shift in the neutral access location when observing deformation at the edge or in the unaffected central region of the tissue. 78

Figure 2.8: A schematic summarizing the changes in NA location experienced by the bulk tissue for both bending directions. In the WC bending direction, the NA shift towards the ventricularis approximately 0.35 of the normalized thickness, demonstrating the whole fibrosa under compression (-) and the majority of the ventricularis under tension (+). In the AC bending direction the NA shifts to approximately 0.79 of the normalized thickness. These results indicate that both the ventricularis and fibrosa are much stiffer under tension (+) than compression.....79

Figure 3.1: Computational homogenization scheme introduced from [36]. 114

Figure 3.2: Macro-micro approach schematic. 114

Figure 3.3: Averaged M vs. Δκ experimental data from AV bending study under inactive (thapsigargin), normal (5mM KCl) and hypertensive (90mM KCl) conditions and bending with (WC) and against (AC) the natural leaflet curvature. 115

Figure 3.4: Macro-micro model overview depicting the application of boundary conditions from the macro nodes to the corresponding micro RVE surface. 115

Figure 3.5: Computational flow of macro-micro model optimization. 116

Figure 3.6: Distribution (a) dimensions (b) and orientation angles (c) of AVICs within the micro-model based on histological measurements from native AV tissue acquired from [40, 41]. 117

Figure 3.7: RVE length vs. stress variation to determine an optimal RVE size of 80μm for the micro-model. 118

Figure 3.8: Micro-model framework 119

Figure 3.9: Modeling AVIC-ECM connectivity within the micro-model framework 119

Figure 3.10: Figure adapted by [42], illustrating force generation from AV leaflet strips using 90mM KCl (a) the FE simulation of the study (b) and the linear correlation between the micro-model α parameter and AVIC force. 120

Figure 3.11: Estimation of the activation parameter necessary to achieve normal and hyper level activation for each chosen basal level AVIC stiffness (μAVICBasal). 120

Figure 3.12: Linearized effective moduli taken from the slope of the averaged M vs. Δκ curve in figure 3.3 at points of maximum common curvature ($0.11mm^{-1}$) determined for the inactive, normal and hypertensive states and bending in both the AC and WC directions. 121

Figure 3.13: Macro-model simulation results of M- Δκ plotted against the experimental AV bending data determined for the inactive, normal and hypertensive states and bending in both the AC and WC directions.122

Figure 3.14: Results of micro-model parametric studies assuming a uniform AVIC-ECM connectivity. Effects of AVIC contractility, α, and AVIC stiffness, μ, for the fibrosa RVE under tensile loading (a) and the ventricularis RVE under tensile loading (b). 123

Figure 3.15: Results of micro-model parametric studies plotted in 3D (new representation of figure 3.13 results) assuming a uniform AVIC-ECM connectivity. Effects of AVIC contractility, α, and AVIC stiffness, μ, for the fibrosa RVE under tensile loading (a) and the ventricularis RVE under tensile loading (b). Flat plane indicates the hypertensive stress (Hyper) measured at the tissue level. 124

Figure 3.16: Immunofluorescent imaging of F-actin in native AV histological tissue sections. F-actin stained with TRITC conjugated phalloidin and AVIC nuclei counterstained with DAPI (blue). Arrows indicate F-actin positive staining in AVIC cytoplasm..125

Figure 3.17: Polyacrylamide gel validation of macro-micro model sensitivity to PMMA inclusions. The macro model is fit against the experimental M vs. Δκ bending data (top left). The micro-model then estimates a moduli value for the inclusion stiffness (top right) and is reported in the table (bottom)...126

Figure 4.1: End-loaded tissue sample (a) and the corresponding macro-model simulation (b) which is then mapped down to the micro tissue scale (c) into the micro-model (d). For details of the macro-micro model framework the reader is referred to **Chapter. 3**. 146

Figure 4.2: Aortic valve leaflet illustrating the size and orientation of the circumferentially oriented tissue strips extracted from the intact leaflet for flexure testing. Schematic adapted from [4]. 147

Figure 4.3: Averaged M vs. Δκ experimental data from AV bending study of control tissue (a) and TGF-β1 tissue (b) under inactive (CytoD), normal (5mM KCl) and hypertensive (90mM) conditions and bending with (WC) and against (AC) the natural leaflet curvature. 148

Figure 4.4: Linearized effective moduli from control and TGF-β1 treated tissue taken from the slope of the averaged M vs. Δκ curves in Fig. 4.3 at points of maximum common curvature (0.11mm^{-1}) determined for the inactive, normal and hypertensive states and bending in the WC (a) and AC (b) directions...149

Figure 4.5: Results of micro-model parametric studies estimating changes in AVIC contractility, Δα, between normal and hyper activation states. Δα is plotted for the fibrosa RVE under tensile loading of control tissue (a) and TGF-β1 treated tissue (b). 150

Figure 4.6: Results of micro-model parametric studies plotted in 3D. Effects of AVIC contractility, α, and AVIC stiffness, μ, for the fibrosa RVE under tensile loading are plotted for control tissue (a) and TGF-β1 treated tissue (b). Flat plane indicates the hypertensive stress (Hyper) measured at the tissue level. 151

Figure 5.1: Schematic of microindentation on an AVIC with a 5 micron glass bead (a) and the two different indentation protocols used in the current study. 164

Figure 5.2: Single AVIC cells during indentation using a 5μm AFM cantilever tip (0.03 N/m). 165

Figure 5.3: Effective modulus measurements from microindentation of AVICs under CytoD, Control and TGF-β1 treatments in response to normal activation conditions (5mM). Results are shown for slow (500ms) and fast (100ms) indentation speeds. 165

Figure 5.4: Effective modulus measurements from microindentation of AVICs under CytoD, Control and TGF-β1 treatments in response to hyper activation conditions (90mM). Results are shown for slow (500ms) and fast (100ms) indentation speeds. 166

Figure 5.5: Effective modulus measurements from microindentation of AVICs under CytoD, Control and TGF-β1 treatments in response to hyper activation conditions (90mM). The same results from Fig. 5.3 and 5.4 are plotted side by side to illustrate the strain-rate dependency of the TGF-β1 effect on AVIC stiffness under 90mM KCl conditions. ...167

Figure 5.6: Fluorescent staining of AVICs on collagen substrates immediately following microindentation experiments in 5mM KCl conditions. Images were taken using a constant exposure time to evaluate F-actin (orange), α-SMA (green), nuclei (blue) and α-SMA positive stress fibers seen in composite images (yellow). All images taken with a 63x objective. 168

Figure 5.7: Fluorescent staining of AVICs on collagen substrates immediately following microindentation experiments in 90mM KCl conditions. Images were taken using a constant exposure time to evaluate F-actin (orange), α-SMA (green), nuclei (blue) and α-SMA positive stress fibers seen in composite images (yellow). All images taken with a 63x objective. 169

Figure 5.8: Relative fluorescent quantification of filamentous actin (orange fluorescent in Figs 5.6 and 5.7) between all 5 treatment groups. Fluorescence was normalized to TGF-β1 fluorescence at 90mM, as this group exhibited the greatest intensity of staining. 170

Figure 5.9: Relative fluorescent quantification of α-SMA protein (green fluorescent in Figs 5.6 and 5.7) between all 5 treatment groups. Fluorescence was normalized to TGF-β1 fluorescence at 90mM, as this group exhibited the greatest intensity of staining. 171

Figure 5.10: Relative fluorescent quantification of α-SMA protein colocalized into F-actin fibers (yellow fluorescent in Figs 5.6 and 5.7) between all 5 treatment groups. Fluorescence was normalized to TGF-β1 fluorescence at 90mM, as this group exhibited the greatest intensity of staining.172

Figure 5.11: A schematic of a computational model of the AVICs that incorporates different mechanical constituent of the stress fibers (Top). Resulting contributions of F-actin and α-SMA to the maximum stress fiber contractile strength measured from the developed model. [This work was submitted to the Summer Biomechanics Bioengineering and Biotransport Conference for presentation in June 2012 in National Harbor, MD.] 173

CHAPTER 1: INTRODUCTION

Preface

Heart valves play a critical role in ensuring unidirectional blood flow in mammalian hearts throughout the cardiac cycle. They are engineered to withstand the demanding mechanical environment of the heart and remaining durable through continuous extracellular matrix (ECM) remodeling. This introductory chapter introduces the link between disease-induced alterations in valve tissue and the subsequent cell mechanobiological responses and tissue remodeling. First, an overview of the fundamentals of heart valve physiology and the characteristics and functions of valve interstitial cells (VIC) is provided. Then current experimental and computational approaches that connect VIC mechanobiological response to organ- and tissue-level deformations and improve our understanding of the underlying functional physiology of heart valves are discussed. A summary is provided of future trends the outlook of heart valve mechanobiology, specifically multi-scale modeling approaches. Finally, the motivation, rationale and research aims of this dissertation are outlined emphasizing the importance of investigating AVIC mechanobiological responses while maintaining native valve tissue micromorphology to gain a more accurate representation of clinical AVIC behavior.

HEART VALVE STRUCTURE AND FUNCTION

Heart valves are complex multi-layered structures that serve to prevent retrograde flow in the right and left ventricles by their opening and closing motion caused by differential blood pressure on each side. The heart contains four valves, two residing within the left heart chamber: mitral valve (MV) and aortic valve (AV) and an additional two within the right chambers: tricuspid valve (TV) and pulmonary valve (PV) shown in

Fig. 1.1. Differences in morphology divide them into two categories: atrioventricular (MV and TV) that assist in unidirectional blood flow between the atria and ventricle as the name implies, and semilunar (AV and PV) that direct blood flow from the ventricles out of the heart through major arteries.

When healthy, heart valves are incredibly resilient, opening and closing approximately 4 billion times throughout an average life-span [1]. The valves residing on the left side of the heart (AV and MV) experience 5-8 fold higher transvalvular pressures (TVP) of 80mmHg for the AV and 120mmHg for the MV, compared with the left side heart valves that experience 10mmHg (PV) and 25mmHg (TV) [1]. Although they function as simple check valves that control the unidirectional flow of blood during the cardiac cycle, these complex structures are uniquely adapted to withstand demanding mechanical and hemodynamic environments unlike any other found in the body. Each heart valve is uniquely engineered by nature to optimize their individual roles in the cardiac cycles, enabling them to maximize flow rate while minimizing flow resistance.

Structure of the AV at multiple length scales

The structure of the native aortic heart valve spans multiple length scales: organ, tissue, cell and molecular. This complex hierarchical structure is what lends to seamless heart valve performance under highly dynamic loading conditions. An overview of heart valve structure-functional relationships is provided in **Fig. 1.2**. As this dissertation focuses specifically on the structure-functional relationship at the tissue-cell interface in the aortic valve, the structure and biomechanics of the other three valves will not be discussed in detail. At the organ level the aortic valve is comprised of three cusps named after their locations relative to the coronary arteria ostia in the sinuses of Valsalva: the left coronary, right coronary, and noncoronary. The leaflets cusps attach to the left ventricle at their basal attachment, forming what is known as the virtual annulus and they attach distally to the aortic root at what is termed the aorto-ventricular junction. The leaflets components can be described by four parts: the hinge, the belly, the coapting surface and the lannula with the noduli of Aranti. The nodule of Arantius is a small fibrous area that forms in the center of the cusp, when the closing edge meets the free edge of the leaflet at the coapting surface. On either side of the nodule is a thin cresent-shaped portion called the 'lannula', which is thin at its free end and continues to the coaptation region where the three leaflets come together during valve closure. The lannulae attach to the aortic wall at the commissure region and form the valvular hinge. The main portion of the leaflet is called the belly [2].

At the tissue level, each AV leaflet is a thin (200-500 micron) heterogeneous membrane structure composed of three histologically distinct layers: the fibrosa, spongiosa, and ventricularis (**Fig. 1.3**). Each layer contains varying amounts of collagen, glycosaminoglycan (GAG), and elastin [3]. The fibrosa layer, facing the outflow surface, consists primarily of a dense network of highly aligned type 1 collagen fibers and contributes to about 45% of the valve thickness. The central spongiosa layer, approximately 30% of the leaflet thickness is rich in glycosaminoglycans and water [4]. The ventricularis layer, the remaining 25% of the leaflet faces the left ventricle inflow surface and is composed of elastin and disorganized collagen. Taken collectively, the three layers of the AV with their elastin, collagen and glycosaminoglycans constituents comprise ECM of the valve. In addition to the biomechanical role the ECM plays in valve function, it provides a support structure for the underlying valve cell network. The ECM influences cell behavior by providing a source of ligands for cell surface receptors, which transfer mechanical strains experienced at the tissue level down to the cells and ultimately initiating intracellular signaling pathways [5]. Furthermore, differences in innate mechanical properties of the constituents can influence the underlying function of the cells as suggested by a growing body of research demonstrating that the phenotype and function of cells, including valve cells, are influenced by the stiffness of the substrate to which they are adhered [6].

Valve endothelial cells

Valve endothelial cells (VEC) play an important role in the establishment of valve structure during embryonic development and are essential for maintaining the valve's lifelong integrity and function. Endothelial cells line the surfaces of both blood vessels as well as heart valve leaflets. These cells are critical in the maintenance of a nonthrombogenic surface, nutrient transport, and mechanotransduction [7]. This said, VECs have been shown to be morphologically different from aortic ECs [7-9]. In healthy valves, VECs form a continuous endothelium and have an important role, which consists of regulating vascular tone, inflammation, thrombosis, and remodeling [10]. This function however, is different in malfunctioning and diseased valves in which VECs are disrupted. Heart valve failure has been traced to endothelial dysfunction and denudation [7], giving rise to valve leaflet thickening (sclerosis) and/or calcification and leading to an attenuation of responses to molecular and hemodynamic cues [11, 12].

Many groups have made important insights on endothelial function in different mechanical environments using different *in vitro* experimental set-ups. Endothelial cells reorganize their cytoskeletal filaments and focal adhesion complexes to align parallel to the direction of unidirectional flow while secreting vasoactive agents, such as nitric oxide and prostaglandin [13-15]. Biomechanical stimuli exerted by blood flow, blood pressure, and cyclic strain cause endothelial cells to alter their morphology, growth rate, metabolism, and gene expression profile to ensure proper morphogenesis but also homeostasis. This is done through the activation of surface glycoproteins, cell adhesion molecules, secondary messengers, and phosphorylation of surface receptors [16]. Several groups have investigated the disruption of the endothelial cell mechanotransduction and its effect on cell mechanobiology through the oscillation of fluid flow direction and signal pathway blockade [17-22]. Data from these studies suggested that disruptions in these signaling events inhibit focal adhesion reorganization and consequently, cell alignment and agent release [7].

Although a significant amount of information is available on vascular endothelial cells, little is known about valve specific endothelial cells or VECs. The work by Nerem *et al.* has been instrumental in understanding VEC morphology, mechanobiology, and mechanotransduction. In vitro, VECs grow into cobblestone-like morphology and align perpendicular to fluid flow but parallel to the leaflet collagen fibers [23, 24], in contrast to vascular endothelial cells, which align parallel to fluid flow. The differing shear stress response of valve endothelial stress and vascular endothelial cells is due to observed differential molecular profiles and functional responses of these cell populations [25, 26]. Recent work by Butcher *et al.* indicates that unlike vascular endothelial alignment, VEC alignment to fluid flow is mediated by the reorganization of focal adhesions within the cell and though it is calpain- and Rho-kinase-dependent like the vascular endothelial cells, it is independent of phosphatidylinositol 3-kinase (PI3K) [7].

Pathological changes in vascular endothelial cell-mediated responses have been associated with atherosclerosis, thrombosis, stroke, and hypertension [16]. Valvular heart disease, a major cause of morbidity in the United States and around the world, is not only due to dysfunctional changes in VIC proliferation and ECM organization, but also VEC histopathological alterations. Some light has been recently shed on the events that initiate VEC dysfunction in diseased valves. Both genetic mutations associated with NOTCH1, Gata5, and endothelial-nitric oxide synthase (eNOS or NOS3) [27, 28], as well as atherosclerosis-related environmental risk factors, such as diet [29, 30], smoking, ageing [30, 31], hypertension, and diabetes, have been associated with valve pathogenesis [32]. This said, hemodynamic flow across the endothelium is the major player in the injury and subsequent dysfunction of both vascular as well as valvular endothelial cells. It is known that in the healthy heart, the left side of the heart is subject to greater stress due to the high-pressure difference that exists between the left atrium and the left ventricle. Thus, hemodynamic forces have a greater impact on the mitral and aortic valves than on the tricuspid and pulmonary valves [33, 34]. Similarly, endothelia on opposing sides of the valves are subjected to very different hemodynamics [12, 35, 36], which can be linked to the distinctly different patterns of focal calcification on the aortic side of the AV [37-39]. Several *in vitro* studies have highlighted the link between hemodynamics and VEC molecular responses and linked it to valvular heart disease. Recent work by Simmons *et al.* and Butcher *et al.* indicates that VECs activate fibro-calcific responses to increases in hemodynamic forces (i.e., fluid shear stress, cyclic strain, and hydrostatic pressure) [40] and does so in a side-specific manner (i.e., VECs from the aortic side are protected from inflammatory processes compared to VECs isolated from the ventricular surface) [41].

Valve interstitial cells

Under the single layer of VECs that line both surfaces of the leaflet, reside a heterogeneous population of cells called VICs. VICs native to each of the four valves are named accordingly as MVICs (mitral), AVICs (aortic), PVICs (pulmonary) and TVICs (triscupid). VICs are evenly dispersed throughout the layers of the valve. Within the proximal third of the leaflets, in which innervation occurs, a feedback mechanism between VECs and VICs exists, wherein the nerves transmit information on released substances from VECs [42]. Release of cytokines has been shown to cause changes in interstitial cell structure and function [43, 44] and it was speculated that there exists some physical VEC/VIC communication. This said, no direct junctions have been observed to date between the two cell populations [45]. The role of VICs is to maintain the extracellular matrix (ECM) of the valve through the constant turnover of constituents through the synthesis of new proteins and the enzymatic digestion of old or damaged proteins [46]. The phenotype of VICs is highly plastic and reversible, indicating the state of the tissue from a developing, remodeling, diseased or normal valve. When healthy, VICs have heterogeneous characteristics that resemble most closely those of fibroblasts and smooth muscle cells and are considered to be in a quiescent state [46-49]. During the onset of injury or disease, the VICs are activated and become highly contractile, showing characteristics of myofibroblasts. The myofibroblast-like VICs have been observed both *in-situ* and using cultured porcine valves through electron microscopy and immunocytochemistry. They are characterized by prominent stress fibers expressing alpha smooth muscle actin (α-SMA). The contractile phenotype initiates an increase in remodeling of the ECM, relative to quiescent AVICs. AVICs are physically connected to the surrounding ECM through integrins, facilitating adhesion and mechanotransduction. [46]. Integrins are composed of α and β subunits, giving rise to at least 24 identified integrins with distinct ligand specificities. Integrins make transmembrane connections to the cytoskeleton via proteins such as talin and α-actinin at focal adhesion complexes. The expression of integrins in aortic valves has been investigated by Latif et al. and reported the highest expression for $\alpha_2\beta_{1,}$ and $\alpha_3\beta_1$ complexes [50]. Furthermore, Stephens et al. provided evidence that actin-mediated VIC force generation coupled to collagen via $\alpha_2\beta_1$ integrins is necessary for force generation in the mitral leaflet [51]. These results may suggest that AVIC-collagen coupling, mediated by $\alpha_2\beta_1$ integrins, is also necessary for KCl induced force generation in the aortic leaflet.

Extensive evidence exists in literature emphasizing the role of the microenvironment on cell behavior. The AVICs are no exception and the surrounding ECM defines the AVIC micromechanical environment by providing resistance to cell-generated traction forces. Through integrin-mediated adhesion and actinmyosin contraction, AVICs are able to sense local elasticity of their ECM by physically pulling on the substrate. These exerted traction forces are transmitted to the substrate at focal adhesion sites. AVICs then respond to the detected elasticity by altering integrin expression, focal adhesions, and cytoskeletal organization in order to establish force balance between substrate resistance and AVIC generated traction force. Cytoskeletal organization and tension in turn regulate intracellular signaling pathways. Therefore, changes in the AVIC microenvironment directly impact valve biomechanical function in this manner, leading to clinical manifestations such as calcific aortic valve disease, to be discussed in a proceeding section.

Biomechanical function

At the tissue level, mechanics of the heart valves can be summarized in three physical loading modes: tension, shear, and flexure. In a cyclical manner the valve opens (flexure), blood passes (shear), the valve closes (flexure) and retrograde blood flow is prevented (tension) (**Fig. 1.4**). Due to the higher prevalence of disease and surgical repair, most research on HV biomechanics has been carried out on the AV [9, 33, 52-58] and MV [59-62]. In healthy individuals, the AV opens during ventricular contraction for 200-300ms, also known as systole, and closes during ventricular relaxation, diastole, with blood flowing through the AV at a peak velocity of 1.35 ± 0.35 m s^{-1} [63]. Valve closure occurs at the end of the deceleration phase of systole with minimal backflow through the valve. This motion creates adverse axial pressure differences along in the developing boundary layer along the aortic wall, causing the inertial flow in this region to decelerate and then, reverse direction, creating vortices in the sinuses behind the AV leaflets. [64]. The creation of these vortices facilitates the closing and coaptation of the AV leaflets. When coupled with the vortices that push the leaflet surfaces towards the closed position, this force leads to a very fast and efficient closure of the valve.

Time dependent behaviors

Our group, along with others, [65-67] have conducted biomechanical tissue analyses at quasi-static (strain rates of 4%/s to 12%/s) experimental conditions and showed that heart valve leaflet deformations can reach strain rates as high as 300%/s, raising an important question on the link between HV quasi-static leaflet mechanical properties and HV physiology. Although strain-rate dependence has been extensively studied in soft-tissue biomechanics, the literature indicates a wide range of findings that are dependent on the specific tissue composition and structure as well as the specific testing methods utilized to characterize it. Thus, to be able to model physiological functions and understand the strain rate dependence of a particular tissue, one needs to property investigate it and quantify its mechanical properties under realistic physiological loading states.

As previously mentioned, the fibrosa layer is composed predominantly of a dense network of collagen fibers and is thought to be the major stress-bearing layer. Collagen fibers have low torsional and flexural stiffness, yet can withstand high tensile forces. As a result, fiber orientation can be used to identify directions in which the tissue is able to withstand the greatest tensile stresses. In this technique, a laser light is passed through a tissue specimen and is then scattered. The spatial intensity distribution of the resulting scattered light represents the sum of all structural information within the light beam envelope. To quantify the changes that occur in AV leaflet structure with increasing transvalvular pressure (TVP), fresh porcine AVs were fixed at TVPs ranging from 0 to 90 mmHg and imaged using small angle light scattering (SALS). Overall, increasing TVP induced the greatest changes in fiber alignment between 0 and 1 mmHg, and past 4 mmHg there was no detectable improvement in fiber alignment **(Fig. 1.5b-d).**

The method of Hilbert *et al.* [68, 69] has previously been used to quantify the amount of collagen fiber crimp in the native pulmonary and aortic HVs by identifying the cross-sectional regions that displayed observable crimp [70].[70] It was found that at 0 mmHg, approximately 60% of the AV transverse cross-sectional area was occupied by crimp structure (**Fig. 1.5b**). As the TVP increased, the percent crimp decreased rapidly until 20 mmHg, with minimal decreases in percent crimp thereafter. For the AV, much of the observed change in collagen structure is due to the finely tuned straightening of the collagen fibers, which must occur at the right strain level and at the right rate to facilitate coaptation without allowing excessive tissue deformations that could lead to regurgitation. The unique structure of the commissure region, which approximately corresponds to the coaptation region, highlights the adaptive structure of HVs. Instead of undergoing TVP differences, the coaptation region is loaded in a uniaxial-like manner due to tethering forces generated at the attachment of the commissures to the aortic root. Unlike the biaxially loaded belly regions of the valve, the uniaxial loading of the commissures makes them more highly aligned, similar to tendon. Fiber uncrimping with stress occurs very rapidly for this highly aligned fiber network, as demonstrated by the short transition region from low to high stiffness. The highly aligned nature of the commissure region at unloaded state and the more rapid realignment with TVP in the commissure regions are consistent with the pre-transition strain level behavior of tendon-like materials.

It has been demonstrated that the individual layers of the aortic valve are not only vastly different in their structure, but also in their mechanical behavior. Two key studies have investigated individual layer behavior of the AV leaflet. Vesely et al. observed the extensibility of intact tissue under uni-axial tension to be significantly different from the individual layer responses [71]. Stella et al. also observed measurably different behaviors under bi-axial loading of separated layers, and reported the intact tissue response to be intermediate to the separated responses [72]. Due to these consistently observed differences in layer behavior, examining the leaflet in an intact state is far more physiologically relevant. Flexural loading of the leaflet allows the leaflet to undergo tensile and compressive loading of each layer by bending with and against the natural leaflet curvature while still remaining intact.

Flexural deformation

Flexure is a major deformation mode of the cardiac cycle [73, 74] and has been extensively used for valve tissue mechanical studies [75-79]. Experimental measurements of the flexure of soft biological materials has two advantages over tensile mechanical testing: 1) the ability to discern very small changes in stiffness at low stress-strain and 2) the ability to assess the contributions and interactions of individual layers of multi-layered structures.

Thus, multi-layered tissue, such as the AV leaflet is expected to reveal a distinct bending response in each direction of bending. As a result, flexural mechanical testing techniques provide a sensitive way to explore the effects of layer-specific contributions to the overall biomechanical function of the AV. Our group has used circumferential strips of porcine AV leaflets to quantify the flexural properties of the belly region (**Fig. 1.5a**) and experimental details have been previously reported [75, 78, 80]. It is important to note that in the unloaded state, the AV leaflet exhibits a natural curved shape both in the circumferential and radial directions. Therefore, the change in curvature $\Delta\kappa$ (in units of mm^{-1}) from the initial unloaded reference state is used to account for the initial curvature of the test specimen. Applying bidirectional flexure can subject both the fibrosa and ventricularis layers to alternate states of tension and compression (**Fig. 1.6a** and 1.**6b**). These flexural directions are referred to as "with curvature" (WC) and "against curvature" (AC), both of which are with respect to the direction of the natural leaflet curvature. The effective stiffness measured in the WC direction is dominated by the ventricular tension with little contribution form the fibrillar collagen in the fibrosa, which is not designed to support compressive loads. On the other hand, when the leaflet is bent in the AC direction, the fibrosa is in tension and the ventricularis is in compression. Data from this study shows how the applied bending moment (M) changes with $\Delta\kappa$. The Euler-Bernoulli equation $M = EI\ \Delta\kappa$ [81], where E is the effective stiffness and I the second moment of inertia, can then be used to estimate the effective (i.e. total) bending stiffness. The moment (M)-change in curvature ($\Delta\kappa$) response of the AV leaflet was found to be linear (**Fig. 1**.**6c** and **1.6d**). This is due to how tissue layers are loaded and can be explained by the micromechanical mechanisms underlying the flexural response, which are quite different than those that play a major role in in-plane tension.

Throughout this body of work, flexural loading is used as the primary mode of deformation for all experimental studies. AV leaflets experience complex bidirectional flexure *in vivo* [82, 83], so to simplify the problem, we focused on bending in the circumferential direction only, as it is the major curvature change in leaflets [84]. As discussed in detail in **Chapter 2**, an appropriate nearly incompressible hyperelastic constitutive model was selected that captures the macroscopic bending behavior of the AV leaflets initially. As the work progressed, this model was modified to incorporate a bimodular component, similar to approaches used in modeling other types of fibrous tissues. [85, 86]. This enabled the model to capture experimentally observed bidirectional differences in the AV bending behavior [75].

AV DISEASE AND TREATMENT OPTIONS

According to Heart Disease and Stroke Statistics—2016 Update published from the American Heart Association [87], valvular heart disease accounts for 24,608 deaths. Disease of the aortic valve is the most prevalent, accounting for 16,908 of the deaths and was a contributing factor in 33,931 cases. The prevalence and incidence of heart valve disease will continue to rise with the aging population and rise in life expectancy.

Calcification is the primary cause of AV failure and currently there exists no proven therapy for halting this progression. Calcified aortic valve disease (CAVD) is a slow, progressive, multi-factorial disorder that is more common with age, without being an inevitable consequence of aging [88-92]. The disease is characterized by a thickening and calcification of the leaflets and is diagnosed in two stages: aortic sclerosis (ASc) and aortic stenosis (AS). ASc, present in more than 25% of patients over the age of 65 [93], represents the early onset of CAVD absent of physical obstruction to the left ventricular outflow. Aortic stenosis exists in 2-5% of the elderly population [93] is characterized by late stage obstruction and associated with impaired leaflet motion, valve tissue adaptation, and resistance to blood flow [94-97]. Although aortic sclerosis causes significant thickening of the AV leaflets, there is little to no change in the mechanical properties of the valve, making the disease relatively asymptomatic. Recent statistics have shown that within 10 years of their initial diagnosis, 10% of aortic sclerotic patients reach a state of severe CAVD that requires immediate AV replacement once symptoms emerge [96]. Despite its clinical prevalence, a limited number of studies have investigated the active cellular process underlying the progression of this disease. Currently, over the last 2 decades research has revealed the disease to be a biologically active process with similarities to atherosclerosis but also with several key differences [98]. One difference is that the hallmark indicator of atherosclerosis is unstable lipid plaque, whereas the hallmark of CAVD is severely progressed calcification that causes physical stiffening of leaflets and can lead to physical obstruction (stenosis) of the AV. More studies must be done to understand contributing mechanisms such as shear forces, genetic factors and regulators of myofibroblast differentiation and osteoblastic calcification. Additionally, it is now understood that significant changes occur at the structural level, changing the organization, composition and mechanical properties of the extracellular matrix (ECM) [99]. The pathological disruption of the AV's normal structure leads to calcification causing the tissue to become thicker and stiffer, ultimately leading to a decreased orifice area and thus, stenosis. The resulting abnormal biomechanics cause lifelong valvular dysfunction, which will ultimately require surgical valve replacement.

AS has been identified as the end-stage of CAVD that progresses from the microscopic early changes of AVSc to, in a subset of patients, asymptomatic and then symptomatic AS [91, 100, 101]. Once AVSc is detected **(Fig. 1.7),** there is an increased risk of cardiovascular events**,** as shown by deviation of the survival curve (purple line in **Fig. 1.7**) from the expected event-free survival (light blue line in **Fig. 1.7**). In early AS, when mild symptoms begin to present, survival rates deviate much more than expected and decline dramatically with the onset of severe symptomatic AS. Over the last decade, several clinical trials, mostly extensions of atherosclerosis-related studies, have been performed to halt the progression of CAVD with randomized studies showing substantial equivalence between treatments and placebo [102-106]. However, there are currently no pharmacological therapies available to treat CAVD symptomatic patients that are considered superior to full valve replacement surgery.

In order to impact the progression of the disease, we need to understand both subclinical and symptomatic stages so we can measure targeted therapy before aortic valve sclerosis proceeds to advanced stages. It is important to link organ-level and tissue-level stresses to cell response and ultimately, to AVIC mechanotransduction, in order to fully understand the function and homeostatic response of the AV to altered local tissue stress.

AV replacements

Currently, full valve replacement remains the gold standard of care for dysfunctioning aortic valves. Since the development of the first replacement valves in the 1950s [107], significant advancements have been made in the realm of valve replacements. In the United States alone, more than 80,000 valve replacement using either bioprosthetic or mechanical valves per year and more than 300,000 worldwide [108]. There are several types of replacement valves available including transcatheter, mechanical, and bioprosthetic replacement valves that are available by Edwards Lifesciences, Medtronic, St. Jude Medical, Sorin Group, Boston Scientific and others [108]. Transcatheter aortic valve replacement (TAVR) is a minimally invasive procedure that replaces the aortic valve by wedging a replacement valve into it its place by way of a catheter. This novel approach circumvents the need for open heart surgery, providing an option for patients who only 10 years ago would be considered high risk surgical candidates and been denied surgical intervention. Mechanical valves have evolved significantly since the first ball-and cage design, spanning a variety of shapes sizes and materials and rarely experiencing mechanical failure. Currently, the most common mechanical design for an aortic valve replacement is the bileaflet design that consists of two semicircular discs surrounded by a sewing ring [108] shown in **Fig. 1.8** (Left). Despite success with mechanical valve replacement outcomes, patients must rely on lifelong anti-coagulation therapy with a vitamin K antagonist to prevent valve-associated thrombosis and thromboembolic stroke. However, this can lead to an increased risk of major bleeding and other complications such as hemorrhagic stroke [109]. The primary advantage of a mechanical valve over a bioprosthetic valve is its durability and is often indicated for use in younger patients. The design of mechanical valves is becoming increasingly more advanced as we gain a gain a deeper understanding of native valve biomechanics and fluid dynamics through both computational model and experimental techniques.

Bioprosthetic heart valve (BHV) replacement options more closely resemble the native anatomy of the aortic valve. The most common bioprosthetic option is either a three porcine valve leaflet cross linked with glutaraldehyde or bovine pericardium (xenografts) [110] shown in **Fig. 1.8** (Right). Less common bioprosthetic options are to replace the diseased valve with allografts and autografts without a stent or sewing rings [110]. Bioprosthetic replacements have a more flexible and biocompatible surface for improved blood flow dynamics which mitigates the need for anticoagulation. BHVs tend to have complications over time due to leaflet deterioration and must be replaced within 15 years in 50% of patients. However, the advantage of using a BHV is it provides a more physiologically realistic flow profile and does not require lifelong anticoagulation therapy.

Ultimately, understanding valve structure and the that exists between scales in healthy and diseased valves is an integral component towards the ultimate goal of engineering tissue valves that structurally and functionally resemble native valves. Thus, it is imperative that fundamental structure-function understanding guides the reproduction of native tissue if it is to emulate its native counterpart successfully. The complex nature of valve biomechanical behavior and function [1] cannot be duplicated with simple homogenous biomaterials. Consequently, to develop replacement valvular tissues we must more fully understand the fundamental micromechanics of the tissue in both healthy and diseased states.

CELL-LEVEL MECHANOBIOLOGY

In biomechanics, the presence of normal tissue stresses is considered to be closely related to tissue homeostasis [111-115]. Strong correlations exist between mechanical stresses and heart valve biology and have been well documented by clinical observations and animal studies [116-120]. Many studies have shown that pathophysiological alterations in mechanical loading lead to stress changes and tissue adaptation that affect tissue structure and composition [121, 122]. In heart valves, the ECM not only provides the tissue with its structural integrity, but it also influences cellular processes through three different mechanisms: 1) matricellular, in which the ECM signals through adhesion receptors, 2) matricrine, which regulates growth factor and cytokine expression in cells, and 3) mechanical, which can be characterized as either matrix elasticity or external forces [99]. In mechanical signaling, the ECM can transmit external forces, such as stretch, shear stress, and pressure to the cells, but it can also regulate cellular function through its intrinsic composition and elasticity. The mechanical interaction of VICs with the surrounding ECM, particularly with the collagen fibrils, is fundamental to its cellular response. The intrinsic ECM composition and its importance in modulating cellular response are apparent in ultrastructural studies by our group, which reveal the micromechanical environment of the cell and highlight the intimate contact between the collagen fibrils and the VIC. Collagen fibrils are circumferentially oriented and the VICs are aligned along the same direction. In heart valves, pathological factors, such as tachycardia-induced cardiomyopathy [123], mitral regurgitation [124], and CAVD [125] have been shown to affect valve tissue structure and composition. The link between tissue-level deformations and ECM remodeling is essential in understanding cardiovascular and in particular, heart valve disease and pathologies.

AVIC contractility has been qualitatively studied with cultured cells on silicone substrates in the presence of multiple contractile chemical agents [45, 126]. In both of these studies, contraction occurred for most agents within 3 minutes and reached a plateau within 10 minutes. The few cells that did not have an initial basal tonus did not respond to the administered vasoconstriction drugs. Isoproterenol was used to elicit relaxation from active cells, from which all cells recovered their previous basal tonus within 25 minutes. Although they do not provide any quantitative information, these findings were the first to demonstrate AVIC contractile response and shed light on VIC contractile behavior.

VIC deformation under physiological loading

The extremely low forces generated by AVICs during contraction are unlikely to directly affect valvular function. This said, VICs are a dynamic source whose biosynthetic capabilities serve an important role in maintaining overall valve leaflet tissue homeostasis. *In vitro* studies of VICs indicate that these cells increase their collagen synthesis in the presence of vasoactive agents, suggesting that VICs use their contractile elements to mechanically communicate with the local microenvironment [127]. The local stress-strain fields in the vicinity of a cell are dependent on a number of factor, including but not limited to, cell shape, orientation, and the relative mechanical properties of the cell and the surrounding ECM [128]. Thus, it is not clear how the pressures imposed on different sides of the heart translate into local stress on the cells. To link observed valve leaflet tissue deformation to cell deformation, our group performed a study on the effects of transvalvular pressure (TVP) on AVIC deformation [129]. As described previously [53], porcine AV leaflets were fixed under varying pressures and Movat stained histological sections were imaged and analyzed. We chose to use AVIC nuclear aspect ratio (NAR), defined as the ratio of the length divided as the width, as an index of overall cellular deformation. Since the AV leaflets consist of histologically-distinct layers with different ECM structural components, we hypothesized that there may be a relationship between the valve tissue layer and the resulting deformation experienced by the cells that reside within that layer under varying applied transvalvular pressure. Results, which were presented as AVIC NAR vs. normalized thickness, indicated that AVIC nuclei underwent minimal deformation at low transvalvular pressures (0 and 4 mmHg) and in fact, maintained an almost constant level toward the ventricularis layer (**Fig. 1.9a**). While there were no detectable changes under 0 mmHg, fibrosa layer AVICs had a slightly higher NAR at 4 mmHg. As expected, high transvalvular pressure (90 mmHg) resulted in much higher aspect ratios in AVIC nuclei than the zero- and low-pressure groups, with a clear demarcation in the fibrosa layer. It is important to note the magnitude of NAR ~5 at 90 mmHg, which highlights the profound region-specific cellular deformations that occur under physiological pressure levels. These deformations occur very rapidly, within ~75 ms, further emphasizing the ability to VICs to withstand stress in a dynamic environment.

The role of VIC contraction as it relates to valve function remains poorly understood. However, it has been established that mechanical forces regulate AVIC physiology by modulating their biosynthetic activity. In Merryman et al. [33], it was shown that VICs residing on the left side of the heart (MVICs and AVICs) not only experience higher transvalvular pressure, but also have a greater measured stiffness measured by micropipette aspiration (**Fig 10a-b**) compared to VICs residing on the right side of the heart (TVICs and PVICs). In addition to this finding, the study showed a strong correlation between increased VIC stiffness and an upregulation in α-SMA and Heat Shock Protein 47 (a molecular chaperone protein involved in collagen production) (**Fig. 1.10c**). By comparing left and right side VICs of the heart, and revealing these intrinsic differences in mechanical properties, the substantial influence of the surrounding microenvironment on the VICs and the associated biosynthetic activity is quite apparent. To further drive home the significance of the VIC microenvironment we turn to a similar study also my Merryman et al. [130]. The stiffness of AVICs and PVICs were compared using a different ex-situ measurement technique, atomic force microscopy. Observed differences between the VICs on each side of the heart were found to be the same as reported from micropipette aspiration (approximately a two-fold increase in stiffness for AVICs), however the magnitude of the stiffness measurements were approximately 10 fold higher than the micropipette values. This discrepancy between measurements taken of non-adherent VICs (micropipette) and VICs seeded on a 2D substrate (AFM) further illustrates the substantial influence of the VIC microenvironment on measured properties. Currently, the only means of measuring the mechanical properties of VICs, or any other cell, is through ex-situ techniques, such as the above mentioned micropipette aspiration and atomic force microscopy, that are not representative of the native VIC microenvironment as they require physical removal of the cell from its native tissue.

Ex-situ methods of measuring cell stiffness

Micropipette Aspiration

Micropipette aspiration (MA) is used on live cells to evaluate their time-dependent deformation under a uniform pressure. The cell is taken up into a glass tube with a chosen inner diameter in a step-wise fashion. The typical range for applied pressure is 0.1-1000 Pa and has a claimed resolution of 0.1Pa. The exerted pressure is maintained for varying time durations and the extension of the cell in the tube and displacement of the membrane are monitored using optical and light microscopy respectively. The cells are unable to adhere to the inner pipette wall as they are coated with 1% agar. The exerted pressure and whole-cell deformation are then correlated using the following equation:

$$F = \pi R_p^2 \Delta p \left(1 - \left[\frac{x_p'}{x_a'}\right]\right) \qquad (1)$$

Where R_p^2 is the micropipette radius, Δp is the applied aspiration pressure and $\frac{x_p'}{x_a'}$ is the ratio of cell velocity in the presence (x_p') over the absence (x_a') of applied pressure. An appropriate viscoelastic model is then needed to calculate the elastic modulus and apparent viscosity of the cell membrane as well as the time constants for deformation/relaxation.

Atomic Force Microscopy (AFM)

Atomic Force Microcopy (AFM) is a specific type of scanning probe microscopy. Images are created by a local application of mechanical force across the sample's surface using a sharp tip positioned normal to the flexible cantilever. The cantilever tip displacement is tracked by a laser that reflects off the back surface of the cantilever onto a photodiode. The voltage is then converted into displacement. This technique is said to give Angstrom-scale accuracy and allows the advantage of imaging and mechanical stimulation simultaneously. A distinction to note with AFM is that it is performed on adherent cells opposed to micropipette aspiration, which is performed on free-floating cells.

Measurable AVIC changes in-situ

The flexural mechanical testing techniques described earlier are sensitive enough to explore the effects of cellular contraction on leaflet mechanical properties. These techniques were used by several groups, including our own, to investigate regional and directional receptor-mediated contractile response of AV leaflet tissue [131, 132]. As described previously [133], circumferential strips of porcine AV leaflets were mechanically tested under flexure in both the WC and AC directions in a normal state, under contraction (induced by potassium chloride), and without contraction (i.e., contraction inhibited by thapsigargin). Results revealed a 48% increase in leaflet stiffness with AVIC contraction when bent in the AC direction ($p = 0.004$) and only a 5% increase when bent in the WC direction (not significant) in the active state (**Fig. 1.6b**). The thapsigargin treated group (contraction-inhibition) experienced a 76% ($p = 0.001$) and a 54% ($p = 0.036$) decrease in leaflet stiffness, in the AC and WC directions respectively at 5 mM KCl levels. Contraction was completely inhibited with the addition of 90 mM KCl as expected (**Fig. 1.6c**). This bidirectional difference in observed bending behavior is indicative of varying ECM mechanical properties between the layers as well as possible differences in AVIC connectivity throughout the layers. While these results demonstrate that AVIC contractile ability is a significant contributor to AV leaflet bending stiffness, its complete role in maintaining AV leaflet tissue homeostasis has yet to be elucidated. The most important finding from this work was that AVIC contractility is not only contributing to AV bending stiffness, but flexure testing is a valuable tool for measuring these changes at the tissue level. The limitation is that these changes are simply observed at the tissue level. To assess changes at the AVIC level, this experimental tool must work in a cohesive manner with computational modeling to map down to the micro-scale.

COMPUTATIONAL MODELING APPROACHES IN BIOMECHANICS

Computational modeling is a valuable tool for investigating the mechanics the heart valves. Due to complex valve anatomy and dynamic biomechanics, there exists no standard approach. As Malvern (1969) once described, a continuum-based constitutive relation describes the gross behavior of a material, which results from its internal constitution, in response to applied loads [134]. However, it is important to recognize that there exists no single ideal constitutive relation that will describe all possible behaviors of a material under all possible conditions. All heart valves exhibit highly non-linear stress-strain relationships, large deformation, viscoelasticity and poorly understood coupling behavior that is difficult to capture using simple experimental methodology and traditional material models. Extensive constitutive material models, including more advanced structural material models, have been developed that effectively capture the broad spectrum of material properties of biological soft tissue [135, 136] in general and valve specific behavior under different loading configurations relevant to the cardiac cycle [136, 137]. To solve the complex governing equations that dictate valve solid mechanics, a discretization must be employed and solved using a numerical approach. In the field of solid mechanics, the finite element (FE) is the most commonly utilized approach, and the method utilized in this dissertation.

A variety of different methods have been developed for studying different aspects of valvular behavior including but not limited to varied anatomical parameters, different portions of the cardiac cycle, fluid dynamics and different material characteristics. In the past two decades, many groups have conducted intensive research on predictive heart valve computational models. Advances in numerical modeling and experimental biomechanics have enabled these newly developed models to become increasingly comprehensive and accurate. For the MV for example, studies have included development of constitutive models [138-142], image-based patient-specific computational models [143-146], fluid-structure interaction modeling [147, 148], inverse models that enable the assessment of the *in vivo* biomechanical properties [149, 150], and coupled modeling of the left ventricle and MV for investigating ischemic MR [151]. For example, Einstein *et al.* modeled the transient vibrations of the MV by constructing a dynamic nonlinear fluid-coupled finite element model of the valve leaflets and chordae tendineae [147, 152]. The application of physiological pressure loads results in valvular movement and small-scale acoustic vibrations of the valvular structures. Material changes that preserved leaflet anisotropy were found to preserve overall valve function. On the other hand, material changes that altered leaflet anisotropy had a profound effect on valvular function. These changes were manifested in the acoustic signatures of the valve closure sounds. Abnormally, stiffened valves closed more slowly and were accompanied by lower peak frequencies. Driessen *et al*. [153, 154] developed a finite-element (FE) model that relates changes in collagen fiber content and orientation to the mechanical loading condition within engineered heart valve constructs, hypothesizing that collagen fibers aligned with principal strain directions and that collagen content increased with fiber stretch. Results from this study indicate that the computed preferred fiber directions are very similar to experimental data from native aortic heart valves. Although these models are a step towards the development of more physiologically relevant models of heart valve structure and function, there is a still a need for true dynamic models that couple tissue (solid) and blood (fluid) and include cell-level interactions. This said, investigators face theoretical, computational, and experimental challenges that makes this a difficult feat.

INTEGRATED COMPUTATIONAL-EXPERIMENTAL APPROACHES IN BIOMECHANICS

As in all areas of scientific investigation, experimental data are necessary and must be used to acquire data on the heart valve response to different stress levels at all size scales. When integrated with computational models, it can provide unique insights into the function and physiology of heart valves and provide a powerful platform that can generate confirmable predictions of heart valve physiological behavior and ultimately, link organ-level and tissue-level deformations to cellular responses. Computational models that are linked to experimental data are formed during three distinct phases in the model development process: observation, fitting, and validation [155]. Below are two examples of this approach from our research group, in addition to the work presented in this dissertation.

Layer specific MVIC-ECM coupling. More recently, several groups have linked tissue-level induced stress and the resulting MV interstitial cell (MVIC) deformation to abnormal biosynthetic activity that can lead to reduced tissue-level maintenance and subsequent organ-level failure. To link tissue-level loading and cellular response and thus, gain more insights into MVIC mechanobiology, an integrated experimental-computational approach was developed that informs us on MVIC biophysical state. First, the *in situ* layer-specific MVIC deformation were quantified for all four layers of the MV under controlled biaxial tension using a biaxial stretching device that is coupled to a multi-photon microscope [156] **(Fig. 1.11).** Then, a macro-micro finite element computational model was used to explore the relationship between layer-specific mechanical and structure properties and MVIC stiffness and deformation. The experimental results indicate a significantly larger deformation in both the ventricularis and fibrosa layers of the MV compared to the spongiosa and atrialis layers, with a nuclear aspect ratio as high as 3.3 at the maximum physiological tension of 150 N/m. The simulated MVIC moduli however were found to be relatively similar and within a narrow range of 4.71–5.35 kPa (**Fig. 1.12 and 1.13**). This is an important finding that suggests that MVIC deformation is controlled by the structure and composition of the microenvironment rather than intrinsic cellular stiffness. From this finding, it can be concluded that while MVICs may phenotypically similar throughout the layers of the leaflet, they experience different mechanical stimuli from the layer-specific microenvironment in which they reside.

Isolated VIC behavior. We recently developed a novel solid-mixture model for VIC biomechanical behavior that captures the modulating mechanical responses of VICs resulting from different activation sates and loading conditions [157]. One major driver for this study was the 100-fold disparity, indicated earlier, between the micropipette and AFM VIC moduli observed, where the micropipette estimated a ~0.5 kPa modulus **(Fig. 1.10)** while the AFM exhibited a ~50 kPa modulus **(Fig. 1.14b).** While differences in experimental loading configurations may account for some of the observed differences, the major discrepancies in activation states (MA – inactivated, AFM – highly activated) are likely the major underlying cause.

To explore this hypothesis, we developed the following model, which incorporated: (1) the underlying cytoskeletal network, (2) the α-SMA stress fibers, and (3) a finite deformable elastic nucleus. In order to handle the material and geometric nonlinearity, we implemented the model in a 3D finite element simulation and calibrated the model parameters using combined mechanical responses of VICs in both micropipette aspiration (MA) and atomic force microscopy (AFM) experiments [33, 130] (**Fig. 1.14**).

We then used the resulting model to examine the mechanical responses of both aortic and pulmonary VICs (AVICs and PVICs, respectively) in both their inactivated states (during MA experiments) and activated states (during AFM experiments) **(Fig. 1.15).**

The resulting simulation indicated that AVICs exhibit 9 to 16 times stronger intrinsic contractile responses to PVICs, highlighting the model's ability to predict the cellular stiffening that is caused by the underlying α-SMA fiber contraction (**Fig. 1.16).** We used the same model to calculate traction forces exerted by the VICs on the substrate and found good agreement with previously reported traction force microscopy results. The estimated nuclear stiffness for both AVIC and PVIC were similar and comparable to the literature, and were unaffected by VIC activation level. Results from this study highlight that in inactivated states, the α-SMA fiber stiffness is the main contributor of the underlying cytoskeletal stiffness, suggesting that any increases that are seen in VIC stiffness when it changes from inactive to active state are due to the contraction of the α-SMA fibers. Although we chose to follow a continuum approach, such a model can be easily incorporated into a multiscale model of the heart valve, wherein the multi-scale model is used to answer important questions on the mechanics and mechanobiology of heart valve disease and surgical repair.

MOTIVATION, RATIONAL, AND SPECIFIC AIMS

As demonstrated in the preceding sections, AVICs are tightly coupled with the surrounding ECM. The necessity of maintaining VIC-ECM coupling in actin-mediated VIC force generation has been demonstrated in mitral valve leaflets [51] and likely exists in AV tissue as well. The ability to assess AVIC responses *in situ* can lead to further understanding of AVIC-ECM mechanical coupling in response to physiological conditions synonymous with valvular disease. The thinness of the valves allows the stimulation of underlying AVICs with chemical cues [158-160], making the AV an ideal platform for *in situ* investigation. While advances have been made toward the understanding of isolated AVIC behavior (*ex situ)*, the AVIC biomechanical state (specifically stiffness and contractile state) in its native microenvironment remains largely unknown. Consequently, changes in AVIC stiffness and contractility resulting from pathological conditions *in situ* remain unidentified**.** This suggests a **need for novel methods that maintain this coupling for probing the effects of mechanical and chemical stimuli on AVIC biomechanical state.**

To address the need for an *in situ* estimation tool of AVIC biomechanical state, a novel integrated computational-experimental approach was developed. Specifically, a computation model was developed and paired with biomechanical experiments to probe AVIC stiffness and contractility responsiveness in normal and TGF-β1 treated AVs. To provide both validation of an *in situ* approach and further insight, microindentation studies of ex-situ cultured AVICs were carried out. Computational models provide a means of investigating experimentally acquired data from *in vitro*, *in situ* and *in vivo* methods. Taken independently, theoretical simulations are only as accurate as the information we provide them and are often limited by insufficient availability of data. Similarly, experimentally acquired data is often difficult to interpret without the aid of mathematical theory. Taken in cohort, an integrated computational-experimental approach can be used to more accurately interpret experimental findings and push computational models even further in their biological accuracy.

The primary goal of the integrated computational-experimental approach is to estimate AVIC biomechanical state while maintaining layer-specific native AVIC-ECM mechanical coupling. Predicting the biomechanical state of AVICs *in situ* provides a significant advantage in that they remain in the native microenvironment, maintaining essential AVIC-ECM coupling. We hypothesize that deriving the biomechanical state of AVICs *in situ* will reveal more accurate information regarding AVIC adaptations to various stimuli. By studying the AV under flexural deformation, layer-specific information regarding AVIC responses can be obtained. Such an approach can reveal important changes resulting from pathological states and corresponding pharmaceutical interventions. This research approach will be addressed using the following specific aims:

Specific Aim 1. Develop a model of the AV leaflet that captures non-viable tissue level behavior

An integrated experimental-computational investigation utilizing flexural deformations of intact AV leaflets will be used as a means to probe layer interactions. This will inform us of individual layer contributions to observed bending in the AV. Parametric simulations of layer interactions will be conducted using a tri-layered leaflet tissue finite element (FE) model to simulate interlayer sliding hypothesized to occur. To validate these findings and further refine the model, experimental studies on porcine AV leaflet tissue will be conducted to examine the bi-directional flexural response, and relative interlayer movement using actual transmural strain responses.

Specific Aim 2. Develop and validate a micro-anatomically realistic macro-micro FE model to estimate i*n situ* AVIC mechanical behavior under activation.

As a first step to developing the model of the normal AV, the non-viable tissue model developed in SA 1 will be extended to formulate a macro-micro FE model to simulate mechanical behavior of viable AVICs under activation. This provides a novel method of extracting AVIC mechanical properties in their native *in situ* environment by utilizing flexure experimental data. The role the AVIC-ECM connection plays in the AV tissue response at different activation states will assessed.

Specific Aim 3. Measure the layer dependent contractile response of AVICs *in situ* using the developed macro-micro model in a simulated pathological state and validate measured responses against microindentation experiments.

To understand differences in AVIC contractile responses due to varied layer connectivity, AVIC contractile responses were measured in-situ using novel experimental biomechanical studies performed with normal and TGF-β1 (pathological) treated porcine AV tissue under flexural loading. The multi-scale FE model developed in SA 2 was used to evaluate how TGF-β1 affects tissue level bending behavior in the AV due to changes in underlying AVIC-ECM coupling and AVIC stiffness. Finally, microindentation studies examining AVIC activation will be run in parallel with *in situ* studies to validate the *in situ* approach. We hypothesize that observed differences between ex-situ and in-situ measurements will further support the need for an *in-situ* assessment approach of AVIC biomechanical state.

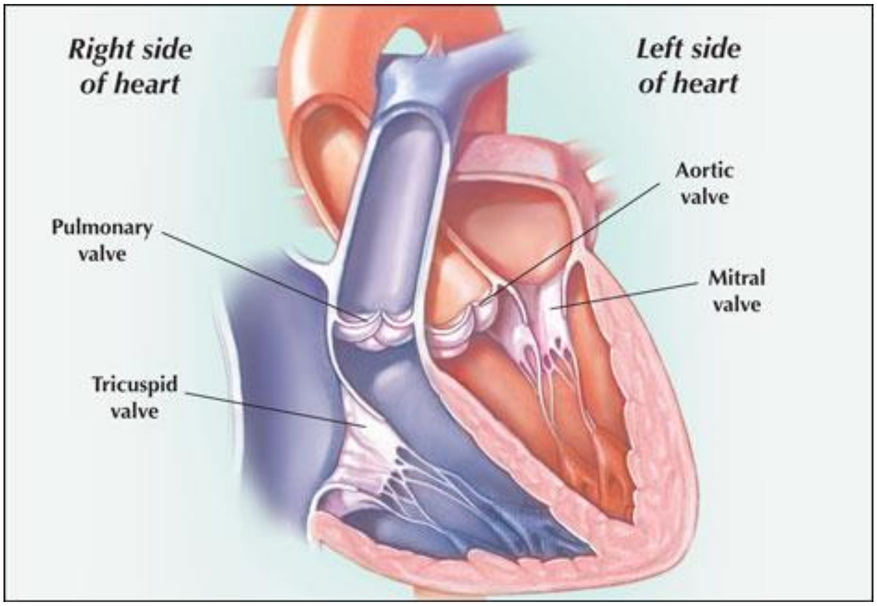

Figure 1.1: Schematic depicting the location of the four heart valves (mayoclinic.com).

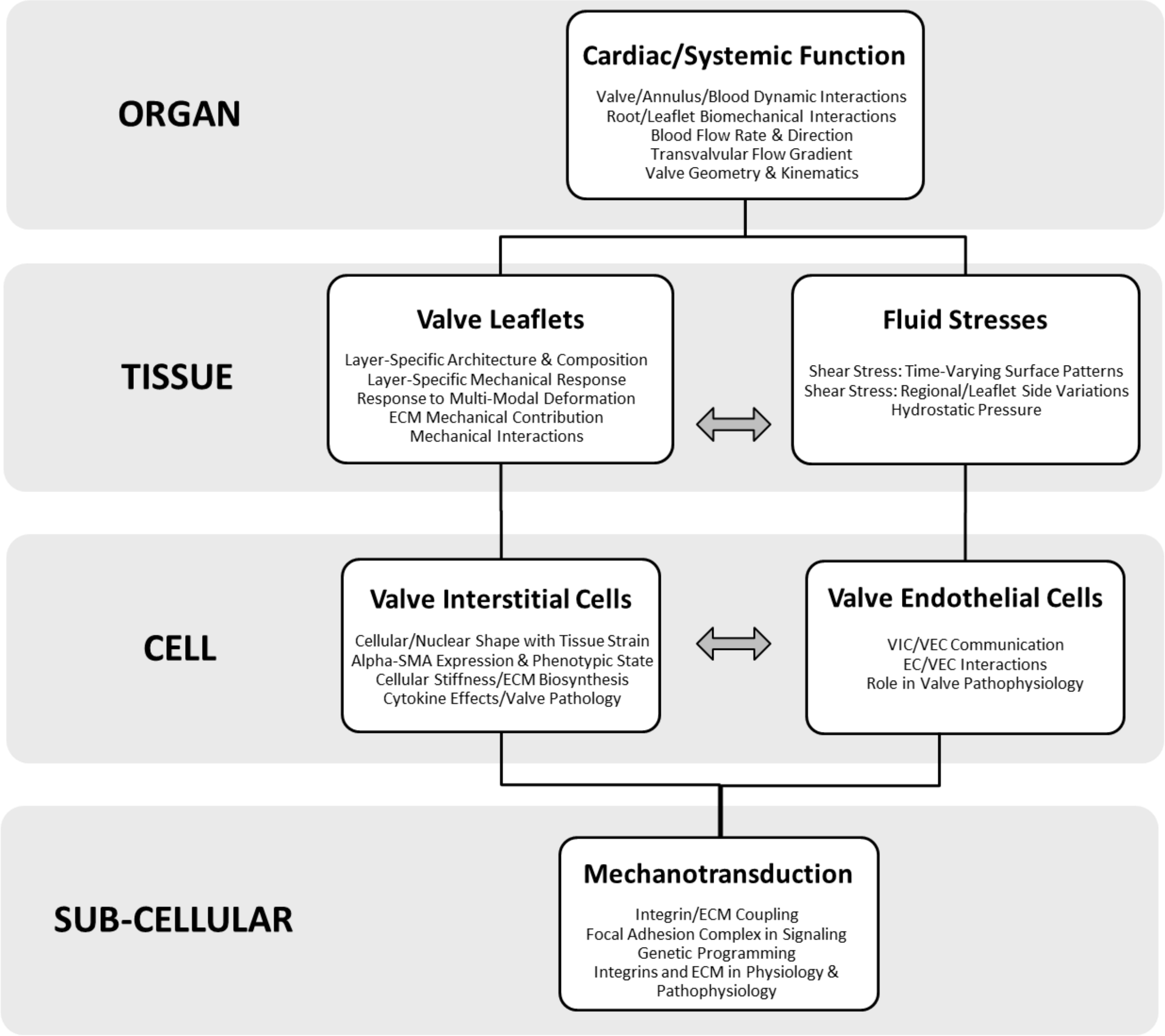

Figure 1.2: A schematic approach to the biomechanics and mechanobiology of heart valve function. Heart valve function can be divided into multiple length scales: organ-, tissue-, cell-, and sub-cell levels.

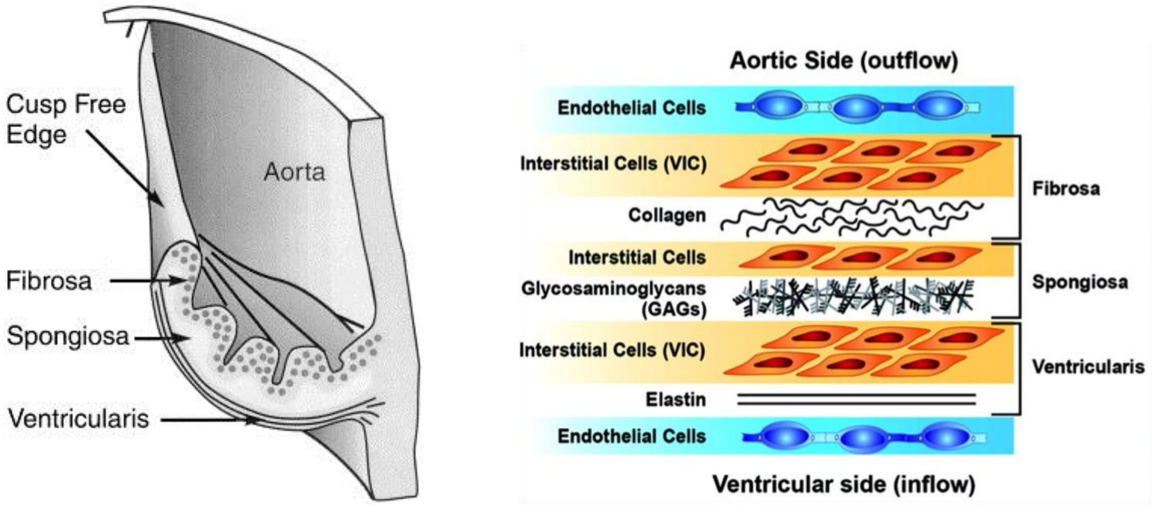

Figure 1.3: Layered architecture of the Aortic Valve illustrated at its attachment [2] to the aorta and a more detailed illustration of the various constituents of the leaflet layers adapted from [161].

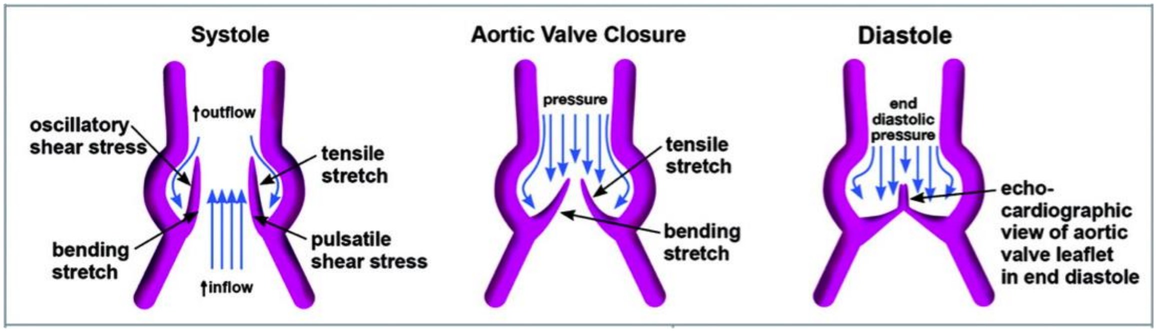

Figure 1.4: Blood flow across the aortic valve adapted from [161].

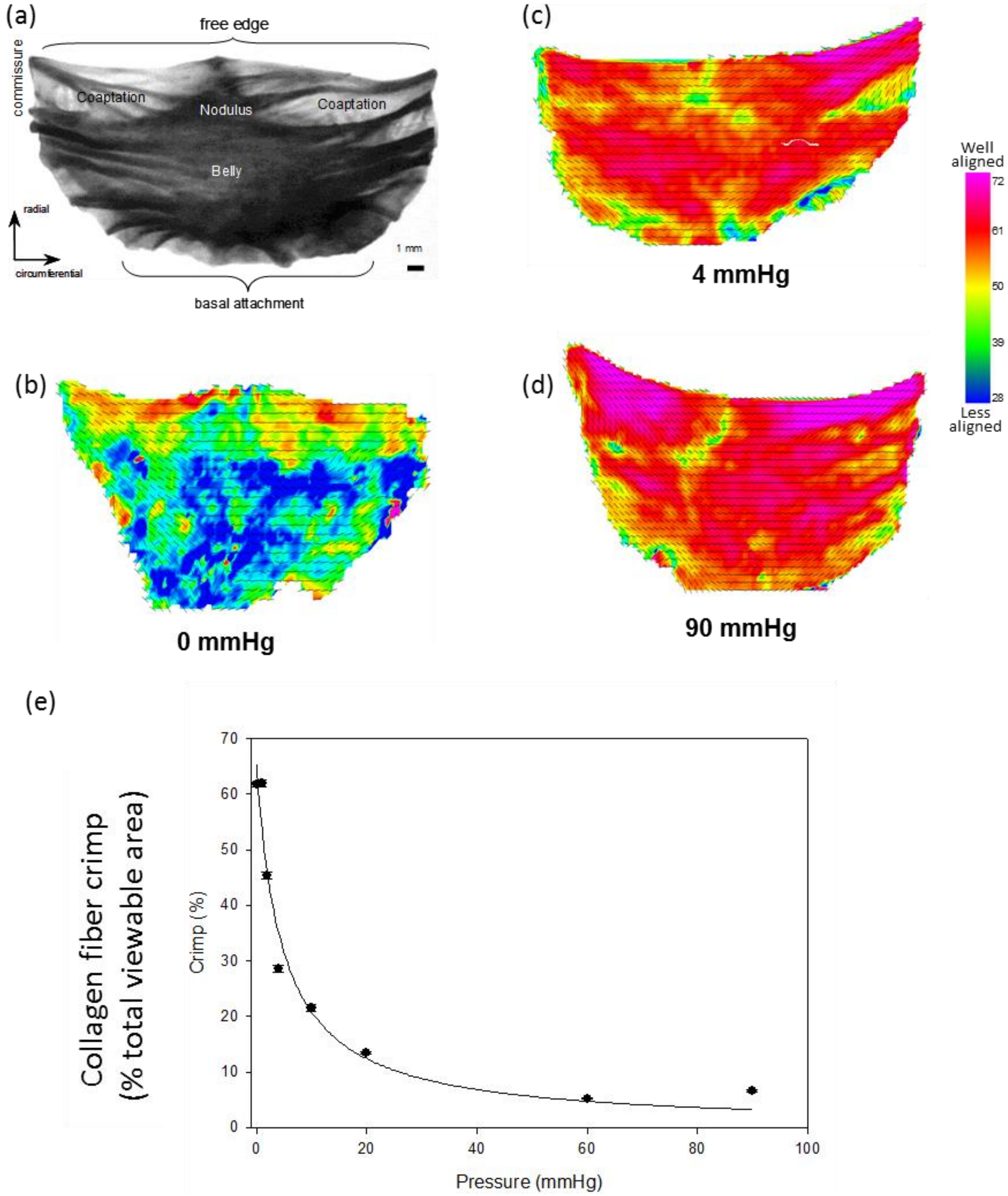

Figure 1.5: (a) Diagram of the AV cusp highlighting the belly, commissures, nodulus, and regions of coaptation. Small angle light scattering results with the orientation index at (b) 0mmHg, (c) 4mmHg, and (d) 90mmHg transvalvular pressure. No further changes in fiber alignment were observed past 4mmHg. These results are consistent with histological-based data that quantifies the percent area of tissue displaying collagen fiber crimp (e). Adapted from Sacks *et al.* [53].

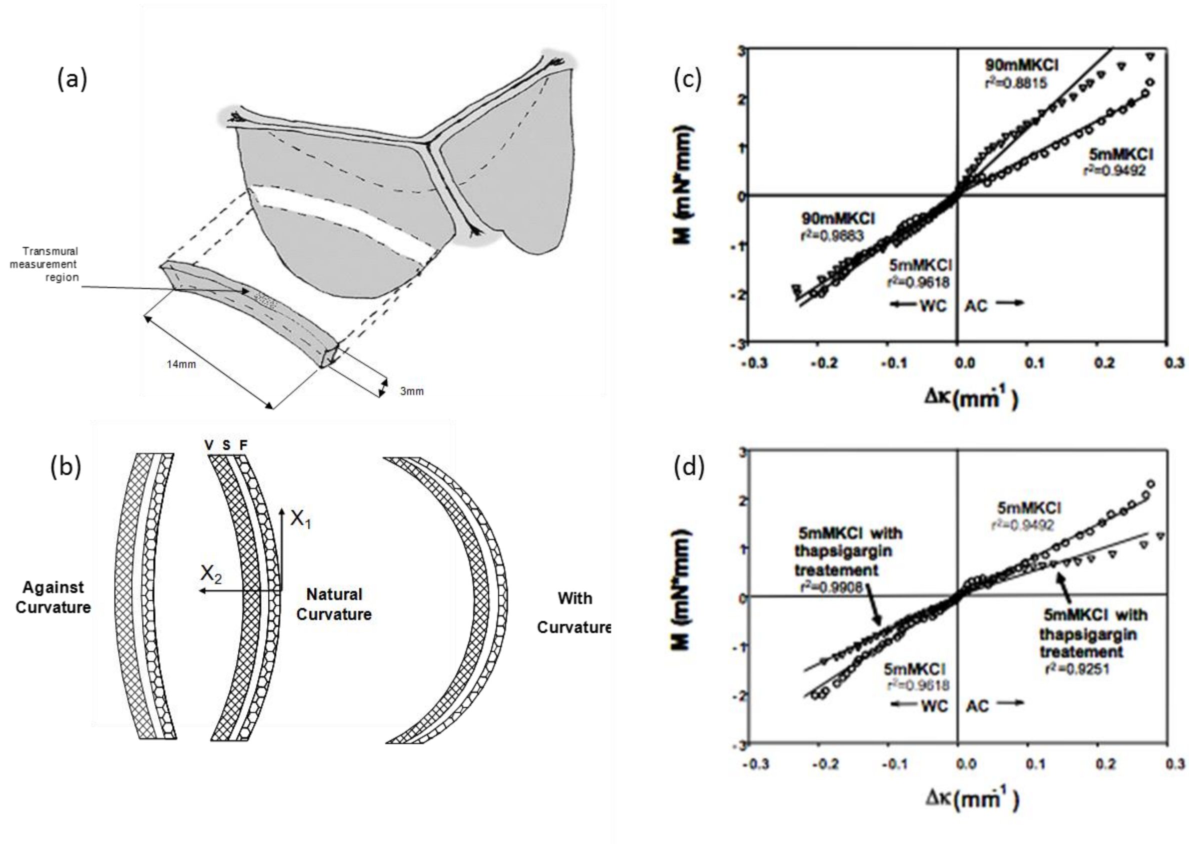

Figure 1.6: (a) Schematic showing the region of tissue used for bending tests in the AV. (b) Schematic showing directions of bending for the AV with respective layers (V: ventricularis, S: spongiosa, and F: fibrosa). M vs. $\Delta\kappa$ relations in both the AC and WC directions for (c) specimens tested in 5 mM and 90 mM KCl, and (d) specimens flexed in 5 mM KCl and samples treated in 10 μM thapsigargin overnight and then flexed in 5 mM KCl. While the application of 90 mM KCL induced an increase in stiffness in the AC direction only, both bending directions experienced a loss of stiffness with the addition of thapsigargin to the bathing medium.

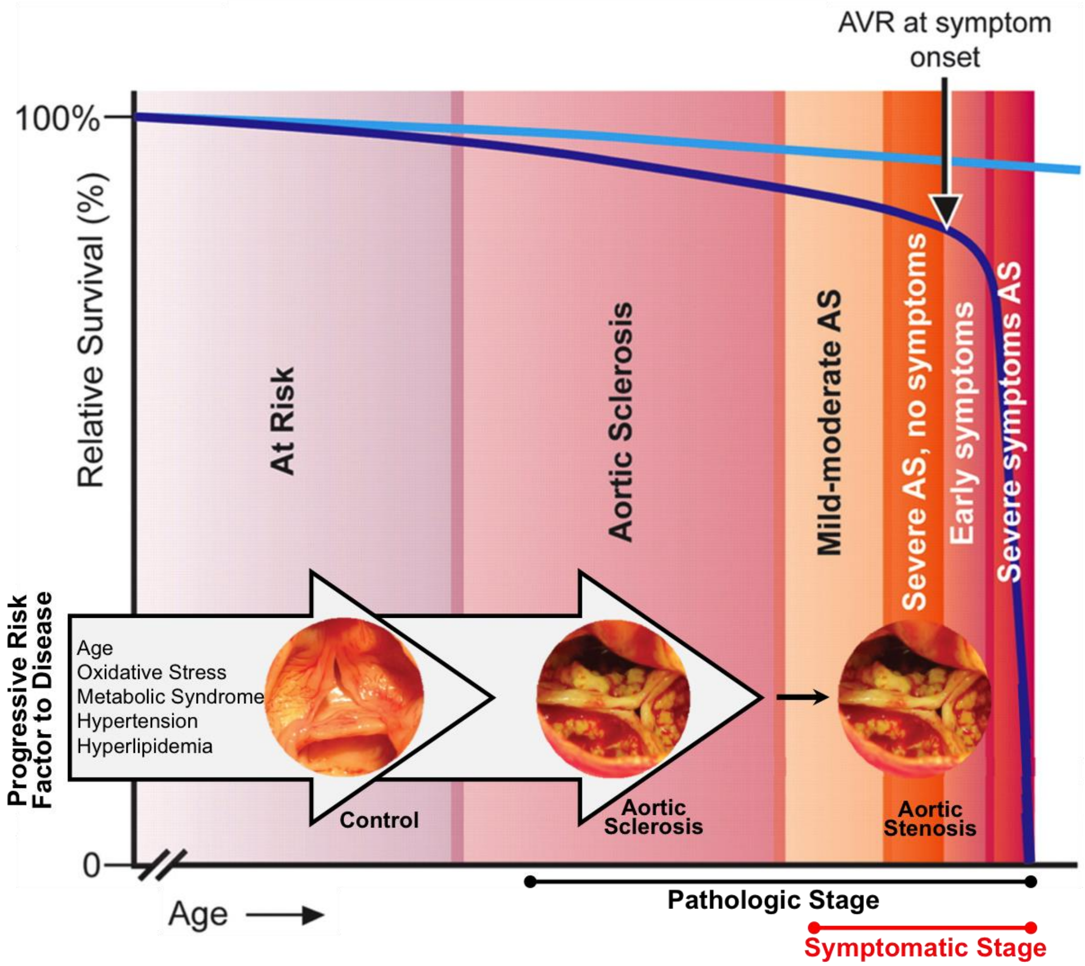

Figure 1.7: Progression of CAVD (modified from Otto et al. [162] and Rajamannan *et al.* [161]). The spectrum of disease ranges from the ‘at risk‘ patient to the patient with end-stage severe symptomatic aortic stenosis. The light blue line represents the expected event-free survival and the purple line represents the survival curve at the onset of aortic sclerosis, which deviates from the expected survival line. Atherosclerotic risk factors involved in the development of aortic valve disease from aortic sclerosis to calcified aortic valve disease are included.

Figure 1.8: Left: Medtronic Open Pivot Mechanic Valve (www.medtronic.com) Right: St. Jude Medical Epic Stented Valve (www.sjm.com).

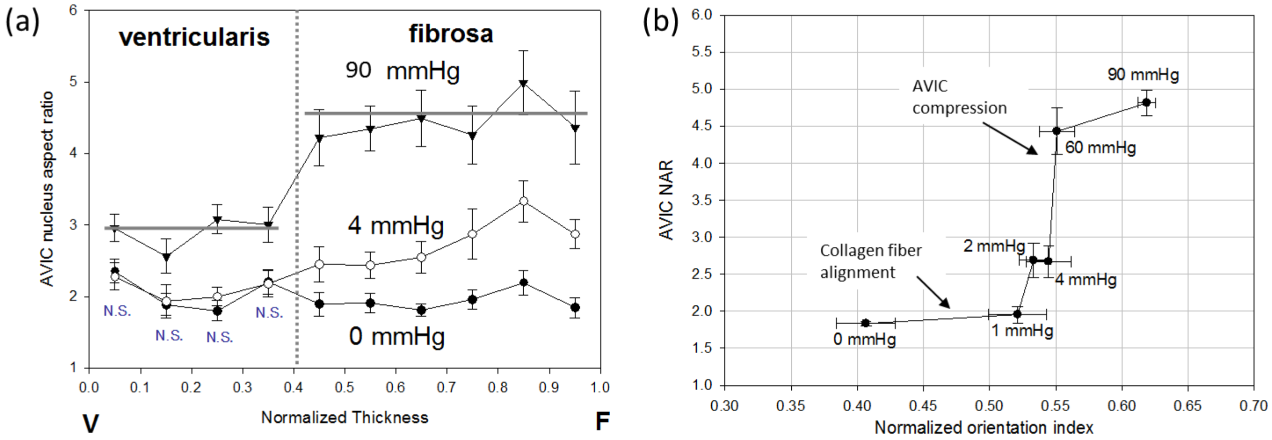

Figure 1.9: (a) The relation between AVIC nuclear aspect ratio (NAR) and transvalvular pressure loading, with values reported over normalized leaflet thickness. (b) AVIC NAR vs. the normalized collagen fiber orientation index (NOI) at different transvalvular pressure levels. These results suggest that AVICs are not appreciably loaded until the collagen fibers fully straighten at transvalvular pressures above ~4 mmHg.

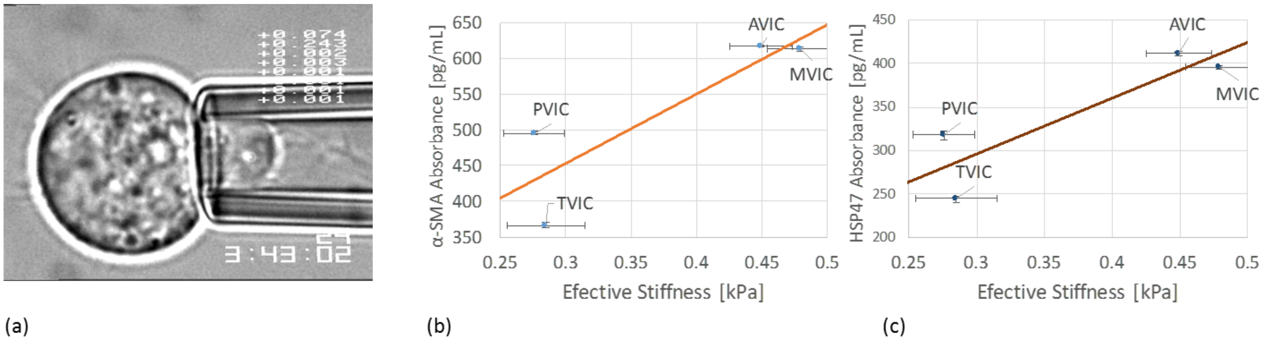

Figure 1.10: (a) A VIC under micropipette aspiration – the vertical bar represents the aspiration length. (b) Functional correlations of effective cell stiffness E vs. transvalvular pressure. (c) Linear correlation between Hsp47 vs. α-SMA, showing a strong correlation between the two proteins ($r = 0.996$) as the one progresses from the right to the left side of the heart.

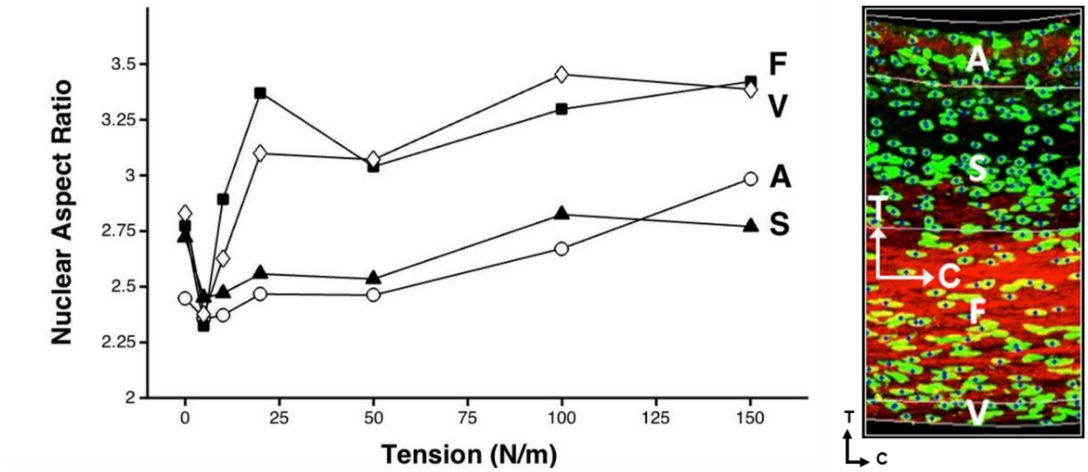

Figure 1.11. Transmural MVIC distribution and deformation in the mitral valve anterior leaflet under controlled biaxial loading. (a) Stack of two-photon excited fluorescence images. Red represents collagen fibers and green represents cell nuclei stained with Cytox Green. Image-stacks were processed and used to quantify cellular deformation by measuring the nuclear aspect ratio (NAR) (b) Measured layer-specific NAR as a function of membrane tension. (A: atrialis, S: spongiosa, F: fibrosa, V: ventricularis). Adapted from Lee *et al.* [163].

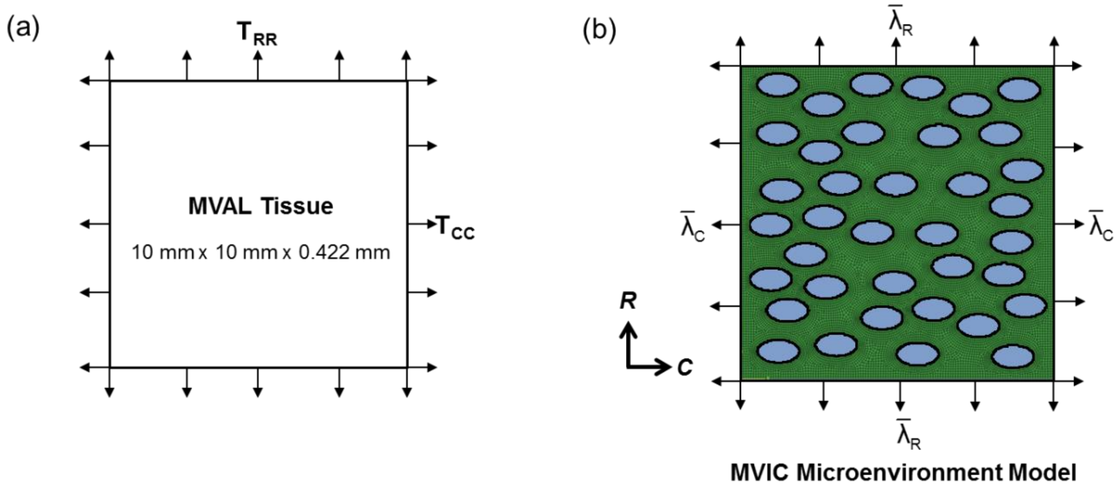

Figure 1.12. The macro-micro finite element (FE) model used to investigate MVIC deformation. (a) Schematic diagram of the tissue-level model: the region of interest of the MVAL tissue under equibiaxial tension loading. (b) Diagram of the cell-level microenvironment model, which consists of 37 uniformly distributed MVICs embedded in the layer-specific representative volume element. The tissue-level deformations are used to prescribe boundary displacements. Adapted from Lee *et al.* [163].

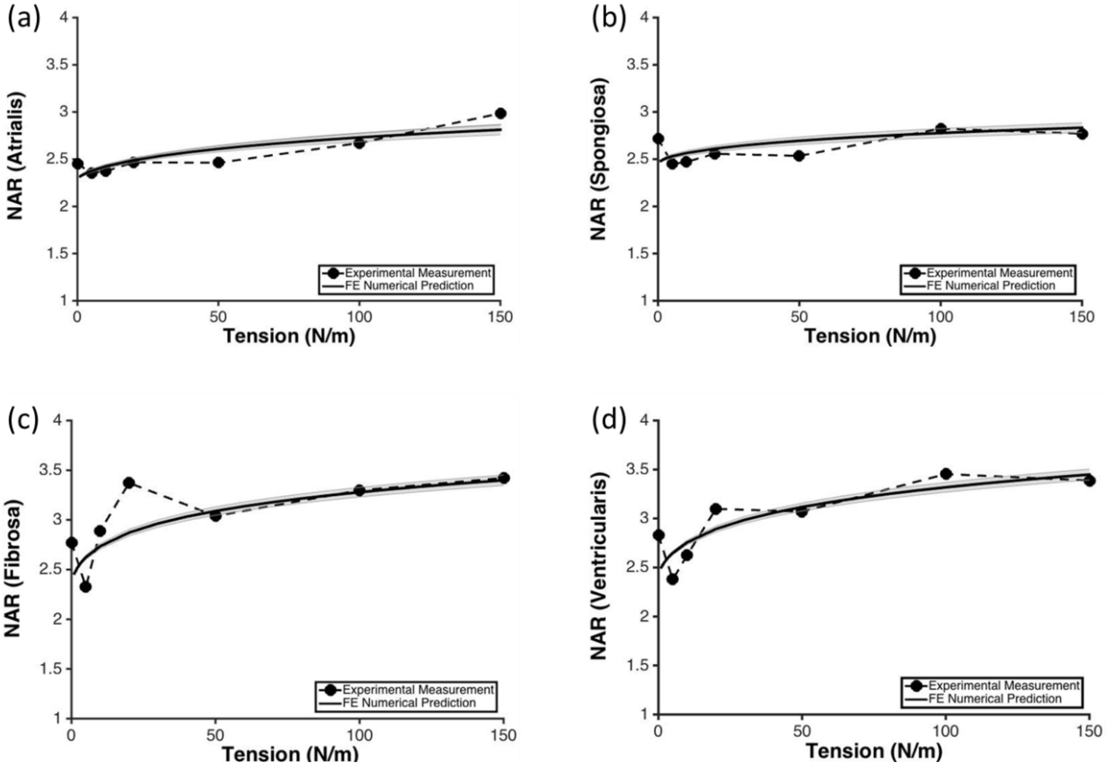

Figure 1.13. Comparisons of the experimentally measured and numerically predicted NARs as a function of tissue-level tension: (a) atrialis layer ($r^2 = 0.8403$), (b) spongiosa layer ($r^2 = 0.9166$), (c) fibrosa layer ($r^2 = 0.8906$), and (d) ventricularis layer ($r^2 = 0.9373$). Adapted from Lee *et al.* [163].

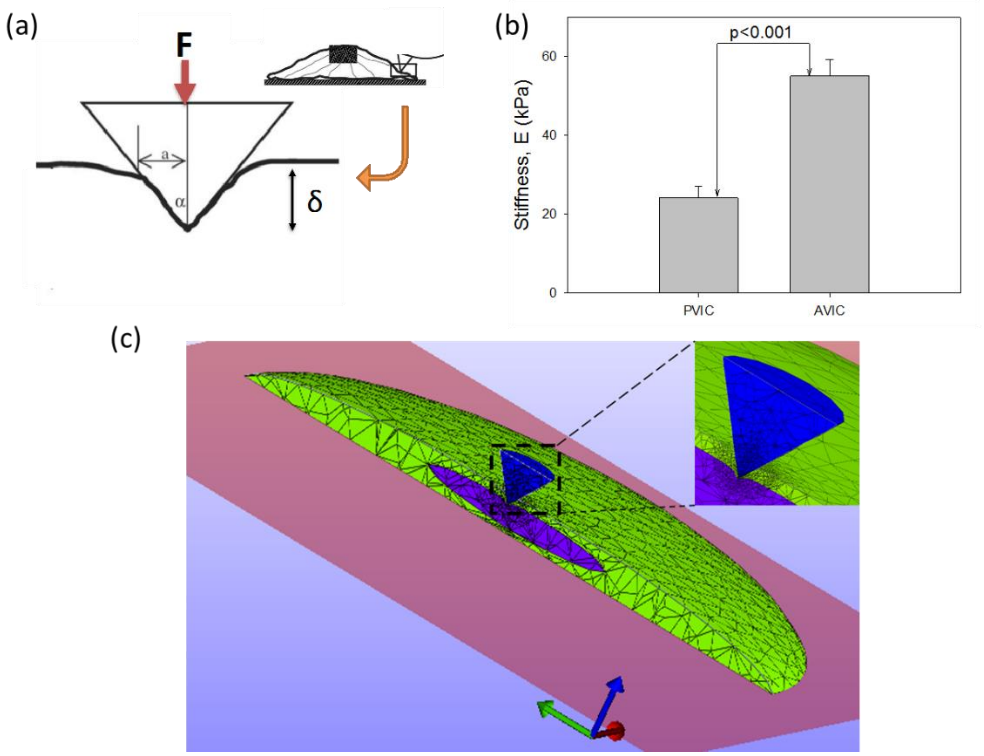

Figure 1.14. (a) Schematic of the AFM experiment, showing how the VIC rests on a collagenous surface and expresses α-SMA. (b) Reported effective moduli of AVIC and PVICs, which were ~100 fold larger than the equivalent micropipette results. (c) AFM simulation setup with finite element mesh. The mesh was refined around the indentation region, with typically 10,000~50,000 linear tetrahedron elements. Note that this is a cross-section of the geometry, but we simulated the whole cell. Adapted from Sakamoto *et al.* [157].

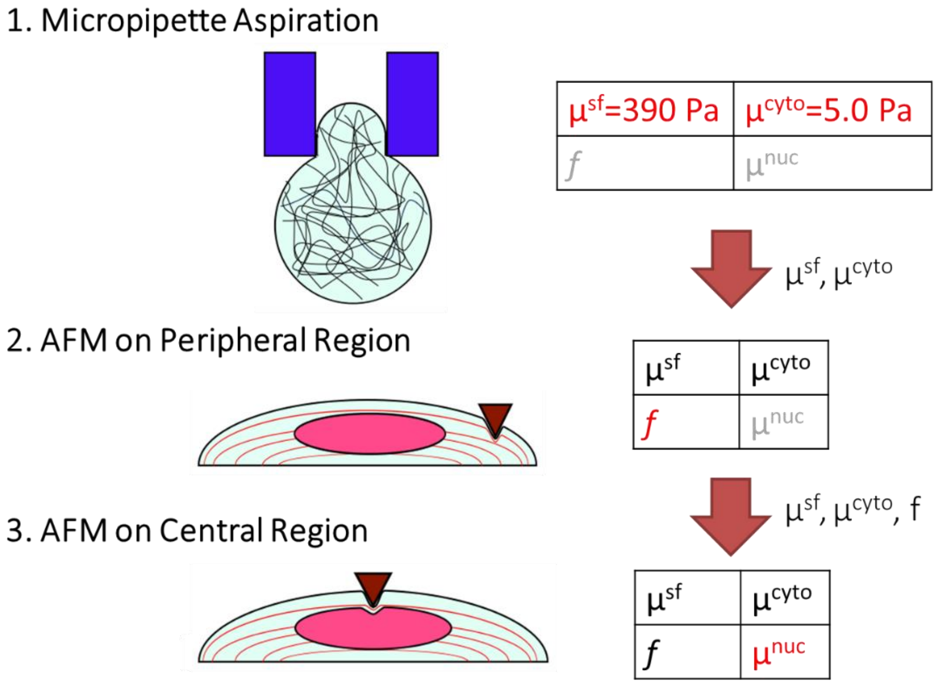

Figure 1.15. The step-by-step calibration process. 1. The cytoskeletal shear modulus (μ_{cyto}) and α-SMA fiber shear modulus (μ_{sf}) were calibrated using the micropipette aspiration data for different types of VICs with different expression levels of α-SMA fibers. 2. Using the AFM indentation data on the cell peripheral regions, the fiber active contraction strength (f) was calibrated for AVICs and PVICs. 3. Using the AFM indentation data on the cell central region, the shear modulus of nucleus (μ_{nuc}) was calibrated for AVICs and PVICs. The parameters in red represents the ones that are being calibrated in the step, the parameters in gray represents the ones that are assumed not contribute to the mechanical response of the VICs (hence ignored) in the step, and the parameters in black represents the ones that are already calibrated from the previous steps and integrated into the model. Adapted from Sakamoto *et al.* [157].

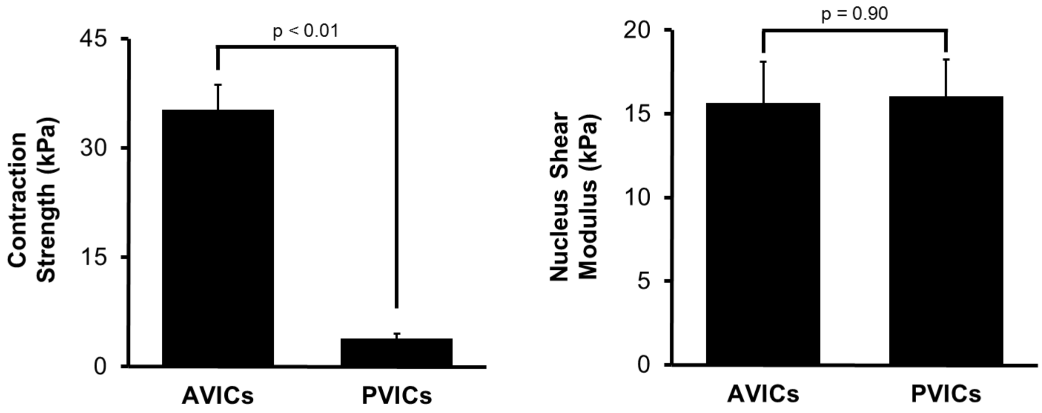

Figure 1.16. (a) Contraction strength of the α-SMA fibers in the AVICs and PVICs. About 9:1 ratio in the contraction strength was observed from AVICs to PVICs. (b) Shear moduli of the AVICs and PVICs nuclei, which exhibited no differences. Adapted from Sakamoto *et al.* [157].

REFERENCES

1. Sacks, M.S., W. David Merryman, and D.E. Schmidt, *On the biomechanics of heart valve function.* J Biomech, 2009. **42**(12): p. 1804-24.
2. Vesely, I., *The role of elastin in aortic valve mechanics.* J Biomech, 1998. **31**(2): p. 115-23.
3. Carruthers, C.A., et al., *Gene Expression and Collagen Fiber Micromechanical Interactions of the Semilunar Heart Valve Interstitial Cell.* Cellular and Molecular Bioengineering, 2012: p. 1-12.
4. Carruthers, C.A., et al., *Gene Expression and Collagen Fiber Micromechanical Interactions of the Semilunar Heart Valve Interstitial Cell.* Cell Mol Bioeng, 2012. **5**(3): p. 254-265.
5. Dena Wiltz, C.A.A., Liezl R. Balaoing, Alicia A. Blancas, Matthew C. Sapp, Xing Zhang and K. Jane Grande-Allen, *Extracellular Matrix Organization, Structure, and Function*, in *Calcific Aortic Valve Disease*, D.E. Aikawa, Editor. 2013.
6. Nemir, S. and J.L. West, *Synthetic materials in the study of cell response to substrate rigidity.* Ann Biomed Eng, 2010. **38**(1): p. 2-20.
7. Butcher, J.T., et al., *Unique morphology and focal adhesion development of valvular endothelial cells in static and fluid flow environments.* Arterioscler Thromb Vasc Biol, 2004. **24**(8): p. 1429-34.

8. Butcher, J.T. and R.M. Nerem, *Porcine aortic valve interstitial cells in three-dimensional culture: comparison of phenotype with aortic smooth muscle cells.* J Heart Valve Dis, 2004. **13**(3): p. 478-85; discussion 485-6.

9. Christie, G.W. and B.G. Barratt-Boyes, *Age-Dependent Changes in the Radial Stretch of Human Aortic Valve Leaflets Determined by Biaxial Stretching.* Annals of Thoracic Surgery, 1995. **60**: p. S156-159.

10. Leask, R.L., N. Jain, and J. Butany, *Endothelium and valvular diseases of the heart.* Microsc Res Tech, 2003. **60**(2): p. 129-37.

11. Butcher, J.T. and R.M. Nerem, *Valvular endothelial cells and the mechanoregulation of valvular pathology.* Philos Trans R Soc Lond B Biol Sci, 2007. **362**(1484): p. 1445-57.

12. Ge, L. and F. Sotiropoulos, *Direction and magnitude of blood flow shear stresses on the leaflets of aortic valves: is there a link with valve calcification?* J Biomech Eng, 2010. **132**(1): p. 014505.

13. Girard, P.R. and R.M. Nerem, *Shear stress modulates endothelial cell morphology and F-actin organization through the regulation of focal adhesion-associated proteins.* J Cell Physiol, 1995. **163**(1): p. 179-93.

14. Cucina, A., et al., *Shear stress induces changes in the morphology and cytoskeleton organisation of arterial endothelial cells.* Eur J Vasc Endovasc Surg, 1995. **9**(1): p. 86-92.

15. Stamatas, G.N. and L.V. McIntire, *Rapid flow-induced responses in endothelial cells.* (8756-7938 (Print)).

16. Tao, G., J.D. Kotick, and J. Lincoln, *Heart valve development, maintenance, and disease: the role of endothelial cells.* Curr Top Dev Biol, 2012. **100**: p. 203-32.

17. Luscinskas, F.W. and J. Lawler, *Integrins as dynamic regulators of vascular function.* FASEB J, 1994. **8**(12): p. 929-38.

18. Prasad, A.R., et al., *Flow-related responses of intracellular inositol phosphate levels in cultured aortic endothelial cells.* Circ Res, 1993. **72**(4): p. 827-36.

19. Davies, P.F., et al., *Turbulent fluid shear stress induces vascular endothelial cell turnover in vitro.* Proc Natl Acad Sci U S A, 1986. **83**(7): p. 2114-7.

20. Helmlinger, G., et al., *Effects of pulsatile flow on cultured vascular endothelial cell morphology.* (0148-0731 (Print)).

21. Chappell, D.C., et al., *Oscillatory shear stress stimulates adhesion molecule expression in cultured human endothelium.* Circ Res, 1998. **82**(5): p. 532-9.

22. Davies, P.F., et al., *Hemodynamics and the focal origin of atherosclerosis: a spatial approach to endothelial structure, gene expression, and function.* Ann N Y Acad Sci, 2001. **947**: p. 7-16; discussion 16-7.

23. Johnson, C.M. and D.N. Fass, *Porcine cardiac valvular endothelial cells in culture. A relative deficiency of fibronectin synthesis in vitro.* Lab Invest, 1983. **49**(5): p. 589-98.

24. Deck, J.D., *Endothelial cell orientation on aortic valve leaflets.* Cardiovasc Res, 1986. **20**(10): p. 760-7.

25. Butcher, J.T. and R.M. Nerem, *Valvular Endothelial Cells Regulate the Phenotype of Interstitial Cells in Co-culture: Effects of Steady Shear Stress.* Tissue Engineering, 2006. **12**(4): p. 905-915.

26. Farivar, R.S., et al., *Transcriptional profiling and growth kinetics of endothelium reveals differences between cells derived from porcine aorta versus aortic valve.* Eur J Cardiothorac Surg, 2003. **24**(4): p. 527-34.

27. Lee, T.C., et al., *Abnormal aortic valve development in mice lacking endothelial nitric oxide synthase.* Circulation, 2000. **101**(20): p. 2345-8.

28. Laforest, B., G. Andelfinger, and M. Nemer, *Loss of Gata5 in mice leads to bicuspid aortic valve.* J Clin Invest, 2011. **121**(7): p. 2876-87.

29. Nus, M., et al., *Diet-induced aortic valve disease in mice haploinsufficient for the Notch pathway effector RBPJK/CSL.* Arterioscler Thromb Vasc Biol, 2011. **31**(7): p. 1580-8.

30. Weiss, R.M., et al., *Calcific aortic valve stenosis in old hypercholesterolemic mice.* Circulation, 2006. **114**(19): p. 2065-9.

31. Tanaka, K., et al., *Age-associated aortic stenosis in apolipoprotein E-deficient mice.* J Am Coll Cardiol, 2005. **46**(1): p. 134-41.

32. Stewart, B.F., et al., *Clinical factors associated with calcific aortic valve disease. Cardiovascular Health Study.* J Am Coll Cardiol, 1997. **29**(3): p. 630-4.

33. Merryman, W.D., et al., *Correlation between heart valve interstitial cell stiffness and transvalvular pressure: implications for collagen biosynthesis.* Am J Physiol Heart Circ Physiol, 2006. **290**(1): p. H224-31.

34. Hinton, R.B. and K.E. Yutzey, *Heart valve structure and function in development and disease.* Annu Rev Physiol, 2011. **73**: p. 29-46.

35. Davies, P.F., A.G. Passerini, and C.A. Simmons, *Aortic Valve: Turning Over a New Leaf(let) in Endothelial Phenotypic Heterogeneity.* Arterioscler Thromb Vasc Biol, 2004. **24**(8): p. 1331-1333.

36. Nicosia, M.A., et al., *A coupled fluid-structure finite element model of the aortic valve and root.* J Heart Valve Dis, 2003. **12**(6): p. 781-9.

37. Otto, C.M., et al., *Characterization of the early lesion of 'degenerative' valvular aortic stenosis. Histological and immunohistochemical studies.* Circulation, 1994. **90**(2): p. 844-53.

38. Thubrikar, M.J., J. Aouad, and S.P. Nolan, *Patterns of calcific deposits in operatively excised stenotic or purely regurgitant aortic valves and their relation to mechanical stress.* Am J Cardiol, 1986. **58**(3): p. 304-8.

39. Thubrikar, M.J., et al., *Stress sharing between the sinus and leaflets of canine aortic valve.* Ann Thorac Surg, 1986. **42**(4): p. 434-40.

40. Butcher, J.T., et al., *Transcriptional profiles of valvular and vascular endothelial cells reveal phenotypic differences: influence of shear stress.* Arterioscler Thromb Vasc Biol, 2006. **26**(1): p. 69-77.

41. Simmons, C.A., et al., *Spatial Heterogeneity of Endothelial Phenotypes Correlates With Side-Specific Vulnerability to Calcification in Normal Porcine Aortic Valves.* Circ Res, 2005. **96**(7): p. 792-799.

42. Marron, K., et al., *Innervation of human atrioventricular and arterial valves.* Circulation, 1996. **94**(3): p. 368-75.

43. Davies, P.F., *Mechanisms involved in endothelial responses to hemodynamic forces.* Atherosclerosis, 1997. **131 Suppl**: p. S15-7.

44. Davies, P.F. and S.C. Tripathi, *Mechanical stress mechanisms and the cell. An endothelial paradigm.* Circ Res, 1993. **72**(2): p. 239-45.

45. Filip, D.A., A. Radu, and M. Simionescu, *Interstitial cells of the heart valve possess characteristics similar to smooth muscle cells.* Circ Res, 1986. **59**(3): p. 310-320.

46. Taylor, P.M., et al., *The cardiac valve interstitial cell.* Int J Biochem Cell Biol, 2003. **35**(2): p. 113-8.

47. Messier, R.H., Jr., et al., *Dual structural and functional phenotypes of the porcine aortic valve interstitial population: characteristics of the leaflet myofibroblast.* J Surg Res, 1994. **57**(1): p. 1-21.

48. Mulholland, D.L. and A.I. Gotlieb, *Cell biology of valvular interstitial cells.* Can J Cardiol, 1996. **12**(3): p. 231-6.

49. Filip, D.A., A. Radu, and M. Simionescu, *Interstitial cells of the heart valves possess characteristics similar to smooth muscle cells.* Circ Res, 1986. **59**(3): p. 310-20.

50. Latif, N., et al., *Molecules mediating cell-ECM and cell-cell communication in human heart valves.* Cell Biochem Biophys, 2005. **43**(2): p. 275-87.

51. Stephens, E.H., et al., *Mitral valvular interstitial cell responses to substrate stiffness depend on age and anatomic region.* Acta Biomaterialia, 2011. **7**(1): p. 75-82.

52. Adamczyk, M.M. and I. Vesely, *Characteristics of compressive strains in porcine aortic valves cusps.* J Heart Valve Dis, 2002. **11**(1): p. 75-83.

53. Sacks, M.S., D.B. Smith, and E.D. Hiester, *The aortic valve microstructure: effects of transvalvular pressure.* Journal of Biomedical Materials Research, 1998. **41**(1): p. 131-41.

54. Billiar, K.L. and M.S. Sacks, *Biaxial mechanical properties of the native and glutaraldehyde-treated aortic valve cusp: Part II--A structural constitutive model.* Journal of Biomechanical Engineering, 2000b. **122**(4): p. 327-35.

55. Billiar, K.L. and M.S. Sacks, *Biaxial mechanical properties of the natural and glutaraldehyde treated aortic valve cusp--Part I: Experimental results.* Journal of Biomechanical Engineering, 2000a. **122**(1): p. 23-30.

56. Vesely, I., *The role of elastin in aortic valve mechanics.* Journal of Biomechanics, 1998. **31**(2): p. 115-123.

57. Vesely, I. and W.J. Mako, *Comparison of the compressive buckling of porcine aortic valve cusps and bovine pericardium.* J Heart Valve Dis, 1998. **7**(1): p. 34-9.

58. Vesely, I. and R. Noseworthy, *Micromechanics of the fibrosa and the ventricularis in aortic valve leaflets.* Journal of Biomechanics, 1992. **25**(1): p. 101-113.

59. Stella, J. and M.S. Sacks, *On the biaxial mechanical properties of the layers of the aortic valve leaflet.* Journal of Biomechanial Engineering, in-press.

60. Sacks, M.S., et al., *Surface strains in the anterior leaflet of the functioning mitral valve.* Annals of Biomedical Engineering, 2002. **30**(10): p. 1281-90.

61. Gorman, J.H., 3rd, et al., *Dynamic three-dimensional imaging of the mitral valve and left ventricle by rapid sonomicrometry array localization.* J Thorac Cardiovasc Surg, 1996. **112**(3): p. 712-26.

62. Gorman, J.H., 3rd, et al., *The effect of regional ischemia on mitral valve annular saddle shape.* Ann Thorac Surg, 2004. **77**(2): p. 544-8.

63. Otto, C.M., *Clinical practice. Evaluation and management of chronic mitral regurgitation.* N Engl J Med, 2001. **345**(10): p. 740-6.

64. Reul, H. and N. Talukder, *Heart valve mechanics*, in *The Heart*. 1989, McGraw Hill.

65. May-Newman, K. and F.C. Yin, *Biaxial mechanical behavior of excised porcine mitral valve leaflets.* Am J Physiol, 1995. **269**(4 Pt 2): p. H1319-27.

66. Mayne, A.S., et al., *An assessment of the mechanical properties of leaflets from four second-generation porcine bioprostheses with biaxial testing techniques.* J Thorac Cardiovasc Surg, 1989. **98**(2): p. 170-80.

67. Christie, G.W. and B.G. Barratt-Boyes, *Biaxial mechanical properties of explanted aortic allograft leaflets.* Ann Thorac Surg, 1995. **60**(2 Suppl): p. S160-4.

68. Hilbert, S.L., V.J. Ferrans, and W.M. Swanson, *Optical methods for the nondestructive evaluation of collagen morphology in bioprosthetic heart valves.* Journal of Biomedical Materials Research, 1986. **20**: p. 1411-1421.

69. Hilbert, S.L., Barrick, M.K., Ferrans, V.J., *Porcine aortic valve bioprostheses: A morphologic comparison of the effects of fixation pressure.* Journal of Biomedical Materials Research, 1990. **24**: p. 773-787.

70. Joyce, E.M., et al., *Functional collagen fiber architecture of the pulmonary heart valve cusp.* Ann Thorac Surg, 2009. **87**(4): p. 1240-9.

71. Vesely, I. and R. Noseworthy, *Micromechanics of the fibrosa and the ventricularis in aortic valve leaflets.* J Biomech, 1992. **25**(1): p. 101-13.

72. Stella, J.A. and M.S. Sacks, *On the biaxial mechanical properties of the layers of the aortic valve leaflet.* J Biomech Eng, 2007. **129**(5): p. 757-66.

73. Sacks, M.S. and A.P. Yoganathan, *Heart valve function: a biomechanical perspective.* Philos Trans R Soc Lond B Biol Sci, 2007. **362**(1484): p. 1369-91.

74. Iyengar, A.K.S., et al., *Dynamic in vitro quantification of bioprosthetic heart valve leaflet motion using structured light projection.* Ann Biomed Eng, 2001. **29**(11): p. 963-73.

75. Merryman, W.D., et al., *The effects of cellular contraction on aortic valve leaflet flexural stiffness.* J Biomech, 2006. **39**(1): p. 88-96.

76. Engelmayr, G.C., Jr., et al., *The independent role of cyclic flexure in the early in vitro development of an engineered heart valve tissue.* Biomaterials, 2005. **26**(2): p. 175-87.

77. Mirnajafi, A., et al., *The flexural rigidity of the aortic valve leaflet in the commissural region.* J Biomech, 2006. **39**(16): p. 2966-73.

78. Gloeckner, D.C., K.L. Billiar, and M.S. Sacks, *Effects of mechanical fatigue on the bending properties of the porcine bioprosthetic heart valve.* Asaio J, 1999. **45**(1): p. 59-63.

79. Gloeckner, D., K. Billiar, and M. Sacks. *The bending behavior of fixed porcine aortic cusp*. in *Third World Congress of Biomechanics*. 1998. Hokaiddo, Japan.

80. Engelmayr, G.C., Jr., et al., *A novel bioreactor for the dynamic flexural stimulation of tissue engineered heart valve biomaterials.* Biomaterials, 2003. **24**(14): p. 2523-32.

81. Frisch-Fay, R., *Flexible bars*. 1962, Washington,DC: Butterworths. 220.

82. Thubrikar, M., et al., *The elastic modulus of canine aortic valve leaflets in vivo and in vitro.* Circ Res, 1980. **47**(5): p. 792-800.

83. Thubrikar, M.J., J. Aouad, and S.P. Nolan, *Comparison of the in vivo and in vitro mechanical properties of aortic valve leaflets.* J Thorac Cardiovasc Surg, 1986. **92**(1): p. 29-36.

84. Sugimoto, B. and M.S. Sacks, *EFFECTS OF LEAFLET STIFFNESS ON IN-VITRO DYNAMIC BIOPROSTHETIC HEART VALVE LEAFLET SHAPE.* Cardiovascular Engineering and Technology, 2013. **in-press**.

85. Curnier, A., Q.C. He, and P. Zysset, *Conewise Linear Elastic-Materials.* Journal of Elasticity, 1995. **37**(1): p. 1-38.

86. Ateshian, G.A., *Anisotropy of fibrous tissues in relation to the distribution of tensed and buckled fibers.* J Biomech Eng, 2007. **129**(2): p. 240-9.

87. Mozaffarian, D., et al., *Heart Disease and Stroke Statistics—2016 Update: A Report From the American Heart Association.* Circulation, 2015.

88. Towler, D.A., *Molecular and cellular aspects of calcific aortic valve disease.* Circ Res, 2013. **113**(2): p. 198-208.

89. Freeman, R.V. and C.M. Otto, *Spectrum of calcific aortic valve disease: pathogenesis, disease progression, and treatment strategies.* Circulation, 2005. **111**(24): p. 3316-26.

90. Freeman, R.V. and C.M. Otto, *Management of asymptomatic valvular aortic stenosis.* Indian Heart J, 2002. **54**(1): p. 31-8.

91. Kurtz, C.E. and C.M. Otto, *Aortic stenosis: clinical aspects of diagnosis and management, with 10 illustrative case reports from a 25-year experience.* Medicine (Baltimore), 2010. **89**(6): p. 349-79.

92. Beckmann, E., et al., *Insights into the use of biomarkers in calcific aortic valve disease.* J Heart Valve Dis, 2010. **19**(4): p. 441-52.

93. O'Brien, K.D., *Pathogenesis of calcific aortic valve disease: a disease process comes of age (and a good deal more).* Arterioscler Thromb Vasc Biol, 2006. **26**(8): p. 1721-8.

94. Poggio, P., et al., *Noggin attenuates the osteogenic activation of human valve interstitial cells in aortic valve sclerosis.* Cardiovasc Res, 2013. **98**(3): p. 402-10.

95. Grau, J.B., et al., *Analysis of osteopontin levels for the identification of asymptomatic patients with calcific aortic valve disease.* Ann Thorac Surg, 2012. **93**(1): p. 79-86.

96. Gharacholou, S.M., et al., *Aortic valve sclerosis and clinical outcomes: moving toward a definition.* Am J Med, 2011. **124**(2): p. 103-10.

97. Pflederer, T. and S. Achenbach, *Aortic valve stenosis: CT contributions to diagnosis and therapy.* J Cardiovasc Comput Tomogr, 2010. **4**(6): p. 355-64.

98. Owens, D.S. and C.M. Otto, *Is it time for a new paradigm in calcific aortic valve disease?* JACC Cardiovasc Imaging, 2009. **2**(8): p. 928-30.

99. Chen, J.H. and C.A. Simmons, *Cell-matrix interactions in the pathobiology of calcific aortic valve disease: critical roles for matricellular, matricrine, and matrix mechanics cues.* Circ Res, 2011. **108**(12): p. 1510-24.

100. Otto, C.M., *Calcific aortic valve disease: new concepts.* Semin Thorac Cardiovasc Surg, 2010. **22**(4): p. 276-84.

101. Aikawa, E. and C.M. Otto, *Look more closely at the valve: imaging calcific aortic valve disease.* Circulation, 2012. **125**(1): p. 9-11.

102. Parolari, A., et al., *Do statins improve outcomes and delay the progression of non-rheumatic calcific aortic stenosis?* Heart, 2011. **97**(7): p. 523-9.

103. Moura, L.M., et al., *Rosuvastatin affecting aortic valve endothelium to slow the progression of aortic stenosis.* J Am Coll Cardiol, 2007. **49**(5): p. 554-61.

104. Cowell, S.J., et al., *A randomized trial of intensive lipid-lowering therapy in calcific aortic stenosis.* N Engl J Med, 2005. **352**(23): p. 2389-97.

105. Benton, J.A., et al., *Statins block calcific nodule formation of valvular interstitial cells by inhibiting alpha-smooth muscle actin expression.* Arterioscler Thromb Vasc Biol, 2009. **29**(11): p. 1950-7.

106. Rossebo, A.B., et al., *Intensive lipid lowering with simvastatin and ezetimibe in aortic stenosis.* N Engl J Med, 2008. **359**(13): p. 1343-56.

107. Marchand, M.A., et al., *Fifteen-year experience with the mitral Carpentier-Edwards PERIMOUNT pericardial bioprosthesis.* Ann Thorac Surg, 2001. **71**(5 Suppl): p. S236-9.

108. Kheradvar, A., et al., *Emerging trends in heart valve engineering: Part II. Novel and standard technologies for aortic valve replacement.* Ann Biomed Eng, 2015. **43**(4): p. 844-57.

109. Goldhaber, S.Z., *"Bridging" and mechanical heart valves: perils, promises, and predictions.* Circulation, 2006. **113**(4): p. 470-2.

110. Dominik, J. and P. Zacek, *Heart valve surgery : an illustrated guide*. 2010, Heidelberg ; New York: Springer. 415 p.

111. Chuong, C.J. and Y.C. Fung, *On Residual Stress in Arteries.* Journal of Biomechanical Engineering, 1986. **108**: p. 189-192.

112. Fung, Y.C., *What are the residual stresses doing in our blood vessels?* Ann Biomed Eng, 1991. **19**(3): p. 237-49.

113. Lanir, Y., *Mechanisms of residual stress in soft tissues.* J Biomech Eng, 2009. **131**(4): p. 044506.

114. Ogden, R., *Nonlinear elasticity, anisotropy, material stability, and residual stresses in soft tissue*, in *Biomechanics of soft tissue in cardiovascular system*, R.W. Ogden, Editor. 2003, Springer: New York.

115. Taber, L.A. and J.D. Humphrey, *Stress-modulated growth, residual stress, and vascular heterogeneity.* J Biomech Eng, 2001. **123**(6): p. 528-35.

116. Weber, K.T., et al., *Connective tissue and repair in the heart. Potential regulatory mechanisms.* Ann N Y Acad Sci, 1995. **752**: p. 286-99.

117. Schneider, P.J. and J.D. Deck, *Tissue and cell renewal in the natural aortic valve of rats: an autoradiographic study.* Cardiovasc Res, 1981. **15**(4): p. 181-9.

118. Willems, I.E., et al., *Structural alterations in heart valves during left ventricular pressure overload in the rat.* Lab Invest, 1994. **71**(1): p. 127-33.

119. Chaput, M., et al., *Mitral leaflet adaptation to ventricular remodeling: occurrence and adequacy in patients with functional mitral regurgitation.* Circulation, 2008. **118**(8): p. 845-52.

120. Dal-Bianco, J.P., et al., *Active adaptation of the tethered mitral valve: insights into a compensatory mechanism for functional mitral regurgitation.* Circulation, 2009. **120**(4): p. 334-42.

121. Fung, Y.C. and S.Q. Liu, *Changes of zero-stress state of rat pulmonary arteries in hypoxic hypertension.* J Appl Physiol, 1991. **70**(6): p. 2455-70.

122. Liu, S.Q. and Y.C. Fung, *Relationship between hypertension, hypertrophy, and opening angle of zero-stress state of arteries following aortic constriction.* J Biomech Eng, 1989. **111**(4): p. 325-35.

123. Stephens, E.H., et al., *Significant changes in mitral valve leaflet matrix composition and turnover with tachycardia-induced cardiomyopathy.* Circulation, 2009. **120**(11 Suppl): p. S112-9.

124. Stephens, E.H., et al., *The effects of mitral regurgitation alone are sufficient for leaflet remodeling.* Circulation, 2008. **118**(14 Suppl): p. S243-9.

125. Stephens, E.H., et al., *Differential proteoglycan and hyaluronan distribution in calcified aortic valves.* Cardiovasc Pathol, 2011. **20**(6): p. 334-42.

126. Messier, R.H., Jr., et al., *Dual structural and functional phenotypes of the porcine aortic valve interstitial population: characteristics of the leaflet myofibroblast.* Journal of Surgical Research, 1994. **57**(1): p. 1-21.

127. Hafizi, S., et al., *Mitogenic and secretory responses of human valve interstitial cells to vasoactive agents.* Journal of Heart Valve Disease, 2000. **9**(3): p. 454-8.

128. Guilak, F. and V.C. Mow, *The mechanical environment of the chondrocyte: a biphasic finite element model of cell-matrix interactions in articular cartilage.PG - 1663-73.* J Biomech, 2000. **33**(12).

129. Huang, H.-Y.S., J. Liao, and M.S. Sacks, *Effects of transvalvular pressure on aortic valve interstitial cell nuclear aspect ratio.* Journal of Biomechanial Engineering, in-press.

130. Merryman, W.D., et al., *Differences in tissue-remodeling potential of aortic and pulmonary heart valve interstitial cells.* Tissue Eng, 2007. **13**(9): p. 2281-9.

131. Chester, A.H., et al. *Specific regional and direcrtional contractile response of aortic cusp tissue-Relevance to valve function*. in *Second Biennial Meeting of the Society for Heart Valve Disease*. 2003. Paris.

132. Chester, A.H., M. Misfeld, and M.H. Yacoub, *Receptor-mediated contraction of aortic valve leaflets.* Journal of Heart Valve Disease, 2000. **9**(2): p. 250-4; discussion 254-5.

133. Merryman, W.D., et al., *The effects of cellular contraction on aortic valve leaflet flexural stiffness.* J Biomech, 2006. **39**(1): p. 88-96.

134. Malvern, L.E., *Introduction to the mechanics of a continuous medium*. Prentice-Hall series in engineering of the physical sciences. 1969, Englewood Cliffs, N.J.,: Prentice-Hall. xii, 713 p.

135. Lanir, Y., *Constitutive equations for fibrous connective tissues.* J Biomech, 1983. **16**(1): p. 1-12.

136. Sacks, M.S., *Incorporation of experimentally-derived fiber orientation into a structural constitutive model for planar collagenous tissues.* J Biomech Eng, 2003. **125**(2): p. 280-7.

137. Billiar, K.L. and M.S. Sacks, *Biaxial mechanical properties of the native and glutaraldehyde-treated aortic valve cusp: Part II--A structural constitutive model.* J Biomech Eng, 2000. **122**(4): p. 327-35.

138. May-Newman, K. and F.C. Yin, *A constitutive law for mitral valve tissue.* J Biomech Eng, 1998. **120**(1): p. 38-47.

139. Prot, V. and B. Skallerud, *Nonlinear solid finite element analysis of mitral valves with heterogeneous leaflet layers.* Comput Mech, 2009. **43**(3): p. 353-368.

140. Prot, V., B. Skallerud, and G. Holzapfel, *Transversely isotropic membrane shells with application to mitral valve mechanics. Constitutive modelling and finite element implementation.* Int J Numer Methods Eng, 2007. **71**(8): p. 987-1008.

141. Skallerud, B., V. Prot, and I.S. Nordrum, *Modeling active muscle contraction in mitral valve leaflets during systole: a first approach.* Biomech Model Mechanobiol, 2011. **10**(1): p. 11-26.

142. Weinberg, E.J. and M.R.K. Mofrad, *Transient, three-dimensional, multiscale simulations of the human aortic valve.* Cardiovascular Engineering, 2007. **7**(4): p. 140-155.

143. Mansi, T., et al., *An integrated framework for finite-element modeling of mitral valve biomechanics from medical images: Application to MitralClip intervention planning.* Medical image analysis, 2012. **16**(7): p. 1330-46.

144. Stevanella, M., et al., *Mitral valve patient-specific finite element modeling from cardiac MRI: application to an annuloplasty procedure.* Cardiovas Eng Tech, 2011. **2**(2): p. 66-76.

145. Votta, E., et al., *Mitral valve finite-element modelling from ultrasound data: a pilot study for a new approach to understand mitral function and clinical scenarios.* Philos Transact A Math Phys Eng Sci, 2008. **366**(1879): p. 3411-34.

146. Wang, Q. and W. Sun, *Finite Element Modeling of Mitral Valve Dynamic Deformation Using Patient-Specific Multi-Slices Computed Tomography Scans.* Ann Biomed Eng, 2013. **41**(1): p. 142-153.

147. Einstein, D.R., et al., *Haemodynamic determinants of the mitral valve closure sound: a finite element study.* Med Biol Eng Comput, 2004. **42**(6): p. 832-46.

148. Kunzelman, K.S., D.R. Einstein, and R.P. Cochran, *Fluid-structure interaction models of the mitral valve: function in normal and pathological states.* Philos Trans R Soc Lond B Biol Sci, 2007. **362**(1484): p. 1393-406.

149. Lee, C.H., et al., *An inverse modeling approach for stress estimation in mitral valve anterior leaflet valvuloplasty for in-vivo valvular biomaterial assessment.* J Biomech, 2014. **47**(9): p. 2055-63.

150. Rausch, M.K., et al., *Mechanics of the mitral valve : A critical review, an in vivo parameter identification, and the effect of prestrain.* Biomech Model Mechanobiol, 2012.

151. Wenk, J.F., et al., *First finite element model of the left ventricle with mitral valve: insights into ischemic mitral regurgitation.* Ann Thorac Surg, 2010. **89**(5): p. 1546-53.

152. Einstein, D.R., et al., *The relationship of normal and abnormal microstructural proliferation to the mitral valve closure sound.* J Biomech Eng, 2005. **127**(1): p. 134-47.

153. Driessen, N.J., C.V. Bouten, and F.P. Baaijens, *Improved prediction of the collagen fiber architecture in the aortic heart valve.* J Biomech Eng, 2005. **127**(2): p. 329-36.

154. Driessen, N.J., et al., *Computational analyses of mechanically induced collagen fiber remodeling in the aortic heart valve.* J Biomech Eng, 2003. **125**(4): p. 549-57.

155. Niederer, S.A. and N.P. Smith, *At the heart of computational modelling.* J Physiol, 2012. **590**(Pt 6): p. 1331-8.

156. Carruthers, C.A., et al. *Alterations in the microstructure of the anterior mitral valve leaflet under physiological stress*. in *ASME 2012 Summer Bioengineering Conference*. 2012. American Society of Mechanical Engineers.

157. Sakamoto, Y., R.M. Buchanan, and M.S. Sacks, *On intrinsic stress fiber contractile forces in semilunar heart valve interstitial cells using a continuum mixture model.* J Mech Behav Biomed Mater, 2016. **54**: p. 244-58.

158. Zeng, Z., et al., *Macromolecular transport in heart valves. III. Experiment and theory for the size distribution of extracellular liposomes in hyperlipidemic rabbits.* American Journal of Physiology-Heart and Circulatory Physiology, 2007. **292**(6): p. H2687-H2697.

159. Zeng, Z.Q., et al., *Macromolecular transport in heart valves. I. Studies of rat valves with horseradish peroxidase.* American Journal of Physiology-Heart and Circulatory Physiology, 2007. **292**(6): p. H2664-H2670.

160. Zeng, Z.Q., et al., *Macromolecular transport in heart valves. II. Theoretical models.* American Journal of Physiology-Heart and Circulatory Physiology, 2007. **292**(6): p. H2671-H2686.

161. Rajamannan, N.M., et al., *Calcific aortic valve disease: not simply a degenerative process: A review and agenda for research from the National Heart and Lung and Blood Institute Aortic Stenosis Working Group. Executive summary: Calcific aortic valve disease-2011 update.* Circulation, 2011. **124**(16): p. 1783-91.

162. Otto, C.M., *Calcific aortic valve disease: outflow obstruction is the end stage of a systemic disease process.* European Heart Journal, 2009. **30**(16): p. 1940-1942.

163. Lee, C.H., et al., *Quantification and simulation of layer-specific mitral valve interstitial cells deformation under physiological loading.* J Theor Biol, 2015. **373**: p. 26-39.

CHAPTER 2: INTERLAYER MICROMECHANICS OF THE AORTIC HEART VALVE LEAFLET

Preface

While the mechanical behaviors of the fibrosa and ventricularis layers of the aortic valve (AV) leaflet are understood, little information exists on their mechanical interactions mediated by the GAG-rich central spongiosa layer (**Fig. 2.1a-b**). Parametric simulations of the interlayer interactions of the AV leaflets in flexure utilized a tri-layered finite element (FE) model of circumferentially oriented tissue sections to investigate inter-layer sliding hypothesized to occur. Simulation results indicated that the leaflet tissue functions as a tightly bonded structure when the spongiosa effective modulus was at least 25% that of the fibrosa and ventricularis layers. Novel studies that directly measured transmural strain in flexure of AV leaflet tissue specimens validated these findings. Interestingly, a smooth transmural strain distribution indicated that the layers of the leaflet indeed act as a bonded unit, consistent with our previous observations [1] of a large number of transverse collagen fibers interconnecting the fibrosa and ventricularis layers. Additionally, when the tri-layered FE model was refined to match the transmural deformations, a layer-specific bimodular material model (resulting in four total moduli) accurately matched the transmural strain and moment-curvature relations simultaneously. Collectively, these results provide evidence, contrary to previous assumptions, that the valve layers function as a bonded structure in the low-strain flexure deformation mode. Most likely, this results directly from the transverse collagen fibers that bind the layers together to disable physical sliding and maintain layer residual stresses. Further, the spongiosa may function as a general dampening layer while the AV leaflets deforms as a homogenous structure despite its heterogeneous architecture[1].

INTRODUCTION

To date, only two studies have investigated the mechanical behavior of individual leaflet layers using micro-dissection techniques. Vesely et al. observed the extensibility of intact tissue under uni-axial tension to be significantly different from the individual layer responses [2]. In the second study, Stella et al. observed measurably different behavior under biaxial loading of the separated layers [1]. The intact tissue response was intermediate to the separated responses. Interestingly, it has been assumed previously that the spongiosa layer enables sliding between the fibrosa and ventricularis during opening and closing [3-7], yet little data exists to support this theory. Vesely and Boughner (1989) and Song et al. (1990) claim evidence of measured sliding between the layers; however, the loading conditions used were artificial and not representative of physiological flexural conditions. Thus, the degree of bonding that exists between the two layers and its effects on AV leaflet bending *in vivo* remains unclear. Moreover, based on these findings, it is apparent that the individual layers function quite differently in the intact configuration than separated and must be evaluated in the intact state.

Historically, the term "tissue engineering" is attributed to Y.C. Fung [8]. The term underscored the importance of "the application of principles and methods of engineering and life sciences toward a *fundamental understanding of structure-function* relationships in normal and pathologic mammalian tissues and the development of biological

---

[1] Portions of this chapter have been previously published in Biomechanics and Modeling in Mechanobiology (Interlayer micromechanics of the aortic heart valve leaflet, vol. 13, pp. 813-26, 2014).

substitutes to restore, maintain, or improve tissue function." Thus, it is imperative that fundamental structure-function understanding guides the reproduction of native tissue if it is to emulate its native counterpart successfully. Clearly, the complex nature of valve biomechanical behavior and function [9] cannot be duplicated with simple homogenous biomaterials. Consequently, to develop replacement valvular tissues we must more fully understand the fundamental micromechanics of the tissue in both healthy and diseased states [10].

In the present study, we conducted an integrated simulation-experimental investigation utilizing flexural deformations of intact AV leaflets as a means to probe interlayer interactions. In addition to being a natural choice to study interlayer micromechanics, flexure is a major deformation mode of the cardiac cycle [11, 12] and has been extensively used for valve tissue mechanical studies [13-17]. Parametric simulations of interlayer interactions were first conducted using a tri-layered leaflet tissue finite element (FE) model to simulate interlayer sliding hypothesized to occur. To validate these findings and further refine the model, experimental studies on porcine AV leaflet tissue were conducted to examine bi-directional flexural response, and relative interlayer movement using actual transmural strain responses.

METHODS

The flexural deformation mode not only represents a major deformation mode of heart valve leaflets, but also allows direct examination of individual layer responses in tension and compression. It should be noted that AV leaflets experience complex bidirectional flexure *in vivo* [18, 19]. To simplify the problem, we focused on bending in the circumferential direction only, as it is the major curvature change in leaflets [20]. A circumferentially oriented rectangular leaflet tissue strip configuration, located below the

Nodulus of Arantius (**Fig. 2.2-a**), was used for simulation since the central belly region is structurally most representative of the leaflet [21]. First, an initial model was used to conduct a parametric study of the deformation through the thickness of the leaflet at varying degrees of layer connectivity. The results of this model were verified with novel experimental flexure studies that quantified the transmural variations in transmural strain. Based on these results, a refined flexural model was then developed to simultaneously match the moment-change in curvature (M-$\Delta\kappa$, where $\Delta\kappa = \kappa-\kappa_0$ and κ_0 the initial curvature) relationship and transmural deformation of the AV in both bending directions. The end result was a clearer picture of interlayer mechanical interactions of the low strain behavior that occurs in flexure.

Initial simulations of AV leaflet tissue flexure

A finite element (FE) model was developed to simulate AV leaflet tissue in flexure using the software package COMSOL Multiphysics v4.3 (Burlington, MA). A rectangular model geometry was used, set to 14 mm in length (circumferential direction) by 3 mm in width (radial) by 0.4 mm thick. The tissue layer geometry was derived on previous histological data [22], which showed that the fibrosa represented 45% of the volume, the spongiosa 30%, and ventricularis 25%. Boundary conditions simulating three-point bending were avoided to ensure no point-loading effects would occur in the center of tissue and end-loading conditions were used instead. The boundary conditions thus consisted of pins at both ends of the model tissue, and a horizontal load was applied at one pin in the X_1 direction, causing the model tissue to undergo transverse deflection (**Fig. 2.2-b**). The mesh consisted of 3612 8-node brick elements, and shape functions for pressure (linear) were set to one order lower than displacement (quadratic) to avoid locking. The geometry was modeled as symmetric along the X_3 axis to decrease computing time (**Fig. 2.2-b**).

To establish both the material model and to obtain an initial set of material parameters, we began with previously published AV flexure data for inactivated tissues [9, 13]. The following Ogden model, assuming incompressibility, was chosen as it provides an additional level of flexibility compared to a neo-Hookean model

$$W=\sum_{p=1}^{N=1}\frac{\mu_p}{\alpha_p}\left(\lambda_1^{\alpha_p}+\lambda_2^{\alpha_p}+\lambda_1^{-\alpha_p}\lambda_2^{-\alpha_p}-3\right) \qquad (2.1)$$

where α is a constant, μ the shear modulus, and λ_1 and λ_2 are the principle stretches. When $\alpha = 2$ and N=1, **Eq. 2.1** will simplify to the standard neo-Hookean form. The classic analytical solution of an incompressible isotropic beam under flexure [23] was used to establish an initial material model for a homogenized single layer beam from **Eq. 2.1**. This was accomplished by matching the non-linear shape of the M-$\Delta\kappa$ relationship of the leaflet bending data to the Ogden model analytical solution from a straight to circular beam (**Fig. 2.3**).

Interlayer bonding simulation

To simulate the effects of various levels of interlayer bonding, the following parametric simulation was performed. The fibrosa and ventricularis moduli were set to 45 kPa based on the prediction of the initial flexure simulation described above. Next, bending simulations were performed up to curvature changes of 0.1, 0.2 and 0.3 mm^{-1} with values for the spongiosa shear modulus μ_S varied. A value of 1 Pa represented relatively unbonded fibrosa and ventricularis layers; then μ_S was assigned increasing values (μ_S= 0.1-10 kPa) to simulate increasing levels of bonded states. Lastly, the spongiosa was assigned the same layer properties as the fibrosa and ventricularis to represent a perfectly bonded state. The deformation gradient tensor was derived from the reference (X_1, X_2) and deformed (x_1, x_2) coordinates of the element nodes using $\mathbf{F}_{ij}=\frac{\partial x_i}{\partial X_j}$. The resulting deformation gradient tensor **F** was decomposed into stretch and rotation tensors, **U** and **R**, respectively. The transmural variation in total axial stretch, $\Lambda_1=\sqrt{\mathbf{U}_{11}^2+\mathbf{U}_{12}^2}$, with respect to the thickness of the tissue was used to determine the overall effects of bonding on transmural deformations. Normalized thickness was defined with the ventricularis at the origin and the fibrosa at unity.

Transmural strain experimental validation studies

A custom device performed flexure tests on AV leaflets, described in detail in [24]. Briefly, two optical systems simultaneously collect flexural rigidity and transmural deformation data. A macro imaging system tracks markers on one edge of the sample. From these markers the curvature was calculated as well as the applied load via a marker on the bending bar transverse linkage. On the opposite edge of the sample a micro imaging system employs micron-sized ink marks to determine transmural strain via post processing techniques. A specially designed tank and tissue holder maintains placement and physiological conditions of the sample being tested.

Native porcine aortic roots were removed from hearts obtained from an abattoir within three hours of sacrifice. Leaflets were dissected from the root along their attachment points, and cut into a circumferentially oriented rectangular strip of tissue for testing using a fresh razor blade to ensure smooth flat surfaces in the reference state (**Fig. 2.2-a**). On average, specimens were 318±46 microns thick, 13.7±2.1 mm long, and 2.8±0.2 mm wide [24]. Five small red ink markers were created on the side of the tissue farthest from the free edge for curvature calculation using the macro imaging system (**Fig. 2.2-c**). Airbrushing the edge of the tissue opposite to the red macro markers using a Badger Sotar airbrush (Badger Air-Brush Co., Franklin Park, IL) and black India ink created microscopic markers for tracking with the micro-imaging system (**Fig. 2.2-d**). A stainless steel sleeve was glued to one end of the tissue using cyanoacrylate and then slipped onto a steel dowel to allow for free rotation and restricted translation of the tissue. The tank-tissue holder assembly was mounted to a bi-directional (X_1 axis movement) stage fitted with two precision linear actuators (model MM-4M-EX80, National Aperture Inc., Salem NH). A small amount of cyanoacrylate glue attached a second stainless steel sleeve to the loading end of the tissue; this sleeve then slipped over a vertically mounted 316V stainless steel bending bar of known stiffness. The stiffness of the bar determined the amount of force produced as a function of the bar's displacement, eliminating the necessity of load cells. Actuation of the bi-directional stage in the X_1-direction moved the entire tank and sample, causing the transverse linkage to bend the bending bar. In this design, both positive and negative changes in curvature could be tracked, allowing a single-run experiment in both the with-curvature (WC) and against-curvature (AC) testing directions.

For the bending data, the following information was recorded for the duration of the experiment: coordinates of red macro markers, displacement of the bending bar, and the current curvature of the tissue. Analysis of the bending data was detailed by [25] and summarized here. A custom-written Mathcad (PTC, Needham, MA) program computed curvature, change in curvature, and moment at the middle five markers for each time point of the experiment. The resulting marker positions were fit to a fourth-order polynomial so that the curvature of the tissue could be determined. The initial curvature, κ_0, was recorded by the control system and subtracted from consequent curvature measurements to obtain the change in curvature $\Delta\kappa = \kappa-\kappa_0$. 18 specimens were tested to a curvature change up to 0.3 mm^{-1} based on recent *in vitro* measurements [20]. For clarity, results are reported for a change in curvature of $0.2mm^{-1}$. The moment was determined by using the position of the central marker and the displacement of the bending bar (**Eq. 2.2** and **Fig. 2.2-b**)

$$M = P\,y \qquad (2.2)$$

where M is the applied moment, y is the deflection from the horizontal axis, and P is the axial force. The displacement of the bending bar was tracked in real-time since the applied axial force, P, was a function of the displacement. The deflection, y (**Fig. 2.2-b**) was computed using the spatial y coordinate of the central tissue marker and the y coordinate of the horizontal axis drawn from post to post. The resulting data is reported as the averaged M/I vs. $\Delta\kappa$ response of the 18 specimens to normalize with respect to specimen geometry.

To determine transmural deformation, captured images from the micro-imaging system that tracked the markers on the edge of the tissue were analyzed (**Fig. 2.2-d**). A telecentric lens was used to avoid loss of accuracy from taking measurements from surface bending, resulting in surfaces not orthogonal to the imaging system, on the strain measurements. From the macro-level images, LabVIEW software (National Instruments, Austin, TX) identified and numbered markers and stored their centroidal coordinates. For the micro images used to determine the transmural stretch, an image-based particle tracking strain-mapping method, detailed in [26], computed the local deformation gradient **F** over the imaged region. Briefly, the reference and deformed states determined the displacement field and were fitted to obtain **F**. Rigid body deformation was removed using polar decomposition. The particle tracking method was shown to measure stretch as small as 1.001 with 0.05% net accuracy [24]. The location of the neutral axis was determined by plotting Λ_1 against the thickness of the tissue to determine the location where Λ_1=1.

Validation of experimental/simulation method

Validation studies were carried out with 1 mm thick silicone rubber sheets cut into rectangular strips of the same dimensions as the experimental studies described above, 14mm in length by 3 mm in width. The shear modulus of the strips was determined using tensile testing with a MTS Tytron 250 Mechanical Test System and in flexure using the same custom flex device. The estimated shear moduli values obtained from the three methods were compared to ensure accuracy of both the computational and experimental methods.

RESULTS

Initial tissue material model

The resulting M-$\Delta\kappa$ relation from the analytical solution was normalized to the maximum achieved moment at a curvature of 0.28 mm^{-1}, the maximum observed experimentally measured value. Although there was some variation with applied moment, we determined that a value for α of ~2.0 captured the shape of the M-$\Delta\kappa$ (**Fig. 2.3**, r^2= 0.93). It is important to note that the analytical solution utilized a single layer and simplified boundary conditions [23], and was thus only used to set the value of the α parameter. Based on these results, we returned to the isotropic incompressible hyperelastic neo-Hookean material model to simulate the AV tissue in flexure

$$W=\frac{\mu_L}{2}(I_1-3) - p(I_3-1) \tag{2.3}$$

where I_1 and I_3 are the first and third invariant of the left Cauchy-Green deformation tensor $\mathbf{C}=\mathbf{F}^T\mathbf{F}$, respectively, p is the Lagrange multiplier to enforce incompressibility, and L indicates the layer (L=F,S, or V). With this model a value of μ_L = 45 kPa fit the data well (0.974) and was used for the fibrosa and ventricularis layers in the unimodular simulations.

Parametric interlayer bonding model study

As expected, the simulated transmural Λ_1 distribution demonstrated substantial sliding between the fibrosa and ventricularis layers at extremely low spongiosa layer moduli values (**Fig. 2.4**). As the spongiosa modulus more closely matched that of the outer layers (i.e. layers becoming more bonded), the transmural variation in Λ_1 became nearly linear. Both bending directions showed an expected shift in the neutral axis (NA) location towards the fibrosa layer since it was assigned a modulus stiffer than the ventricularis based on previous studies. From these basic simulations, we determined that in order for the spongiosa to exhibit measurable differences in transmural stretch from the fibrosa and ventricularis, μ_s must be less than 1 kPa. This estimated threshold is independent of imposed curvature.

Transmural strain experimental results

The M-$\Delta\kappa$ response of AV tissue strips was observed to be slightly nonlinear in both bending directions (**Fig. 2.5**). It should be noted that our previous work assumed a linear M-$\Delta\kappa$ relationship to simplify parameter estimation [9]. The current approach was more accurate since the moduli were estimated directly from the M-$\Delta\kappa$ data (**Fig. 2.5**), including accounting for the observed small non-linearity. Interestingly, as in our three-point bending study [9], no significant directional differences were found in the overall flexural response (**Fig. 2.5**)

However, we noted that the transmural strain measurements varied with bending direction. AV results revealed specimens flexed in the AC direction exhibited a maximum Λ_1 stretch that increased from 1.016 to 1.026, with a respective increase in the change of curvature from 0.1 to 0.3 mm^{-1}. The minimum Λ_1 stretches decreased, indicating an increase in strain, with increasing curvature with typical values progressing from 0.984 to 0.969. The average neutral plane location for all specimens showed a shift towards the fibrosa in the AC direction, but was not statistically significant (**Table 2.2**). The NA results indicated a shift towards the stiffer fibrosa layer.

Refined leaflet model

The motivation for refining the initial model was the observed differences between the WC and AC bending directions in the transmural Λ_1 distributions (**Fig. 2.6**). That is, the M-$\Delta\kappa$ and transmural strain responses could not be simultaneously fit in both bending directions (**Fig. 2.6c-d**). This suggests an asymmetry in the tissue layer tensile-compressive responses. Thus, to capture the bidirectional M-$\Delta\kappa$ and transmural response of the leaflet observed in flexure, a refined FE model was created using a bimodular material model. Further, since the parametric interlayer bonding study and experimental validation indicated the leaflet tissue is a functionally bonded unit, we developed the following refined model by absorbing the spongiosa equally into the two outer layers, resulting in a bilayer model. Geometry and initial curvature of the model was matched to the AV experimental specimens. The following bimodular incompressible neo-Hookean material model was implemented

$$W^{\pm}=\frac{\mu_L^{\pm}}{2}(I_1-3) - p(I_3-1) \tag{2.4}$$

which has four total moduli, $\mu_F^{\pm}$ and $\mu_V^{\pm}$, with the subscripts indicating the fibrosa and ventricularis layer and the superscripts indicating in tension (+) or compression (-), respectively.

As in the first model, we conducted simulations in both flexural directions and simultaneously matched to the experimental data. Selected nodal positions on the edge of the specimen, representing tissue marker positions used in experimental configuration, were used to compute and equivalent change in curvature for each applied moment. The moment was plotted with respect to curvature change taken from the point of maximum curvature at the center of the specimen. The experimental M-Δk data was averaged and fit to the FE model. The fitting procedure was carried out in a two-step process. First, the interrelationship of the moduli for each bending direction was determined by matching the location of the NA to experimental data for both directions (**Table 2.2**). Secondly, the layer moduli values were determined by fitting the M-Δκ with the experimental data using a minimization of the mean squared error (MSE) (**Table 2.3**). The MSE was defined as $\frac{1}{n}(\hat{y} - y)^2$, where n is number of experimental data points and $\hat{y}$ and y are the simulation and experiment derived M-Δκ relation, respectively. It was crucial to perform the fitting procedure in this way to ensure both the transmural deformation and the M-Δκ aligned with the experimental measurements. The magnitude values reported are within ±0.5 kPa, and the computed Λ_1 through the thickness of the tissue is within the range experimental error (± 0.0141) of the experimental measurements (**Fig. 2.6**).

An aspect of our approach is accounting for distortion of a beam of rectangular cross section undergoing large strains, which is a well-known effect [27]. This distortion causes out-of-plane warping, and was observed experimentally in the AV tissue strips. In the present experimental setup, out-of-plane warping (in the X_3 direction) was estimated to affect the transmural stretch measurements by ~0.02 in the net axial stretch between the center of the specimen and the edge (Fig 7). Warping also affected the measured location of the neutral axis, making it appear almost unchanged with each bending direction when taken from the edge of the specimen (Figs. 7 b-c). This edge warping affected approximately 40% of the tissue volume (20% from each edge), leaving the interior 60% of the tissue largely unaffected. To account for this warping effect, we utilized the edge deformations to match the experimental data, as well as reported the predicted interior deformation responses that represent bulk tissue behavior as would occur *in vivo*.

The resulting simulations indicated that Λ_1 in the center of the specimen (representing the bulk of the tissue) demonstrated significant changes in NA location with bending direction (**Fig. 2.8**). In the WC bending direction, the NA shifted towards the ventricularis approximately 0.35 of the normalized thickness. Interestingly, this indicates the whole fibrosa is under compression and the tensile load is carried entirely by the ventricularis (**Fig. 2.8**). This shift in the NA towards the ventricularis was reflected in the estimated moduli (**Table 2.3**) indicating greater tensile stiffness in the ventricularis than compressive stiffness in the fibrosa (a ratio of approximately 2:1). In the AC bending direction the NA shifts to approximately 0.79 of the normalized thickness, indicating the fibrosa was much stiffer under tension than compression (**Fig. 2.8**). Again, this shift was reflected in the estimated moduli values, indicating greater tensile stiffness of the fibrosa compared with compressive stiffness of both the fibrosa and ventricularis (ratio of approximately 4:1).

Model validation

Silicone rubber test specimens demonstrated good agreement with tensile test shear moduli measurements. Specifically, the model estimated 6.454± 0.168 MPa, the experimental flex measurement was 6.658± 0.366, and the tensile tests measuring 6.211 ± 0.225 MPa (**Table 2.1**).

DISCUSSION

Overview

The present study investigated the interlayer micromechanics of the AV leaflet undergoing flexure using an integrated simulation/experimental approach. While the modeling effort was rather straightforward, we noted the need for examining both the macro-level flexural behavior (M-$\Delta\kappa$) and the micro-level transmural deformation, integrated into a 3D beam model, to accurately capture AV leaflet layer interactions. Our major findings were that 1) the AV leaflet layers function in flexure as a perfectly bonding unit, and 2) the spongiosa layer did not have measurably different mechanical properties compared to the fibrosa and ventricularis. This last point was primarily evidenced by the smooth transmural stretch distributions (**Fig. 2.4**). Thus, in the low strain environment, the spongiosa may be described mechanically as contiguous extension of the two outer layers.

Bimodular material model for leaflet tissue in flexure

It is important to emphasize here that a standard Neo-Hookean material, single layer model was only used in the first part of the study to set the basic model form and a range for the material model parameters. Interestingly in the refined model, a bimodular material model for the AV leaflet tissue in flexure was identified, similar to approaches used for other fibrous tissues and part of a larger sub-class of bimodular materials [28, 29]. We also determined that both the fibrosa and ventricularis have greater stiffness in tension than in compression (a ratio of approximately 4:1, **Table 2.3**). The fibrosa was found to be consistently stiffer than the ventricularis, approximately 2:1 in both tension and compression (**Table 2.3**). The bimodular behavior was not entirely surprising based on the unique arrangement of ECM components throughout the three layers. Moreover, the transmural deformation of the AV leaflet tissue indicated that the NA shifted closer to the ventricularis in the WC direction at all curvature levels. This implied that when the ventricularis was under mainly tensile loading in the circumferential direction and the fibrosa was fully under compression, the ventricularis provided most of the stiffness (**Fig. 2.8**). When the valve flexed in the opposite direction (AC), the NA shifted closer to the fibrosa, leaving the entire ventricularis and one third of the fibrosa under compressive loading in the circumferential direction, and the remaining two thirds of the fibrosa under tension, providing most of the stiffness (**Fig. 2.8**). Structurally, this behavior was likely due to the greater concentration of the comparatively stiff type I collagen within the fibrosa and the greater concentration of the more compliant elastin found in the ventricularis. Previous studies have shown that the elastin in the ventricularis forms a honeycomb network around the collagen fibers, allowing the fibers to stretch and return to their initial state [30, 31]. The collagen fibers in the fibrosa do not possess an extensive or organized elastin network and are bound together more tightly [32]. Additionally, proteoglycans intimately bind to collagen fibers and may provide significant reinforcement to the fibrosa in doing so, compared to the collagen-depleted ventricularis.

Implications for AV micromechanical function

Functionally, the leaflet's ability to present low flexural stiffness during valve opening (WC) and high stiffness during closure (AC) is only attainable through its distinctive hierarchical structure in which all elements act in unison to provide seamless transition from the diastole to systole cycle. The present study indicated that, contrary to previous hypotheses [3-7], the spongiosa did not allow the fibrosa and ventricularis layers to slide with respect to one another. If this did occur (i.e. when functioning as loosely bonded layers), each layer would have its own neutral axis (**Fig. 2.4**), greatly complicating intra-layer deformation patterns. Instead, the leaflets appear to function as a fully bonded unit. These findings are also consistent with our observations [1] of the presence of a large number of collagen fiber interconnections between the fibrosa and ventricularis layers. While recent work by Tseng et al. [33] shows intriguing results of elastin presence in the spongiosa layer, the nature of the fibrous interconnections between the layers at a gross level appears to be dominated by collagenous fibers. However, the exact composition and structure of these interconnecting fibers remains unknown. More importantly, the composition of these fibers has no effect on the findings of the current study, since what is important is that they exist and appear to bind the fibrosa and ventricularis layers.

The question remains: what is the mechanical role, if any, of the spongiosa layer? In a recent study we noted that viscoelastic behavior of heart valve tissues only manifested themselves in the low strain region [34]. Also, other studies have demonstrated a functionally elastic behavior for native valvular tissues in tension [35-37]. Yet, it can be speculated that the centrally located spongiosa layer functions to reduce high frequency motions of the leaflet during the opening/closing phases. Such dampening-like behavior might be a mechanism to reduce hemodynamic energy loss during the opening and closing phases. Current information on this aspect of valve function is scant, and must be the subject of future investigations.

Limitations and the need for an integrated experimental/simulation approach

In actual heart valves, flexure occurs during the opening/closing phases and is bidirectional [12, 20]. Since it is not currently possible to experimentally investigate this behavior directly, we chose instead to approximate this behavior with a strip model in circumferential bending [20]. While not accounting for bending in both directions, this is also the primary fiber direction and any measured behavior should approximate the native tissue response *in vivo*. It should also be noted that Vesely et al. (1989) investigated the flexural behavior of native AV leaflets and found that the NA was close to the fibrosa surface under AC flexure, suggesting a very low compressive modulus compared to tensile in agreement with the present study. However, testing was performed under unrealistic loading conditions, making it difficult to correlate to *in vivo* function. In the present approach, an end-loading configuration was used, which should be more representative of the *in vivo responses* of the bulk leaflet tissue since it avoided any artificial contact points. We also note that the measured transmural deformation data must be matched with the computational model at the edge of the specimen and then reported from the central region in order to represent the bulk tissue behavior accurately.

CONCLUSIONS

In summary, the behavior of AV leaflet tissue as a composite beam was determined by examining the M-Δk relationship and the stretch along the edge of the tissue during bending. We conclude that while it has been previously speculated that valve layers slide with respect to one another during valve opening/closing, our evidence suggests that the leaflet layers function as a *single bonded unit*. Layers appear to be bonded by transverse collagen fibers that hold residual strains in place. Thus, despite a heterogeneous structure and differences in stress distribution throughout the layers, the AV leaflet deforms as a homogenous structure. Furthermore, the valve tissue in flexure requires a bimodular material model. Further studies are needed to investigate the leaflet micromechanics in activated cellular conditions that represent healthy and diseased physiological conditions.

Specimen	**Model**	**Flexure**	**Tensile**
1	5.973	5.805	5.551
2	6.501	6.558	6.557
3	6.593	6.677	6.333
4	6.749	7.591	6.403
Average	6.454	6.658	6.211
SEM	0.168	0.366	0.225

Table 2.1: Silicone material validation study, showing E (MPa).

	Against Curvature (AC)		With Curvature (WC)	
Δκ (mm^{-1})	Experiment	Simulation	Experiment	Simulation
0.1	0.5987 ± 0.0929	0.6209	0.5453 ± 0.1012	0.4935
0.2	0.5903 ± 0.1022	0.5994	0.5571 ± 0.1021	0.5495
0.3	0.6026 ± 0.0730	0.5835	0.5629 ± 0.0315	0.5670

Table 2.2: Predicted and measured neutral axis locations.

n=18	Estimated Moduli Values (kPa)		Relative Moduli Values		Layer Moduli Ratios
	μ^+	μ^-	μ^+	μ^-	μ^+/ μ^-
Fibrosa	139.5	29.55	100%	21.2%	4.72:1
Ventricularis	65.00	16.74	46.6%	12.0%	3.88:1

Table 2.3: Normalized material parameters

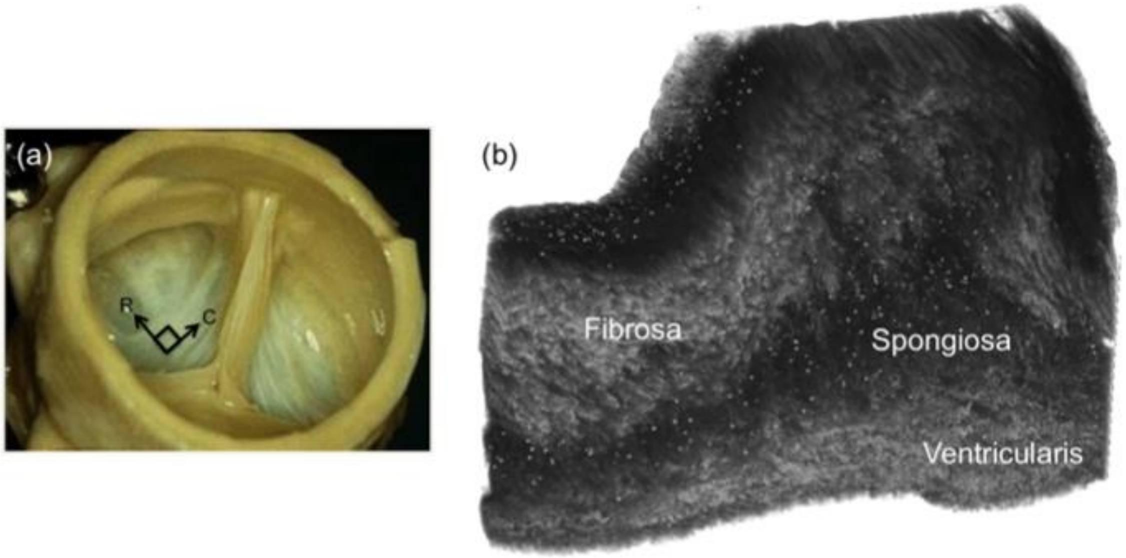

Figure 2.1: (a) The aortic valve (b) A 1 mm x 1 mm section from the central belly region illustrating the 3D the tri-layered leaflet structure.

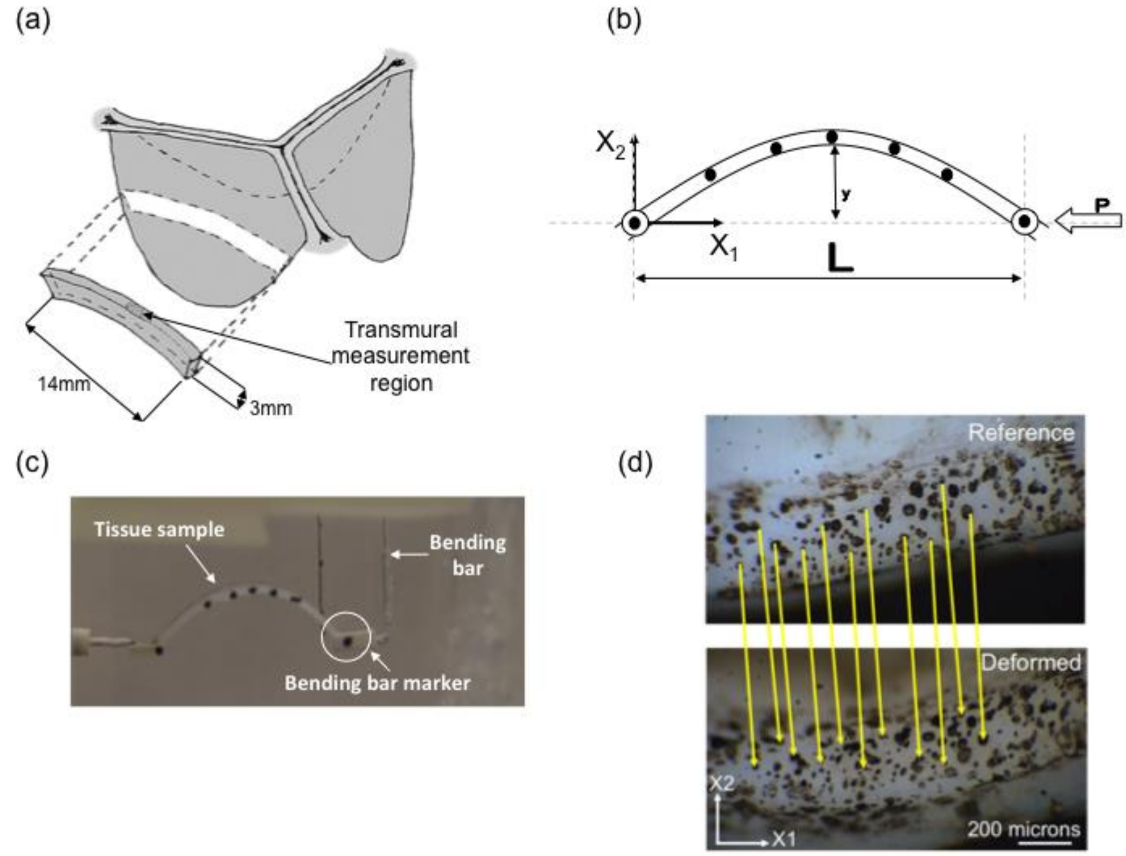

Figure 2.2: (a) A schematic showing the orientation of the tissue strip and leaflet, and the location of the transmural strain measurement, (b) A free body diagram of tissue mounted in the testing device with a force, P, applied to its free end. The orientation of the X_1 and X_2 coordinate system specifies the X_1 axis coincident with the circumferential direction and the X_2 axis to reflect the thickness of the leaflet, (c) Markers used by the macro-imaging system shown on the edge of the tissue strip, (d) Transmural strain images obtained using micro camera, showing the reference and deformed tissue states.

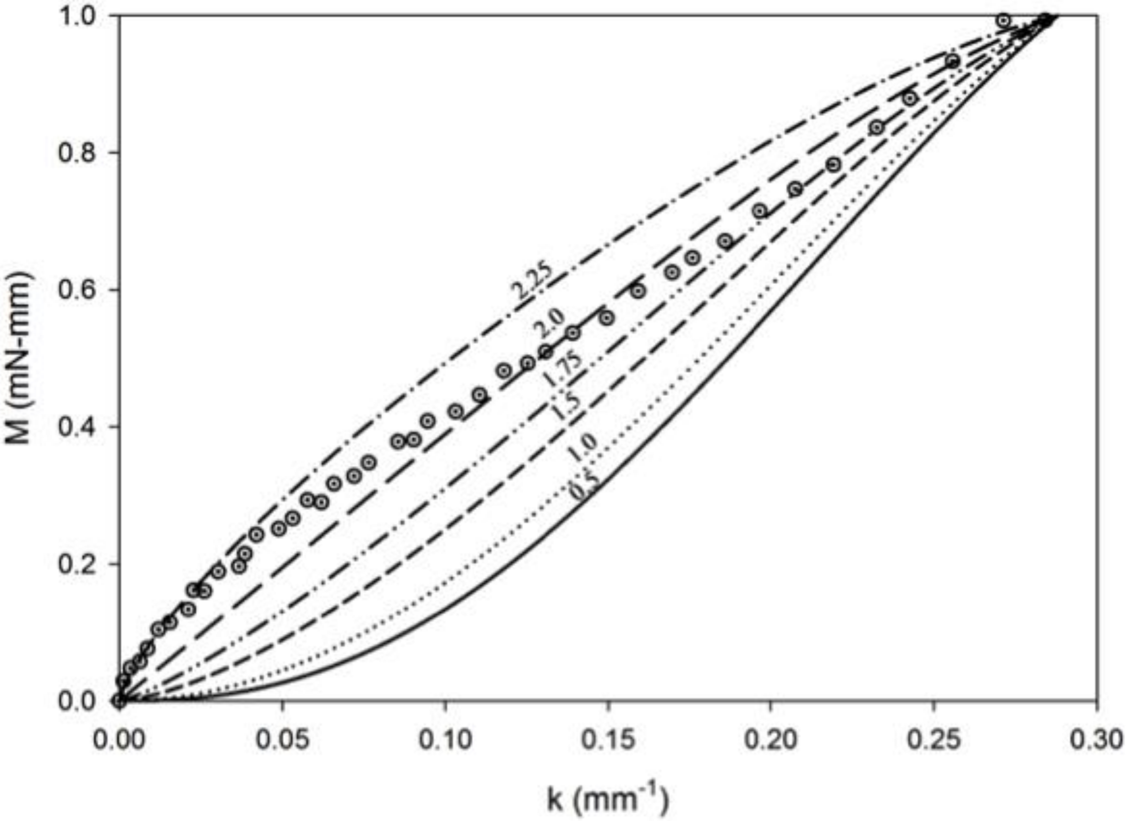

Figure 2.3: Comparison of the M-Δκ data [13] with the analytical solution of the one-term Ogden model using various α parameter values. Note that the experimental data was normalized to the maximum achieved moment at a Δκ of 0.28 mm^{-1} A value for α of 2.0 approximately captured the shape of the M-Δκ.

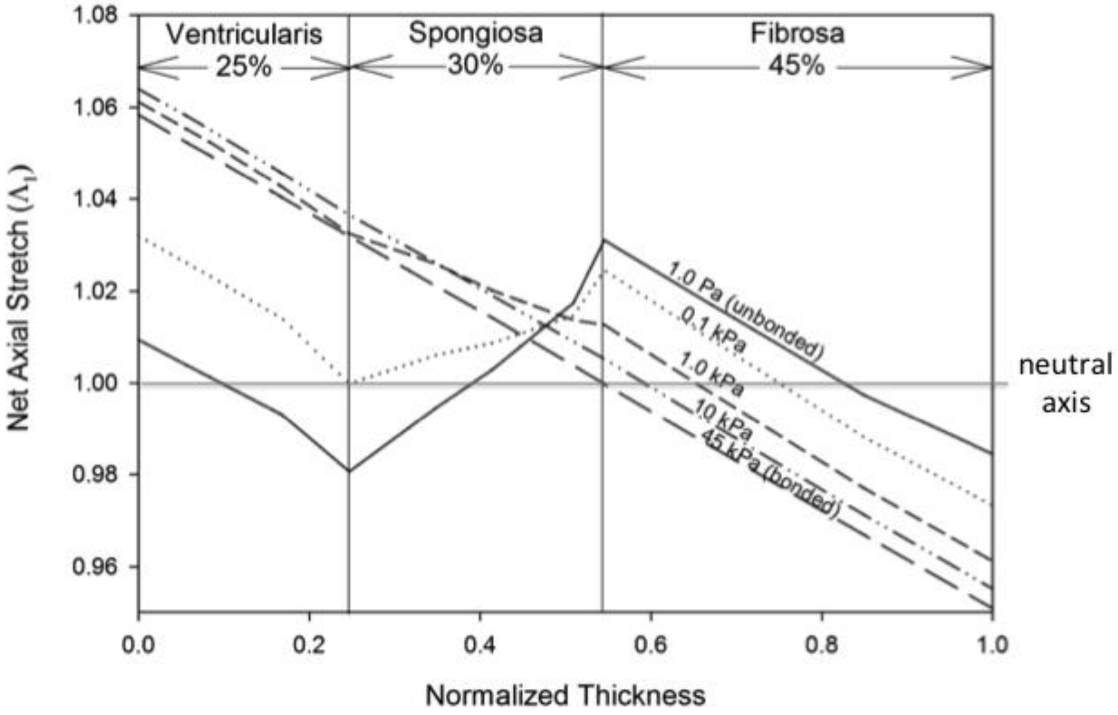

Figure 2.4: Transmural stretch Λ_1 simulation results plotted against the normalized leaflet thickness. For measurable differences to occur in transmural stretch between the fibrosa and ventricularis, simulations indicate the spongiosa must possess a shear modulus less than 1 kPa. The WC bending direction simulation results are shown for sake of clarity, although the same simulation results were observed for the AC bending direction. The cuvature change reported is 0.2mm^{-1} since the reported results demonstrated independence of curvature change.

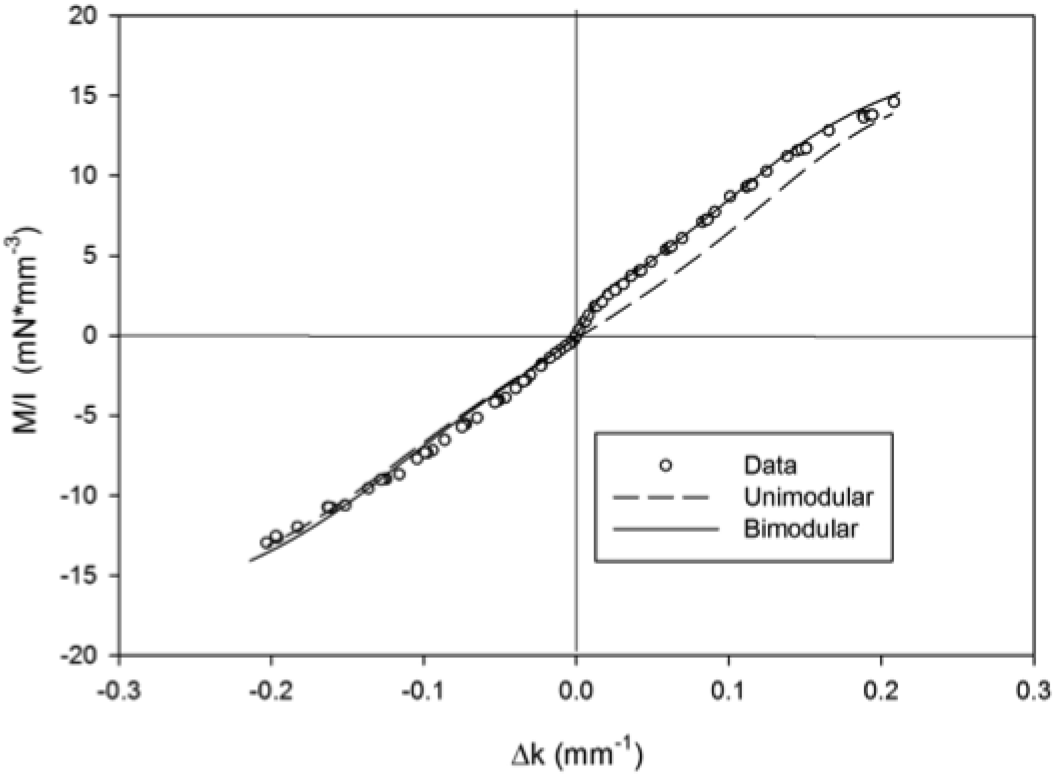

Figure 2.5: The M-Δκ response of a native porcine AV leaflet in the AC and WC directions that has been bent to a Δκ of 0.2 mm^{-1} in either direction. Simulations using a unimodular (dashed line) and bimodular material model (solid line) are superimposed over experimental data. The bimodular model represents the bidirectional bending behavior slightly better than the unimodular material.

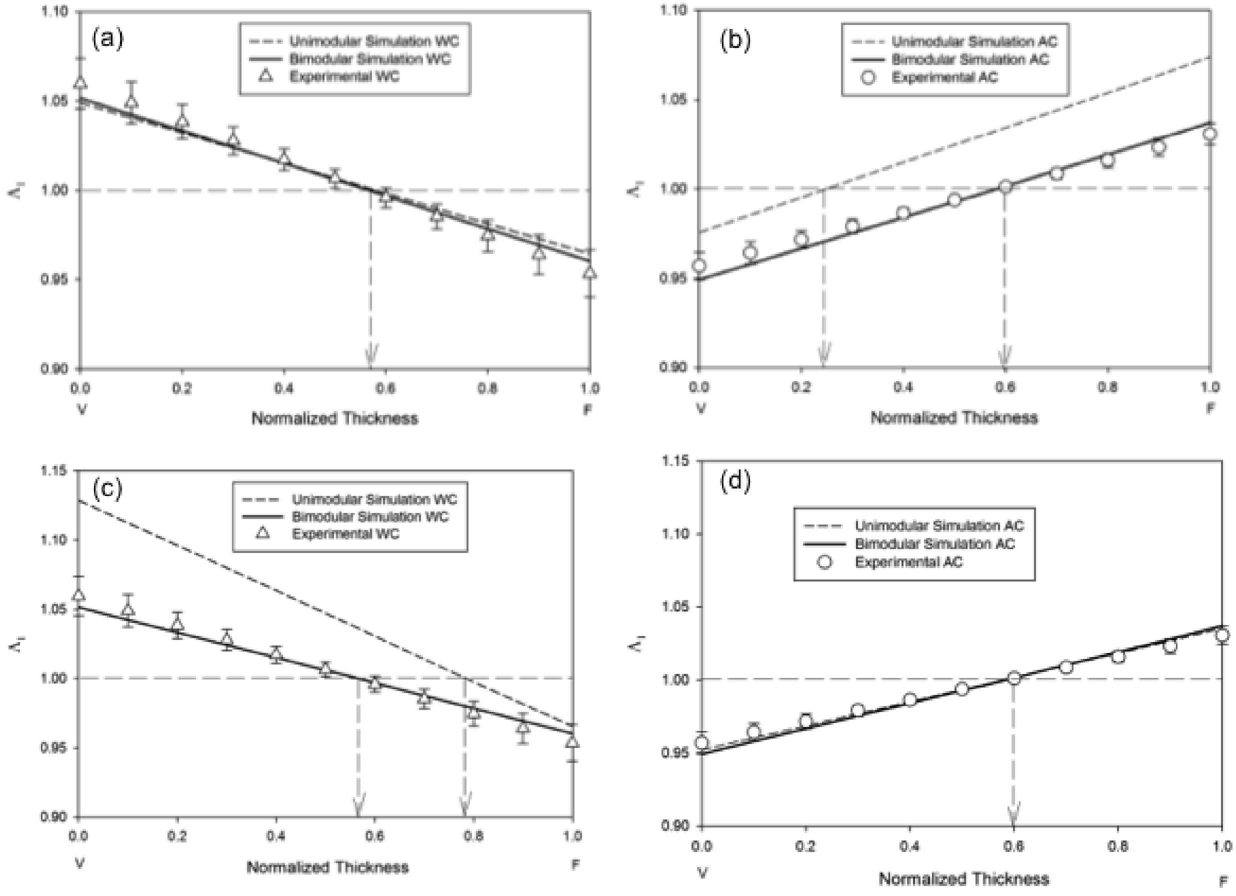

Figure 2.6: Experimental transmural Λ_1 results plotted against the normalized thickness for (a,c) WC and (b,d) AC samples at $\Delta\kappa=0.2$ mm^{-1}, along with the corresponding unimodular (dashed line) and bimodular (solid line) simulation results. (a)-(b) represent strain matched in the WC direction, showing the resulting discrepancy in the AC fit using a unimodular model. Similarly, (c)-(d) represent strain matched in the AC direction, resulting in a poor WC fit using the unimodular model. Although the M-Δk behavior is captured with unimodular model, the transmural deformation response can only be captured in both the WC and AC directions using the bimodular material model.

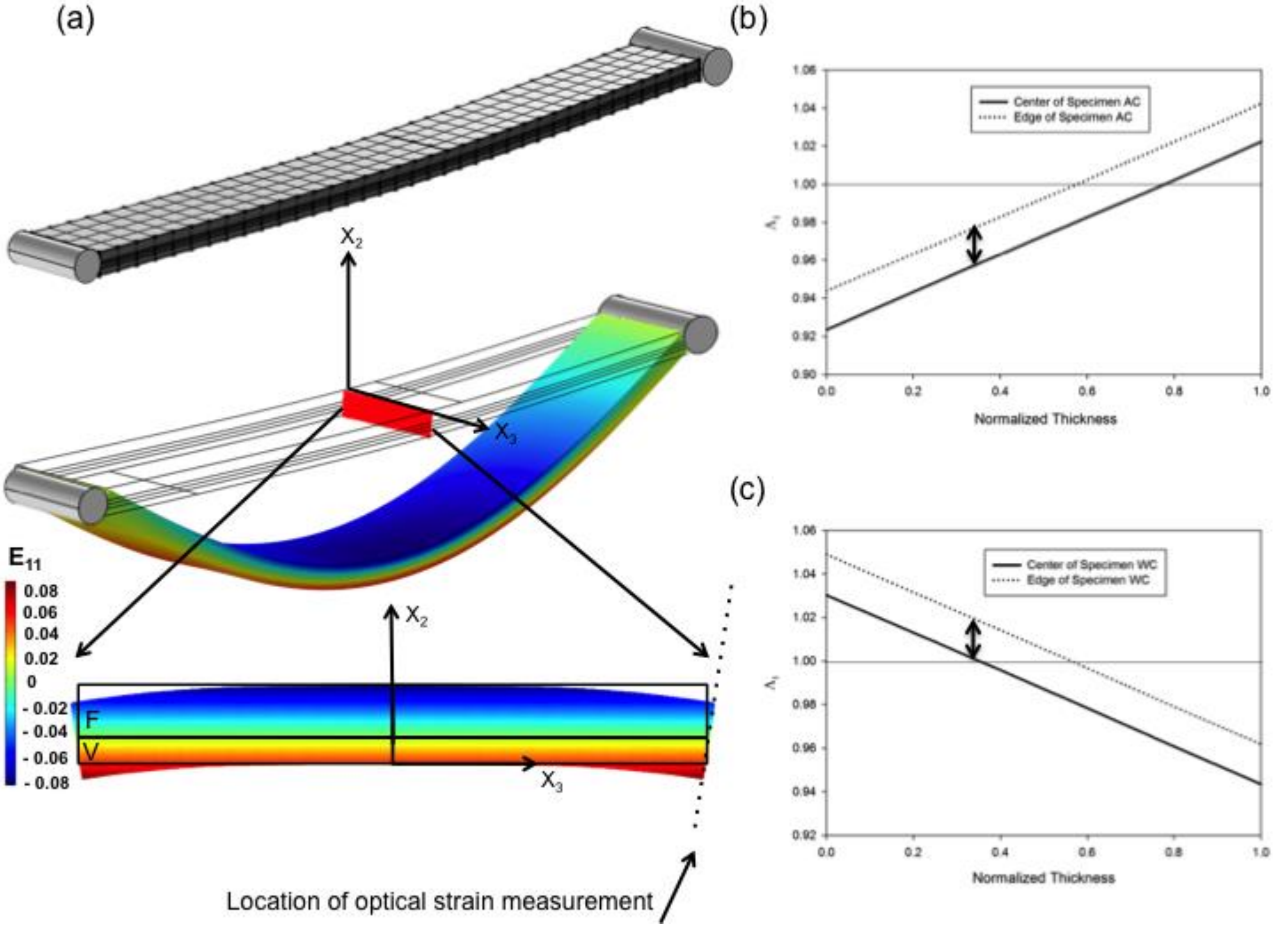

Figure 2.7: (a) Transmural Green-Lagrange strain distribution (E_{11}) from the simulated flexure model demonstrating a disruption at the edges due to standard warping that occurs during bending. (b) A significant shift (2% stretch) in axial deformation is observed by plotting Λ_1 vs. normalized thickness in both the WC and (c) AC bending directions. It is important to note the associated shift in the neutral access location when observing deformation at the edge or in the unaffected central region of the tissue.

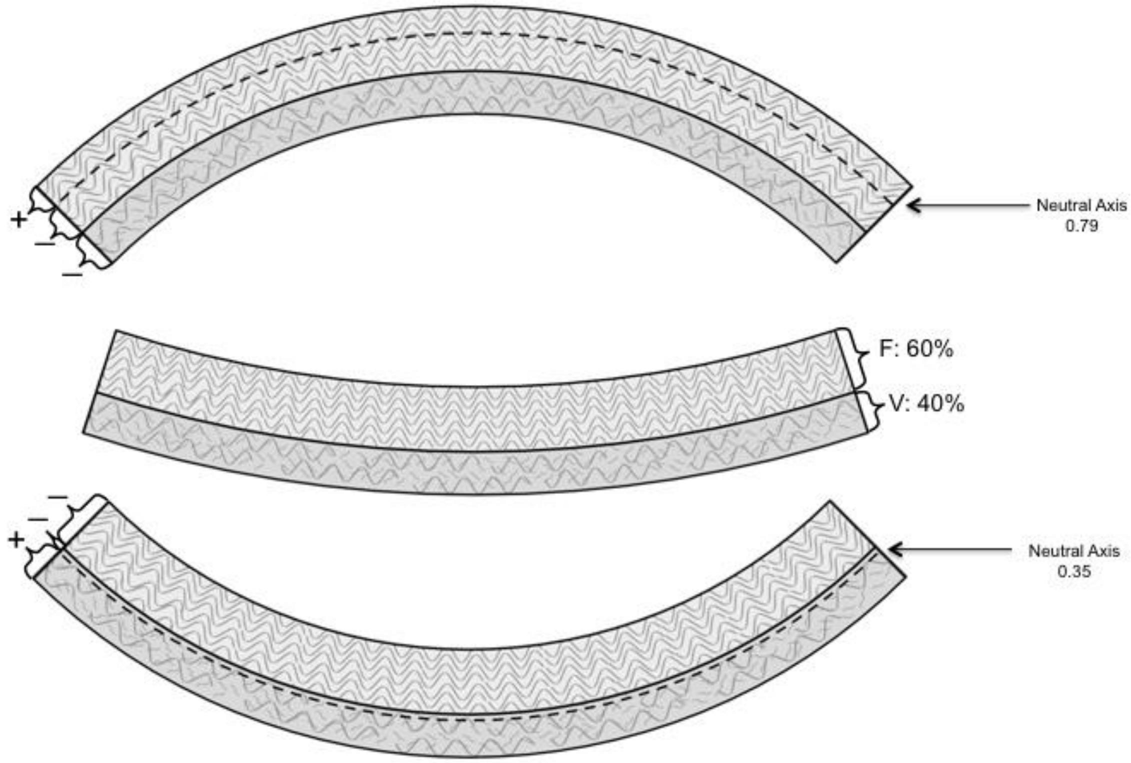

Figure 2.8: A schematic summarizing the changes in NA location experienced by the bulk tissue for both bending directions. In the WC bending direction, the NA shift towards the ventricularis approximately 0.35 of the normalized thickness, demonstrating the whole fibrosa under compression (-) and the majority of the ventricularis under tension (+). In the AC bending direction the NA shifts to approximately 0.79 of the normalized thickness. These results indicate that both the ventricularis and fibrosa are much stiffer under tension (+) than compression.

REFERENCES

1. Stella, J.A. and M.S. Sacks, On the biaxial mechanical properties of the layers of the aortic valve leaflet. J Biomech Eng, 2007. 129(5): p. 757-66.
2. Vesely, I. and R. Noseworthy, Micromechanics of the fibrosa and the ventricularis in aortic valve leaflets. Journal of Biomechanics, 1992. 25(1): p. 101-113.
3. Mohri, H., D. Reichenback, and K. Merendino, Biology of homologous and heterologous aortic valves, in Biological Tissue in Heart Valve Replacement, M. Ionescu, D. Ross, and G. Wooler, Editors. 1972, Butterworths: London. p. 137.
4. Talman, E.A. and D.R. Boughner, Glutaraldehyde fixation alters the internal shear properties of porcine aortic heart valve tissue. Annals of Thoracic Surgery, 1995. 60: p. S369-S373.
5. Thubrikar, M., The Aortic Valve. 1990, Boca Raton: CRC. 221.
6. Vesely, I. and D. Boughner, Analysis of the bending behaviour of porcine xenograft leaflets and of neutral aortic valve material: bending stiffness, neutral axis and shear measurements. J Biomech, 1989. 22(6-7): p. 655-71.
7. Song, T., I. Vesely, and D. Boughner, Effects of dynamic fixation on shear behaviour of porcine xenograft valves. Biomaterials, 1990. 11(3): p. 191-6.
8. Woo, S.L.Y. and Y. Seguchi, Tissue Engineering - 1989. BED ed. Vol. 14. 1989, New York: Asme. 146.
9. Sacks, M.S., W. David Merryman, and D.E. Schmidt, On the biomechanics of heart valve function. J Biomech, 2009. 42(12): p. 1804-24.
10. Butler, D.L., S.A. Goldstein, and F. Guilak, Functional tissue engineering: The role of biomechanics. Journal of Biomechanical Engineering-Transactions of the Asme, 2000. 122(6): p. 570-575.
11. Sacks, M.S. and A.P. Yoganathan, Heart valve function: a biomechanical perspective. Philos Trans R Soc Lond B Biol Sci, 2007. 362(1484): p. 1369-91.
12. Iyengar, A.K.S., et al., Dynamic in vitro quantification of bioprosthetic heart valve leaflet motion using structured light projection. Ann Biomed Eng, 2001. 29(11): p. 963-73.
13. Merryman, W.D., et al., The effects of cellular contraction on aortic valve leaflet flexural stiffness. J Biomech, 2006. 39(1): p. 88-96.
14. Engelmayr, G.C., Jr., et al., The independent role of cyclic flexure in the early in vitro development of an engineered heart valve tissue. Biomaterials, 2005. 26(2): p. 175-87.
15. Mirnajafi, A., et al., The flexural rigidity of the aortic valve leaflet in the commissural region. J Biomech, 2006. 39(16): p. 2966-73.

16. Gloeckner, D.C., K.L. Billiar, and M.S. Sacks, Effects of mechanical fatigue on the bending properties of the porcine bioprosthetic heart valve. Asaio J, 1999. 45(1): p. 59-63.

17. Gloeckner, D., K. Billiar, and M. Sacks. The bending behavior of fixed porcine aortic cusp. in Third World Congress of Biomechanics. 1998. Hokaiddo, Japan.

18. Thubrikar, M., et al., The elastic modulus of canine aortic valve leaflets in vivo and in vitro. Circ Res, 1980. 47(5): p. 792-800.

19. Thubrikar, M.J., J. Aouad, and S.P. Nolan, Comparison of the in vivo and in vitro mechanical properties of aortic valve leaflets. J Thorac Cardiovasc Surg, 1986. 92(1): p. 29-36.

20. Sugimoto, B. and M.S. Sacks, EFFECTS OF LEAFLET STIFFNESS ON IN-VITRO DYNAMIC BIOPROSTHETIC HEART VALVE LEAFLET SHAPE. Cardiovascular Engineering and Technology, 2013. in-press.

21. Billiar, K.L. and M.S. Sacks, Biaxial mechanical properties of the natural and glutaraldehyde treated aortic valve cusp--Part I: Experimental results. J Biomech Eng, 2000. 122(1): p. 23-30.

22. Carruthers, C.A., et al., Gene Expression and Collagen Fiber Micromechanical Interactions of the Semilunar Heart Valve Interstitial Cell. Cellular and Molecular Bioengineering, 2012: p. 1-12.

23. Rivlin, R.S., Large Elastic Deformations of Isotropic Materials .5. The Problem of Flexure. Proceedings of the Royal Society of London Series a-Mathematical and Physical Sciences, 1949. 195(1043): p. 463-473.

24. Lam, T., The mechanical properties of native porcine aortic and pulmonary heart valve leaflets, in Department of Bioengineering. 2004, University of Pittsburgh: Pittsburgh, PA.

25. Engelmayr, G.C., Jr., et al., A novel bioreactor for the dynamic flexural stimulation of tissue engineered heart valve biomaterials. Biomaterials, 2003. 24(14): p. 2523-32.

26. Buchanan, R.M. and M.S. Sacks, Interlayer micromechanics of the aortic heart valve leaflet. Biomech Model Mechanobiol, 2014. 13(4): p. 813-26.

27. Timoshenko, S., History of strength of materials, with a brief account of the history of theory of elasticity and theory of structures. 1953, New York,: McGraw-Hill. 452 p.

28. Curnier, A., Q.C. He, and P. Zysset, Conewise Linear Elastic-Materials. Journal of Elasticity, 1995. 37(1): p. 1-38.

29. Ateshian, G.A., Anisotropy of fibrous tissues in relation to the distribution of tensed and buckled fibers. J Biomech Eng, 2007. 129(2): p. 240-9.

30. Scott, M. and I. Vesely, Aortic valve cusp microstructure: The role of elastin. Annals of Thoracic Surgery, 1995. 60: p. S391-S394.

31. Vesely, I., The role of elastin in aortic valve mechanics. Journal of Biomechanics, 1998. 31(2): p. 115-123.

32. Schoen, F. and R. Levy, Tissue heart valves: Current challenges and future research perspectives. Journal of Biomedical Materials Research, 1999. 47: p. 439-465.

33. Tseng, H. and K.J. Grande-Allen, Elastic fibers in the aortic valve spongiosa: A fresh perspective on its structure and role in overall tissue function (vol 7, pg 2101, 2011). Acta Biomaterialia, 2012. 8(2): p. 924-924.

34. Eckert, C.E., et al., On the biomechanical role of glycosaminoglycans in the aortic heart valve leaflet. Acta Biomaterialia, 2013. 9(1): p. 4653-4660.

35. Stella, J.A., J. Liao, and M.S. Sacks, Time-dependent biaxial mechanical behavior of the aortic heart valve leaflet. J Biomech, 2007. 40(14): p. 3169-77.

36. Grashow, J.S., A.P. Yoganathan, and M.S. Sacks, Biaxial stress-stretch behavior of the mitral valve anterior leaflet at physiologic strain rates. Ann Biomed Eng, 2006b. 34(2): p. 315-25.

37. Grashow, J.S., et al., Planar biaxial creep and stress relaxation of the mitral valve anterior leaflet. Ann Biomed Eng, 2006a. 34(10): p. 1509-18.

CHAPTER 3: IN SITU CONTRACTILE BEHAVIOR OF THE AORTIC VALVE INTERSTITIAL CELL

Preface

As a first step in understanding AVIC behavior in the normal AV, the non-viable tissue model developed in SA 1 (**Chapter 2**) was extended to formulate a macro-micro FE model to simulate mechanical behavior of AVICs under activation. As a brief overview, the developed macro (tissue) level model presented in this chapter captures the bidirectional flexural response of AV intact layers at different activation states from previous studies [1]. At the micro-level tissue AVIC size, shape, distribution and orientation were quantified from histological data from all layers. A representative volumetric element (RVE) was then optimized statistically for each layer to represent the native 3D structure. AVIC stiffness, contraction and connectivity were built into the micro-model framework as variable parameters. Displacements at the RVE boundaries in the macro-model were then applied as boundary conditions to the micro model RVE. For each parametric iteration, resulting stress was averaged over the entire RVE and compared to the stress of the homogenized RVE in the macro-model until an acceptable fit was met, arriving at a parameter estimation for each AVIC activation state. The objective of this study was to create a macro-micro model to use in conjunction with new and existing tissue level bending data to probe the effects of AVIC stiffness, AVIC contraction and AVIC-ECM connectivity on the tissue level response during flexure. As mentioned prior, the numerical-experimental methodology presented in this chapter can be paired with biomechanical experimental testing to probe the activation state of the AVIC in response to different activation stimuli. Predicting the physical state of AVICs *in-situ* provides a significant advantage from ex-situ measurements in that AVICs remain in the native microenvironment, maintaining essential AVIC-ECM coupling.

International prize

The work presented in this chapter won 1st place overall in the Cardiovascular Biomechanics Ph.D. paper competition at the 7th World Congress of Biomechanics in Boston, MA in 2014 for the paper entitled “In Situ Estimation of Aortic Valve Interstitial Cell Mechanical State from Tissue Level Measurements”.

INTRODUCTION

As discussed previously, the aortic valve (AV) is comprised of three layers (fibrosa, spongiosa, ventricularis), the division of these layers is characterized by distinct variations of collagen, glycosaminoglycan (GAG), and elastin. Each tissue layer is maintained by aortic valve interstitial cells (AVICs), which are highly contractile and known to possess plastic phenotypes. During normal valve function, AVICs exhibit a heterogeneous phenotype, with characteristics reminiscent of both fibroblasts and smooth muscle cells. With the onset of disease, AVICs transition into a highly contractile phenotype and are loosely referred to as the commonly known myofibroblast. Calcified valves have been shown to possess a large population of myofibroblastic-like cells [2] that are characterized by an upregulation of alpha smooth muscle actin (αSMA) and an associated increase in contractile behavior. AVICs are often referred to as “activated” as they transition to the myofibroblast phenotype during growth and disease and contribute to altered extracellular matrix (ECM) composition seen in diseased valves [3].

The key role the microenvironment plays during the progression of disease is highlighted by the variability of disease manifestation throughout the layers. Severely stenotic aortic valves exhibit calcified nodules almost exclusively on the fibrosa side, the ventricularis otherwise appears healthy [4]. To date, there has been little characterization of the surrounding AVIC microenvironment, however, its role in shaping AVIC behavior is clearly demonstrated by numerous studies [5-11]. AVICs are physically coupled with the surrounding ECM, via $\alpha_2\beta_1$ integrins, a major collagen-binding protein. The necessity of maintaining VIC-ECM coupling in actin-mediated VIC force generation has been demonstrated in mitral valve leaflet tissue [12] and is hypothesized to be as essential in the aortic valve.

AVIC culture in 3D synthetic and natural gels have provided valuable insight and aided in characterization of VIC healthy and diseased phenotypes [13-15]. The advantage to these simple systems is their tunability, allowing tailoring for each study to answer specific biological questions. However, gel systems are severely limited in that they lack the complexity of native tissue. In particular, Butcher et al. [16] found that the VIC expression of αSMA in 3D collagen gel culture was significantly reduced compared to expression on 2D substrates. This further highlights the role of matrix interaction in modulating AVIC phenotype. Similarly, as mentioned in **Chapter 1**, our research group has demonstrated that measuring mechanical stiffness of nonadherant VICs using micropipette aspiration [17] and monolayer (2D) cultured VICs using atomic force microscopy [18] provide similar trends when comparing pulmonary VICs (PVICs) vs. AVICs, yet with stark differences in magnitude (approximately 10-fold). This further implies the significance of the VIC microenvironment in dictating phenotypic activity.

Given the overwhelming body of evidence that VIC-ECM connectivity plays a crucial role in VIC biomechanical state, the need for assessing VIC behavior in its native environment seems obvious, yet unattainable using existing experimental methodologies. Existing methods of measuring cell mechanics are all destructive in nature: micropipette aspiration (MA), atomic force microscopy (AFM), and magnetocytometry (MCT) for example. To assess the underlying mechanical behavior of cells in dense connective tissues a computational approach is necessary.

Continuum based constitutive models are limited to macroscopic tissue behavior, and do not have the ability to capture mechanical behavior at the lower microscale making them insufficient for studying structure-functional relationships in hierarchical tissue structures such as the AV. Like heart valves, bone, cartilage and tendons are all hierarchical structures. Therefore, developing computational models for these dense connective tissues involves spanning multiple length-scales using what are loosely termed “multi-scale models”. Multiscale modeling allows the integration of microstructural level details into a modeling framework, thereby providing a more realistic representation of tissue complexity and relating the underlying structure mechanics to the overall tissue mechanics. Variations of multi-scale models have been poised for bone [19-22], cartilage [23-26], tendons [27, 28], heart valves [29-31], and generalized dense connective tissue [32-34]. However, many of these examples do not include the contributions of cells, only incorporating ECM structural details. The few models that do include cells, such as the work by Lai et al. [32], only consider the passive contribution, ignoring any contractile capabilities. A further limitation to this work is that it is built using experiments observing cell behavior in 3D collagen gels, which greatly underestimates the complexity of native tissue as mentioned previously.

Traditional multi-scale methodology

Multiscale modeling approaches in mechanics aim to link the macro and micro scales of materials. Homogenization is the process of obtaining a macroscopic-level stress-strain response from a material’s underlying microstructure. The macro-scale problem is discretized using FE absent of any assumptions regarding the material constitutive response. Instead, at every material point where the constitutive response is needed, the macro deformation gradient tensor $\mathbf{F}_M$ (**Fig. 3.1**) is calculated and used to formulate and solve a micro-scale boundary value problem (BVP) imposed on a representative volumetric element or RVE. The micro-scale problem is solved to find the microscopic stress distribution in the entire micro-scale domain. Using the computational homogenization method, the macroscale stress tensor, $\mathbf{P}_{\mathrm{M}}$ is calculated from the stress distribution in the micro-scale problem and fed back to the macro-scale. Consequently, the macroscopic stress tensor is calculated at every material point by solving the corresponding RVE problem. The RVE size can be identified one of two ways, first, it can be based on the statistical nature of the material microstructure in that it must be the smallest material volume statistically representative of the microstructure [35]. Second, the RVE can be defined as the smallest volume of the heterogeneous material whose behavior represents accurately the actual macroscopic behavior. The homogenization theory facilitates carrying out microstructural and continuum analyses separately and then combing them systematically in this manner. This schematic introduced by Kouznetsova et al. [36] is introduced in **Fig. 3.1.**

Limitation for biological materials

When applying a traditional macro-micro homogenization approach to the context of the AV, the sizing requirement between scales must be revisited. The basic scaling requirement for the macro-micro approach described above is for the microscopic length scale to be significantly smaller than the characteristic size of the macroscopic sample. This implies that the average size of the AVICs, the underlying constituents, must be far smaller than the thickness of the individual valve layers if we are to treat each layer as a separate material model with its own individual RVE. The AV has an average thickness of approximately 500 microns, with the thinner ventricularis and spongiosa layers averaging around 30% of this volume (~150 microns), and AVIC sizes have been reported to be approximately 15 microns. When sizing the RVE appropriately in this context, the upper bound would be 150 microns (macro), with a lower bound of 15 microns (micro). This represents a scale separation of 10:1 at best between the RVE and the underlying constituents if the RVE were to be at the upper bound of size. This similarity in scale simply does not satisfy these requirements for a traditional multi-scale framework.

Furthermore, the multi-scale approach is also dependent upon known behavior at the micro-scale. For non-biological materials this approach works well, however for living tissues, microstructures are often non-uniform and are difficult to study without significantly altering the tissue during preparation or the process itself. Therefore, given the presented scale separation challenges, as well as the poorly characterized underlying microstructure, utilizing a traditional multi-scale framework is not feasible in this context. To accomplish a reasonable approach for estimating changes in underlying AVIC behavior in response to various stimuli, a variation of the traditional macro-micro mapping methodology is introduced in detail in this chapter and summarized in **Fig. 3.2**. Briefly, unlike traditional multi-scale methods, a constitutive material model at the macro level is used to represent AV observed bending behavior. Experimental data acquired from our laboratory from non-viable [37] and activated viable AV tissue under flexure [1] enabled the development of a tissue-level model with an accurate representation of observed layer differences. To estimate the contribution of the underlying AVIC changes in stiffness and contraction to observed tissue changes under flexure [1], a second FE model was developed that is microanatomically representative of what we currently understand of AV microstructure. To inversely compute AVIC changes from tissue level flexure measurements, AVIC material properties were varied parametrically, and optimized by minimizing the difference between the volumetric averaged homogenized stress of the RVE between scales. To summarize, the following two objectives will be addressed in this chapter by the development of a macro-micro FE model:

1) Identify a unique constitutive model that captures the bidirectionality of the AV leaflet flexure response under varying contractile states based on experimental data (macro-model)
2) Map the measured layer specific tissue response down to the micro cell (AVIC) level and inversely estimate contributions of AVIC stiffness, contraction and ECM connectivity to the macro tissue-level response (micro-model)

METHODS

Flexural tissue testing

Examining the leaflet under bending deformation is ideal for several reasons: it is physiologically relevant representing the opening and closing of the leaflets, it is exquisitely sensitive to low force measurements and most importantly it allows us to observe the layer effects of the leaflet which have been shown to be a key contributor to bending behavior. Experimental data acquired from [1] were used to develop the macro component of the macro-micro model. Briefly as described in [1], viable strips of porcine tissue from the belly region of the AV were tested under 3-point bending using a custom flexure testing device [38]. Leaflets were bent with the natural leaflet curvature (WC) and against (AC) the natural leaflet curvature under three activation levels: inactive (thapsigargin), normal (norm: 5Mm KCl) and hypertensive (hyper: 90Mm KCl). Each specimen was first tested in Dulbecco’s Modified Eagle Medium (DMEM) with high glucose supplemented with 5 mM KCl. Testing media was then changed to DMEM with 90mM KCl and specimens were allowed to incubate for 3 minutes prior to testing a second time in both WC and AC bending directions using the same procedure. A separate group of specimens was incubated overnight in 10µm thapsigargin and tested using the same procedure.

The mean strip thickness, t, was calculated from averaged measurements over the strip's entire length. Between 8 and 12 graphite markers were attached to the cut surface nearest the coapting edge using cyanoacrylate. The specimen was held upright with two sleeves, which were supported by stationary posts while the bending bar was applied to the center of the tissue. In order to determine the deflection of the bending bar during testing, a reference rod was attached to the stage that was displaced equivalently with the bending bar base. Therefore, with all the aforementioned components, it was possible to record while testing, the stationary posts, bending bar, reference rod, and specimen markers. As the specimen was deflected, the image was recorded on a VHS tape which was used for data analysis after testing. The marker, post, and bending bar positions were entered into a custom Matlab program that calculated the resulting moment, M (mN*mm), about the right post from the centrally applied load, P (mN); and the change-in- curvature, Δκ (mm^{-1}), of the tissue at small time increments during the loading. The local radius of curvature was determined from the parabolic curve fit to the markers. The applied moment M versus the measured change in curvature Δκ is related by the Bernoulli-Euler moment-curvature equation:

$$M = E_{eff} I \Delta\kappa \tag{3.1}$$

Where $E_{eff}I$, or flexural rigidity corresponds to the slope of the measured M- Δκ curve, and I is the second moment of inertia defined as:

$$I = \frac{1}{12t^3w} \tag{3.2}$$

Where t and w refer to the thickness and width of the sample respectively. The average bending response of the tissue was taken for each bending direction and each activation state. Outliers were determined as specimens lying outside of 2.5 times the standard deviation and not included in the final average in **Fig. 3.3.**

The effective modulus, E_{eff}, was determined from a linear regression of the M vs. $\Delta\kappa$ plots at the maximum $\Delta\kappa$ reached. A one-way Repeated Measures Analysis of Variance was performed on the WC group between normal and hypertensive and the AC group also between normal and hypertensive since the same samples were treated with both conditions. All statistical analyses were performed with SigmaPlot (San Jose, CA, USA). All additional pairwise multiple comparison procedures used a one-tailed t-test with an overall significance level of 0.05.

Macro-model

For clarity, a summary of nomenclature used in the macro and micro FE models as well as general acronyms is provided in **Table. 3.1**.

Formulation

The macro and micro FE models were created in the framework of ABAQUS version 6.14 (Dassault Systemes, Johnston, RI, USA). All FE simulations were run on a Linux machine equipped with 16 core Intel Xeon E5-2650 CPU.

In **Chapter 2** it was demonstrated that modeling the AV leaflet tissue as a bilayered bonded unit under bending deformation was accurate in capturing the overall tissue stiffness as well as the underlying strain [39]. Accordingly, the macro model tissue strip was modeled in 3D as a bilayered and biomodular neo-Hookean isotropic nearly incompressible material (**Eq. 3.3**) based on the extensive analysis provided in **Chapter 2** [39].

$$W^{\pm} = \frac{{}_{state}\mu_{Macro}^{layer\pm}}{2}(I_1 - 3) - p(I_3 - 1) \tag{3.3}$$

${}_{state}\mu_{Macro}^{layer\pm}$ represents the shear modulus of the Macro material for a given layer (F-fibrosa and V-ventricularis) under tensile load (+) or compressive load (-). I_1 and I_3 are the first and third invariant of the left Cauchy-Green deformation tensor $\mathbf{C}=\mathbf{F}^T\mathbf{F}$, respectively, and p is the Lagrange multiplier to enforce incompressibility. It is important to point out the macro subscript, which indicates a material parameter specific to the macro model, not to be confused with the subsequent Micro model. This model is used at the continuum level FE simulations to accurately represent the bending behavior of AV tissue strips.

Boundary conditions

The boundary conditions used in the FE simulation consisted of the left edge of the specimen treated as a pin constraint and the right edge subjected to incremental controlled displacement (**Fig. 3.4**). End-loading was used in place of 3-point loading due to the necessity of collecting detailed information from representative volumetric elements (RVEs) from the center of the specimen, at the point of greatest moment and curvature. End-loading constraints avoided the effects of point loads in the vicinity of the RVEs and facilitated faster computational time. Practically speaking, future flexural testing of AV tissue will also exhibit end-loading as it allows for acquisition of transmural strain at the center of the specimen. The value of this additional information is discussed in detail in [39].

Mesh

The macro mesh represented the native geometry of the experimentally tested AV leaflet strips. A bilayered beam slightly bent (0.01 mm^{-1} curvature) with averaged length and thickness of the experimental samples (15mm in length x 4mm width x 0.462mm thickness). The fibrosa (F) layer was modeled as 60% of the beam thickness and the ventricularis (V) the remaining 40% as previously reported based on native tissue measurements [40] and the determination to model the tissue as bilayered as opposed to trilayered [39]. The finalized mesh contained 12,200 isoparametric second order hybrid brick elements. A single element of the macro model was representative of the micro RVE in each of the layers (RVE^{layer}).

Estimating tissue parameters

Nodal displacements and elemental and nodal stress and strain fields were output from the FE simulations. Parametric simulations were carried out to estimate the shear modulus of the bulk tissue for each layer (F and V) $({}_{state}\mu_{Macro}^{layer\pm})$ at each activation state (inactive, norm and hyper). Using displacement of nodal "markers" the M-$\Delta\kappa$ response was computed for each parametric iteration and a MSE was computed against the experimental data M-$\Delta\kappa$ response. A custom script was written to minimize the MSE using the scipy.optimize Python package and is summarized in **Fig. 3.5**. The location of the neutral axis was determined by plotting the stretch tensor component along the length of the beam (U_{11}) against the thickness of the tissue beginning with the ventricularis side (0.0) through to the fibrosa (1.0). The depth of the tissue that coincided with the U_{11} value of unity was the corresponding location of the neutral axis.

Macro RVE averaged stress

We assume the macroscopic stress at a material point is equal to the averaged RVE stress over the volume of the RVE as follows:

$$ {}_{\text{state}}\bar{\boldsymbol{\sigma}}^{layer\pm}_{Macro} = \frac{1}{V}\int \tilde{\sigma}(\hat{x})dV \tag{3.4} $$

The average stress of the macro RVE (**Eq. 3.3**) was computed using a custom Python script, extracting the FE estimated stress at all 27 nodes and numerically integrating using a 3-point Gauss quadrature in three dimensions.

Micro-model

RVE geometry and mesh

Drugan and Willis (1996) identified that to determine the appropriate size of an RVE it must be the smallest material volume that statistically represents the microstructure [35]. The density and spatial distribution of AVICs within the micro mesh were defined using data from [40] and [41]. The detailed data was used to establish an appropriate size range through the use of statistical dimensional analysis [40, 41]. AVICs were modeled as ellipsoid inclusions 14.16 microns along their long axis, and 7.49 microns along the short axes (**Fig. 3.6b**). A density of 270 million AVICs per mL was maintained in all RVE sizes. The orientation of the AVICs had a preferred nuclear direction along the circumferential direction in the circumferential-radial plane, with orientation angles normally distributed around 9.7 and 5.3 respectively (**Fig. 3.6c**). Second, using the study by [42] to determine the maximum AVIC contractile force that may occur under uniaxial isometric conditions, in combination with the AV experimental bending data to determine the maximum strain any RVE would experience, a "worst case scenario" condition was developed. A maximum contractile force of 100nN per cell (method of imposing contractile force described in detail in subsequent section) was imposed on the AVIC inclusions embedded within the mesh and the RVE was subjected to 8% uniaxial extension. The resulting volumetric stress was then computed. The size of the RVE was increased from 20 microns to 120 microns to examine the stress variation within the RVE as a result of increasing cube length (**Fig. 3.7**). The averaged stress was taken (**Eq. 3.4)** and the standard deviation of each component of the averaged tensor was determined from the stress at each RVE node described in (**Eq. 3.5**). Lastly, a scalar index (Frobenius norm **Eq. 3.6**) was used and minimized to identify the appropriate RVE size without compromising computational time. This was determined as the appropriate RVE length when the stress variation stabilized.

$$\sigma_{STDEV} = \sqrt{\frac{1}{N}\sum_{i=1}^{N}(\tilde{\sigma}(\hat{x}) - \bar{\sigma}_{RVE})^2} \tag{3.5}$$

$$\|\sigma\|_F = \sqrt{\sum_{i=1}^{m}(\sum_{j=1}^{n}|\sigma_{ij}|^2)} \tag{3.6}$$

The final RVE size was determined to be 80 μm^3 after the stress variation stabilized at a constant 0.2% deviation from the mean stress of all nodes (**Fig. 3.7**). The final RVE volume contained 138 AVIC inclusions and 210,708 first order hybrid tetrahedron elements. The volume fraction of AVICs is approximately 10% which corresponds to the established 270 million AVICs/mL density.

Formulation

An overview of the micro-model framework is provided in **Fig. 3.8**. The same bilayered and biomodular nearly incompressible neo-Hookean material was used to model the ECM of the micro model. The material model used for the AVIC ellipsoidal inclusions was also a neo-Hookean nearly incompressible material, with the addition of isometric thermal expansion [43]. The addition of thermal expansion was used as a means to emulate AVIC contraction by inducing an isothermal deformation of the inclusions:

$$W^{\pm} = \frac{\mu_{AVIC}^{layer}}{2}(\bar{I}_1 - 3) + \frac{1}{D_1}(J^{el} - 1)^2 \tag{3.7}$$

Where D_1 is a material constant defined by $\frac{2}{\kappa}$, κ being the bulk modulus of the material and J^{el} is the elastic volume ratio defined by:

$$J^{el} = \frac{J}{J^{th}} \tag{3.8}$$

$$J^{th} = (1 + \varepsilon^{th})^3 \tag{3.9}$$

Where ε^{th} is the thermal expansion strain that is obtained from the temperature (T) and the isotropic temperature dependent thermal expansion coefficient (α) here:

$$\varepsilon^{th} = \alpha \Delta \mathrm{T} \tag{3.10}$$

For all parametric simulations of the micro model, ΔT was kept constant and α values were later correlated to AVIC forces as described in detail below.

Layer-specific connectivity

Layer-specific microstructural ECM composition was not incorporated into the material model of the ECM, however AVIC-ECM connectivity differences throughout the layers were represented by the addition of a thin interface boundary around each AVIC (0.650μm). The modulus of this interfacial layer is assumed to be equivalent to the modulus of the AVIC, $\mu_{AVIC}^{F,V\pm}$, and can be tailored by multiplying the variable, $\beta_{AVIC}^{F,V\pm}$, which encompasses a range $\beta_{AVIC}^{F,V\pm} \in [0,1]$. When β=1, the AVIC is continuously bounded to the surrounding material (ECM) and as β approaches zero, it becomes less connected **(Fig. 3.9).**

Recent work in our group mentioned in **Chapter 1**, discovered that in the mitral valve, MVICs are phenotypically similar and differences in MVIC deformation throughout the layers is a result of varying mechanical stimuli due to changes in ECM microstructure and not necessarily MVIC behavior [44]. In the current model, this assumption was carried over to the micro model framework. The level of contractile force (α) exerted by the AVIC on the surrounding matrix was held constant for each activation state amongst all the layers. Instead, the β connectivity parameter was introduced to emulate AVIC-ECM layer differences. This enables the macro-micro model to capture the bidirectional behavior discovered experimentally and in particular the stark differences between the AC and WC response to hypertensive conditions.

Macro-micro coupling

Micro-model boundary conditions

Isoparametric interpolation using the displacement at the nodes of a single macro hexahedral element (80 μm^3) was used to compute the displacement on the 6,144 surface nodes of the refined micro mesh. This procedure was done for the fibrosa layer RVE (RVE^F) as well as the ventricularis layer RVE (RVE^V). Boundary conditions for each layer's RVE were computed using a custom Python script and an ABAQUS input file for the micro-model FE simulation was generated.

Macro-micro matching method

The volumetric averaged stress is computed for the micro model RVE (${}_{\text{state}}\bar{\sigma}_{Micro}^{layer\pm}$) using the same method described for the macro model RVE (**Eq. 3.4**). The averaged stress for both the macro and micro RVE is expressed as the von Mises stress defined as:

$$\bar{\sigma}^{VM}_{MicroRVE} = \sqrt{\frac{3}{2}\sigma' : \sigma'} \tag{3.11}$$

where σ' is the deviatoric stress and the difference between the two homogenized von Mises stresses is computed and minimized:

$$\Delta = \bar{\sigma}^{VM}_{MacroRVE} - \bar{\sigma}^{VM}_{MicroRVE} \tag{3.12}$$

$$\|\Delta\| = \sqrt{\Delta : \Delta}\Big]_{min} \tag{3.13}$$

Systematic error check

To determine the systemic error of using this macro-micro mapping approach, two internal validations were performed. First, a homogenized macro material was mapped down to a homogenized micro material mesh using identical material parameters from the baseline inactive (thapsigargin treatment) state. This was done for both layer's RVEs under tension and compression and a maximum error was found to be 1.48% between the macro and micro homogenized stress amongst all cases. Second, to ensure that modeling the macro RVE as a single 27-node hexahedral element was sufficient, a mesh refinement study was performed using 1, 27 and 64 element RVEs. The error between the macro and micro volume change was examined to ensure the appropriate level of incompressibility was maintained in both models. The error was sufficiently low with a single RVE (0.01%) and not much improvement was gained with 64 RVEs (0.005 %). To keep computational costs low, a single RVE was used in all simulations reported.

Preliminary micro model parametric studies

Several preliminary steps were taken prior to running parameter estimation studies to back out changes in AVIC stiffness, contractility and connectivity for each of the activation states. First, the baseline modulus of the ECM in the micro model ($\mu_{ECM}^{F,V\pm}$) and the basal shear modulus of the AVIC μ_{AVIC}^{Basal}, were computed using the following information from the inactive (thapsigargin) state (**Eq. 3.14).** For clarity purposes, all examples provided, including **Eq. 3.14**, will be for the fibrosa RVE (RVE^F) under tensile loading. The same procedure was executed for the fibrosa under compression, and the ventricularis under tension and compression and are reported in the results.

$$_{\text{inactive}}\mu_{Macro}^{F+} = \mu_{ECM}^{F+}\,\Phi_{ECM} + \mu_{AVIC}^{Basal}\Phi_{AVIC} \tag{3.14}$$

Where $\Phi_{ECM}$and Φ_{AVIC} are the mass fractions of the ECM and AVICs respectively. The value of μ_{AVIC}^{Basal} represents passive AVIC stiffness. A physically realistic range of AVIC stiffness values for the basal AVIC stiffness are identified as ranging from micropipette aspiration estimates of 0.15 kPa, to 50 kPa. This is equivalent to a linearized elastic modulus (E) range of 0.45kPa to 55 kPa.

For each assigned value for μ_{AVIC}^{Basal}, a parametric study of AVIC contractility (α_{AVIC}^{F+}) was performed. Since $_{\text{inactive}}\mu_{Macro}^{F+}$ represents the bulk moduli estimated from the macro-model, for every assigned μ_{AVIC}^{Basal} value, μ_{ECM}^{F+} can be solved for (**Eq. 3.14**) to obtain the baseline shear modulus of the ECM in the micro-model. After μ_{AVIC}^{Basal} is assigned and $\mu_{ECM}^{F+}$is solved for accordingly, these parameters remain constant while the AVIC contractility is varied (α_{AVIC}^{F+}). For each assigned basal AVIC stiffness μ_{AVIC}^{Basal}, the necessary contractility parameters to achieve the normal and hypertensive stress states determined by the macro model, were determined.

A key part of these preliminary steps was determining the appropriate value for μ_{AVIC}^{Basal}, moving forward by validating the initial parametric study results (varying α_{AVIC}^{F+}).

against an independent data source under separate loading conditions [42]. Briefly, porcine AV leaflets were cut into circumferential strips from the belly region of the AV (same region as the flexure study presented here). The strips were oriented circumferentially, set up in isolated organ baths with on end attached to a strain gauge force transducer and the other end fixed to a steel rod. Tissues were allowed to stabilize in Krebs solution (approximately 2.7Mm KCl) for 10 minutes before being loaded with a pre-tension of 3mN. After stabilizing to a baseline force (not reported) over a period of 40 minutes, the viable tissue was tested in 90Mm KCl and the contractile response was measured. This study provided an indication of the collective contractile force of the AVICs to achieve a hypertensive state (90mM KCl) from a normal baseline (5mM) (**Fig. 3.9a**). This experiment was simulated using the developed micro-model, constraining the two faces of the RVE perpendicular to the circumferential direction, varying the contractility of the AVICs using the α term and computing the resulting force on the faces (**Fig. 3.9b**). This resulting axial force computed by the simulation was then directly compared to the force measured directly by the experiment, accounting for changes in size of the true vs. simulated tissue strips. The change in the α term (Δα) needed in the model to achieve the change in force measured from normal (5mM KCl) to hyper (90mM) activation states was determined to be approximately 6E-5 (1/K).

Lastly, understanding that it should take a Δα of approximately 6E-5 (1/K) to achieve hyper stress levels from the normal state, the estimated Δα values for each of the assigned μ_{AVIC}^{Basal} values was evaluated. Results revealed that a basal AVIC modulus of 18kPa was appropriate given that it takes a Δα of approximately 6.98E-5 1/K to reach the hyper state from the normal state (**Fig. 3.10**). Additionally, a modulus of 18kPa aligns with previous AFM data measurements of AVICs [18]. For these reasons, a μ_{AVIC}^{Basal} of 18kPa was established moving forward.

Micro model parametric studies: estimating AVIC stiffness, contractility and connectivity

After the appropriate ranges of parameter values were chosen for $\mu_{\mathrm{AVIC}}^{\mathrm{F+}}$ and $\alpha_{\mathrm{AVIC}}^{\mathrm{F+}}$, a parametric simulation was run using the micro FE model with the computed macro model boundary conditions. Resulting homogenized stress of the micro RVE ${}_{\mathrm{state}}\bar{\sigma}_{Micro}^{F+}$ was computed at each perturbation using **Eq. 3.4** and compared to the macro RVE homogenized stress (${}_{\mathrm{state}}\bar{\sigma}_{Macro}^{F+}$) as described in **Eqs. 3.11-3.13** for each activation state.

Validation of macro-micro methodology

The developed model was validated in two ways. First, to validate the custom FE code and macro-micro mapping procedure, the model was run against experimental results using hydrogel tissue phantoms with embedded inclusions of known stiffness. Polyacrylamide (PAM) gel strips similar in size to the AV tissue strips were created with polymethylmethacrylate (PMMA) microspheres inclusions with diameters between 20-27µm. This represents an exaggerated stiffness relative to the surrounding matrix using particles of the same scale as AVICs. PAM gels were cast with reagents from Bio-Rad (Hercules, CA) following manufacturer instructions. Briefly, the appropriate concentration of acrylamide/bis-acrylamide solution was mixed in distilled H_2O, 10% sodium dodecyl sulfate and 1.5M Tris HCL buffer to obtain a final acrylamide concentration of 20%. PMMA particles were added to the gel at a 10% volume fraction to match that of the AVICs in the micro model. Polymerization was initiated through the addition of freshly prepared 10% ammonium persulfate and tetramethylenediamine (TEMED) was used as a catalyst. The gels were left to polymerize through free radical polymerization of the acrylamide monomers and the bis-acrylamide cross-linker for 1 hour at room temperature. Polymerized gels were cut using a mold to be 1mm thick, 4mm wide and approximately 15mm in length prior to testing and mounted on a custom end-loading flexural testing apparatus described in detail in [39]. The M vs. $\Delta\kappa$ bending response was measured and parameters were estimated from the macro FE model by fitting against the acquired data. The boundary conditions extracted from the macro model were then applied to a modified micro-model using 20 μm spherical inclusions and using the methodology described previously, the stiffness of the inclusions was estimated through parametric perturbations until the homogenized stress was matched to that of the macro-model.

Second, the estimated values for AVIC stiffness and contraction using the macro-micro model were validated against the independent data source under separate loading conditions as described in detail previously. This study provided an indication of the collective contractile force of the AVICs to achieve a hypertensive state (90mM KCl) from a normal baseline (5mM), of approximately 1.41μN per AVIC.

Immunofluorescence

To qualitatively investigate layer differences in AVIC connectivity to the surrounding ECM, F-actin networks were stained in native AV tissue. Fresh porcine aortic valves were obtained from the local abattoir (Harvest House Farms, Johnson City, TX) and transported in HypoThermosol FRS (StemCell Technologies, Vancouver, BC) on ice. Within 2 hours of sacrifice, fresh pieces of valve tissue were cut into 5mm x 7mm (average thickness of 400 μm) rectangular sections, fixed in 2% paraformaldehyde (Electron Microscopy Sciences, Hatfield, PA) for 30 minutes. Tissue was processed through a sucrose gradient (10%, 20%, 30%) for 30 minutes each at 4°C. over dry ice in optimum cutting temperature embedding compound (Tissue-Tek, Sakura Finetek, Torrance, CA) and shipped to Histoserv (Germantown, MD) where they were cryosectioned into 5 micron thick sections (transmural) and kept frozen at -80°C until staining. Slides were removed from -80°C, brought to room temperature and rehydrated with a series of PBS washes. Sections were treated with 0.1% Triton X-100 in PBS for 5 minutes at room temperature to permeabilize cells. Sections were washed and blocked from non-specific staining between primary antibodies and tissue by incubating in blocking buffer of 10% goat serum in PBS for 45 minutes. Slides were rinsed and surrounded with a hydrophobic barrier prior to incubating with TRITC-conjugated Phalloidin (1:100, Millipore, Billerica, MA), a high-affinity filamentous actin (F-actin) probe, for 1 hour at room temperature. AVICs nuclei were stained with DAPI (Life Technologies, Carlsbad, CA) for 5 minutes prior to mounting with ProLong Diamond Antifade mountant (ThermoFisher Scientific). Fluorescent images were taken with a fluorescent microscope using standard TRITC and DAPI filters (Zeiss Axiovert 200M, Zeiss, Germany).

RESULTS

Effective moduli values and fold increase

Statistics revealed a significant difference (p=0.024) between the measured effective modulus at the normal state (5mM KCl) compared to the hyper state (90mM KCl) when bending in the AC direction (**Fig. 3.12**). However, no statistical difference (p=0.839) was found between the normal and hyper modulus values for the WC bending direction. This knowledge prompted the hypothesis that additional increases in tissue stiffness from 5mM to 90mM KCl could be attributed primarily to the fibrosa layer. Parameter estimation results discussed below did in fact reveal that truly unique parameter sets matching tissue stiffness in both bending directions for activation states were only attainable by increasing the tensile shear modulus in the fibrosa layer.

Increasing the shear modulus of the fibrosa layer alone caused the neutral axis in the AC bending direction to shift from 0.75 of the normalized thickness to 0.87 when stimulated with 90mM KCl (**Table 3.2**). Contrasting with the WC bending direction, where upon an initial shift from the inactive state to the 5mM normal state (0.36 to 0.28) towards the ventricularis, no further shift occurs with the addition of 90mM KCl.

Parameter estimation of the macro-model

Using the established moduli relationships discovered in [39], the thapsigargin or "inactive" tissue state moduli were estimated by fitting the FE simulations to the experimental data (**Fig. 3.13**). The reported parameters (**Table 3.2)** differed slightly in magnitude from the previously reported estimates, however this was anticipated due to variability of tissue samples and an independent protocol for the study. With the addition of 5mM KCl, the fibrosa layer stiffens 7.25-fold from the inactive state in contrast with the ventricularis which stiffened approximately 3.24-fold from the inactive state. With the addition of 90mM KCl, the model revealed an additional 1.5-fold increase in stiffness from the normal state. In contrast, the ventricularis revealed no further increase in stiffness from the normal state. As mentioned above, the increasing stiffness of the fibrosa under tensile loading corresponds with an expected shift in the neutral axis (10% shift towards the fibrosa). Similarly, there was a slightly less 8% shift towards the ventricularis that accompanied the stiffness increase from the inactive to normal/hyper activation states.

Macro RVE averaged stress

Extracted nodal and elemental values for displacement and stress from the simulation were taken at 0.15mm^{-1} change in curvature and provided to the micro-model study for AVIC property estimation studies. The homogenized von Mises stresses are reported in **Table 3.3**. All values are reported within ±0.02 kPa.

Micro model estimates of AVIC stiffness, contractility and connectivity

The micro-model parametric studies were completed in two steps. First, parametric studies of stiffness and contractility for the fibrosa and ventricularis under tension were carried out while maintaining a constant connectivity parameter of β_{AVIC}^{layer+}=1. Therefore, initially all AVICs were assumed to be continuously bound to the surrounding matrix. Second, using a priori results from the first study, the connectivity parameter was decreased for AVICs (β_{AVIC}^{layer+}<1) in the ventricularis layer using a uniform contractile force and stiffness. This second parametric study allowed for the estimation of relevant layer differences in AVIC-ECM connectivity. Since the macro-model indicated negligible contribution from the layers under compression, parametric studies are only reported for the layers under tension.

Fibrosa and ventricularis under tension: uniform connectivity

The first micro parametric studies of AVIC stiffness ($\mu_{AVIC}^{F+,V+}$) revealed little to no changes in RVE homogenized stress with no contractility implemented in the model ($\alpha_{AVIC}^{F+,V+}$=0). Even a substantial increase in AVIC modulus to 50kPa was incapable of achieving normal stress states. However, parametric studies of AVIC contractility ($\alpha_{AVIC}^{F+,V+}$) revealed a substantial measured change in stress of the RVE (**Fig. 3.14a-b**). It took an approximate α_{AVIC}^{F+} value of 25E-5 (1/K), to achieve normal activation levels and an additional 7E-5 (1/K) to achieve hyper activation states **(Fig. 3.14a).** The trends observed for the ventricularis under tension were the same, requiring a lower contractile force parameter (α_{AVIC}^{V+}) of 23E-5 (1/K) to achieve the macro-level contractile state (**Fig. 3.14b**). Results are illustrated in 3D in **Fig. 3.15a-b** showing the relationship between

AVIC stiffness ($\mu_{AVIC}^{F+,V+}$), contraction ($\alpha_{AVIC}^{F+,V+}$) and average von Mises stress for the fibrosa and ventricularis RVEs under tension.

AVIC layer differences under tension: varied connectivity

With these observations, and knowledge that AVICs may behave phenotypically similar throughout the layers, a second parametric study was carried out. The objective was to estimate differences in connectivity between the fibrosa and venticularis AVICs. A constant AVIC stiffness of 18kPa was used in these studies and the contractility parameter measured from the fibrosa AVICs under tension (α_{AVIC}^{F+}) was applied to the ventricularis under tension, RVE_V^+. The connectivity parameter, β_{AVIC}^{V+} , was altered until the activated tissue stress was matched using the same AVIC stiffness and contractile force.

The approach assumptions are summarized as follows:

1) The fibrosa AVICs are assumed to be continuously bound to the surrounding matrix ($\beta_{AVIC}^{layer+} = 1$)
2) The contractile response of the AVICs under all conditions was assumed to be uniform
3) AVICs in the ventricularis have reduced connectivity to the surrounding matrix relative to the fibrosa layer (β_{AVIC}^{layer+}<1).
4) The fibrosa and ventricularis AVICs have negligible connectivity to the surrounding matrix when under compression.

Results revealed that AVICs residing in the ventricularis layer appear to have approximately 70% less connectivity to the surrounding matrix ($\beta_{AVIC}^{layer\pm}$=0.32) relative to the fibrosa layer. The model assumes that under compression AVICs behave as if they are essentially disconnected from the ECM entirely as results from macro model revealed no contribution from the layers of the AV under compression. Therefore, only the relative connectivity between the fibrosa and ventricularis was of interest and reported here (**Table 3.4**).

AVIC-ECM connectivity differences in the native AV

Immunofluorescent staining of native porcine AV tissue revealed layer differences in F-actin content (**Fig. 3.16**). Although F-actin content was present in both layers, as expected, there appeared to be far higher concentrations in the fibrosa layer relative to the ventricularis.

Pam gel validation

The macro-micro model detected a shear modulus of approximately 1.8 GPa for PMMA particles (**Fig. 3.17)**. Despite this unrealistically high stiffness for biological inclusions, the model was still able to capture the shear modulus of the inclusions quite accurately. When taken on average, literature reported shear moduli values for PMMA using both a torsion pendulum test (1.367GPa) and an anticlastic plate bending test (1.575 GPa) [45] were within ± 0.329 GPa of the model's estimated modulus.

Validation of the macro-micro model against the Kershaw et al. independent data set [42] revealed that to achieve an equivalent contractile response from the normal to the hypertensive activation state, the AVICs must exhibit a basal stiffness of 18kPa (μ_{AVIC}^{Basal}) and a change in the contractility parameter, $\alpha_{AVIC}^{layer\pm}$. The micro-model estimated underlying contributions of AVIC contraction to the macro level changes in tissue stiffness from the normal to the hyper state to be equivalent to a contractility parameter value of 6.98E-5 (1/K). The simulation of the Kershaw study indicated a measured contractility change equivalent to approximately 6E-5 (1/K), indicating good agreement with the micro-model estimates.

DISCUSSION

AV flexure studies eliciting AVIC contraction observed substantial differences in layered behavior [1] as previously noted. The macro-micro model presented above aimed to not only capture this bidirectionality of flexure behavior between states, but also shed light on possible differences between AVIC contractility in the layers. The model suggests that the observed changes at the tissue level are almost entirely due to AVIC contraction, with little to no contributions from changes in AVIC intrinsic stiffness (**3.15**).

By examining the AV under flexural loading more information on layer differences was obtained than would have been if examining the layers under simple uniaxial tension. Another major finding of this study, although not surprising, is that the fibrosa layer appears to be primarily responsible for the observed bidirectional differences in bending behavior upon activation. Under tension (AC), the micro-model results revealed substantial contributions of AVIC contractility to the tissue-level stiffness changes. The ventricularis AVIC contribution was estimated to be approximately 70% less than that of the fibrosa AVIC estimated contributions. This finding implies that there are significant layer differences between AVIC-ECM connectivity causing these differences in force transduction to the surrounding matrix. This observation was reinforced by IHC results staining for F-actin networks (indicating attachment to the surrounding matrix) which revealed a much more substantial cytoplasmic network of F-actin in the fibrosa layer relative to the ventricularis. Additionally, it has been reported that the main mechanism by which VICs attach to collagen within the mitral valve leaflet are through $\alpha_2\beta_1$ integrins and these connections are necessary for KCl-induced force generation to occur [46]. Given that the fibrosa layer is primarily composed of type 1 collagen, these previous observations along with the layer differences reported in this study strongly suggest that $\alpha_2\beta_1$ mediated force generation is occurring in the AV as well, contributing to substantially different layer contributions to overall observed tissue behavior under flexure.

Results from the estimation of PAM gel inclusions provide a picture of the macro-micro model sensitivity. Given the ability for the model to detect changes in underlying stiffness, it is reasonable to assume that the model is sensitive to changes in stiffness of the underlying AVICs. However, this sensitivity is entirely independent of the experimental data acquired at the macro scale. The experimental flexural testing methodology has previously been validated using silicone rubber sheets, estimating shear moduli values within 7% error compared with tensile testing results [39]. The independent study performed by Kershaw et al. [42] provided an indication of the collective contractile force of the AVICs to achieve a hypertensive state (90mM KCl) from a normal baseline (5mM) of approximately 1.41μN per AVIC. This estimate provides a realistic number to contrast with the model's final estimated results for AVIC contractility. The reported contractility parameter change of 7E-5 (1/K) between normal to hyper states correlates approximately with an AVIC force of 1.60 μN, which is a similar value to the Kershaw study estimate of 1.41μN. It is important to note that these force correlations are merely estimates based on the assumption that all AVICs are contracting in the axial direction and exerting equal forces. They are not meant to be a definitive value, only to relate the contractility term in the model to a physiologically relevant value.

CONCLUSIONS

In summary, given the model's ability to detect small changes in stiffness, we have demonstrated that the additional rise in tissue stiffness, measured by the flexure studies, was due to an active contraction by the underlying AVICs. Realistically, the AVICs stiffness may exhibit a slight increase in intrinsic stiffness, however the model indicates this contribution is negligible relative to contractility. Furthermore, observed differences in activation response at the tissue level are likely due to vast differences in AVIC-ECM connectivity with the surrounding matrix as indicated by the macro-micro model estimates of AVIC contractility in the layers. This study further supports the pressing need for an *in-situ* approach given the complexity of the native ECM and the intricate variation throughout the layers. Currently, replicating such an environment using 3D gels (natural or synthetic) is unattainable with current knowledge of the valve microstructure. The introduced experimental-computational approach offers a method to obtain substantial information regarding layer-dependent AVIC behavior.

AV	Aortic Valve
ECM	Extracellular Matrix
AC	Flexure direction directed against the natural curvature of the leaflet
WC	Flexure direction directed with the natural curvature of the leaflet
FE	Finite Element
I	Second moment of inertia
$\Delta\kappa$	Change in valve leaflet curvature during flexure testing
M	Applied bending moment
$W^{\pm}$	Bimodular strain energy function
$E_{eff}\mathrm{I}$	Flexural stiffness
F	Fibrosa layer
V	Ventricularis layer
$RVE^{layer\pm}$	Representative Volumetric Element Layer: Fibrosa (F), Ventricularis (V)
${}_{\text{state}}\mu_{Macro}^{layer\pm}$	Shear modulus of the macro model State: inactive, normal, hypertensive Layer: Fibrosa (F), Ventricularis (V) Under Tension (+) or Compression (-)
${}_{\text{state}}\bar{\sigma}_{Macro}^{layer\pm}$	Volumetric averaged stress of the macro model RVE State: inactive, normal, hypertensive Layer: Fibrosa (F), Ventricularis (V) Under Tension (+) or Compression (-)
${}_{\text{state}}\bar{\sigma}_{Micro}^{layer\pm}$	Volumetric averaged stress of the micro model RVE State: inactive, normal, hypertensive Layer: Fibrosa (F), Ventricularis (V) Under Tension (+) or Compression (-)
Φ_{AVIC}	Mass fraction of AVICs
Φ_{ECM}	Mass fraction of ECM
$\mu_{ECM}^{layer\pm}$	Baseline shear modulus of ECM Layer: Fibrosa (F), Ventricularis (V) Under tension (+) and compression
μ_{AVIC}^{Basal}	Basal shear modulus of AVIC in the inactivated state
${}_{\text{state}}\mu_{AVIC}^{layer\pm}$	AVIC stiffness
${}_{\text{state}}\alpha_{AVIC}^{layer\pm}$	AVIC contractility
$\beta_{AVIC}^{layer\pm}$	AVIC connectivity to ECM Layer: Fibrosa (F), Ventricularis (V) $\beta_{AVIC}^{layer\pm} \in [0,1]$

Table 3.1: List of symbols and nomenclature.

Activation State	Layer	μ^{+}_{Macro}	μ^{-}_{Macro}	Tension/ Compression Layer Moduli Ratios	R^2	Neutral Axis WC	Neutral Axis AC
Inactive	F	206.42	43.76	~5:1	0.990	0.36	0.75
	V	96.19	24.77	~4:1			
Normal	F	1496.67	43.76	~34:1	0.998	0.28	0.87
	V	311.93	24.77	~13:1			
Hyper	F	2250.78	43.76	~51:1	0.989	0.28	0.88
	V	311.93	24.77	13:1			

Table 3.2: Estimated moduli values for each layer under tension and compression at each activation state: inactive, normal and hypertensive. R^2 goodness of fit values as well as neutral axis locations are also reported for each activation state

Activation State	$\bar{\sigma}_{Macro}^{F+}$	$\bar{\sigma}_{Macro}^{F-}$	$\bar{\sigma}_{Macro}^{V+}$	$\bar{\sigma}_{Macro}^{V-}$
Inactive	4.58	3.08	3.46	2.76
Normal	6.92	3.29	4.90	2.89
Hyper	8.18	3.29	4.90	2.99

Table 3.3: Macro homogenized von Mises stress values for each layer under tension and compression for each activation state: inactive, normal and hypertensive. Units in kPa.

	RVE^{F+}	RVE^{V+}
β_{AVIC}	1	0.32

Table 3.4: Estimated relative ventricularis connectivity (β_{AVIC}) parameter using the estimated uniform AVIC stiffness (μ_{AVIC}) of 18kPa and hyper contractility (α_{AVIC}) of 32E-5.

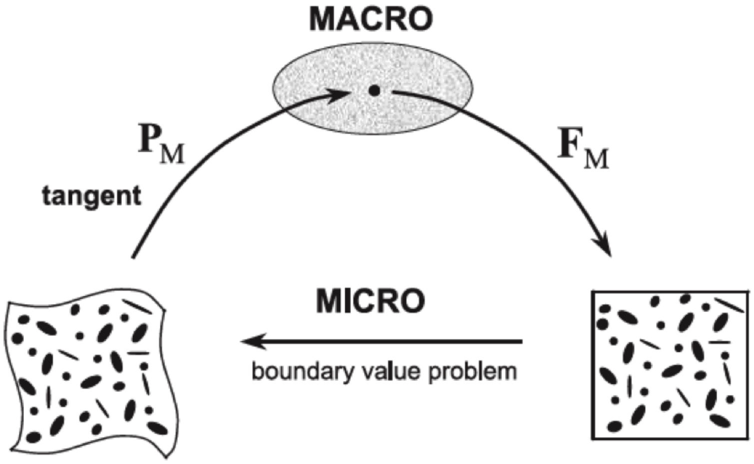

Figure 3.1: Computational homogenization scheme introduced from [36].

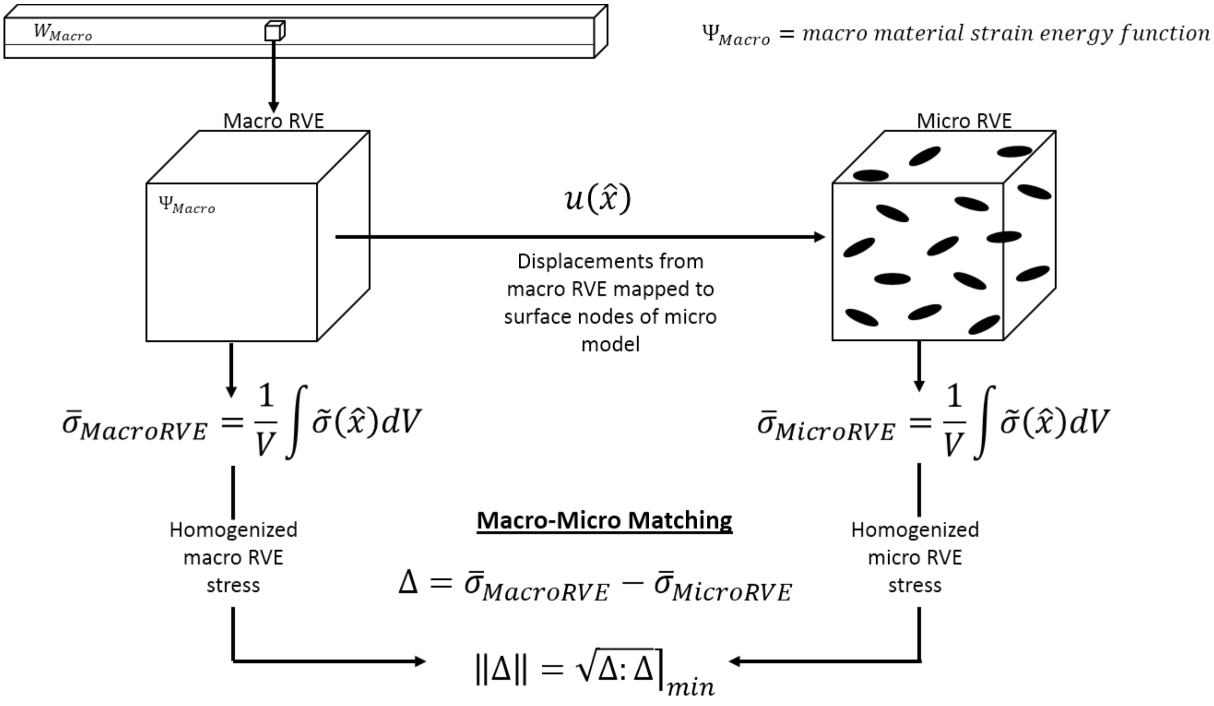

Figure 3.2: Macro-micro approach schematic.

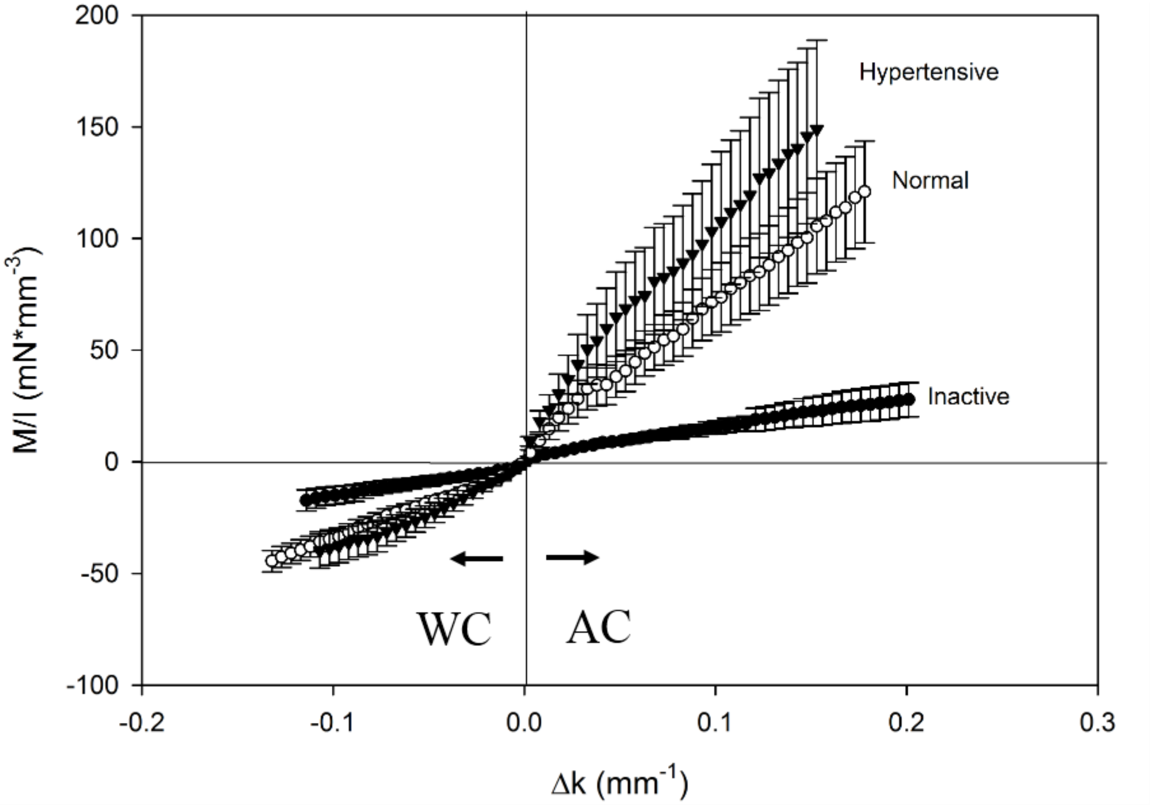

Figure 3.3: Averaged M vs. Δκ experimental data from AV bending study under inactive (thapsigargin), normal (5mM KCl) and hypertensive (90mM KCl) conditions and bending with (WC) and against (AC) the natural leaflet curvature.

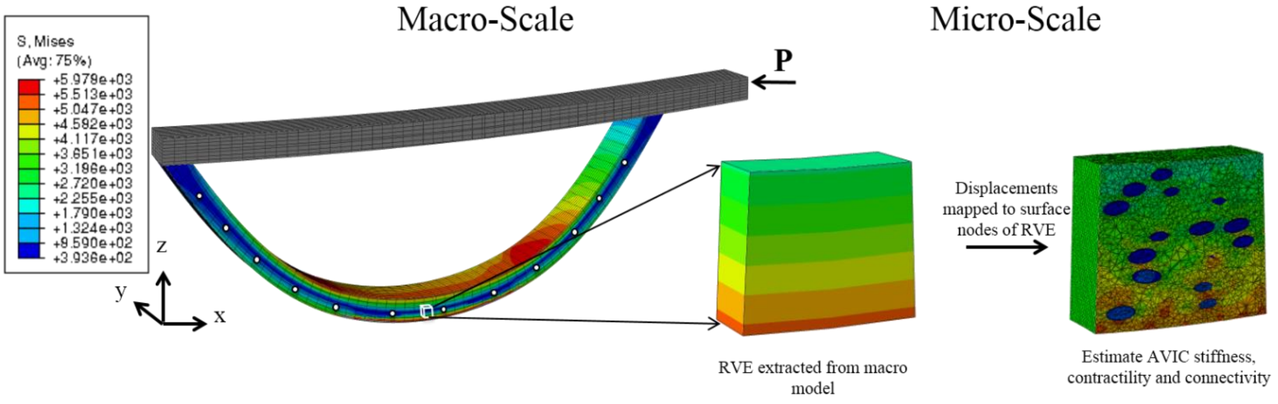

Figure 3.4: Macro-micro model overview depicting the application of boundary conditions from the macro nodes to the corresponding micro RVE surface.

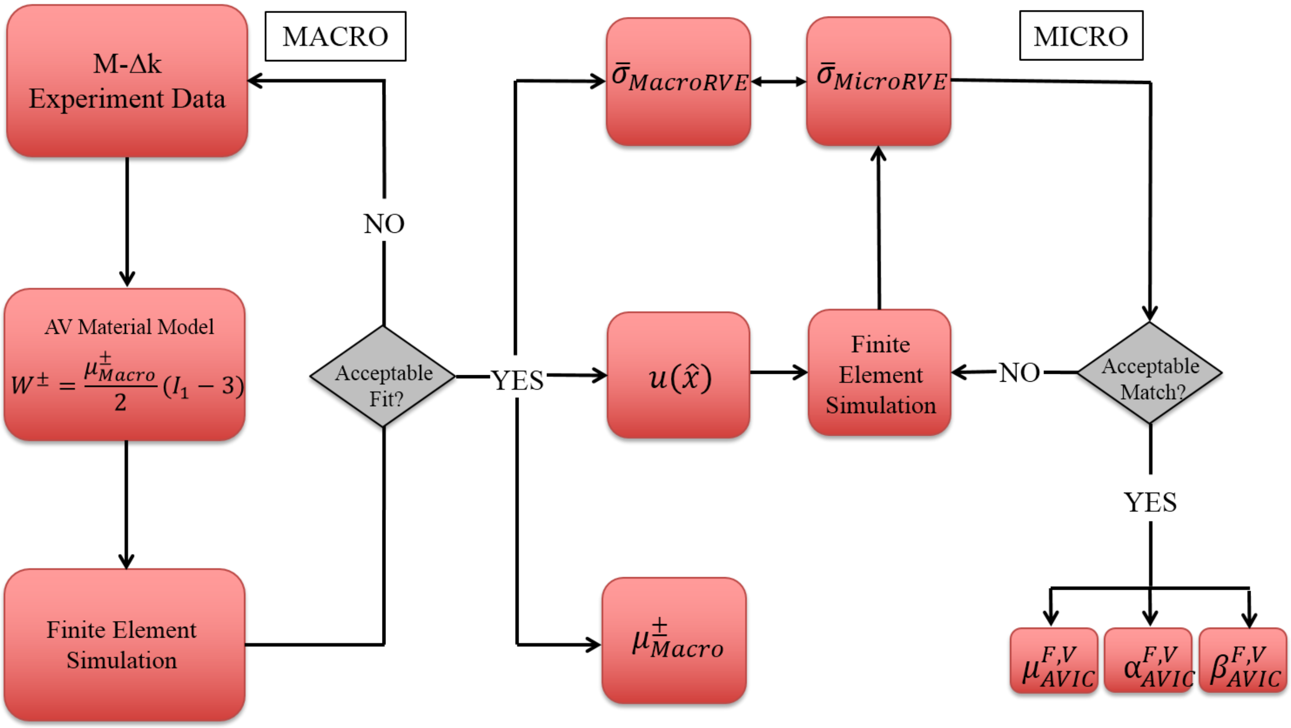

Figure 3.5: Computational flow of macro-micro model optimization.

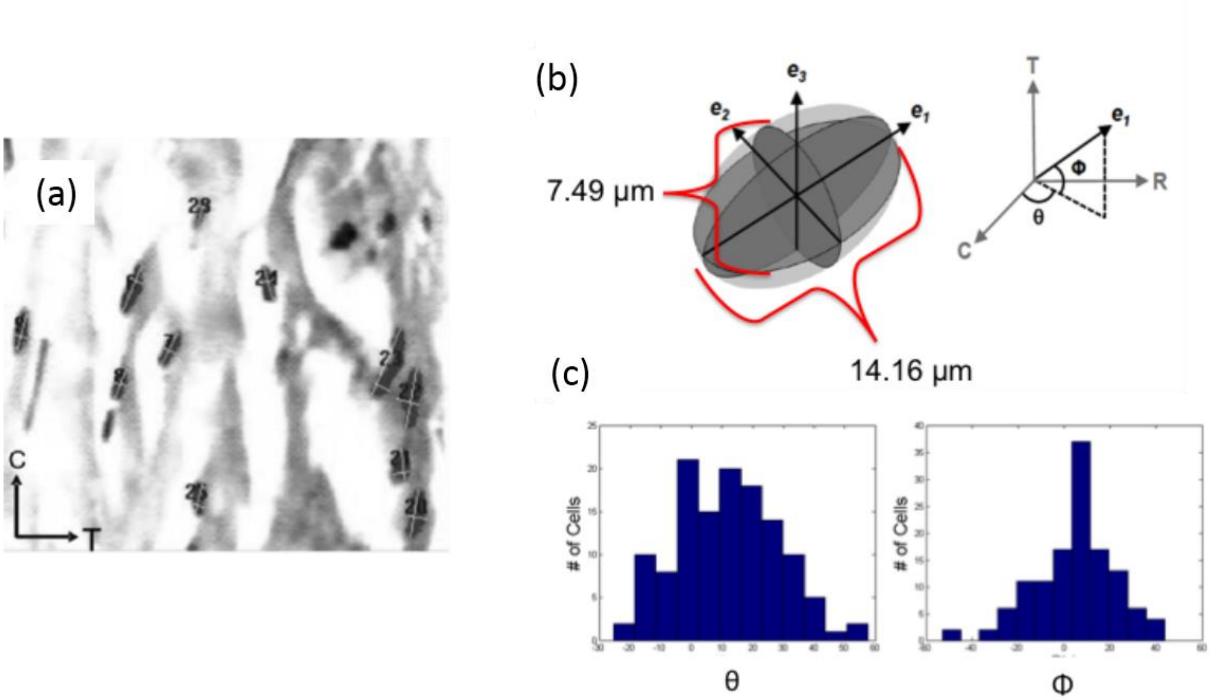

Figure 3.6: Distribution (a) dimensions (b) and orientation angles (c) of AVICs within the micro-model based on histological measurements from native AV tissue acquired from [40, 41].

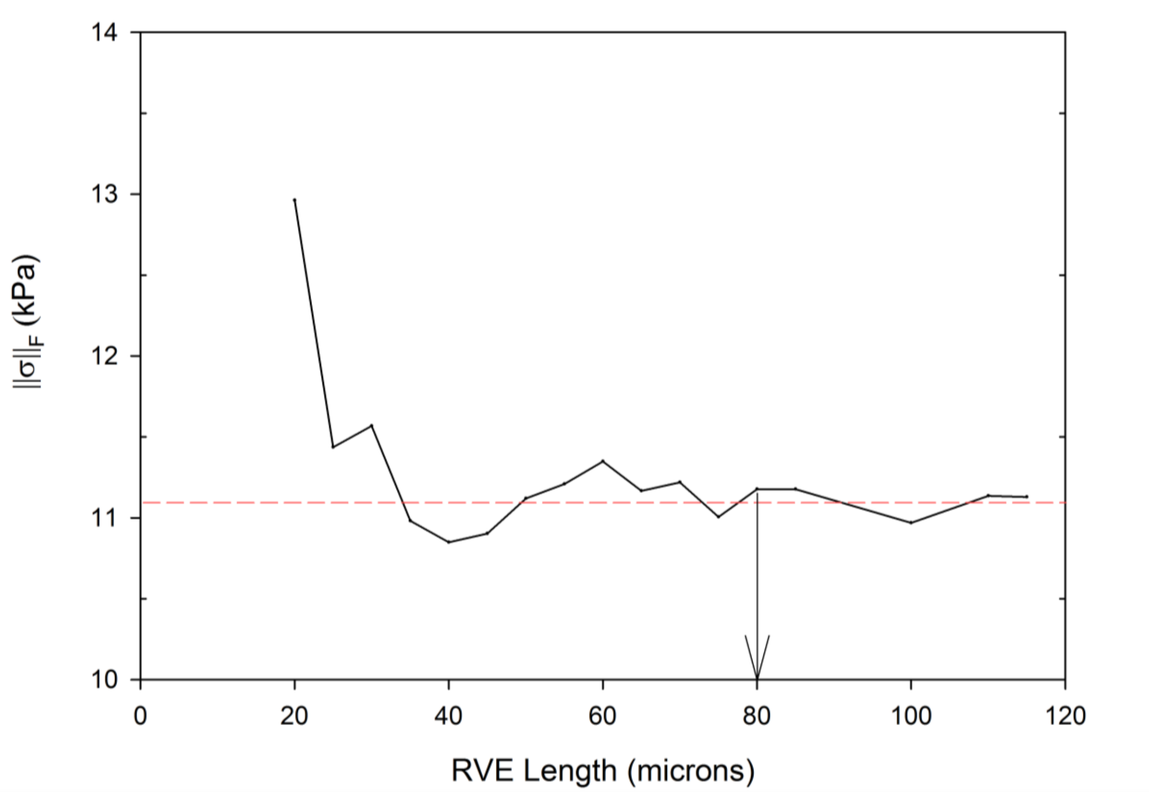

Figure 3.7: RVE length vs. stress variation to determine an optimal RVE size of 80μm for the micro-model.

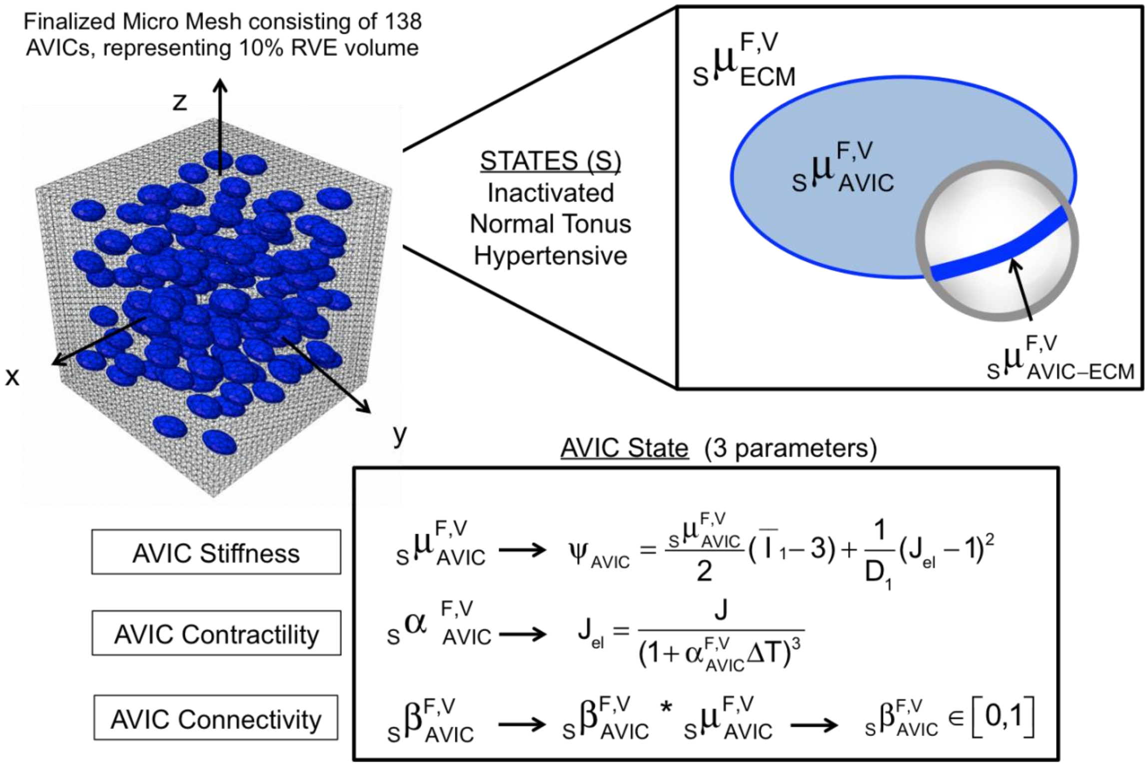

Figure 3.8: Micro-model framework

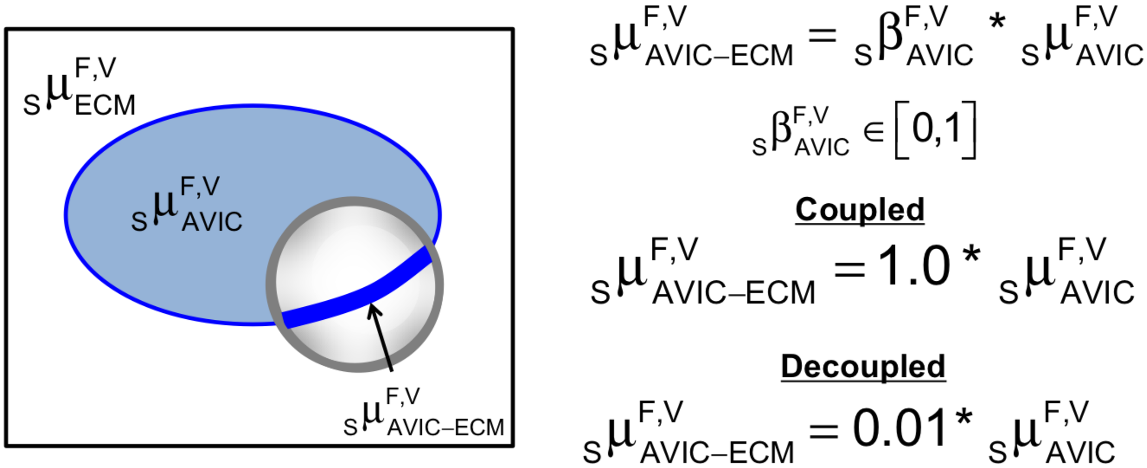

Figure 3.9: Modeling AVIC-ECM connectivity within the micro-model framework

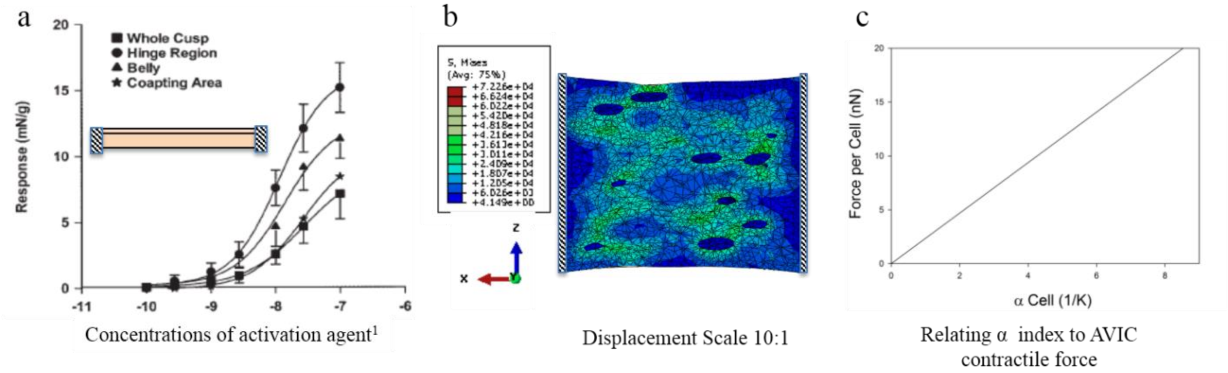

Concentrations of activation agent[1]

Displacement Scale 10:1

Relating α index to AVIC contractile force

Figure 3.10: Figure adapted by [42], illustrating force generation from AV leaflet strips using 90mM KCl (a) the FE simulation of the study (b) and the linear correlation between the micro-model α parameter and AVIC force.

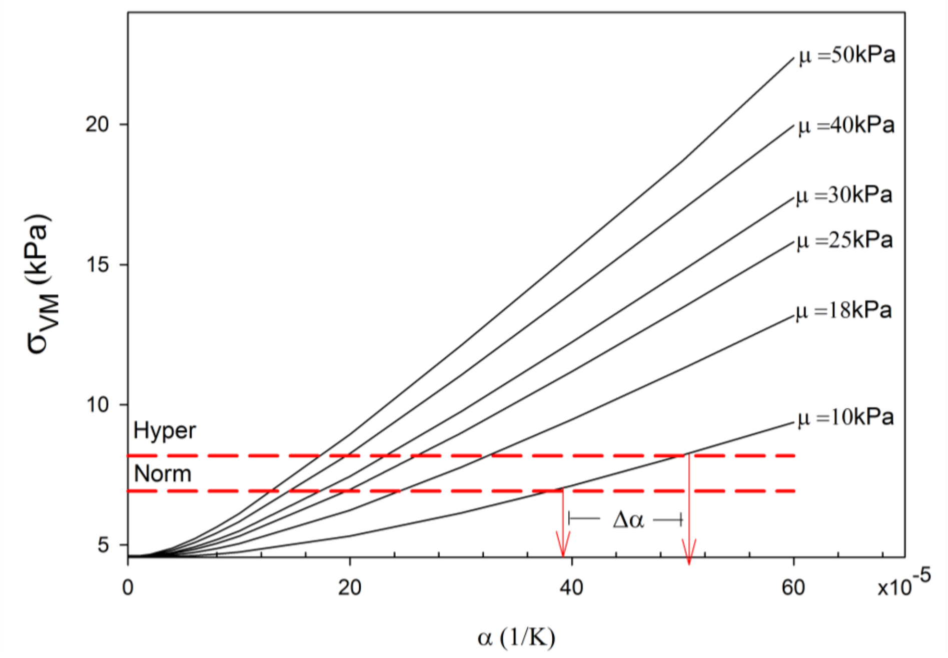

Figure 3.11: Estimation of the activation parameter necessary to achieve normal and hyper level activation for each chosen basal level AVIC stiffness (μ_{AVIC}^{Basal}).

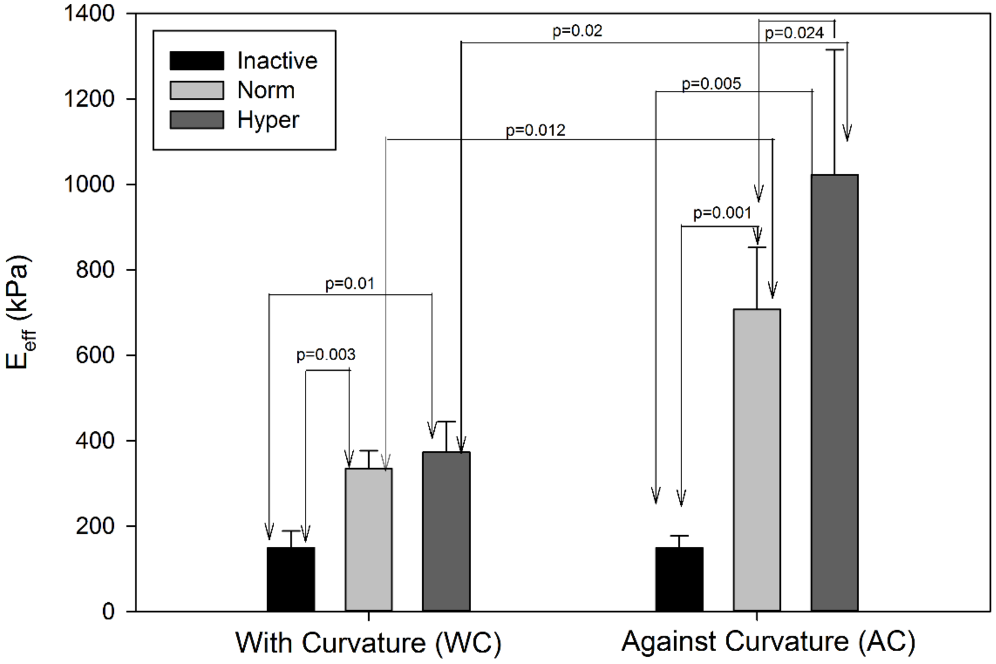

Figure 3.12: Linearized effective moduli taken from the slope of the averaged M vs. Δκ curve in figure 3.3 at points of maximum common curvature ($0.11mm^{-1}$) determined for the inactive, normal and hypertensive states and bending in both the AC and WC directions.

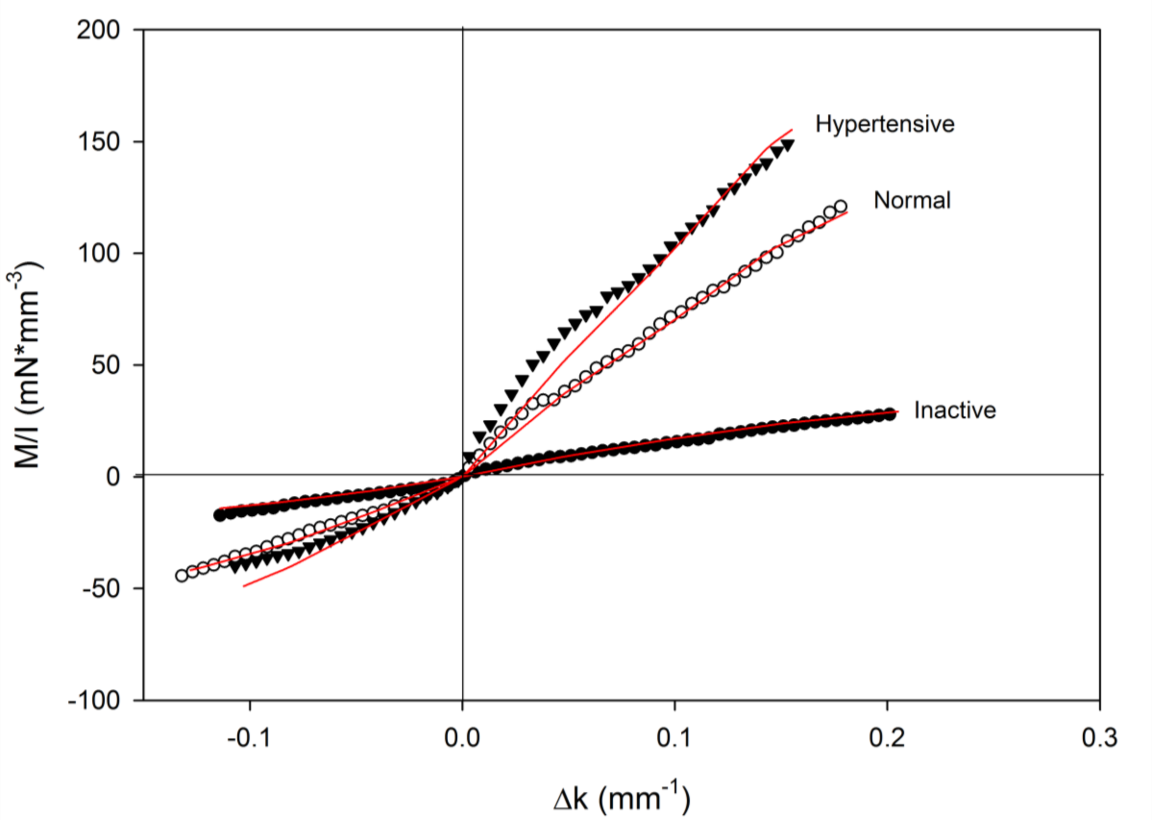

Figure 3.13: Macro-model simulation results of M- Δκ plotted against the experimental AV bending data determined for the inactive, normal and hypertensive states and bending in both the AC and WC directions.

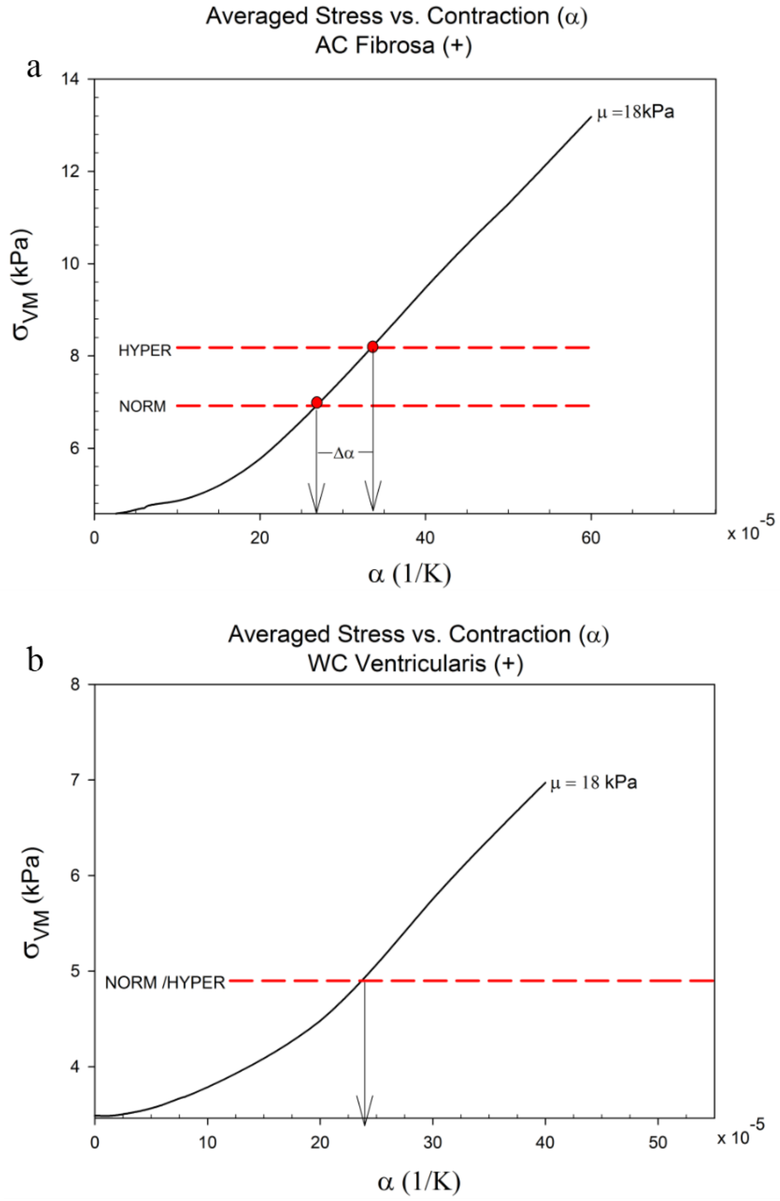

Figure 3.14: Results of micro-model parametric studies assuming a uniform AVIC-ECM connectivity. Effects of AVIC contractility, α, and AVIC stiffness, μ, for the fibrosa RVE under tensile loading (a) and the ventricularis RVE under tensile loading (b).

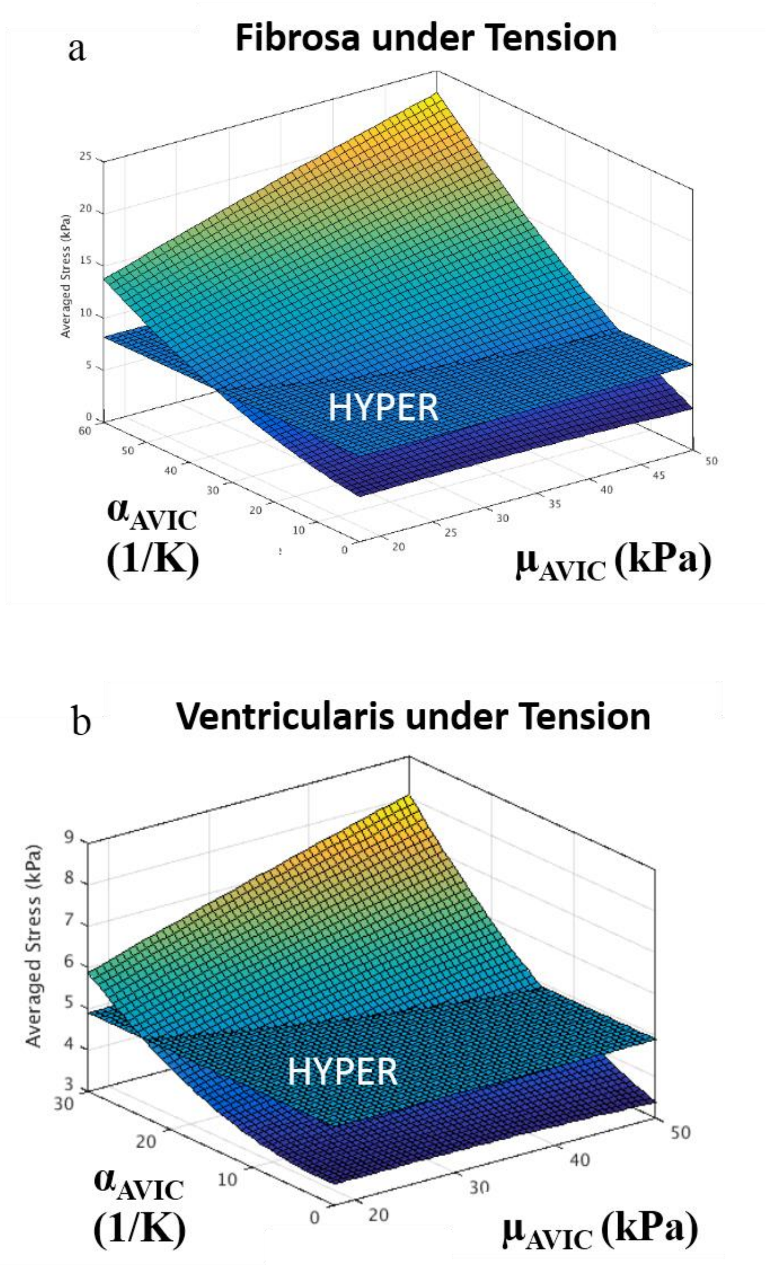

Figure 3.15: Results of micro-model parametric studies plotted in 3D (new representation of figure 3.13 results) assuming a uniform AVIC-ECM connectivity. Effects of AVIC contractility, α, and AVIC stiffness, μ, for the fibrosa RVE under tensile loading (a) and the ventricularis RVE under tensile loading (b). Flat plane indicates the hypertensive stress (Hyper) measured at the tissue level.

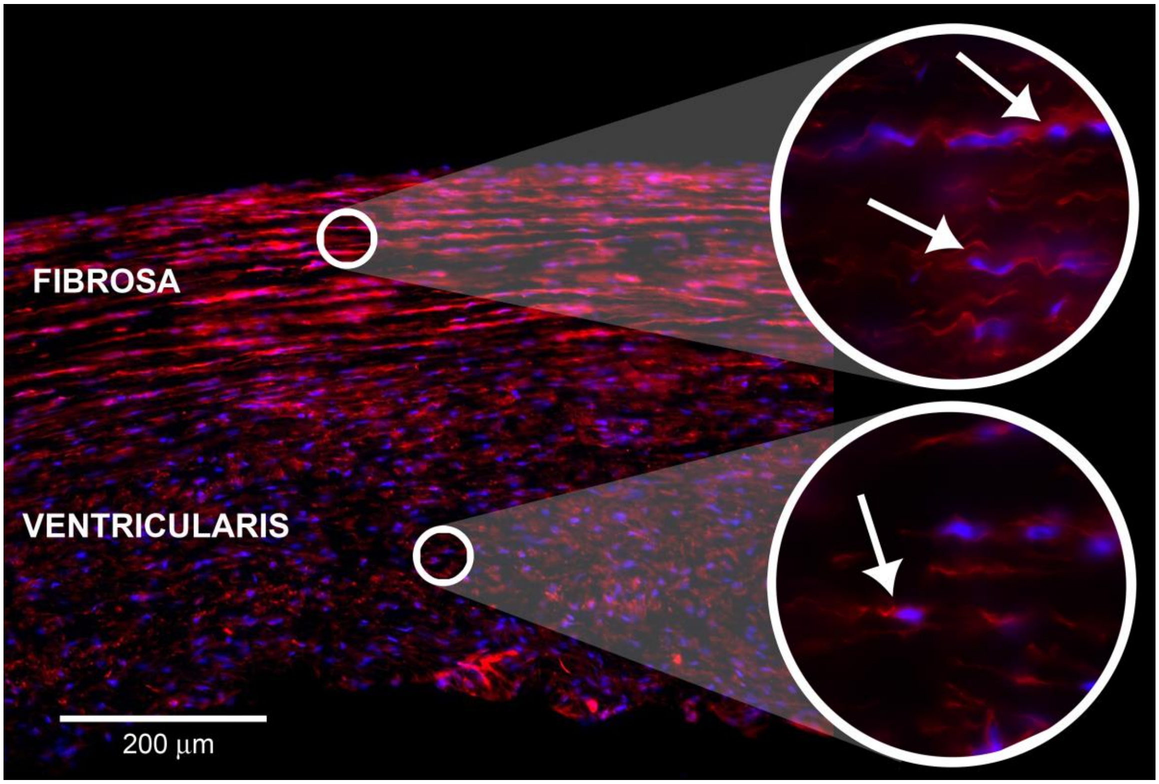

Figure 3.16: Immunofluorescent imaging of F-actin in native AV histological tissue sections. F-actin stained with TRITC conjugated phalloidin and AVIC nuclei counterstained with DAPI (blue). Arrows indicate F-actin positive staining in AVIC cytoplasm.

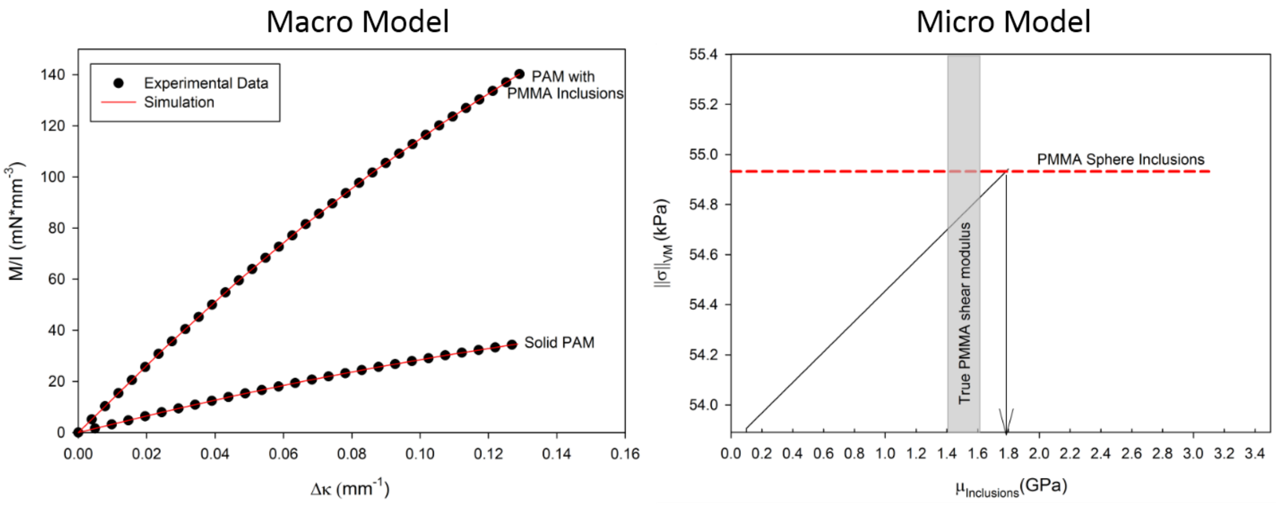

Estimated Modulus

	Macro Stiffness (kPa)	$R^2_{\text{Macro-Fit}}$	Predicted shear modulus	True PMMA shear modulus
PAM with PMMA Inclusions	400.84	0.992	1.8 GPa	1.4-1.6 GPa

Figure 3.17: Polyacrylamide gel validation of macro-micro model sensitivity to PMMA inclusions. The macro model is fit against the experimental M vs. Δκ bending data (top left). The micro-model then estimates a moduli value for the inclusion stiffness (top right) and is reported in the table (bottom).

REFERENCES

1. Merryman, W.D., et al., The effects of cellular contraction on aortic valve leaflet flexural stiffness. J Biomech, 2006. 39(1): p. 88-96.
2. Gu, X. and K.S. Masters, Role of the Rho pathway in regulating valvular interstitial cell phenotype and nodule formation. Am J Physiol Heart Circ Physiol, 2011. 300(2): p. H448-58.
3. Hinton, R.B., Jr., et al., Extracellular matrix remodeling and organization in developing and diseased aortic valves. Circ Res, 2006. 98(11): p. 1431-8.
4. Simmons, C.A., et al., Spatial heterogeneity of endothelial phenotypes correlates with side-specific vulnerability to calcification in normal porcine aortic valves. Circ Res, 2005. 96(7): p. 792-9.

5. Weber, K.T., et al., Connective tissue and repair in the heart. Potential regulatory mechanisms. Ann N Y Acad Sci, 1995. 752: p. 286-99.

6. Schneider, P.J. and J.D. Deck, Tissue and cell renewal in the natural aortic valve of rats: an autoradiographic study. Cardiovasc Res, 1981. 15(4): p. 181-9.

7. Willems, I.E., et al., Structural alterations in heart valves during left ventricular pressure overload in the rat. Lab Invest, 1994. 71(1): p. 127-33.

8. Chaput, M., et al., Mitral leaflet adaptation to ventricular remodeling: occurrence and adequacy in patients with functional mitral regurgitation. Circulation, 2008. 118(8): p. 845-52.

9. Dal-Bianco, J.P., et al., Active adaptation of the tethered mitral valve: insights into a compensatory mechanism for functional mitral regurgitation. Circulation, 2009. 120(4): p. 334-42.

10. Yip, C.Y., et al., Calcification by valve interstitial cells is regulated by the stiffness of the extracellular matrix. Arterioscler Thromb Vasc Biol, 2009. 29(6): p. 936-42.

11. Chen, J.H. and C.A. Simmons, Cell-matrix interactions in the pathobiology of calcific aortic valve disease: critical roles for matricellular, matricrine, and matrix mechanics cues. Circ Res, 2011. 108(12): p. 1510-24.

12. Stephens, E.H., et al., Mitral valvular interstitial cell responses to substrate stiffness depend on age and anatomic region. Acta Biomaterialia, 2011. 7(1): p. 75-82.

13. Ye, Q., et al., Fibrin gel as a three dimensional matrix in cardiovascular tissue engineering. European Journal of Cardio-Thoracic Surgery, 2000. 17(5): p. 587-591.

14. Benton, J.A., B.D. Fairbanks, and K.S. Anseth, Characterization of valvular interstitial cell function in three dimensional matrix metalloproteinase degradable PEG hydrogels. Biomaterials, 2009. 30(34): p. 6593-603.

15. Gupta, V., et al., Reversible secretion of glycosaminoglycans and proteoglycans by cyclically stretched valvular cells in 3D culture. Ann Biomed Eng, 2008. 36(7): p. 1092-103.

16. Butcher, J.T. and R.M. Nerem, Porcine aortic valve interstitial cells in three-dimensional culture: comparison of phenotype with aortic smooth muscle cells. J Heart Valve Dis, 2004. 13(3): p. 478-85; discussion 485-6.

17. Merryman, W.D., et al., Viscoelastic properties of the aortic valve interstitial cell. J Biomech Eng, 2009. 131(4): p. 041005.

18. Merryman, W.D., et al., Differences in tissue-remodeling potential of aortic and pulmonary heart valve interstitial cells. Tissue Eng, 2007. 13(9): p. 2281-9.

19. Hollister, S.J., J.M. Brennan, and N. Kikuchi, A homogenization sampling procedure for calculating trabecular bone effective stiffness and tissue level stress. J Biomech, 1994. 27(4): p. 433-44.

20. Hambli, R., H. Katerchi, and C.L. Benhamou, Multiscale methodology for bone remodelling simulation using coupled finite element and neural network computation. Biomechanics and Modeling in Mechanobiology, 2011. 10(1): p. 133-145.

21. Goncalves Coelho, P., P. Rui Fernandes, and H. Carrico Rodrigues, Multiscale modeling of bone tissue with surface and permeability control. J Biomech, 2011. 44(2): p. 321-9.

22. Podshivalov, L., A. Fischer, and P.Z. Bar-Yoseph, On the Road to Personalized Medicine: Multiscale Computational Modeling of Bone Tissue. Archives of Computational Methods in Engineering, 2014. 21(4): p. 399-479.

23. Haider, M.A. and F. Guilak, Application of a Three-Dimensional Poroelastic BEM to Modeling the Biphasic Mechanics of Cell-Matrix Interactions in Articular Cartilage (REVISION). Comput Methods Appl Mech Eng, 2007. 196(31-32): p. 2999-3010.

24. Kim, E., F. Guilak, and M.A. Haider, The dynamic mechanical environment of the chondrocyte: a biphasic finite element model of cell-matrix interactions under cyclic compressive loading. J Biomech Eng, 2008. 130(6): p. 061009.

25. Guilak, F. and V.C. Mow, The mechanical environment of the chondrocyte: a biphasic finite element model of cell-matrix interactions in articular cartilage. J Biomech, 2000. 33(12): p. 1663-73.

26. Halloran, J.P., et al., Multiscale mechanics of articular cartilage: potentials and challenges of coupling musculoskeletal, joint, and microscale computational models. Ann Biomed Eng, 2012. 40(11): p. 2456-74.

27. Lavagnino, M., et al., A finite element model predicts the mechanotransduction response of tendon cells to cyclic tensile loading. Biomech Model Mechanobiol, 2008. 7(5): p. 405-16.

28. Multiscale computer modeling in biomechanics and biomedical engineering. 2013, New York: Springer.

29. Weinberg, E.J. and M.R. Kaazempur Mofrad, A multiscale computational comparison of the bicuspid and tricuspid aortic valves in relation to calcific aortic stenosis. J Biomech, 2008. 41(16): p. 3482-7.

30. Weinberg, E.J., D. Shahmirzadi, and M.R. Mofrad, On the multiscale modeling of heart valve biomechanics in health and disease. Biomech Model Mechanobiol, 2010. 9(4): p. 373-87.

31. Weinberg, E.J. and M.R. Kaazempur Mofrad, Transient, three-dimensional, multiscale simulations of the human aortic valve. Cardiovasc Eng, 2007. 7(4): p. 140-55.

32. Lai, V.K., et al., A multiscale approach to modeling the passive mechanical contribution of cells in tissues. J Biomech Eng, 2013. 135(7): p. 71007.

33. Hadi, M.F., E.A. Sander, and V.H. Barocas, Multiscale model predicts tissue-level failure from collagen fiber-level damage. J Biomech Eng, 2012. 134(9): p. 091005.

34. Agoram, B. and V.H. Barocas, Coupled macroscopic and microscopic scale modeling of fibrillar tissues and tissue equivalents. J Biomech Eng, 2001. 123(4): p. 362-9.

35. Drugan, W.J. and J.R. Willis, A micromechanics-based nonlocal constitutive equation and estimates of representative volume element size for elastic composites. Journal of the Mechanics and Physics of Solids, 1996. 44(4): p. 497-524.

36. Galvanetto, U. and M.H. Aliabadi, Multiscale modeling in solid mechanics : computational approaches. Computational and experimental methods in structures. 2010, London ; New York: Imperial College ; Distributed by World Scientific. xiii, 334 p.

37. Lam, T.S., The Mechanical Properties of Native Porcine Aortic and Pulmonary Heart Valve Leaflets, in Bioengineering. 2005, University of Pittsburgh: University of Pittsburgh.

38. Engelmayr, G.C., Jr., et al., A novel bioreactor for the dynamic flexural stimulation of tissue engineered heart valve biomaterials. Biomaterials, 2003. 24(14): p. 2523-32.

39. Buchanan, R.M. and M.S. Sacks, Interlayer micromechanics of the aortic heart valve leaflet. Biomech Model Mechanobiol, 2014. 13(4): p. 813-26.

40. Carruthers, C.A., et al., Gene Expression and Collagen Fiber Micromechanical Interactions of the Semilunar Heart Valve Interstitial Cell. Cell Mol Bioeng, 2012. 5(3): p. 254-265.

41. Huang, H.Y., J. Liao, and M.S. Sacks, In-situ deformation of the aortic valve interstitial cell nucleus under diastolic loading. J Biomech Eng, 2007. 129(6): p. 880-89.

42. Kershaw, J.D., et al., Specific regional and directional contractile responses of aortic cusp tissue. J Heart Valve Dis, 2004. 13(5): p. 798-803.

43. Lu, S.C.H. and K.S. Pister, Decomposition of deformation and representation of the free energy function for isotropic thermoelastic solids. International Journal of Solids and Structures, 1975. 11(7–8): p. 927-934.

44. Lee, C.H., et al., Quantification and simulation of layer-specific mitral valve interstitial cells deformation under physiological loading. J Theor Biol, 2015. 373: p. 26-39.

45. Farshad, M., M.W. Wildenberg, and P. Flueler, Determination of shear modulus and Poisson's ratio of polymers and foams by the anticlastic plate-bending method. Materials and Structures, 1997. 30(200): p. 377-382.

46. Stephens, E.H., et al., Functional Coupling of Valvular Interstitial Cells and Collagen Via alpha(2)beta(1) Integrins in the Mitral Leaflet. Cellular and Molecular Bioengineering, 2010. 3(4): p. 428-437.

CHAPTER 4: MEASURING THE EFFECTS OF CONTRACTILE STIMULI ON AVIC BIOMECHANICAL BEHAVIOR IN SITU

Preface

Chapters 4 and 5 encompass the final specific aim in this body of work: To measure the layer dependent contractile response of AVICs *in situ* using the developed computational-experimental approach in a simulated pathological state. The goal of these studies was to measure the *in situ* layer dependent contractile response of AVICs in a simulated pathological state using TGF-β1 and subsequently validate the observed contractile response against microindentation experiments (**Chapter 5**).

INTRODUCTION

Transforming growth factor-beta1 (TGF-β1) is a prolific growth factor and has been shown to initiate calcification *in vitro* and accelerate valvular stenosis *in vivo* [4,5]. Immunohistochemical studies revealed the presence of high levels of TGF-β1 in calcified human aortic valves when compared to noncalcified [6]. TGF-β1 has also been shown to mediate differentiation of VICs into active myofibroblasts *in vitro* determined by a significant increase in α-SMA, a gold standard marker for identifying myofibroblasts, augment stress fiber formation and alignment, and increase VIC contractility [7]. The role that TGF-β1 plays in calcification of the aortic valve remains unclear, however a number of *in vitro* studies have shown convincing evidence that TGF-β1 induces cell apoptosis, cellular aggregation, and calcified nodule formation in VICs.

To further understand differences in AVIC contractile responses due to varied layer connectivity, TGF-β1 was used as a biochemical agent to induce an activated AVIC simulating a pathological state [1]. It was hypothesized that observed layer differences in AVIC contractile responses would be more pronounced with TGF-β1 treatment due to an enhanced cytoskeletal network, creating even stronger connections to the surrounding matrix that would translate to stronger forces. The multi-scale FE model described in detail in **Chapter 3** was used to evaluate how TGF-β1 affects tissue level bending behavior in the AV due to changes in underlying AVIC-ECM coupling and AVIC stiffness. An overview of the macro-micro model for end-loading is provided in **Fig. 4.1.**

PROTOCOLS

Tissue preparation and treatment

All reagents were purchased from ThermoFisher Scientific (Waltham, Ma) unless otherwise indicated. Viable porcine AVs were acquired at a local abattoir (Harvest House Farms, Johnson City, TX) and kept on ice to ensure AVIC survival during transport. Within 1-2 hour of sacrifice, leaflets were dissected from the AVs from the root along their attachment points from four animals for a total of 12 AV leaflets. Resected leaflets were washed 3 times in cold sterile PBS with 1% Penicillin Streptomycin and transferred to Hypothermosol biopreservation media (BioLife Solutions, Bothell, WA). Circumferential strips approximately 4mm wide x 14mm long were removed from the whole leaflet by cutting just below the nodulus of Arantus with razor blades of a constant width (**Fig. 4.2**). Tissue strips were randomized between the 2 pre-treatment conditions: Control and TGF-β1, in a 24 well plate. Each pre-treatment condition had 6 specimens (n=6). No distinction was made between the right, left or non-coronary leaflets. Control tissue was incubated for a period of five days in low serum culture media consisting of: 1% fetal bovine serum, 1% L-Glutamine, 1% Penicillin Streptomycin, and 0.5% Fungizone Antimycotic in advanced DMEM base media. TGF-β1 samples were incubated in the same base media with the addition of 5ng/mL of TGF-β1. Specimens were maintained at 37°C at 5% CO_2 for the five day incubation period with fresh media exchanges every 48 hours.

End-loading bending protocol

After five days of incubation, tissue strips were removed from culture and immediately tested under flexure deformation. Leaflets were bent with (WC) and against (AC) the natural leaflet curvature under three activation levels: inactive (cytochalasinD), normal (5mM KCl) and hypertensive (90mM KCl). Each specimen was first tested in both directions in 37°C Dulbecco's Modified Eagle Medium (DMEM), no phenol red with high glucose supplemented with 5 mM KCl. Testing media was then changed to DMEM with 90mM KCl and the same specimen was allowed to incubate for 10 minutes prior to testing a second time in both WC and AC bending directions using the same procedure. Last, the same tissue strip was incubated for 10 minutes in 20μM Cytochalasin D (CytoD) (Sigma, St. Louis, MO) at 37°C prior to testing again in both the WC and AC direction. Several control tissue samples were tested with both 5mM and 90mM KCl after incubation with CytoD to demonstrate effectiveness of CytoD in inhibiting actin polymerization. After no change was observed in stiffness (i.e. no contraction) upon addition of 90mM KCl, tissue samples were only tested in 5mM base media after CytoD treatment.

The end-loading flexure testing protocol was introduced in **Chapter 2**, and summarized here with minor modifications. Five small red bead markers were glued on the side of the tissue farthest from the free edge for curvature calculation using the macro imaging system described in **Chapter 2** (**Fig. 4.1a**). A hollow 19 gauge Teflon needle sleeve was glued to one end of the tissue using cyanoacrylate and then slipped onto a steel dowel to allow for free rotation and restricted translation of the tissue. The tank-tissue holder assembly was mounted to a bi-directional (X_1 axis movement) stage fitted with two precision linear actuators (model MM-4M-EX80, National Aperture Inc., Salem NH). A small amount of cyanoacrylate glue attached a second Teflon needle sleeve to the loading end of the tissue; this sleeve then slipped over a vertically mounted 316V stainless steel bending bar of known stiffness. The stiffness of the bar determined the amount of force produced as a function of the bar's displacement, eliminating the necessity of load cells. Actuation of the bi-directional stage in the X_1-direction moved the entire tank and sample, causing the transverse linkage to bend the bending bar. In this design, both positive and negative changes in curvature could be tracked, allowing a single-run experiment in both the with-curvature (WC) and against-curvature (AC) testing directions. For the bending data acquisition, the following information was recorded for the duration of the experiment: coordinates of red macro markers, displacement of the bending bar, and the current curvature of the tissue. Analysis of the bending data was detailed by [2] and summarized in **Chapter 2**. A custom-written LabVIEW (National Instruments, Austin,TX) program computed curvature, change in curvature, and moment at the middle five markers for each time point of the experiment during testing. The resulting marker positions were fit to a fourth-order polynomial to determine the curvature of the tissue. The initial curvature, κ_0, was recorded by the control system and subtracted from consequent curvature measurements to obtain the change in curvature $\Delta\kappa = \kappa - \kappa_0$. Five specimens were tested to a curvature change up to 0.1-0.20 mm^{-1}. The moment was determined by using the position of the central marker and the displacement of the bending bar (Eq. 4.1 and **Chapter 2, Fig. 2.2a**)

$$M = P\,y \qquad (4.1)$$

where M is the applied moment, y is the deflection from the horizontal axis, and P is the axial force. The displacement of the bending bar was tracked in real-time since the applied axial force, P, was a function of the displacement. The deflection, y (Fig. 2-b) was computed using the spatial y coordinate of the central tissue marker and the y coordinate of the horizontal axis drawn from post to post. The resulting data is reported as the averaged M/I vs. $\Delta\kappa$ response of all specimens from each group to normalize with respect to specimen geometry (**Fig. 4.3a-b).**

Linearized effective modulus

The effective modulus, E_{eff}, was determined from a linear regression of the M vs. $\Delta\kappa$ plots at the maximum $\Delta\kappa$ reached for both the control and TGF-β1 groups (Fig. 4.3). It is important to clarify that E_{eff} is simply an estimated index of tissue stiffness as the AV bending behavior is not entirely linear. All reported pairwise multiple comparison procedures used a one-tailed t-test with an overall significance level of 0.05 performed with SigmaPlot (San Jose, CA, USA).

Tissue bulk modulus estimates using the macro-micro model

The same moduli relations for inactivated tissue found in [3] and used for fitting Merryman et al. data in **Chapter 3** were maintained here for the cytochalasin D activation state since it was considered to be inactivated through the depolymerization of filamentous actin (F-actin). Similarly, the layer differences between relative increase in stiffness between the normal and hypertensive states discovered from fitting the same data set **(Chapter 3**) were also maintained. For example, the fibrosa was found to increase in tensile stiffness from the inactive to the normal state approximately 4 times more than the ventricularis. Therefore, when performing the optimization procedure to fit the moduli values from the inactive to the normal state, the fibrosa tensile stiffness was optimized and the ventricularis always proceeded with an increase from inactive of 4 times less than the fibrosa. Additionally, the compressive moduli values remained the same for all three states due to the finding in **Chapter 3** that the bidirectional response can only be captured when dictated by the layers under tension. Using these assumptions based on previous findings, the data from all 4 treatment groups for all activation states were fit to the macro model.

Macro RVE averaged stress

Extracted nodal and elemental values for displacement and stress from the simulation were taken at 0.15mm^{-1} change in curvature. The average stress of the macro RVE (**Chapter 3**, **Eq. 3.4 and Eq. 3.11**) was computed using a custom Python script, extracting the FE estimated stress at all 27 nodes and numerically integrating using a 3-point Gauss quadrature in three dimensions.

AVIC stiffness and contractile force estimates using the macro-micro model

As discussed in detail in **Chapter 3**, a baseline basal stiffness of AVICs (μ_{AVIC}^{Basal}) was established and validated to be 18kPa. Also, as described previously, AVIC contractility ${}_{\text{state}}\alpha_{AVIC}^{layer+}$ was determined from the fibrosa RVE under tension by performing a parametric study of the parameter until homogenized macro stress levels (${}_{\text{state}}\bar{\sigma}_{Macro}^{layer+}$) were achieved.

RESULTS

Linearized effective modulus of AV leaflets

There was an observed stiffness increase between the control and TGF-β1 treated AVs under flexural deformation (**Fig. 4.3**). Although direct comparison between the activation studies introduced in **Chapter 3** and the current study cannot be made due to differences in experimental design, the observed bidirectional response remained aligned with previous findings. For example, the linearized modulus estimates (max curvature reached common amongst the samples or $0.11mm^{-1}$) revealed an insignificant increase in stiffness from normal to hyper states when bending in the WC direction for both the control and the TGF-β1 treated groups (**Fig. 4.4**). This contrasts with a statistically significant increase in stiffness ($p=0.01$) from the normal to hyper activation states in the control group as well as the TGF-β1 treated samples ($p=0.007$). Comparing control tissue against TGF-β1 treated samples, there was no observed statistically significant difference in the WC bending direction. However, there was a notable increase in stiffness of the TGF-β1 relative to the control for all three activation states ($p<0.05$) in the AC direction.

There was a slight fold increase in stiffness change between the normal to hypertensive activation observed between the two treatment groups. Control tissue increased stiffness approximately 1.48 fold when stimulated with 90mM KCl (hyper) from the normal state (5mM). TGF-β1 treated tissue increased stiffness slightly more upon 90mM KCl activation with a 1.58-fold increase from normal conditions.

CytoD treatment was successful in decreasing the F-actin cytoskeletal contributions to AVIC stiffness as indicated by the significant decrease in stiffness amongst both groups for each bending direction ($p<0.05$). The inactivated TGF-β1 was interestingly found to be significantly stiffer than the control activated group ($p=0.011$). Although reporting the linearized effective modulus E_{eff} provides a general estimate of bending behavior, the true layer behavior must be captured by the estimated shear moduli from the macro-model fits to the experimental M vs. $\Delta\kappa$.

Tissue bulk modulus estimates using the macro-micro model

Estimated parameters for each treatment group at each different activation level are reported in **Table. 4.2.** Parameter estimates for the inactivated tissue, although substantially lower in magnitude, fit the experimental data well using the same moduli relations established for non-viable tissue. To summarize, it was established that an approximate 5:1 bimodular relationship exists in the fibrosa layer, contrasted with a 4:1 relationship found in the ventricularis for inactivated AV tissue. Using these same established moduli relationships between tensile and compressive behavior, the goodness of fit was more than sufficient with reported R^2 values of 0.990 and 0.964 for the inactivated control and TGF-β1 groups respectively. The TGF-β1 treated tissue was found to exhibit an overall higher stiffness (approximately 45%) than the control tissue under both tension and compression in both layers for the inactivated state.

As discussed in the methods, moduli relationships established in **Chapter 3** for the control tissue were maintained and only the fibrosa modulus was optimized with the model. Therefore, the remaining results will be discussed highlighting the fibrosa layer responses and comparing the differences between the control and TGF-β1 treated tissue.

Examining the parameter fits at the normal state (5mM KCl), we observe an approximate 2-fold increase in stiffness from the control tissue, contrasted with a similar 1.8-fold increase from the TGF-β1 group. Although the fold increase from inactive to normal is similar amongst the two treatments, the TGF-β1 group had a higher inactivated stiffness to start with. This nearly insignificant difference is reflected by the tensile/compressive layer moduli ratios reported in **Tables 4.3 and 4.4**. The fibrosa layer of the control tissue was approximately 10 times stiffer under tension than compression, contrasted with the TGF-β1 treated tissue showing a fibrosa that was 9 times stiffer under tension. However, it is important to point out that in the normal state, the TGF-β1 treated tissue was still found to be approximately 25% stiffer than the control.

The most substantial difference between the control and TGF-β1 treated tissue is the observed stiffness change between the normal and hyper activation states. The control tissue increased in fibrosa tensile stiffness approximately 1.48-fold, compared with a 2.26-fold increase in fibrosa tensile stiffness with TGF-β1 treatment. This is reflected in the tensile/compressive layer moduli ratios as a 15:1 ratio in the control tissue, compared with a nearly 20:1 ratio for the TGF-β1 treated tissue.

Underlying changes in AVIC stiffness and contractile forces

The estimated contractile force for AVICs in the control specimen at hypertensive conditions was approximately 26E-5 1/K (**Fig. 4.5a**). This value was significantly lower than the estimated contractile parameter for AVICs within the TGF-β1 treated tissue of approximately 35E-5 (**Fig. 4.5b**). These results are also plotted in 3D to illustrate consistency of the model with findings from **Chapter 3**, demonstrating insignificant contribution of AVIC stiffness to changes in tissue stiffness (**Fig. 4.6**). It is important to also examine what this means in terms of contractile change between normal and hyper conditions ($\Delta\alpha$ in **Fig.4.5**). For the control tissue, the contractility increased 1.39-fold from normal to hyper, contrasted with an increase of 2.05 from the TGF-β1 treated tissue. This marks an increase in AVIC contractility of nearly 50% upon activation with TGF-β1. The connectivity parameter results reveal that relative to the fibrosa layer, the AVICs residing in the ventricularis layer are drastically less connected to the surrounding ECM (**Tables 4.6 and 4.7**).

DISCUSSION AND CONCLUSIONS

The TGF-β1 treated tissue was found to exhibit an overall higher stiffness than the control tissue. It is possible that over the five day incubation period, the TGF-β1 treatment could have prompted the AVICs to begin producing ECM at a relatively higher rate than the control groups. Additional histological analysis would need to be carried out to determine whether or not new collagen had been produced. However, the average thickness of the specimens was not higher than that of the control groups indicating that whatever new matrix was synthesized is most likely subtle and the flexure test is capable of detecting such small changes in stiffness prior to noticeable valve thickening.

In summary, the study revealed a significant increase in stiffness of the fibrosa layer with exogenous TGF-β1 treatment. The layer-dependent increase in stiffness was reflected in estimated AVIC contraction, depicting a 1.50-fold increase in AVIC contraction relative to the control upon TGF-β1 activation. Whether examining linearized estimates of tissue stiffness or the estimated AVIC contraction force, there is a consistent 45-50% increase in tissue stiffness and underlying AVIC contractility when stimulated with TGF-β1 treatment. Furthermore, AVIC connectivity within the ventricularis under tension is drastically reduced (>96%) relative to the fibrosa connectivity for both control and TGF-β1 treated tissue. This may suggest an increase in ECM degradation in the ventricularis caused by matrix metalloproteinases activation due to static incubation for a five day period. This would require further investigation such as gene expression of metalloproteinases as well as zymography.

AV	Aortic Valve
ECM	Extracellular Matrix
AC	Flexure direction directed against the natural curvature of the leaflet
WC	Flexure direction directed with the natural curvature of the leaflet
FE	Finite Element
I	Second moment of inertia
$\Delta\kappa$	Change in valve leaflet curvature during flexure testing
M	Applied bending moment
$W^{\pm}$	Bimodular strain energy function
$E_{eff}\mathrm{I}$	Flexural stiffness
F	Fibrosa layer
V	Ventricularis layer
$RVE^{layer\pm}$	Representative Volumetric Element Layer: Fibrosa (F), Ventricularis (V)
${}_{\text{state}}\mu_{Macro}^{layer\pm}$	Shear modulus of the macro model State: inactive, normal, hypertensive Layer: Fibrosa (F), Ventricularis (V) Under Tension (+) or Compression (-)
${}_{\text{state}}\bar{\sigma}_{Macro}^{layer\pm}$	Volumetric averaged stress of the macro model RVE State: inactive, normal, hypertensive Layer: Fibrosa (F), Ventricularis (V) Under Tension (+) or Compression (-)
${}_{\text{state}}\bar{\sigma}_{Micro}^{layer\pm}$	Volumetric averaged stress of the micro model RVE State: inactive, normal, hypertensive Layer: Fibrosa (F), Ventricularis (V) Under Tension (+) or Compression (-)
Φ_{AVIC}	Mass fraction of AVICs
Φ_{ECM}	Mass fraction of ECM
$\mu_{ECM}^{layer\pm}$	Baseline shear modulus of ECM Layer: Fibrosa (F), Ventricularis (V) Under tension (+) and compression
μ_{AVIC}^{Basal}	Basal shear modulus of AVIC in the inactivated state
${}_{\text{state}}\mu_{AVIC}^{layer\pm}$	AVIC stiffness
${}_{\text{state}}\alpha_{AVIC}^{layer\pm}$	AVIC contractility
$\beta_{AVIC}^{layer\pm}$	AVIC connectivity to ECM Layer: Fibrosa (F), Ventricularis (V) $\beta_{AVIC}^{layer\pm} \in [0,1]$

Table 4.1: List of symbols and nomenclature.

<u>Control</u>	Layer	μ^{+}_{Macro}	μ^{-}_{Macro}	Tension/ Compression Layer Moduli Ratios	R^2	Neutral Axis WC	Neutral Axis AC
Inactive	F	40.0	8.40	~4.72:1	0.990	0.36	0.75
	V	18.64	4.80	~3.88:1			
Norm	F	83.29	8.40	~10:1	0.970	0.34	0.83
	V	27.96	4.80	~5.83:1			
Hyper	F	123.62	8.40	~14.72:1	0.984	0.34	0.84
	V	27.96	4.80	~5.83:1			

Table 4.2: Estimated shear moduli values for the control treatment group at all three activation states. Moduli relations were derived from the in depth analysis presented in **Chapter 3**. Schematic detailing neutral axis location trends during AV bending is provided in **Fig. 2.8**.

TGF-β1	Layer	μ^{+}_{Macro}	μ^{-}_{Macro}	Tension/ Compression Layer Moduli Ratios	R^2	Neutral Axis WC	Neutral Axis AC
Inactive	F	58.38	12.26	~5:1	0.964	0.36	0.75
	V	27.21	7.0	~4:1			
Norm	F	105.36	12.26	~9:1	0.990	0.34	0.83
	V	40.82	7.0	~6:1			
Hyper	F	238.73	12.26	~20:1	0.972	0.34	0.84
	V	40.82	7.0	~6:1			

Table 4.3: Estimated shear moduli values for the TGF-β1 treatment group at all three activation states. Moduli relations were derived from the in depth analysis presented in **Chapter 3**.

Control	$\bar{\sigma}_{Macro}^{F+}$	$\bar{\sigma}_{Macro}^{F-}$	$\bar{\sigma}_{Macro}^{V+}$	$\bar{\sigma}_{Macro}^{V-}$
Inactive	1.049	0.893	0.965	0.674
Norm	2.14	0.893	1.065	0.674
Hyper	2.66	0.893	1.065	0.674

Table 4.4: Macro homogenized von Mises stress values for the control tissue for each layer under tension and compression for each activation state: inactive, normal and hypertensive. Units in kPa.

TGF-β1	$\bar{\sigma}_{Macro}^{F+}$	$\bar{\sigma}_{Macro}^{F-}$	$\bar{\sigma}_{Macro}^{V+}$	$\bar{\sigma}_{Macro}^{V-}$
Inactive	1.53	1.30	1.41	0.983
Norm	2.66	1.30	1.54	0.983
Hype	4.39	1.30	1.54	0.983

Table 4.5: Macro homogenized von Mises stress values for the TGF-β1 tissue for each layer under tension and compression for each activation state: inactive, normal and hypertensive. Units in kPa.

<u>Control</u>	RVE^{F+}	RVE^{V+}
β_{AVIC}	1	0.034

Table 4.6: Estimated connectivity (β_{AVIC}) parameters for Control tissue using the estimated uniform stiffness of 18kPa (μ_{AVIC}), and the uniform estimated hypertensive contraction force of 26E-5 1/K (α_{AVIC}).

TGF-β1	RVE^{F+}	RVE^{V+}
β_{AVIC}	1	0.035

Table 4.7: Estimated connectivity (β_{AVIC}) parameters for TGF-β1 treated tissue using the estimated uniform stiffness of 18kPa (μ_{AVIC}), and the uniform estimated hypertensive contraction force of 35E-5 1/K (α_{AVIC}).

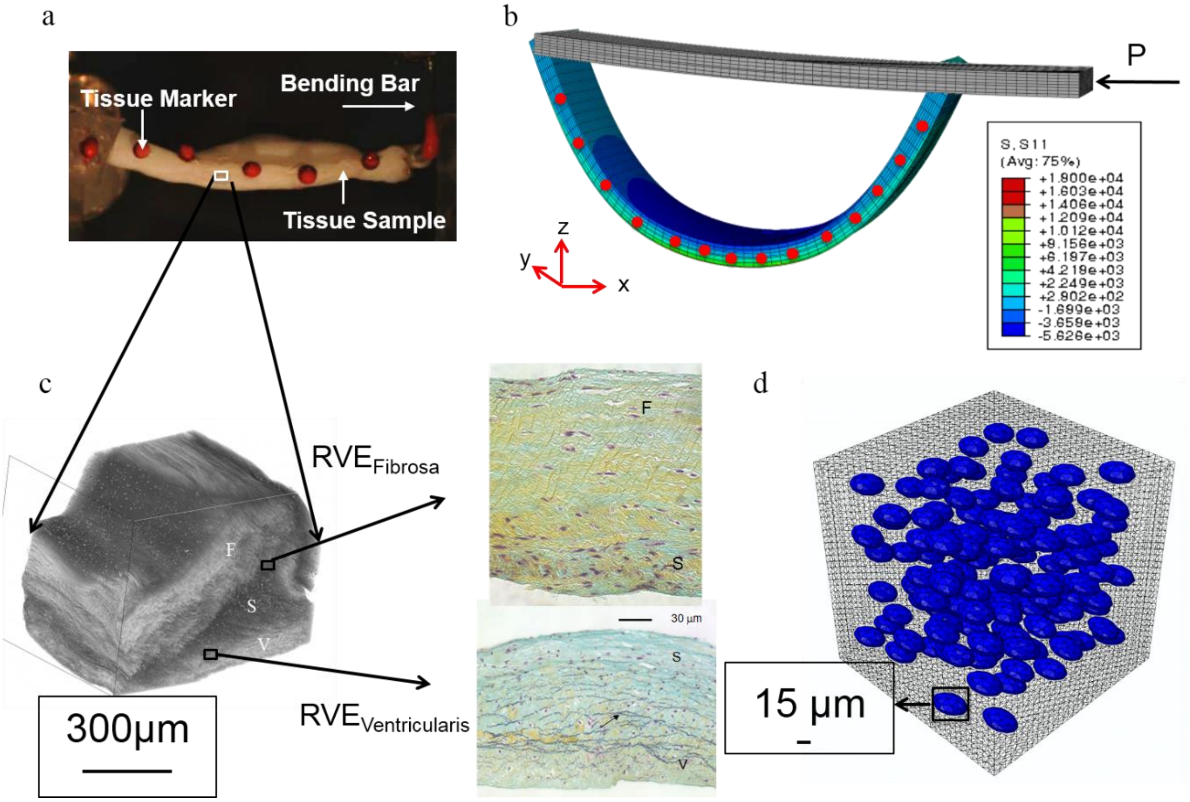

Figure 4.1: End-loaded tissue sample (a) and the corresponding macro-model simulation (b) which is then mapped down to the micro tissue scale (c) into the micro-model (d). For details of the macro-micro model framework the reader is referred to **Chapter. 3**.

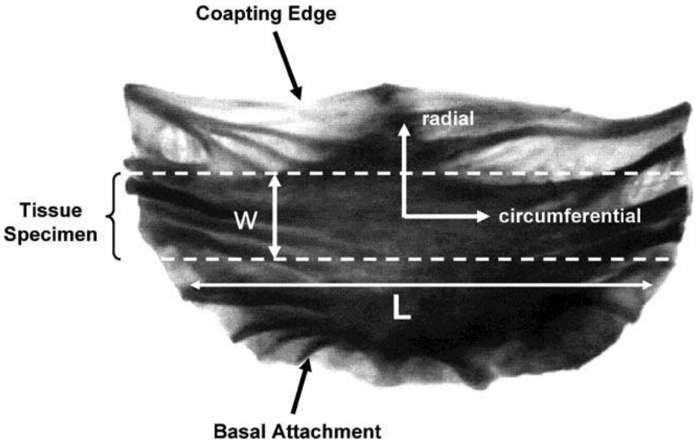

Figure 4.2: Aortic valve leaflet illustrating the size and orientation of the circumferentially oriented tissue strips extracted from the intact leaflet for flexure testing. Schematic adapted from [4].

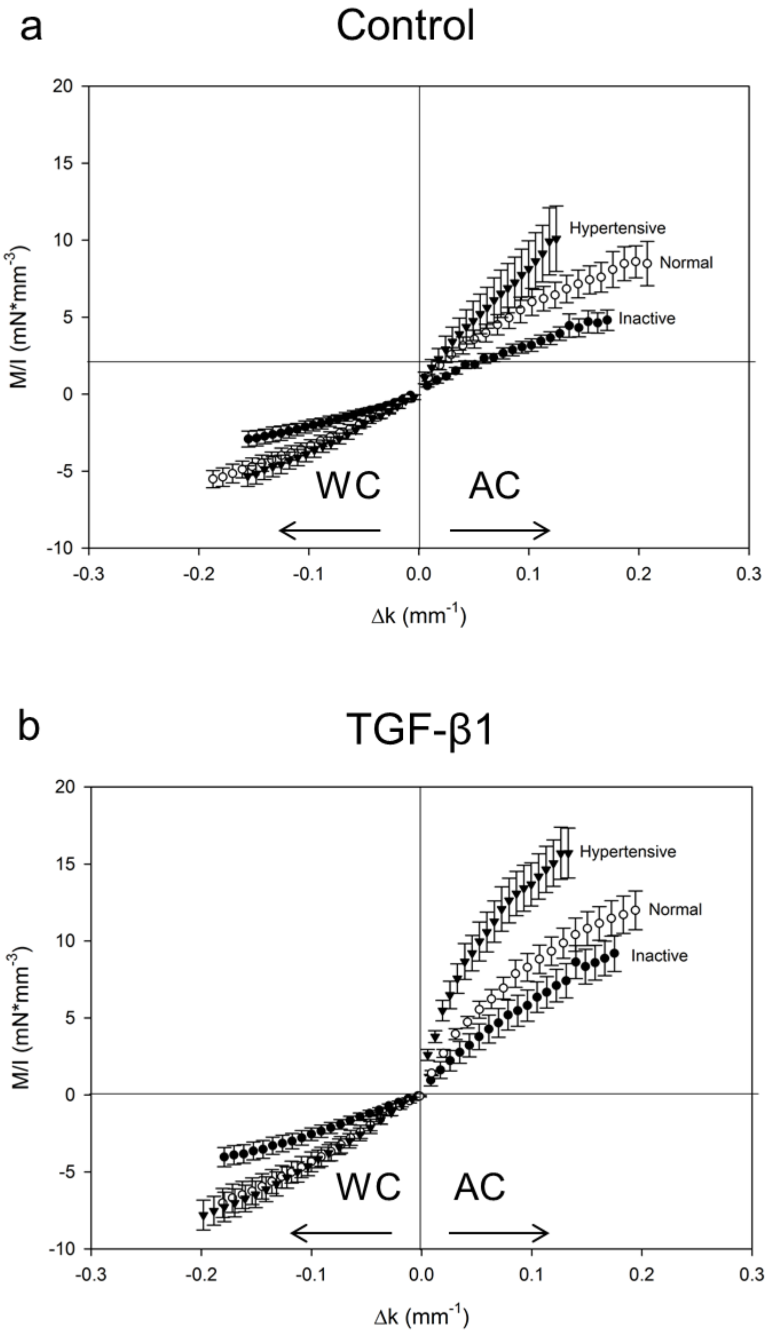

Figure 4.3: Averaged M vs. Δκ experimental data from AV bending study of control tissue (a) and TGF-β1 tissue (b) under inactive (CytoD), normal (5mM KCl) and hypertensive (90mM) conditions and bending with (WC) and against (AC) the natural leaflet curvature.

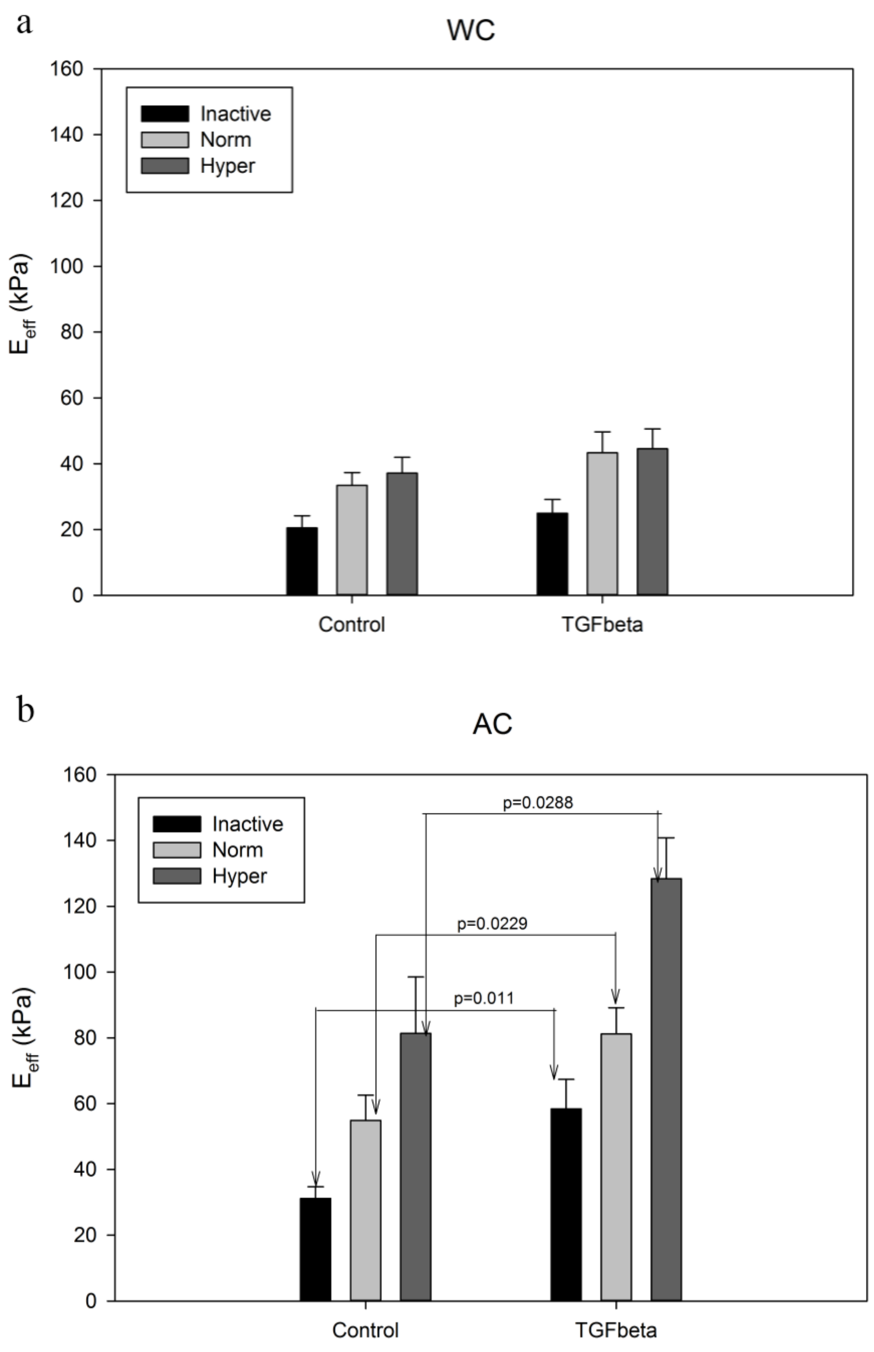

Figure 4.4: Linearized effective moduli from control and TGF-β1 treated tissue taken from the slope of the averaged M vs. Δκ curves in Fig. 4.3 at points of maximum common curvature ($0.11mm^{-1}$) determined for the inactive, normal and hypertensive states and bending in the WC (a) and AC (b) directions.

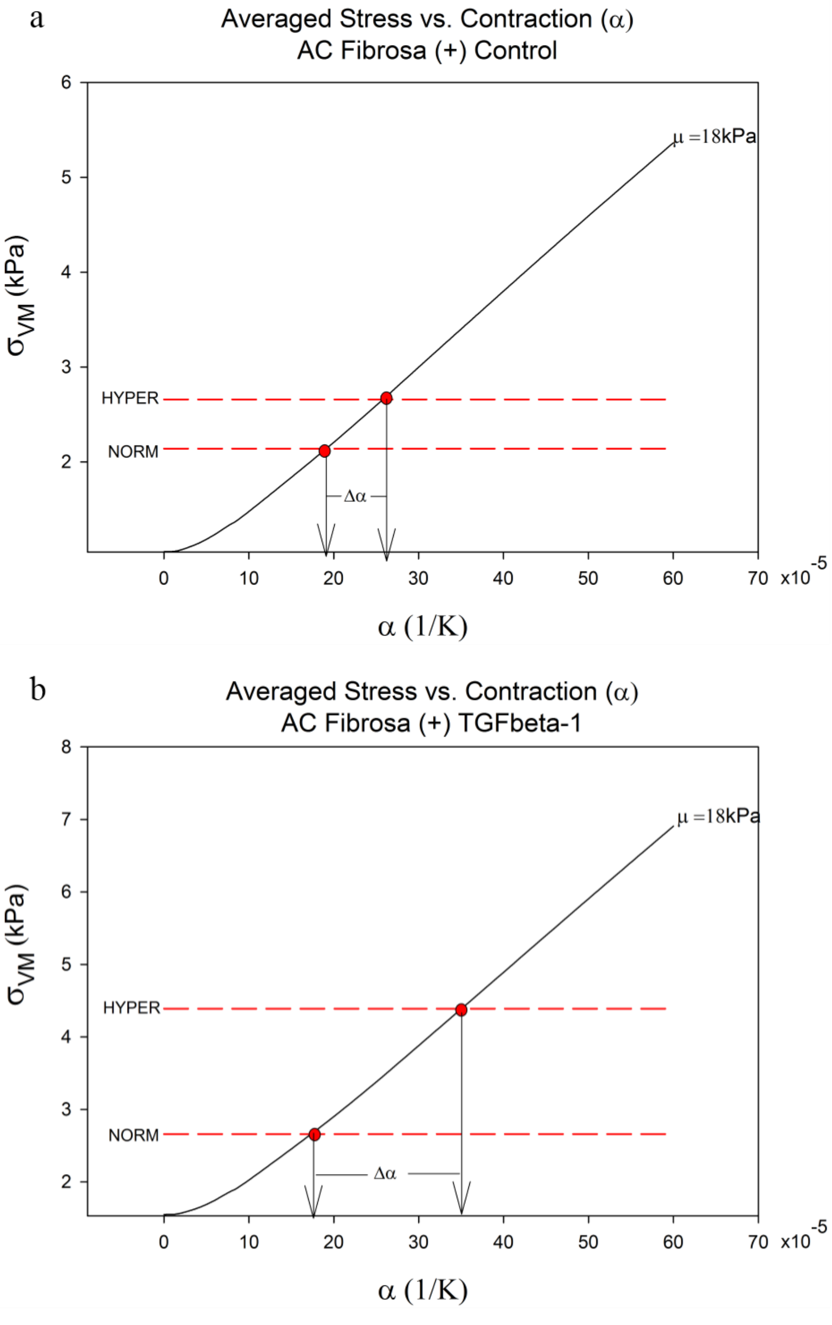

Figure 4.5: Results of micro-model parametric studies estimating changes in AVIC contractility, Δα, between normal and hyper activation states. Δα is plotted for the fibrosa RVE under tensile loading of control tissue (a) and TGF-β1 treated tissue (b).

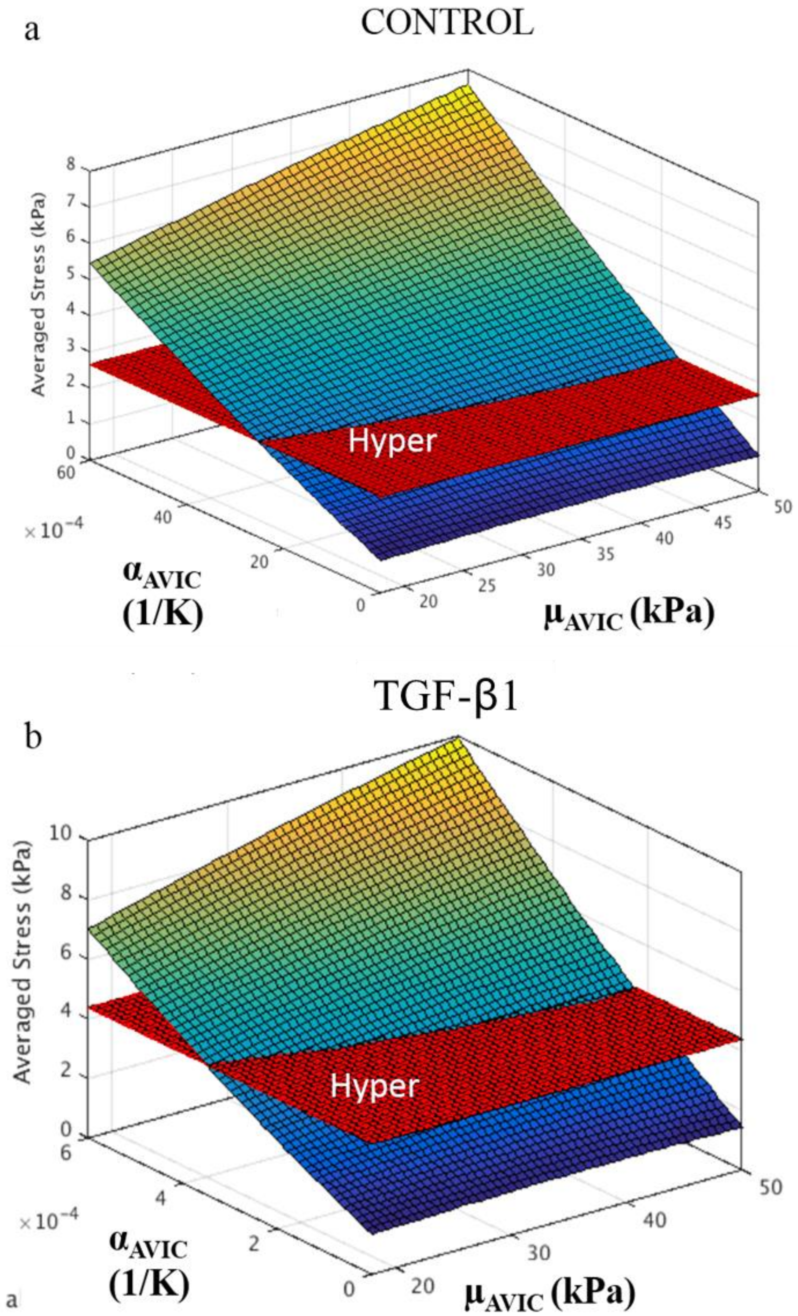

Figure 4.6: Results of micro-model parametric studies plotted in 3D. Effects of AVIC contractility, α, and AVIC stiffness, μ, for the fibrosa RVE under tensile loading are plotted for control tissue (a) and TGF-β1 treated tissue (b). Flat plane indicates the hypertensive stress (Hyper) measured at the tissue level.

REFERENCES

1. Monzack, E.L., X. Gu, and K.S. Masters, Efficacy of simvastatin treatment of valvular interstitial cells varies with the extracellular environment. Arterioscler Thromb Vasc Biol, 2009. 29(2): p. 246-53.
2. Engelmayr, G.C., Jr., et al., A novel bioreactor for the dynamic flexural stimulation of tissue engineered heart valve biomaterials. Biomaterials, 2003. 24(14): p. 2523-32.
3. Buchanan, R.M. and M.S. Sacks, Interlayer micromechanics of the aortic heart valve leaflet. Biomech Model Mechanobiol, 2014. 13(4): p. 813-26.
4. Merryman, W.D., et al., The effects of cellular contraction on aortic valve leaflet flexural stiffness. J Biomech, 2006. 39(1): p. 88-96.

CHAPTER 5: MEASURING THE EFFECTS OF CONTRACTILE STIMULI ON AVIC MECHANICAL BEHAVIOR USING MICROINDENTATION TECHNIQUES

Preface

The mechanical properties of VICs have been studied using various experimental techniques mentioned previously in **Chapter 1**, such as micropipette aspiration (MA) [1-3], collagen-gel contraction [4], and atomic force microscopy (AFM) [4]. These ex-situ studies analyzed VICs isolated from the different heart valve leaflet tissues when suspended in an aqueous solution (MA), and seeded on a 2D flat substrates (AFM), or seeded on collagen gels. Findings from these studies taken with supporting literature [5-10] suggest that the expression of α-SMA into the stress fibers may enhance the contractility and stiffness of these cells. Similarly, upon the disruption of the α-SMA rich cytoskeleton, the contractile activity is abolished [5, 11, 12]. The case can be made that AVIC stiffness measured through AFM allows for a more accurate representation of biomechanical properties compared with micropipette aspiration. This is due to the fact that during measurements, AVICs are seeded on a collagen substrate, allowing for the cytoskeleton to form anchors via focal adhesions on one side of the cell. This is in contrast to micropipette aspiration measurements where AVICs are entirely non-adherent, making it physically impossible for reaction forces to be generated. However, this ex-situ technique remains far from physiologically representative of the AVIC's native ECM connectivity in 3D. The overall objective of this study is not to derive conclusions on AVIC responses to contractile reagents, but instead to compare relative contractile responses of AVICs, from a normal or basal tonus state (5mM KCl) to a hypertensive state (90mM KCl) with the same relative contractile response measured from the developed *in situ* approach (**Chapter 4**). We hypothesize that due to additional focal adhesions in the AVIC 3D native environment, the relative increase in contraction and associated stiffness will be substantially different than what is measured using microindentation techniques. To test this, microindentation studies were carried out in collaboration with the Guilak research group at Duke University.

INTRODUCTION

The effective stiffness of AVICs is a strong indicator of its biosynthetic phenotype. In normal healthy valves, AVICs are quiescent with a fibroblast-like phenotype [13]. AVIC phenotypic plasticity has been demonstrated through their adjustment to dynamic environments through the activation and secretion of proteolytic enzymes that mediate extracellular matrix remodeling. Transforming growth factor-beta1 (TGF-β1) is a prolific growth factor and has been shown to initiate calcification *in vitro* and accelerate valvular stenosis *in vivo* [4,5]. Immunohistochemical studies have revealed the presence of high levels of TGF-β1 in calcified human AVs when compared to noncalcified [6]. It has been shown to mediate differentiation of VICs into active myofibroblasts *in vitro*, determined by a significant increase in α-SMA, a gold standard marker for identifying myofibroblasts, augmentation of stress fiber formation and alignment, and increases in VIC contractility [7]. The role that TGF-β1 plays in calcification of the AV remains unclear, however a number of *in vitro* studies have shown convincing evidence that TGF-β1 induces cell apoptosis, cellular aggregation, and calcified nodule formation in VICs. To understand differences in AVIC biomechanical responses in a simulated disease state and validate the *in situ* approach in **Chapter 4**, microindentation studies were used to examine AVIC activation with and without TGF-β1. The effective modulus of AVICs cultured on a flat thin-layered collagen substrate over glass was measured using AFM technique, modified with a larger spherical indenter with 5 μm diameter (i.e. microindentation) to obtain a global response of AVIC mechanics. The activation states of the AVICs were then controlled with different chemical reagents to alter the biomechanical properties of the stress fibers. Then, using the experimental data, we studied both resulting changes in AVIC stiffness and observed differences in components of the stress fibers (α-SMA and F-actin). Five experimental treatment groups were used: Cytochalasin D pretreated group (CytoD), Control groups with 5 mM and 90 mM KCl treatments (C5 and C90 groups, respectively), and transforming growth factor-beta1 (TGF-β1) pretreated groups with 5 mM and 90 mM KCl treatments (T5 and T90 groups, respectively). For each group, the indentation depth vs. force curves were extracted and later fit to a computational model to derive the effective modulus (E_{eff}) of the AVIC.

PROTOCOLS

AVIC culture

Glass bottom culture dishes (MatTek, Ashland, MA) were coated with collagen type 1 (BD Biosciences, San Jose, CA) in 0.02N acetic acid at a concentration of 10ug/mL. The solubilized collagen solution was incubated on the glass for 1 hour at 37°C. Excess solution was aspirated and coated dishes were left to dry under UV overnight and then rinsed with PBS. Primary porcine VICs were generously provided by Dr. Giovanni Ferrari's research group at the University of Pennsylvania's Perelman School of Medicine. The VICs were isolated from porcine AVs using a modification of the method described by Branchetti *et al.* [14], cryopreserved and shipped on dry ice to our laboratory. Primary VICs were thawed and cultured in Dulbecco's Modified Eagle

Medium (DMEM) with high glucose and 10% fetal bovine serum) at 37°C and 5% CO_2 until reaching 80% confluence in monolayer.

VICs (P2-P4) were lifted from tissue-culture treated flasks and seeded on collagen coated coverslips at a concentration of 7,000/cm^2 and cultured in Dulbecco's Modified Eagle Medium (DMEM) with high glucose and low-serum (LS) medium (1% FBS supplemented). VICs were treated for a period of 5 days with additional TGF-β1 (5ng/mL) (Sigma-Aldrich, St Louis, MO) and control cells were cultured in plain media (all conditions were LS). Cultures were replenished with TGF-β1 and fresh media every 48 hours.

Pretreatment

Cytochalasin D (CytoD) is a potent inhibitor of actin polymerization. It binds to F-actin and prevents the polymerization of actin monomers. It is thought that the mechanism for this action is through binding specifically to the net polymerizing end of the filament, preventing the addition of new monomer, while allowing the rate of actin monomer loss to continue [2]. As actin monomer loss remains uninhibited, depolymerization occurs. Immediate disruption of the ordered cytoskeleton occurs within eukaryotes exposed to CytoD, involving breaking of actin filaments. Additionally, a secondary response is known to occur where fragmented actin filaments engage in a contractile event, causing the formation of filament foci [3]. By disassembling the actin network of the VICs, microindentation can be used to measure the baseline global stiffness of the AVIC and serve as a negative control throughout the study. The resulting stiffness was expected to be similar to that which has been measured using micropipette aspiration in previous studies (0.45 kPa) [1].

VICs cultured in standard low serum media, served as a second negative control for the TGF-β1 treated VICs. Testing in 5mM KCl mimics a normal physiological environment, creating a passive stiffness in the AVIC cytoskeleton. Addition of 90mM KCl during microindentation testing initiates active contraction within the VIC cytoskeleton and mimics a hypertensive physiological condition. Similarly, testing in 5mM KCl with the addition of TGF-β1 represents a normal physiological environment, enabling the measurement of VIC passive stiffness in a "myofibroblast"-like state. The addition of 90mM KCl will allow the measurement of active VIC stiffness under these simulated pathological conditions. It is hypothesized that the addition of α-SMA into the stress fibers will initiate a more pronounced increase in activated stiffness compared to the activated control group (Control 90mM). A summary of the five experimental conditions is provided in **Table 5.1**.

Microindentation

After 5 days of incubation, the biomechanical properties of control and TGF-β1 treated AVICs were measured using an atomic force microscope (MFP-3D, Asylum Research, Santa Barbara, CA). The TGF-β1 and non-treated AVICs were first tested under normal physiological levels of 5mM KCl at 37°C. The same AVIC sample was then incubated at 37°C for 10 minutes in hypertensive levels of KCl (90mM) and retested. Finally, the same AVIC sample was treated with 20μM Cytochalasin-D (Sigma-Aldrich, St Louis, MO) for 10 minutes at 37°C to cause complete depolymerization of the actin network and tested using microindentation a third time. To ensure CytoD concentration and incubation time was effective, samples were given CytoD supplemented with 90mM KCl and measured using microindentation. There was no measured increase in stiffness between the 5mM and 90mM controls when delivered with CytoD (data not shown).

Cantilevers with a borosilicate glass sphere (5μm diameter, Novascan Technologies, Ames, IA) were used for all microindentation testing. The cantilever spring constant (typically 0.027 N/m) was determined from the spectral density of the thermal noise fluctuation prior to testing. Single AVICs were indented (**Fig. 5.1a**) with an approximate step displacement (Z) and the resulting force response was recorded. The indentation depth is approximate since it varies with the mechanical properties of each AVIC as the experiment is trigger force controlled with a trigger force value of 2.5nN. On average, the indentation depth of the TGF-β1 treated AVICs ranged from 0.26-0.30 microns and the control AVICs experienced a similar 0.3-0.38 indentation depth representing approximately 4-6% of the AVIC height. Due to destruction of the cytoskeletal network, the CytoD treated AVICs were indented nearly 2 microns prior to hitting the 2.5nN trigger force. Three different indentation speeds were used to achieve a slow and fast loading cycle to reveal potential strain-rate dependent properties of the AVICs **(Fig. 5.1b**). First, a slow indentation speed was used representing a 300ms indentation followed by an immediate 300ms release. Second, a different sampling of AVICs from the same sample was indented with a more physiologically relevant speed of 50ms loading (speed of valve opening and closing), followed by a 50ms release. For each of the five experimental conditions (**Table 5.1**), 60 total AVICs were tested on 3 different coverslips using the slow indentation speed and a total of 20 AVICs were tested on 3 different coverslips using the faster indentation speed. Indentations were performed consistently over the nucleus of each AVIC for consistency in measurements (**Fig. 5.2**).

AVIC elastic modulus analysis

To estimate AVIC effective moduli values, the indentation depth vs. force curves were fit to a thin-layer Hertz equation (**Eq. 5.1-5.2**) as described in the methods by [15]. The model assumes an infinitely hard sphere indenting a flat, deformable substrate, and is defined by:

$$F = \frac{4E_Y R^{1/2}}{3(1-\nu^2)}\delta^{3/2}\left[1 - \frac{2\alpha_o}{\pi}\chi + \frac{4\alpha_0^2}{\pi^2}\chi^2 - \frac{8}{\pi^3}\left(\alpha_o^3 + \frac{4\pi^2}{15}\beta_o\right)\chi^3 + \frac{16\alpha_o}{\pi^4}\left(\alpha_0^3 + \frac{3\pi^2}{5}\beta_0\right)\chi^4\right] \tag{5.1}$$

$$R = \left(\frac{1}{R_{probe}} + \frac{1}{h/2}\right)^{-1} \tag{5.2}$$

where F is the applied force, E_Y is the Young's modulus, R is the relative radius, for spread cells analyzed here, $R = R_{probe}$, where R_{probe} is the probe radius, h is the cell height, ν is Poisson's ratio, δ is the indentation, $\chi = \frac{\sqrt{R\delta}}{h}$, and the constants α_o and

where F is the applied force, E_Y is the Young's modulus, R is the relative radius ($R=R_{probe}$), h is the cell height, ν is Poisson's ratio, δ is the indentation. $\chi=(\sqrt{R\delta})/h$. α_0 and β_0 are functions of the Poisson's ratio defined for a material bonded to a surface as:

$$\alpha_o = \frac{1.2876 - 1.4678\nu + 1.3442\nu^2}{1-\nu} \tag{5.3}$$

$$\beta_o = \frac{0.6387 - 1.0277\nu + 1.5164\nu^2}{1-\nu} \tag{5.4}$$

The thin-layer model is appropriate for samples where h$\leq R$ [15]. Since all AVIC samples tested were far less than 64μm, this model remains appropriate. Additionally, the geometry of the sample did not affect the data analysis as applied strains were less than 10%. For each single AVIC indentation, the initial indentation phase of the acquired force-indentation curve, representing the elastic response of the AVIC, was fit to **Eq. 5.1** to determine the elastic modulus, $E_{Y.}$

Immunofluorescence quantitative analysis

Immediately following microindentation, AVIC coverslips were washed twice with PBS to remove excess media then fixed in 4% Paraformaldehyde (Electron Microscopy Sciences, Hatfield, PA) in PBS for 15 minutes. Following fixation, AVICs were permeabilized using 0.1% Triton-X-100/PBS and nonspecific binding was blocked using 1% BSA for 30 minutes. AVICs were incubated for 1 hour with α-SMA monoclonal antibody (1:125, mouse anti-porcine, ThermoFisher Scientific, Waltham, MA). The primary antibody was removed through PBS washes and AVICs were incubated with a FITC conjugated secondary antibody (1:125 goat anti-mouse, Millipore, Billerica, MA) and TRITC-conjugated Phalloidin (1:100, Millipore) to stain for filamentous actin (F-actin). AVICs were stained with DAPI (Life Technologies, Carlsbad, CA) for 5 minutes prior to mounting with ProLong Diamond Antifade mountant (ThermoFisher Scientific).

Fluorescent images were taken from each of the 5 experimental groups (CytoD, Control 5mM, Control 90mM, TGF-β1 5mM and TGF-β1 90mM). A minimum of 10 images was taken from each group (20x objective, TRITC, FITC, DAPI filters) with a fluorescent microscope (Zeiss Axiovert 200M, Zeiss, Germany). Exposure time remained constant to allow for a relative quantitative analysis between groups. A custom Python script was then used to quantify relative amounts of free α-SMA protein, F-actin and α-SMA positive F-actin (colocalization of α-SMA into the F-actin cytoskeleton).

RESULTS

Observed differences in measured AVIC biomechanical state

In all cases, the CytoD treatment (negative control) significantly reduced the modulus of the AVICs more than 10-fold compared to the control (C5), indicating its effectiveness in abolishing the AVIC cytoskeleton ($p<0.001$, one-way ANOVA). The resulting stiffness of 0.52 kPa was found to be similar to that which has been measured using micropipette aspiration in previous studies (0.45 kPa) [1].

Normal activation conditions (5mM KCl) revealed no differences in stiffness between the control vs. TGF-β1 treated AVICs (**Fig. 5.3**). Additionally, there were no observed difference resulting from different indentation speeds at this particular activation level.

Both control and TGF-β1 AVICs experienced a significant increase in stiffness with the addition of 90mM KCl ($p<0.04$, using two-tailed t-test comparisons of each treatment group)**.** Interestingly, when examining differences between control and TGF-β1 treated AVICs at the normal activation state using the slow indentation speed, differences were insignificant. However, when the speed of indentation increased (5 times the speed), there was a significant change in estimated moduli values for the TGF-β1, establishing a statistical difference between the control AVICs ($p=0.007$) **Fig. 5.4**. For clarity, the estimated moduli values are also reported comparing groups within a single indentation speed in **Fig. 5.5a** (slow) and **Fig. 5.5b** (Fast).

Examining the fold change upon activation with 90mM KCl, the differences are quite pronounced when compared to the slower indentation rate. Control AVICs exhibited an approximate 1.54-fold increase, contrasted with a 1.45-fold increase from TGF-β1 treated AVICs when evaluated with a slower indentation speed**.** Interestingly, higher rates of indentation increased this difference in fold change tremendously. Measured changes in control stiffness from 5 to 90mM KCl jumped from 1.54 to 1.75, with an even more drastic change in the TGF-β1 from 1.45 to 2.09.

Immunofluorescent staining of samples immediately after microindentation testing revealed interesting changes in relative F-actin and α-SMA protein content between groups (**Fig. 5.6-5.7**). Under 5mM activation conditions, there were no observed differences in α-SMA content between groups, however, as expected CytoD treatment eliminated nearly all of the F-actin cytoskeleton. These results are quantitatively reported in **Figs. 5.8**). Upon activation with 90mM KCl, both control and TGF-β1 AVICs experienced an upregulation of F-actin formation as well as an increase in α-SMA content (**Fig. 5.8-5.9**). The most marked change in α-SMA protein content was observed in the TGF-β1 treated AVICs. Furthermore, when examining the composite image (yellow **Fig. 5.7**) it is clear that the α-SMA has been incorporated in the F-actin network through both qualitative observation and quantitative measurements (**Fig. 5.10**). This is in contrast to control AVICs at 90mM, which did exhibit an upregulation in α-SMA protein, although modest (30% less than TGF-β1 AVICs).

DISCUSSION

Significant differences in fold change from underlying AVIC contraction upon TGF-β1 may be alluded to α--sma recruitment into the f-actin stress fibers as observed from immunofluorescent imaging. Referencing ongoing related work in our group by

Yusuke Sakamoto, the presented microindentation data is being used to develop an improved computational model of a VIC by incorporating a more realistic stress fiber model. Then, by integrating the experimental data of the AVICs into the model, how the stress fibers in the AVICs adapt to different activation states can be observed. Even more importantly the model is capable of capturing how different components of the stress fibers, F-actin and α-SMA, affect the stress fiber biomechanics (**Fig. 5.11**).

The most interesting and unexpected finding from this study was the strain rate sensitivity observed in the AVIC response to activation stimuli. Higher rates of indentation revealed significant differences between the TGF-β1 treated AVICs in the 90mM hypertensive condition and control AVICs. These differences were not evident using a slower strain rate (5-fold reduction in speed) and may suggest a rate dependence of the cytoskeletal structure, particularly α-SMA positive stress fibers. This may be linked to physiological responses of AVICs. AVICs reside in a high speed, dynamic environment *in vivo*, suggesting that larger cyclic strain magnitude on tissue may activate the AVICs. This suggests that a time-dependent model may be needed that captures inertial effects, viscoelasticity and poroelasticity of the AVICs in future modeling efforts.

When comparing the results from the microindentation study with the observed fold increase from *in situ* measurements (**Chapter 4**) relative trends comparing control vs. TGF-β1 contractile behavior appear consistent. The estimated contractility increase measured with the *in situ* approach for control tissue was found to be approximately 1.4, compared with a 2.0-fold increase observed in TGF-β1 treated tissue. If we contrast this with the observed fold change from physiologically relevant strain rates: 1.75 for control and 2.0 for TGF-β1. Although the trends remain the same between microindentation and *in situ* estimates of AVIC contractility, it seems that the relative effects of TGF-β1 treatment were more pronounced when measured *in situ*. **To summarize, the *in situ***

estimates revealed a 45-50% increase in contractile response upon TGF-β1 activation, contrasted with a mere 14% increase difference from microindentation measurements.

	Control	TGF-β1
Inactive (Cytochalasin-D)	CytoD	----
Normal (5mM KCl)	C5	TGF5
Hypertensive (90mM)	C90	TGF90

Table 5.1: Summary of treatment groups and abbreviated names. Two pre-treatments (control and TGF-β1 tested under 3 different activation states: inactive, normal (5mM) and hypertensive (90mM). CytoD treatment served as a negative control for an inactivated cytoskeletal network.

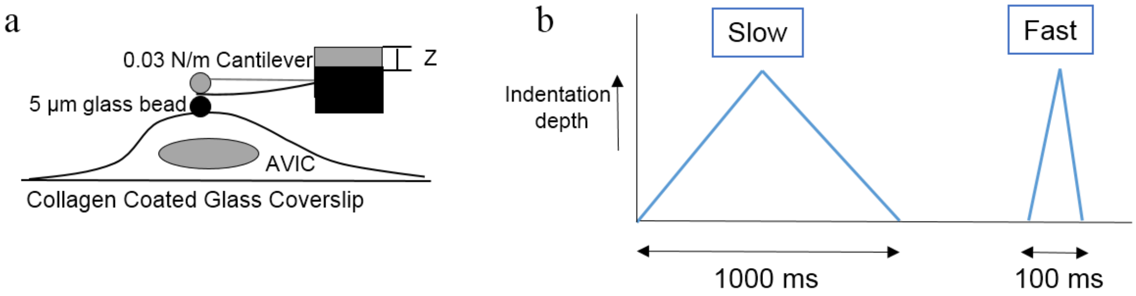

Figure 5.1: Schematic of microindentation on an AVIC with a 5 micron glass bead (a) and the two different indentation protocols used in the current study.

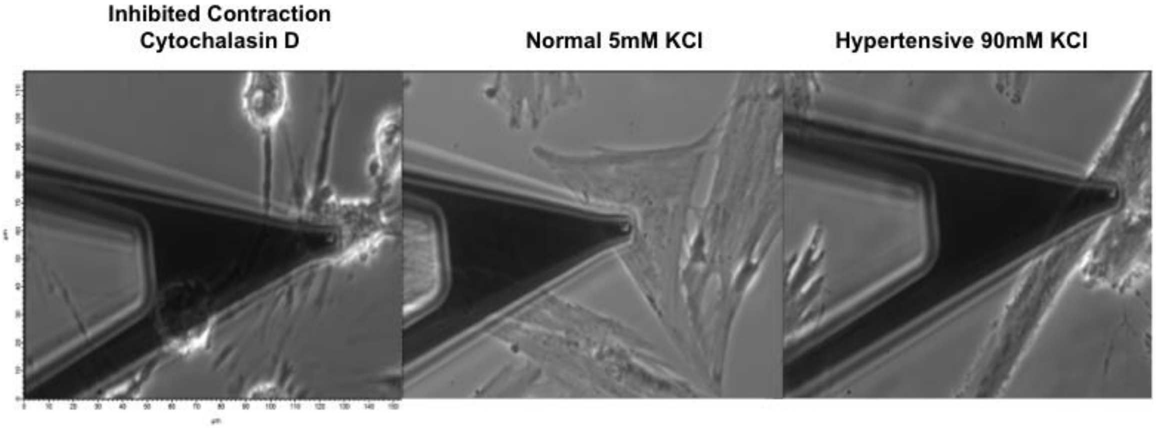

Figure 5.2: Single AVIC cells during indentation using a 5µm AFM cantilever tip (0.03 N/m).

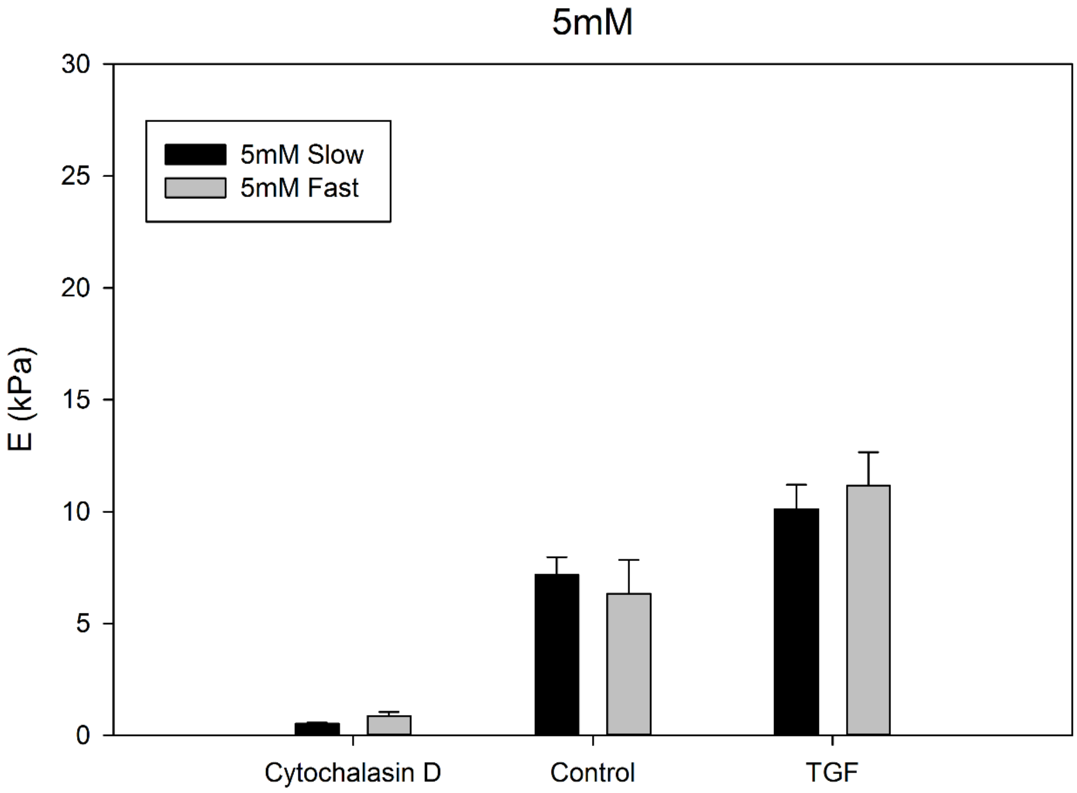

Figure 5.3: Effective modulus measurements from microindentation of AVICs under CytoD, Control and TGF-β1 treatments in response to normal activation conditions (5mM). Results are shown for slow (500ms) and fast (100ms) indentation speeds.

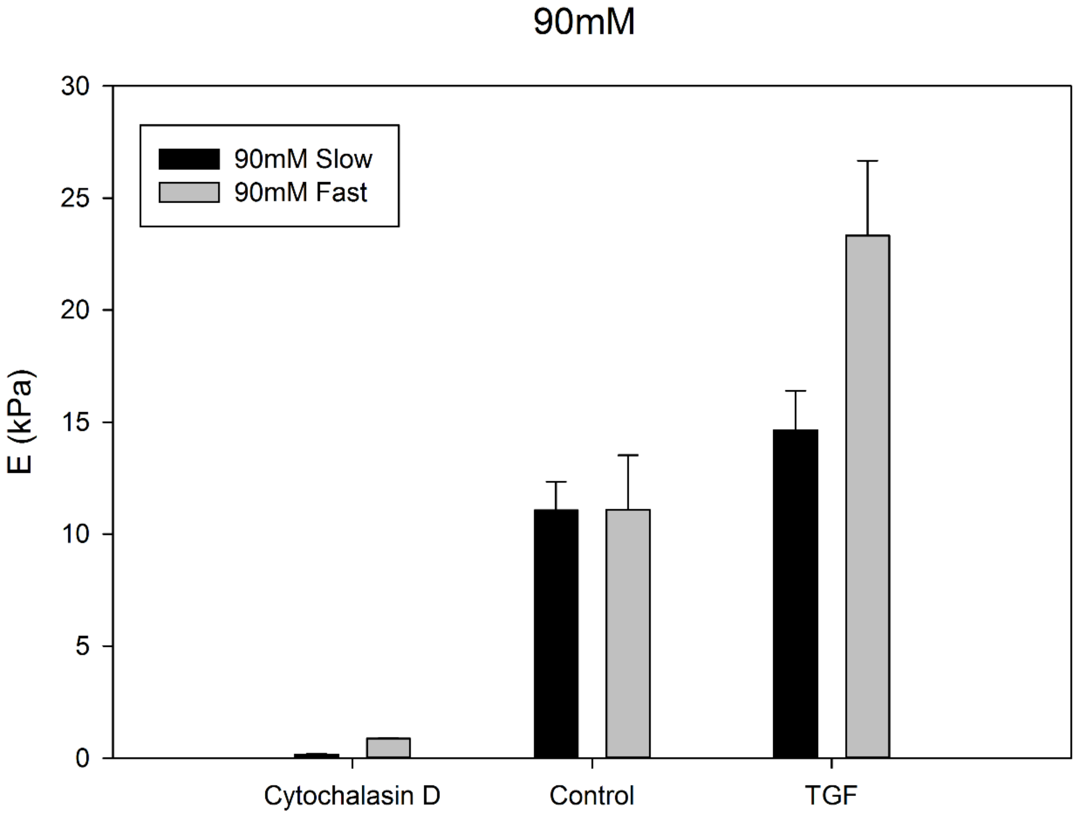

Figure 5.4: Effective modulus measurements from microindentation of AVICs under CytoD, Control and TGF-β1 treatments in response to hyper activation conditions (90mM). Results are shown for slow (500ms) and fast (100ms) indentation speeds.

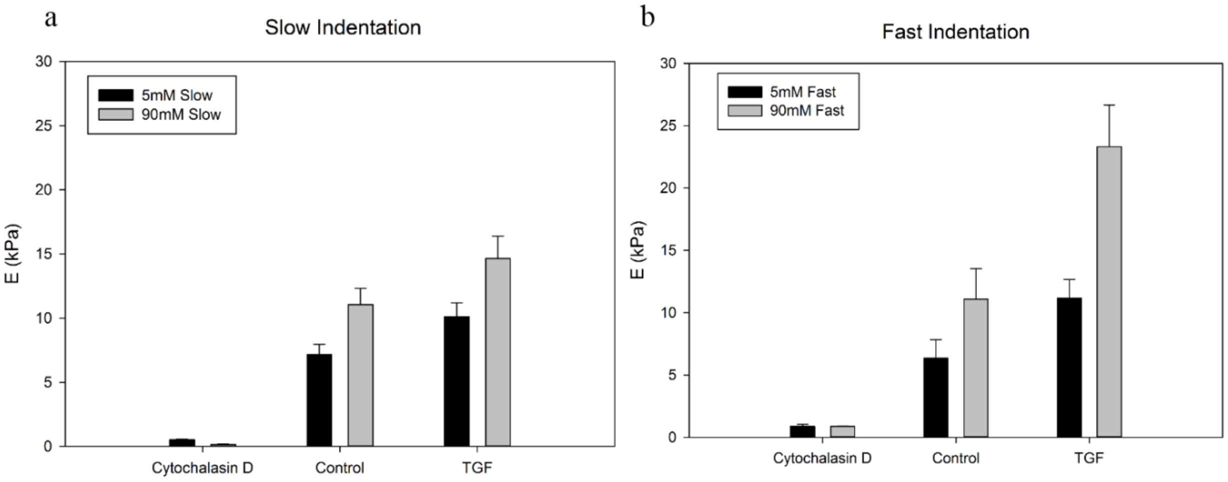

Figure 5.5: Effective modulus measurements from microindentation of AVICs under CytoD, Control and TGF-β1 treatments in response to hyper activation conditions (90mM). The same results from Fig. 5.3 and 5.4 are plotted side by side to illustrate the strain-rate dependency of the TGF-β1 effect on AVIC stiffness under 90mM KCl conditions.

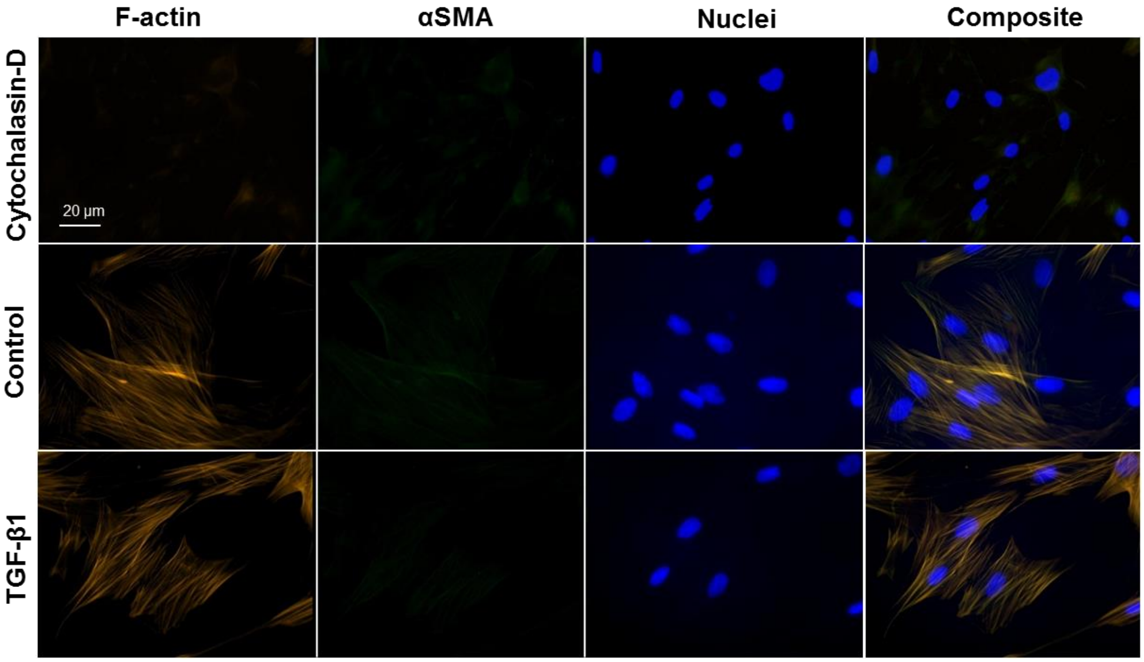

Figure 5.6: Fluorescent staining of AVICs on collagen substrates immediately following microindentation experiments in 5mM KCl conditions. Images were taken using a constant exposure time to evaluate F-actin (orange), α-SMA (green), nuclei (blue) and α-SMA positive stress fibers seen in composite images (yellow). All images taken with a 63x objective.

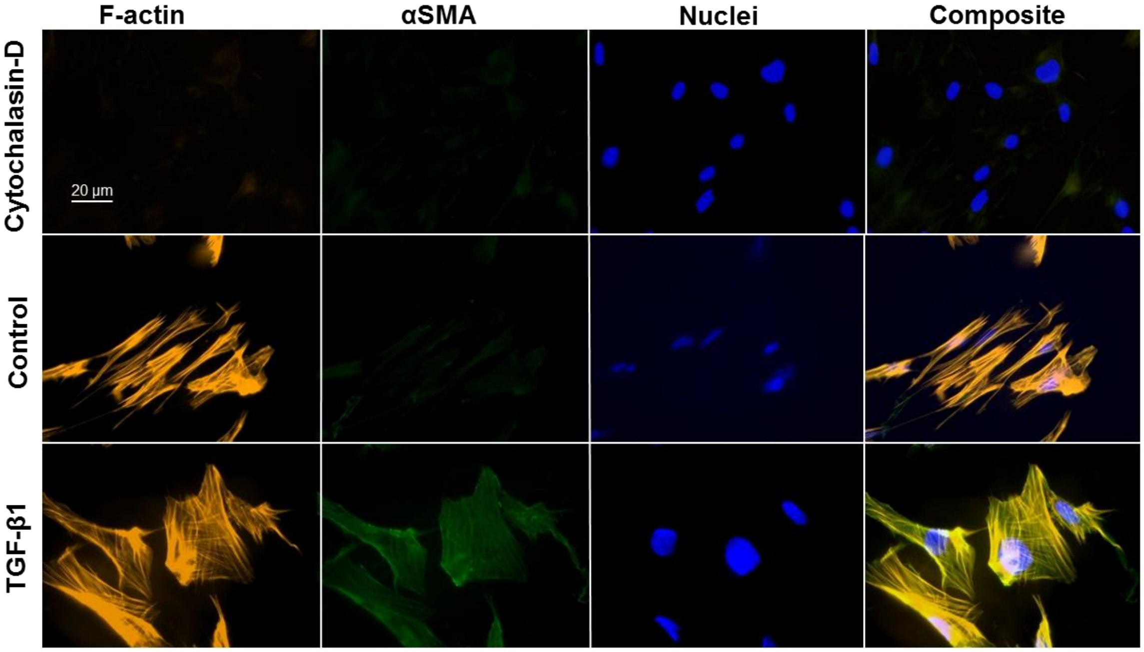

Figure 5.7: Fluorescent staining of AVICs on collagen substrates immediately following microindentation experiments in 90mM KCl conditions. Images were taken using a constant exposure time to evaluate F-actin (orange), α-SMA (green), nuclei (blue) and α-SMA positive stress fibers seen in composite images (yellow). All images taken with a 63x objective.

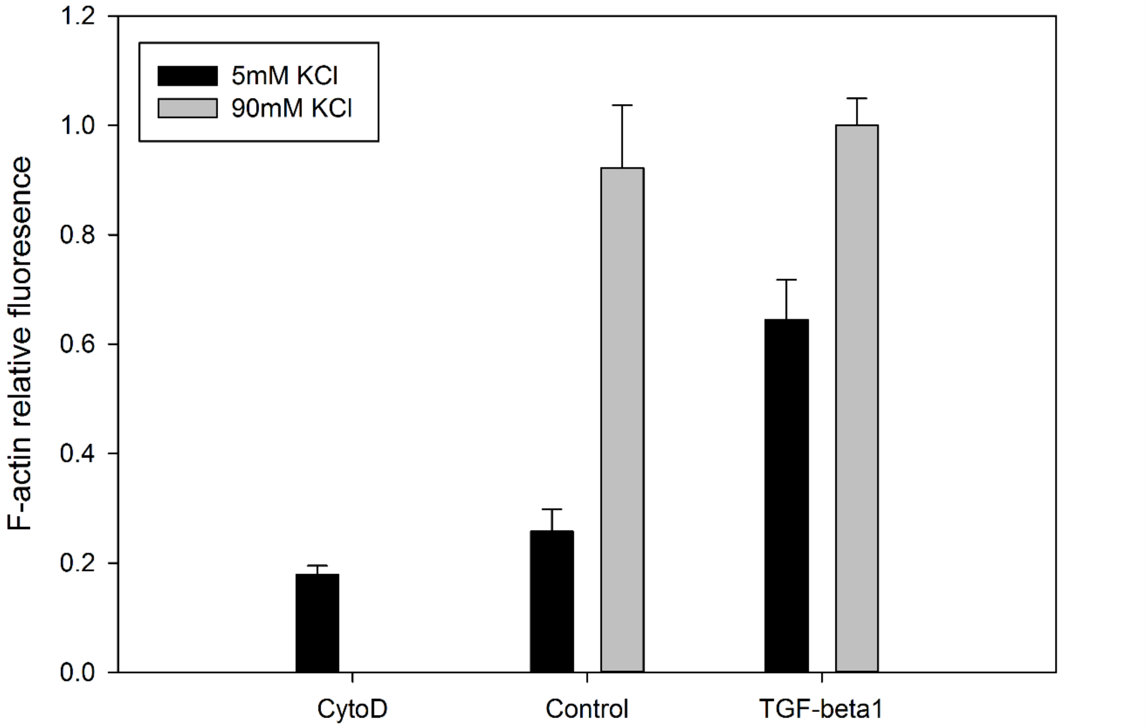

Figure 5.8: Relative fluorescent quantification of filamentous actin (orange fluorescent in Figs 5.6 and 5.7) between all 5 treatment groups. Fluorescence was normalized to TGF-β1 fluorescence at 90mM, as this group exhibited the greatest intensity of staining.

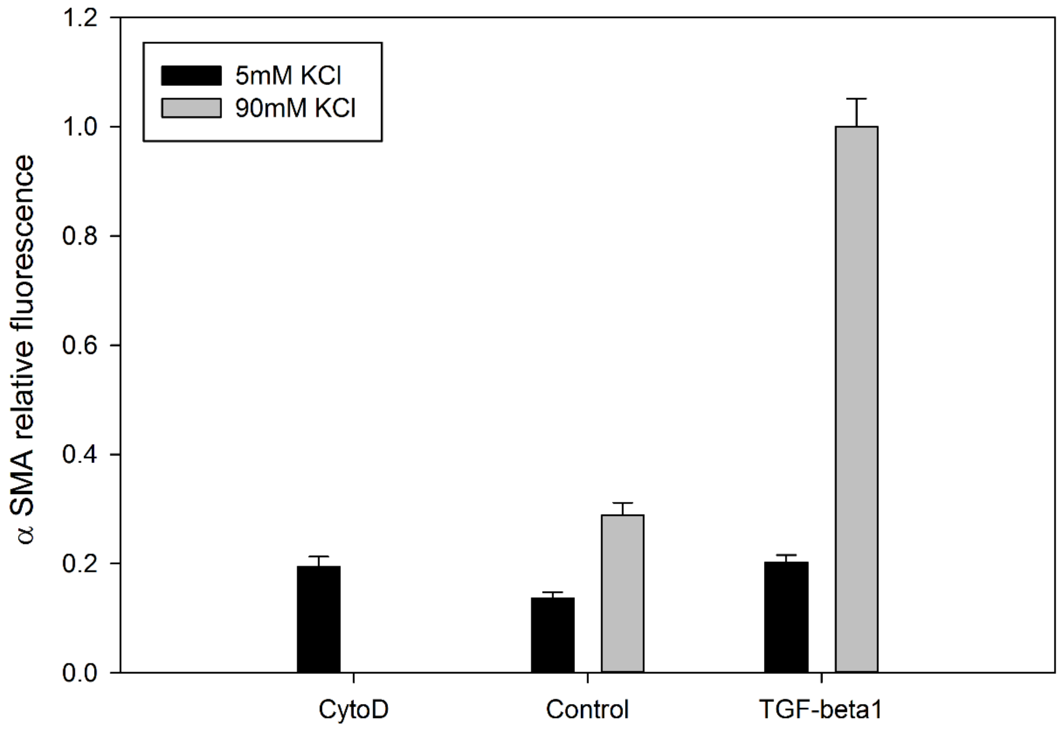

Figure 5.9: Relative fluorescent quantification of α-SMA protein (green fluorescent in Figs 5.6 and 5.7) between all 5 treatment groups. Fluorescence was normalized to TGF-β1 fluorescence at 90mM, as this group exhibited the greatest intensity of staining.

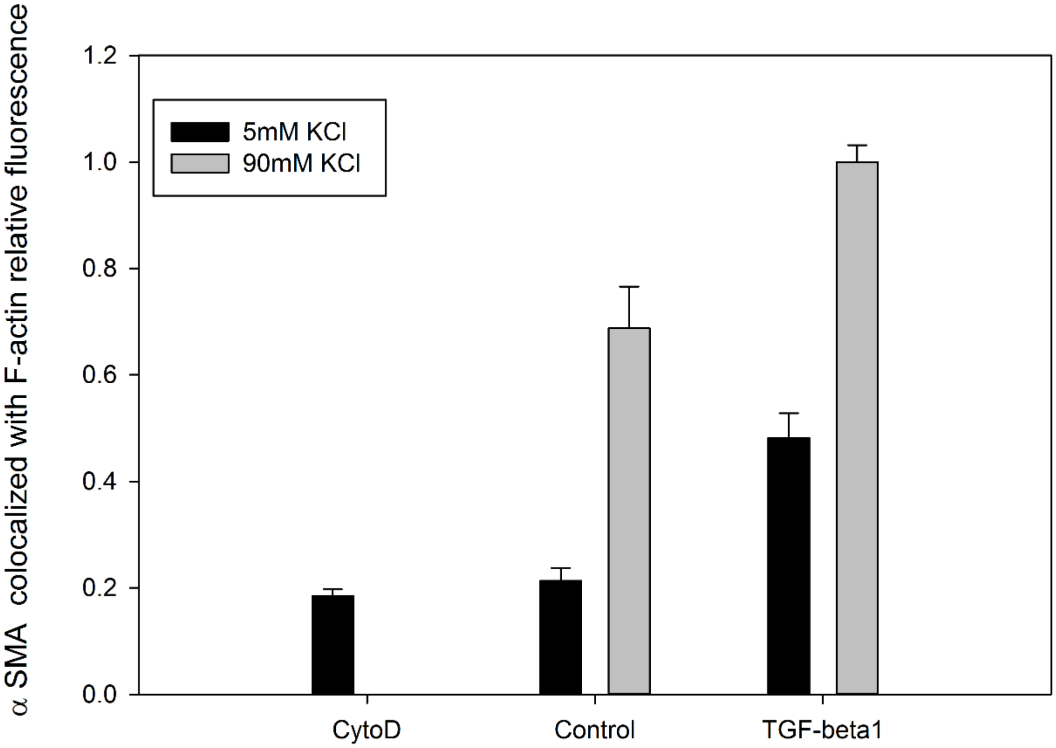

Figure 5.10: Relative fluorescent quantification of α-SMA protein colocalized into F-actin fibers (yellow fluorescent in Figs 5.6 and 5.7) between all 5 treatment groups. Fluorescence was normalized to TGF-β1 fluorescence at 90mM, as this group exhibited the greatest intensity of staining.

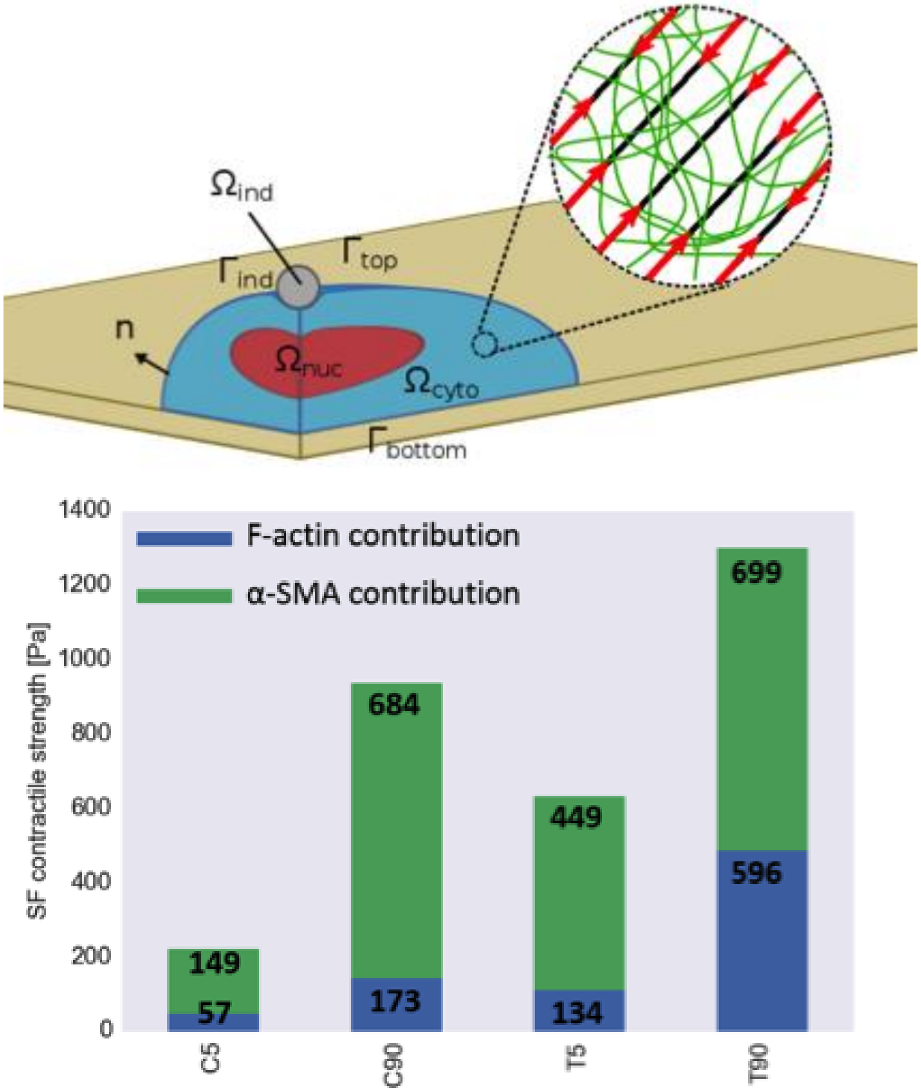

Figure 5.11: A schematic of a computational model of the AVICs that incorporates different mechanical constituent of the stress fibers (Top). Resulting contributions of F-actin and α-SMA to the maximum stress fiber contractile strength measured from the developed model. [This work was submitted to the Summer Biomechanics Bioengineering and Biotransport Conference for presentation in June 2012 in National Harbor, MD.]

REFERENCES

1. Merryman, W.D., et al., Correlation between heart valve interstitial cell stiffness and transvalvular pressure: implications for collagen biosynthesis. Am J Physiol Heart Circ Physiol, 2006. **290**(1): p. H224-31.
2. Merryman, W.D., et al., Viscoelastic properties of the aortic valve interstitial cell. J Biomech Eng, 2009. **131**(4): p. 041005.
3. Wyss, K., et al., The elastic properties of valve interstitial cells undergoing pathological differentiation. J Biomech, 2012. **45**(5): p. 882-7.
4. Merryman, W.D., et al., Differences in tissue-remodeling potential of aortic and pulmonary heart valve interstitial cells. Tissue Eng, 2007. **13**(9): p. 2281-9.
5. Clement, S., et al., The N-terminal Ac-EEED sequence plays a role in alpha-smooth-muscle actin incorporation into stress fibers. Journal of Cell Science, 2005. **118**(7): p. 1395-1404.
6. Hinz, B., et al., Alpha-smooth muscle actin expression upregulates fibroblast contractile activity. Molecular Biology of the Cell, 2001. **12**(9): p. 2730-2741.
7. Hinz, B., et al., The myofibroblast - One function, multiple origins. American Journal of Pathology, 2007. **170**(6): p. 1807-1816.
8. Hinz, B., et al., Recent Developments in Myofibroblast Biology Paradigms for Connective Tissue Remodeling. American Journal of Pathology, 2012. **180**(4): p. 1340-1355.
9. Wang, J., R. Zohar, and C.A. McCulloch, Multiple roles of alpha-smooth muscle actin in mechanotransduction. Exp Cell Res, 2006. **312**(3): p. 205-14.
10. Wang, J.H. and J.S. Lin, Cell traction force and measurement methods. Biomech Model Mechanobiol, 2007. **6**(6): p. 361-71.
11. Chaponnier, C., et al., The specific NH2-terminal sequence Ac-EEED of alpha-smooth muscle actin plays a role in polymerization in vitro and in vivo. J Cell Biol, 1995. **130**(4): p. 887-95.
12. Hinz, B., G. Gabbiani, and C. Chaponnier, The NH2-terminal peptide of alpha-smooth muscle actin inhibits force generation by the myofibroblast in vitro and in vivo. J Cell Biol, 2002. **157**(4): p. 657-63.
13. Rabkin-Aikawa, E., et al., Dynamic and reversible changes of interstitial cell phenotype during remodeling of cardiac valves. J Heart Valve Dis, 2004. **13**(5): p. 841-7.
14. Branchetti, E., et al., Antioxidant enzymes reduce DNA damage and early activation of valvular interstitial cells in aortic valve sclerosis. Arterioscler Thromb Vasc Biol, 2013. **33**(2): p. e66-74.

15. Darling, E.M., et al., A thin-layer model for viscoelastic, stress-relaxation testing of cells using atomic force microscopy: do cell properties reflect metastatic potential? Biophys J, 2007. **92**(5): p. 1784-91.

CHAPTER 6: SUMMARY, CONCLUSIONS AND FUTURE DIRECTIONS

SUMMARY

The overall goal of this work was to estimate AVIC biomechanical state from tissue-level measurements to gain physiologically relevant information regarding AVIC layer dependent behavior under different activation states**.** The ability to predict the biomechanical state of the AVIC from biomechanical tissue experiments provides a significant advantage in that they remain in their native environment. The developed novel computational-experimental approach is a means of deconvoluting changes in AVIC stiffness and AVIC-ECM coupling. This information will provide insight into disease and treatment mechanisms of calcific aortic valve disease giving rise to early detection and better treatment options.

As a first step, a tissue-level bilayer model that accurately captures the bidirectional flexural response of AV intact layers in a passive state was developed. Through this study, the behavior of AV leaflet tissue as a composite beam was determined by examining the M-Δk relationship and the transmural strain of the tissue during bending. It was concluded that while it has been previously speculated that valve layers slide with respect to one another during valve opening/closing, our evidence suggests that the leaflet layers function as a *single bonded unit*. Furthermore, the valve tissue in flexure requires a bimodular material model to capture the layer dependent responses imposed from underlying AVIC activation.

Next, tissue micromorphology was incorporated in a macro-micro scale framework to simulate layer-specific AVIC-ECM interactions. The macro-micro AV model built using an integrated computational-experimental approach, demonstrated the ability to probe layer differences in AVIC-ECM connectivity. Findings suggest that observed layer differences under flexural deformation at the tissue level during AVIC contraction are due to differences in AVIC connectivity with the surrounding matrix. Specifically, it was estimated that AVIC connectivity to the surrounding matrix was approximately 70% less than AVIC connectivity in the fibrosa layer.

The developed macro-micro model was then used to assess differences in AVIC activation states *in situ* by simulating AVIC pathological state through exogenous TGF-β1 treatment. The study revealed a significant increase in stiffness of the fibrosa layer with exogenous TGF-β1 treatment. The layered-dependent increase in stiffness was reflected in estimated AVIC contraction, depicting a 1.50-fold increase in AVIC contraction relative to the control upon TGF-β1 activation. Whether examining linearized estimates of tissue stiffness or the estimated AVIC contraction force, there was a consistent 45-50% increase in tissue stiffness and underlying AVIC contractility when stimulated with TGF-β1 treatment.

Last, we have shown that using an *in situ* approach to estimate the biomechanical state of AVICs under varying activation stimuli tells a different story than using *ex situ* measurements alone. Microindentation studies examining AVIC activation were run in parallel with *in-situ* studies to emphasize the necessity of an *in-situ* approach, and the advantage it affords over existing *ex-situ* methodology. When comparing the results from the microindentation study with the *in situ* measurements, relative trends comparing control vs. TGF-β1 contractile behavior appear consistent. The estimated contractility increase measured with the *in situ* approach for control tissue was found to be approximately 1.4, compared with a 2.0-fold increase observed in TGF-β1 treated tissue. If we contrast this with the observed fold change from micro indentation measurements using physiologically relevant strain rates: 1.75 for control and 2.0 for TGF-β1, <u>the trends remain the same between microindentation and *in situ* estimates of AVIC contractility,</u>

however the relative effects of TGF-β1 treatment were more pronounced when measured *in situ*. Specifically, the *in situ* estimates revealed a 45-50% increase in contractile response upon TGF-β1 activation compared to controls, contrasted with a mere 14% increase difference from microindentation measurements.

CONCLUSIONS

In conclusion, the developed numerical-experimental methodology can be used to obtain AVIC properties *in-situ*, uncovering AVIC-ECM coupling behavior present in native tissue that is otherwise unattainable using existing experimental techniques or computational approaches alone. This work represents the first evidence that AVICs couple in a layer specific manner during contraction, contributing to observed layer differences at the tissue level under flexural loading patterns. Information gained using this developed analytical tool will provide insight into disease and treatment mechanisms of calcific aortic valve disease giving rise to early detection and better treatment options.

FUTURE DIRECTIONS

The developed macro-micro framework should be considered a first step to understanding the complex interactions between the AVICs and surrounding ECM. This simplified model focuses on one component of the complete cardiac cycle: opening and closing of leaflets under systolic stress levels. Future experimental studies of the AV will be done in the loaded state (diastole) under equibiaxial tension. These future experiments will aid in developing a model of the AVIC-ECM interactions under the complete cardiac cycle.

Currently our group is working on subcellular models that incorporate the intricacy of the cytoskeletal network. Particularly the differences observed in the discussed microindentation experiments between the α-sma positive fibers. Initial findings have observed that the incorporation of α-SMA is what contributes to the measured increase in contractile force of the AVICs. The next step would be to incorporate this improved AVIC model into the micro framework of the macro-micro model. As we gain further insight into the AV microenvironment, we can continue to add to the complexity of the macro-micro model while maintaining the computational-experimental approach.

As mentioned previously, although 3D gel studies are not physically realistic, they can provide valuable insight due to their tunability. For example, to further validate these findings of contractile differences due to varied coupling, an artificial type 1 collagen gel system could be engineered to replicate native density differences of integrins. This simple approach would enable the evaluation of AVICs with known connectivity to the matrix under contractile stimuli. These experiments could be used in conjunction with the developed macro-micro model to estimate AVIC contractile responses in this artificial environment.

As mentioned throughout this work, calcification is the primary cause of AV failure and currently no approved medical means of halting progression exists. However, a pharmaceutical class of 3-hydroxy-3-methylglutarylcoenzyme A (HMG-CoA) reductase inhibitors commonly referred to as statins has shown potential in slowing calcification. Statins are used clinically to mitigate mortality rates in atherosclerotic patients by lowering LDL serum cholesterol. Additionally, statins have been shown to inhibit calcified nodule formation in AVIC *in vitro* cultures via contraction regulation [1, 2]. Despite the knowledge gained from these *in vitro* studies, the *in situ* effects of statins on AVICs remain largely unknown. *In vitro* findings have demonstrated a high ECM dependence of statin influence on AVIC behavior, highlighting the importance of *in situ* investigation [3, 4]. Thus, deriving the biomechanical state of AVICs *in situ* using the developed computational-experimental modeling approach could reveal more accurate information regarding AVIC responses to statins and other potential pharmaceutical interventions for mitigating AVIC pathological progression.

REFERENCES

1. Wu, B., et al., Paradoxical effects of statins on aortic valve myofibroblasts and osteoblasts: implications for end-stage valvular heart disease. Arterioscler Thromb Vasc Biol, 2005. 25(3): p. 592-7.
2. Benton, J.A., et al., Statins block calcific nodule formation of valvular interstitial cells by inhibiting alpha-smooth muscle actin expression. Arterioscler Thromb Vasc Biol, 2009. 29(11): p. 1950-7.
3. Rodriguez, K.J. and K.S. Masters, Regulation of valvular interstitial cell calcification by components of the extracellular matrix. J Biomed Mater Res A, 2009. 90(4): p. 1043-53.
4. Monzack, E.L., X. Gu, and K.S. Masters, Efficacy of simvastatin treatment of valvular interstitial cells varies with the extracellular environment. Arterioscler Thromb Vasc Biol, 2009. 29(2): p. 246-53.

BIBLIOGRAPHY

(2013). Multiscale computer modeling in biomechanics and biomedical engineering. New York, Springer.

Adamczyk, M. M. and I. Vesely (2002). "Characteristics of compressive strains in porcine aortic valves cusps." J Heart Valve Dis **11**(1): 75-83.

Agoram, B. and V. H. Barocas (2001). "Coupled macroscopic and microscopic scale modeling of fibrillar tissues and tissue equivalents." J Biomech Eng **123**(4): 362-369.

Aikawa, E. and C. M. Otto (2012). "Look more closely at the valve: imaging calcific aortic valve disease." Circulation **125**(1): 9-11.

Ateshian, G. A. (2007). "Anisotropy of fibrous tissues in relation to the distribution of tensed and buckled fibers." J Biomech Eng **129**(2): 240-249.

Beckmann, E., J. B. Grau, R. Sainger, P. Poggio and G. Ferrari (2010). "Insights into the use of biomarkers in calcific aortic valve disease." J Heart Valve Dis **19**(4): 441-452.

Benton, J. A., B. D. Fairbanks and K. S. Anseth (2009). "Characterization of valvular interstitial cell function in three dimensional matrix metalloproteinase degradable PEG hydrogels." Biomaterials **30**(34): 6593-6603.

Benton, J. A., H. B. Kern, L. A. Leinwand, P. D. Mariner and K. S. Anseth (2009). "Statins block calcific nodule formation of valvular interstitial cells by inhibiting alpha-smooth muscle actin expression." Arterioscler Thromb Vasc Biol **29**(11): 1950-1957.

Billiar, K. L. and M. S. Sacks (2000a). "Biaxial mechanical properties of the natural and glutaraldehyde treated aortic valve cusp--Part I: Experimental results." Journal of Biomechanical Engineering **122**(1): 23-30.

Billiar, K. L. and M. S. Sacks (2000b). "Biaxial mechanical properties of the native and glutaraldehyde-treated aortic valve cusp: Part II--A structural constitutive model." Journal of Biomechanical Engineering **122**(4): 327-335.

Branchetti, E., R. Sainger, P. Poggio, J. B. Grau, J. Patterson-Fortin, J. E. Bavaria, M. Chorny, E. Lai, R. C. Gorman, R. J. Levy and G. Ferrari (2013). "Antioxidant enzymes reduce DNA damage and early activation of valvular interstitial cells in aortic valve sclerosis." Arterioscler Thromb Vasc Biol **33**(2): e66-74.

Buchanan, R. M. and M. S. Sacks (2014). "Interlayer micromechanics of the aortic heart valve leaflet." Biomech Model Mechanobiol **13**(4): 813-826.

Butcher, J. T. and R. M. Nerem (2004). "Porcine aortic valve interstitial cells in three-dimensional culture: comparison of phenotype with aortic smooth muscle cells." J Heart Valve Dis **13**(3): 478-485; discussion 485-476.

Butcher, J. T. and R. M. Nerem (2006). "Valvular Endothelial Cells Regulate the Phenotype of Interstitial Cells in Co-culture: Effects of Steady Shear Stress." Tissue Engineering **12**(4): 905-915.

Butcher, J. T. and R. M. Nerem (2007). "Valvular endothelial cells and the mechanoregulation of valvular pathology." Philos Trans R Soc Lond B Biol Sci **362**(1484): 1445-1457.

Butcher, J. T., A. M. Penrod, A. J. Garcia and R. M. Nerem (2004). "Unique morphology and focal adhesion development of valvular endothelial cells in static and fluid flow environments." Arterioscler Thromb Vasc Biol **24**(8): 1429-1434.

Butcher, J. T., S. Tressel, T. Johnson, D. Turner, G. Sorescu, H. Jo and R. M. Nerem (2006). "Transcriptional profiles of valvular and vascular endothelial cells reveal phenotypic differences: influence of shear stress." Arterioscler Thromb Vasc Biol **26**(1): 69-77.

Butler, D. L., S. A. Goldstein and F. Guilak (2000). "Functional tissue engineering: The role of biomechanics." Journal of Biomechanical Engineering-Transactions of the Asme **122**(6): 570-575.

Carruthers, C. A., C. M. Alfieri, E. M. Joyce, S. C. Watkins, K. E. Yutzey and M. S. Sacks (2012). "Gene Expression and Collagen Fiber Micromechanical Interactions of the Semilunar Heart Valve Interstitial Cell." Cell Mol Bioeng **5**(3): 254-265.

Carruthers, C. A., B. Good, A. D'Amore, J. Liao, R. Amini, S. C. Watkins and M. S. Sacks (2012). Alterations in the microstructure of the anterior mitral valve leaflet under physiological stress. ASME 2012 Summer Bioengineering Conference, American Society of Mechanical Engineers.

Chaponnier, C., M. Goethals, P. A. Janmey, F. Gabbiani, G. Gabbiani and J. Vandekerckhove (1995). "The specific NH2-terminal sequence Ac-EEED of alpha-smooth muscle actin plays a role in polymerization in vitro and in vivo." J Cell Biol **130**(4): 887-895.

Chappell, D. C., S. E. Varner, R. M. Nerem, R. M. Medford and R. W. Alexander (1998). "Oscillatory shear stress stimulates adhesion molecule expression in cultured human endothelium." Circ Res **82**(5): 532-539.

Chaput, M., M. D. Handschumacher, F. Tournoux, L. Hua, J. L. Guerrero, G. J. Vlahakes and R. A. Levine (2008). "Mitral leaflet adaptation to ventricular remodeling: occurrence and adequacy in patients with functional mitral regurgitation." Circulation **118**(8): 845-852.

Chen, J. H. and C. A. Simmons (2011). "Cell-matrix interactions in the pathobiology of calcific aortic valve disease: critical roles for matricellular, matricrine, and matrix mechanics cues." Circ Res **108**(12): 1510-1524.

Chester, A. H., J. D. B. Kershaw, M. Misfeld, H.-H. Sievers and M. H. Yacoub (2003). Specific regional and direcrtional contractile response of aortic cusp tissue-Relevance to valve function. Second Biennial Meeting of the Society for Heart Valve Disease, Paris.

Chester, A. H., M. Misfeld and M. H. Yacoub (2000). "Receptor-mediated contraction of aortic valve leaflets." Journal of Heart Valve Disease **9**(2): 250-254; discussion 254-255.

Christie, G. W. and B. G. Barratt-Boyes (1995). "Age-Dependent Changes in the Radial Stretch of Human Aortic Valve Leaflets Determined by Biaxial Stretching." Annals of Thoracic Surgery **60**: S156-159.

Christie, G. W. and B. G. Barratt-Boyes (1995). "Biaxial mechanical properties of explanted aortic allograft leaflets." Ann Thorac Surg **60**(2 Suppl): S160-164.

Chuong, C. J. and Y. C. Fung (1986). "On Residual Stress in Arteries." Journal of Biomechanical Engineering **108**: 189-192.

Clement, S., B. Hinz, V. Dugina, G. Gabbiani and C. Chaponnier (2005). "The N-terminal Ac-EEED sequence plays a role in alpha-smooth-muscle actin incorporation into stress fibers." Journal of Cell Science **118**(7): 1395-1404.

Cowell, S. J., D. E. Newby, R. J. Prescott, P. Bloomfield, J. Reid, D. B. Northridge and N. A. Boon (2005). "A randomized trial of intensive lipid-lowering therapy in calcific aortic stenosis." N Engl J Med **352**(23): 2389-2397.

Cucina, A., A. V. Sterpetti, G. Pupelis, A. Fragale, S. Lepidi, A. Cavallaro, Q. Giustiniani and L. Santoro D'Angelo (1995). "Shear stress induces changes in the morphology and cytoskeleton organisation of arterial endothelial cells." Eur J Vasc Endovasc Surg **9**(1): 86-92.

Curnier, A., Q. C. He and P. Zysset (1995). "Conewise Linear Elastic-Materials." Journal of Elasticity **37**(1): 1-38.

Dal-Bianco, J. P., E. Aikawa, J. Bischoff, J. L. Guerrero, M. D. Handschumacher, S. Sullivan, B. Johnson, J. S. Titus, Y. Iwamoto, J. Wylie-Sears, R. A. Levine and A. Carpentier (2009). "Active adaptation of the tethered mitral valve: insights into a compensatory mechanism for functional mitral regurgitation." Circulation **120**(4): 334-342.

Darling, E. M., S. Zauscher, J. A. Block and F. Guilak (2007). "A thin-layer model for viscoelastic, stress-relaxation testing of cells using atomic force microscopy: do cell properties reflect metastatic potential?" Biophys J **92**(5): 1784-1791.

Davies, P. F. (1997). "Mechanisms involved in endothelial responses to hemodynamic forces." Atherosclerosis **131 Suppl**: S15-17.

Davies, P. F., A. G. Passerini and C. A. Simmons (2004). "Aortic Valve: Turning Over a New Leaf(let) in Endothelial Phenotypic Heterogeneity." Arterioscler Thromb Vasc Biol **24**(8): 1331-1333.

Davies, P. F., A. Remuzzi, E. J. Gordon, C. F. Dewey, Jr. and M. A. Gimbrone, Jr. (1986). "Turbulent fluid shear stress induces vascular endothelial cell turnover in vitro." Proc Natl Acad Sci U S A **83**(7): 2114-2117.

Davies, P. F., C. Shi, N. Depaola, B. P. Helmke and D. C. Polacek (2001). "Hemodynamics and the focal origin of atherosclerosis: a spatial approach to endothelial structure, gene expression, and function." Ann N Y Acad Sci **947**: 7-16; discussion 16-17.

Davies, P. F. and S. C. Tripathi (1993). "Mechanical stress mechanisms and the cell. An endothelial paradigm." Circ Res **72**(2): 239-245.

Deck, J. D. (1986). "Endothelial cell orientation on aortic valve leaflets." Cardiovasc Res **20**(10): 760-767.

Dena Wiltz, C. A. A., Liezl R. Balaoing, Alicia A. Blancas, Matthew C. Sapp, Xing Zhang and K. Jane Grande-Allen (2013). Extracellular Matrix Organization, Structure, and Function. Calcific Aortic Valve Disease. D. E. Aikawa.

Dominik, J. and P. Zacek (2010). Heart valve surgery : an illustrated guide. Heidelberg ; New York, Springer.

Driessen, N. J., R. A. Boerboom, J. M. Huyghe, C. V. Bouten and F. P. Baaijens (2003). "Computational analyses of mechanically induced collagen fiber remodeling in the aortic heart valve." J Biomech Eng **125**(4): 549-557.

Driessen, N. J., C. V. Bouten and F. P. Baaijens (2005). "Improved prediction of the collagen fiber architecture in the aortic heart valve." J Biomech Eng **127**(2): 329-336.

Drugan, W. J. and J. R. Willis (1996). "A micromechanics-based nonlocal constitutive equation and estimates of representative volume element size for elastic composites." Journal of the Mechanics and Physics of Solids **44**(4): 497-524.

Eckert, C. E., R. Fan, B. Mikulis, M. Barron, C. A. Carruthers, V. M. Friebe, N. R. Vyavahare and M. S. Sacks (2013). "On the biomechanical role of glycosaminoglycans in the aortic heart valve leaflet." Acta Biomaterialia **9**(1): 4653-4660.

Einstein, D. R., K. S. Kunzelman, P. G. Reinhall, R. P. Cochran and M. A. Nicosia (2004). "Haemodynamic determinants of the mitral valve closure sound: a finite element study." Med Biol Eng Comput **42**(6): 832-846.

Einstein, D. R., K. S. Kunzelman, P. G. Reinhall, M. A. Nicosia and R. P. Cochran (2005). "The relationship of normal and abnormal microstructural proliferation to the mitral valve closure sound." J Biomech Eng **127**(1): 134-147.

Engelmayr, G. C., Jr., D. K. Hildebrand, F. W. Sutherland, J. E. Mayer, Jr. and M. S. Sacks (2003). "A novel bioreactor for the dynamic flexural stimulation of tissue engineered heart valve biomaterials." Biomaterials **24**(14): 2523-2532.

Engelmayr, G. C., Jr., E. Rabkin, F. W. Sutherland, F. J. Schoen, J. E. Mayer, Jr. and M. S. Sacks (2005). "The independent role of cyclic flexure in the early in vitro development of an engineered heart valve tissue." Biomaterials **26**(2): 175-187.

Farivar, R. S., L. H. Cohn, E. G. Soltesz, T. Mihaljevic, J. D. Rawn and J. G. Byrne (2003). "Transcriptional profiling and growth kinetics of endothelium reveals differences between cells derived from porcine aorta versus aortic valve." Eur J Cardiothorac Surg **24**(4): 527-534.

Farshad, M., M. W. Wildenberg and P. Flueler (1997). "Determination of shear modulus and Poisson's ratio of polymers and foams by the anticlastic plate-bending method." Materials and Structures **30**(200): 377-382.

Filip, D. A., A. Radu and M. Simionescu (1986). "Interstitial cells of the heart valves possess characteristics similar to smooth muscle cells." Circ Res **59**(3): 310-320.

Freeman, R. V. and C. M. Otto (2002). "Management of asymptomatic valvular aortic stenosis." Indian Heart J **54**(1): 31-38.

Freeman, R. V. and C. M. Otto (2005). "Spectrum of calcific aortic valve disease: pathogenesis, disease progression, and treatment strategies." Circulation **111**(24): 3316-3326.

Frisch-Fay, R. (1962). Flexible bars. Washington,DC, Butterworths.

Fung, Y. C. (1991). "What are the residual stresses doing in our blood vessels?" Ann Biomed Eng **19**(3): 237-249.

Fung, Y. C. and S. Q. Liu (1991). "Changes of zero-stress state of rat pulmonary arteries in hypoxic hypertension." J Appl Physiol **70**(6): 2455-2470.

Galvanetto, U. and M. H. Aliabadi (2010). Multiscale modeling in solid mechanics : computational approaches. London ; New York, Imperial College ; Distributed by World Scientific.

Ge, L. and F. Sotiropoulos (2010). "Direction and magnitude of blood flow shear stresses on the leaflets of aortic valves: is there a link with valve calcification?" J Biomech Eng **132**(1): 014505.

Gharacholou, S. M., B. L. Karon, C. Shub and P. A. Pellikka (2011). "Aortic valve sclerosis and clinical outcomes: moving toward a definition." Am J Med **124**(2): 103-110.

Girard, P. R. and R. M. Nerem (1995). "Shear stress modulates endothelial cell morphology and F-actin organization through the regulation of focal adhesion-associated proteins." J Cell Physiol **163**(1): 179-193.

Gloeckner, D., K. Billiar and M. Sacks (1998). The bending behavior of fixed porcine aortic cusp. Third World Congress of Biomechanics, Hokaiddo, Japan.

Gloeckner, D. C., K. L. Billiar and M. S. Sacks (1999). "Effects of mechanical fatigue on the bending properties of the porcine bioprosthetic heart valve." Asaio J **45**(1): 59-63.

Goldhaber, S. Z. (2006). "Bridging" and mechanical heart valves: perils, promises, and predictions." Circulation **113**(4): 470-472.

Goncalves Coelho, P., P. Rui Fernandes and H. Carrico Rodrigues (2011). "Multiscale modeling of bone tissue with surface and permeability control." J Biomech **44**(2): 321-329.

Gorman, J. H., 3rd, K. B. Gupta, J. T. Streicher, R. C. Gorman, B. M. Jackson, M. B. Ratcliffe, D. K. Bogen and L. H. Edmunds, Jr. (1996). "Dynamic three-dimensional imaging of the mitral valve and left ventricle by rapid sonomicrometry array localization." J Thorac Cardiovasc Surg **112**(3): 712-726.

Gorman, J. H., 3rd, B. M. Jackson, Y. Enomoto and R. C. Gorman (2004). "The effect of regional ischemia on mitral valve annular saddle shape." Ann Thorac Surg **77**(2): 544-548.

Grashow, J. S., M. S. Sacks, J. Liao and A. P. Yoganathan (2006a). "Planar biaxial creep and stress relaxation of the mitral valve anterior leaflet." Ann Biomed Eng **34**(10): 1509-1518.

Grashow, J. S., A. P. Yoganathan and M. S. Sacks (2006b). "Biaxial stress-stretch behavior of the mitral valve anterior leaflet at physiologic strain rates." Ann Biomed Eng **34**(2): 315-325.

Grau, J. B., P. Poggio, R. Sainger, W. J. Vernick, W. F. Seefried, E. Branchetti, B. C. Field, J. E. Bavaria, M. A. Acker and G. Ferrari (2012). "Analysis of osteopontin levels for the identification of asymptomatic patients with calcific aortic valve disease." Ann Thorac Surg **93**(1): 79-86.

Gu, X. and K. S. Masters (2011). "Role of the Rho pathway in regulating valvular interstitial cell phenotype and nodule formation." Am J Physiol Heart Circ Physiol **300**(2): H448-458.

Guilak, F. and V. C. Mow (2000). "The mechanical environment of the chondrocyte: a biphasic finite element model of cell-matrix interactions in articular cartilage." J Biomech **33**(12): 1663-1673.

Gupta, V., J. A. Werdenberg, B. D. Lawrence, J. S. Mendez, E. H. Stephens and K. J. Grande-Allen (2008). "Reversible secretion of glycosaminoglycans and proteoglycans by cyclically stretched valvular cells in 3D culture." Ann Biomed Eng **36**(7): 1092-1103.

Hadi, M. F., E. A. Sander and V. H. Barocas (2012). "Multiscale model predicts tissue-level failure from collagen fiber-level damage." J Biomech Eng **134**(9): 091005.

Hafizi, S., P. M. Taylor, A. H. Chester, S. P. Allen and M. H. Yacoub (2000). "Mitogenic and secretory responses of human valve interstitial cells to vasoactive agents." Journal of Heart Valve Disease **9**(3): 454-458.

Haider, M. A. and F. Guilak (2007). "Application of a Three-Dimensional Poroelastic BEM to Modeling the Biphasic Mechanics of Cell-Matrix Interactions in Articular Cartilage (REVISION)." Comput Methods Appl Mech Eng **196**(31-32): 2999-3010.

Halloran, J. P., S. Sibole, C. C. van Donkelaar, M. C. van Turnhout, C. W. Oomens, J. A. Weiss, F. Guilak and A. Erdemir (2012). "Multiscale mechanics of articular cartilage: potentials and challenges of coupling musculoskeletal, joint, and microscale computational models." Ann Biomed Eng **40**(11): 2456-2474.

Hambli, R., H. Katerchi and C. L. Benhamou (2011). "Multiscale methodology for bone remodelling simulation using coupled finite element and neural network computation." Biomechanics and Modeling in Mechanobiology **10**(1): 133-145.

Helmlinger, G., S. Geiger Rv Fau - Schreck, R. M. Schreck S Fau - Nerem and R. M. Nerem "Effects of pulsatile flow on cultured vascular endothelial cell morphology." (0148-0731 (Print)).

Hilbert, S. L., Barrick, M.K., Ferrans, V.J. (1990). "Porcine aortic valve bioprostheses: A morphologic comparison of the effects of fixation pressure." Journal of Biomedical Materials Research **24**: 773-787.

Hilbert, S. L., V. J. Ferrans and W. M. Swanson (1986). "Optical methods for the nondestructive evaluation of collagen morphology in bioprosthetic heart valves." Journal of Biomedical Materials Research **20**: 1411-1421.

Hinton, R. B., Jr., J. Lincoln, G. H. Deutsch, H. Osinska, P. B. Manning, D. W. Benson and K. E. Yutzey (2006). "Extracellular matrix remodeling and organization in developing and diseased aortic valves." Circ Res **98**(11): 1431-1438.

Hinton, R. B. and K. E. Yutzey (2011). "Heart valve structure and function in development and disease." Annu Rev Physiol **73**: 29-46.

Hinz, B., G. Celetta, J. J. Tomasek, G. Gabbiani and C. Chaponnier (2001). "Alpha-smooth muscle actin expression upregulates fibroblast contractile activity." Molecular Biology of the Cell **12**(9): 2730-2741.

Hinz, B., G. Gabbiani and C. Chaponnier (2002). "The NH2-terminal peptide of alpha-smooth muscle actin inhibits force generation by the myofibroblast in vitro and in vivo." J Cell Biol **157**(4): 657-663.

Hinz, B., S. H. Phan, V. J. Thannickal, A. Galli, M. L. Bochaton-Piallat and G. Gabbiani (2007). "The myofibroblast - One function, multiple origins." American Journal of Pathology **170**(6): 1807-1816.

Hinz, B., S. H. Phan, V. J. Thannickal, M. Prunotto, A. Desmouliere, J. Varga, O. De Wever, M. Mareel and G. Gabbian (2012). "Recent Developments in Myofibroblast Biology Paradigms for Connective Tissue Remodeling." American Journal of Pathology **180**(4): 1340-1355.

Hollister, S. J., J. M. Brennan and N. Kikuchi (1994). "A homogenization sampling procedure for calculating trabecular bone effective stiffness and tissue level stress." J Biomech **27**(4): 433-444.

Huang, H.-Y. S., J. Liao and M. S. Sacks (in-press). "Effects of transvalvular pressure on aortic valve interstitial cell nuclear aspect ratio." Journal of Biomechanial Engineering.

Huang, H. Y., J. Liao and M. S. Sacks (2007). "In-situ deformation of the aortic valve interstitial cell nucleus under diastolic loading." J Biomech Eng **129**(6): 880-889.

Iyengar, A. K. S., H. Sugimoto, D. B. Smith and M. S. Sacks (2001). "Dynamic in vitro quantification of bioprosthetic heart valve leaflet motion using structured light projection." Ann Biomed Eng **29**(11): 963-973.

Johnson, C. M. and D. N. Fass (1983). "Porcine cardiac valvular endothelial cells in culture. A relative deficiency of fibronectin synthesis in vitro." Lab Invest **49**(5): 589-598.

Joyce, E. M., J. Liao, F. J. Schoen, J. E. Mayer, Jr. and M. S. Sacks (2009). "Functional collagen fiber architecture of the pulmonary heart valve cusp." Ann Thorac Surg **87**(4): 1240-1249.

Kershaw, J. D., M. Misfeld, H. H. Sievers, M. H. Yacoub and A. H. Chester (2004). "Specific regional and directional contractile responses of aortic cusp tissue." J Heart Valve Dis **13**(5): 798-803.

Kheradvar, A., E. M. Groves, C. J. Goergen, S. H. Alavi, R. Tranquillo, C. A. Simmons, L. P. Dasi, K. J. Grande-Allen, M. R. Mofrad, A. Falahatpisheh, B. Griffith, F. Baaijens, S. H. Little and S. Canic (2015). "Emerging trends in heart valve engineering: Part II. Novel and standard technologies for aortic valve replacement." Ann Biomed Eng **43**(4): 844-857.

Kim, E., F. Guilak and M. A. Haider (2008). "The dynamic mechanical environment of the chondrocyte: a biphasic finite element model of cell-matrix interactions under cyclic compressive loading." J Biomech Eng **130**(6): 061009.

Kunzelman, K. S., D. R. Einstein and R. P. Cochran (2007). "Fluid-structure interaction models of the mitral valve: function in normal and pathological states." Philos Trans R Soc Lond B Biol Sci **362**(1484): 1393-1406.

Kurtz, C. E. and C. M. Otto (2010). "Aortic stenosis: clinical aspects of diagnosis and management, with 10 illustrative case reports from a 25-year experience." Medicine (Baltimore) **89**(6): 349-379.

Laforest, B., G. Andelfinger and M. Nemer (2011). "Loss of Gata5 in mice leads to bicuspid aortic valve." J Clin Invest **121**(7): 2876-2887.

Lai, V. K., M. F. Hadi, R. T. Tranquillo and V. H. Barocas (2013). "A multiscale approach to modeling the passive mechanical contribution of cells in tissues." J Biomech Eng **135**(7): 71007.

Lam, T. (2004). The mechanical properties of native porcine aortic and pulmonary heart valve leaflets. MS, University of Pittsburgh.

Lanir, Y. (1983). "Constitutive equations for fibrous connective tissues." J Biomech **16**(1): 1-12.

Lanir, Y. (2009). "Mechanisms of residual stress in soft tissues." J Biomech Eng **131**(4): 044506.

Latif, N., P. Sarathchandra, P. M. Taylor, J. Antoniw and M. H. Yacoub (2005). "Molecules mediating cell-ECM and cell-cell communication in human heart valves." Cell Biochem Biophys **43**(2): 275-287.

Lavagnino, M., S. P. Arnoczky, E. Kepich, O. Caballero and R. C. Haut (2008). "A finite element model predicts the mechanotransduction response of tendon cells to cyclic tensile loading." Biomech Model Mechanobiol **7**(5): 405-416.

Leask, R. L., N. Jain and J. Butany (2003). "Endothelium and valvular diseases of the heart." Microsc Res Tech **60**(2): 129-137.

Lee, C. H., R. Amini, R. C. Gorman, J. H. Gorman, 3rd and M. S. Sacks (2014). "An inverse modeling approach for stress estimation in mitral valve anterior leaflet valvuloplasty for in-vivo valvular biomaterial assessment." J Biomech **47**(9): 2055-2063.

Lee, C. H., C. A. Carruthers, S. Ayoub, R. C. Gorman, J. H. Gorman, 3rd and M. S. Sacks (2015). "Quantification and simulation of layer-specific mitral valve interstitial cells deformation under physiological loading." J Theor Biol **373**: 26-39.

Lee, T. C., Y. D. Zhao, D. W. Courtman and D. J. Stewart (2000). "Abnormal aortic valve development in mice lacking endothelial nitric oxide synthase." Circulation **101**(20): 2345-2348.

Liu, S. Q. and Y. C. Fung (1989). "Relationship between hypertension, hypertrophy, and opening angle of zero-stress state of arteries following aortic constriction." J Biomech Eng **111**(4): 325-335.

Lu, S. C. H. and K. S. Pister (1975). "Decomposition of deformation and representation of the free energy function for isotropic thermoelastic solids." International Journal of Solids and Structures **11**(7–8): 927-934.

Luscinskas, F. W. and J. Lawler (1994). "Integrins as dynamic regulators of vascular function." FASEB J **8**(12): 929-938.

Malvern, L. E. (1969). Introduction to the mechanics of a continuous medium. Englewood Cliffs, N.J.,, Prentice-Hall.

Mansi, T., I. Voigt, B. Georgescu, X. Zheng, E. A. Mengue, M. Hackl, R. I. Ionasec, T. Noack, J. Seeburger and D. Comaniciu (2012). "An integrated framework for finite-element modeling of mitral valve biomechanics from medical images: Application to MitralClip intervention planning." Medical image analysis **16**(7): 1330-1346.

Marchand, M. A., M. R. Aupart, R. Norton, I. R. Goldsmith, L. C. Pelletier, M. Pellerin, T. Dubiel, W. J. Daenen, P. Herijgers, F. P. Casselman, M. P. Holden and T. E. David (2001). "Fifteen-year experience with the mitral Carpentier-Edwards PERIMOUNT pericardial bioprosthesis." Ann Thorac Surg **71**(5 Suppl): S236-239.

Marron, K., M. H. Yacoub, J. M. Polak, M. N. Sheppard, D. Fagan, B. F. Whitehead, M. R. de Leval, R. H. Anderson and J. Wharton (1996). "Innervation of human atrioventricular and arterial valves." Circulation **94**(3): 368-375.

May-Newman, K. and F. C. Yin (1995). "Biaxial mechanical behavior of excised porcine mitral valve leaflets." Am J Physiol **269**(4 Pt 2): H1319-1327.

May-Newman, K. and F. C. Yin (1998). "A constitutive law for mitral valve tissue." J Biomech Eng **120**(1): 38-47.

Mayne, A. S., G. W. Christie, B. H. Smaill, P. J. Hunter and B. G. Barratt-Boyes (1989). "An assessment of the mechanical properties of leaflets from four second-generation porcine bioprostheses with biaxial testing techniques." J Thorac Cardiovasc Surg **98**(2): 170-180.

Merryman, W. D., P. D. Bieniek, F. Guilak and M. S. Sacks (2009). "Viscoelastic properties of the aortic valve interstitial cell." J Biomech Eng **131**(4): 041005.

Merryman, W. D., H. Y. Huang, F. J. Schoen and M. S. Sacks (2006). "The effects of cellular contraction on aortic valve leaflet flexural stiffness." J Biomech **39**(1): 88-96.

Merryman, W. D., J. Liao, A. Parekh, J. E. Candiello, H. Lin and M. S. Sacks (2007). "Differences in tissue-remodeling potential of aortic and pulmonary heart valve interstitial cells." Tissue Eng **13**(9): 2281-2289.

Merryman, W. D., I. Youn, H. D. Lukoff, P. M. Krueger, F. Guilak, R. A. Hopkins and M. S. Sacks (2006). "Correlation between heart valve interstitial cell stiffness and transvalvular pressure: implications for collagen biosynthesis." Am J Physiol Heart Circ Physiol **290**(1): H224-231.

Messier, R. H., Jr., B. L. Bass, H. M. Aly, J. L. Jones, P. W. Domkowski, R. B. Wallace and R. A. Hopkins (1994). "Dual structural and functional phenotypes of the porcine aortic valve interstitial population: characteristics of the leaflet myofibroblast." J Surg Res **57**(1): 1-21.

Mirnajafi, A., J. M. Raymer, L. R. McClure and M. S. Sacks (2006). "The flexural rigidity of the aortic valve leaflet in the commissural region." J Biomech **39**(16): 2966-2973.

Mohri, H., D. Reichenback and K. Merendino (1972). Biology of homologous and heterologous aortic valves. Biological Tissue in Heart Valve Replacement. M. Ionescu, D. Ross and G. Wooler. London, Butterworths**:** 137.

Monzack, E. L., X. Gu and K. S. Masters (2009). "Efficacy of simvastatin treatment of valvular interstitial cells varies with the extracellular environment." Arterioscler Thromb Vasc Biol **29**(2): 246-253.

Moura, L. M., S. F. Ramos, J. L. Zamorano, I. M. Barros, L. F. Azevedo, F. Rocha-Goncalves and N. M. Rajamannan (2007). "Rosuvastatin affecting aortic valve endothelium to slow the progression of aortic stenosis." J Am Coll Cardiol **49**(5): 554-561.

Mozaffarian, D., E. J. Benjamin, A. S. Go, D. K. Arnett, M. J. Blaha, M. Cushman, S. R. Das, S. de Ferranti, J.-P. Després, H. J. Fullerton, V. J. Howard, M. D. Huffman, C. R. Isasi, M. C. Jiménez, S. E. Judd, B. M. Kissela, J. H. Lichtman, L. D. Lisabeth, S. Liu, R. H. Mackey, D. J. Magid, D. K. McGuire, E. R. Mohler, C. S. Moy, P. Muntner, M. E. Mussolino, K. Nasir, R. W. Neumar, G. Nichol, L. Palaniappan, D. K. Pandey, M. J. Reeves, C. J. Rodriguez, W. Rosamond, P. D. Sorlie, J. Stein, A. Towfighi, T. N. Turan, S. S. Virani, D. Woo, R. W. Yeh and M. B. Turner (2015). "Heart Disease and Stroke Statistics—2016 Update: A Report From the American Heart Association." Circulation.

Mulholland, D. L. and A. I. Gotlieb (1996). "Cell biology of valvular interstitial cells." Can J Cardiol **12**(3): 231-236.

Nemir, S. and J. L. West (2010). "Synthetic materials in the study of cell response to substrate rigidity." Ann Biomed Eng **38**(1): 2-20.

Nicosia, M. A., R. P. Cochran, D. R. Einstein, C. J. Rutland and K. S. Kunzelman (2003). "A coupled fluid-structure finite element model of the aortic valve and root." J Heart Valve Dis **12**(6): 781-789.

Niederer, S. A. and N. P. Smith (2012). "At the heart of computational modelling." J Physiol **590**(Pt 6): 1331-1338.

Nus, M., D. MacGrogan, B. Martinez-Poveda, Y. Benito, J. C. Casanova, F. Fernandez-Aviles, J. Bermejo and J. L. de la Pompa (2011). "Diet-induced aortic valve disease in mice haploinsufficient for the Notch pathway effector RBPJK/CSL." Arterioscler Thromb Vasc Biol **31**(7): 1580-1588.

O'Brien, K. D. (2006). "Pathogenesis of calcific aortic valve disease: a disease process comes of age (and a good deal more)." Arterioscler Thromb Vasc Biol **26**(8): 1721-1728.

Ogden, R. (2003). Nonlinear elasticity, anisotropy, material stability, and residual stresses in soft tissue. Biomechanics of soft tissue in cardiovascular system. R. W. Ogden. New York, Springer.

Otto, C. M. (2001). "Clinical practice. Evaluation and management of chronic mitral regurgitation." N Engl J Med **345**(10): 740-746.

Otto, C. M. (2009). "Calcific aortic valve disease: outflow obstruction is the end stage of a systemic disease process." European Heart Journal **30**(16): 1940-1942.

Otto, C. M. (2010). "Calcific aortic valve disease: new concepts." Semin Thorac Cardiovasc Surg **22**(4): 276-284.

Otto, C. M., J. Kuusisto, D. D. Reichenbach, A. M. Gown and K. D. O'Brien (1994). "Characterization of the early lesion of 'degenerative' valvular aortic stenosis. Histological and immunohistochemical studies." Circulation **90**(2): 844-853.

Owens, D. S. and C. M. Otto (2009). "Is it time for a new paradigm in calcific aortic valve disease?" JACC Cardiovasc Imaging **2**(8): 928-930.

Parolari, A., E. Tremoli, L. Cavallotti, M. Trezzi, S. Kassem, C. Loardi, F. Veglia, G. Ferrari, D. Pacini and F. Alamanni (2011). "Do statins improve outcomes and delay the progression of non-rheumatic calcific aortic stenosis?" Heart **97**(7): 523-529.

Pflederer, T. and S. Achenbach (2010). "Aortic valve stenosis: CT contributions to diagnosis and therapy." J Cardiovasc Comput Tomogr **4**(6): 355-364.

Podshivalov, L., A. Fischer and P. Z. Bar-Yoseph (2014). "On the Road to Personalized Medicine: Multiscale Computational Modeling of Bone Tissue." Archives of Computational Methods in Engineering **21**(4): 399-479.

Poggio, P., R. Sainger, E. Branchetti, J. B. Grau, E. K. Lai, R. C. Gorman, M. S. Sacks, A. Parolari, J. E. Bavaria and G. Ferrari (2013). "Noggin attenuates the osteogenic activation of human valve interstitial cells in aortic valve sclerosis." Cardiovasc Res **98**(3): 402-410.

Prasad, A. R., S. A. Logan, R. M. Nerem, C. J. Schwartz and E. A. Sprague (1993). "Flow-related responses of intracellular inositol phosphate levels in cultured aortic endothelial cells." Circ Res **72**(4): 827-836.

Prot, V. and B. Skallerud (2009). "Nonlinear solid finite element analysis of mitral valves with heterogeneous leaflet layers." Comput Mech **43**(3): 353-368.

Prot, V., B. Skallerud and G. Holzapfel (2007). "Transversely isotropic membrane shells with application to mitral valve mechanics. Constitutive modelling and finite element implementation." Int J Numer Methods Eng **71**(8): 987-1008.

Rabkin-Aikawa, E., M. Farber, M. Aikawa and F. J. Schoen (2004). "Dynamic and reversible changes of interstitial cell phenotype during remodeling of cardiac valves." J Heart Valve Dis **13**(5): 841-847.

Rajamannan, N. M., F. J. Evans, E. Aikawa, K. J. Grande-Allen, L. L. Demer, D. D. Heistad, C. A. Simmons, K. S. Masters, P. Mathieu, K. D. O'Brien, F. J. Schoen, D. A. Towler, A. P. Yoganathan and C. M. Otto (2011). "Calcific aortic valve disease: not simply a degenerative process: A review and agenda for research from the National Heart and Lung and Blood Institute Aortic Stenosis Working Group. Executive summary: Calcific aortic valve disease-2011 update." Circulation **124**(16): 1783-1791.

Rausch, M. K., N. Famaey, T. O. Shultz, W. Bothe, D. C. Miller and E. Kuhl (2012). "Mechanics of the mitral valve : A critical review, an in vivo parameter identification, and the effect of prestrain." Biomech Model Mechanobiol.

Reul, H. and N. Talukder (1989). Heart valve mechanics. The Heart, McGraw Hill.

Rivlin, R. S. (1949). "Large Elastic Deformations of Isotropic Materials .5. The Problem of Flexure." Proceedings of the Royal Society of London Series a-Mathematical and Physical Sciences **195**(1043): 463-473.

Rodriguez, K. J. and K. S. Masters (2009). "Regulation of valvular interstitial cell calcification by components of the extracellular matrix." J Biomed Mater Res A **90**(4): 1043-1053.

Rossebo, A. B., T. R. Pedersen, K. Boman, P. Brudi, J. B. Chambers, K. Egstrup, E. Gerdts, C. Gohlke-Barwolf, I. Holme, Y. A. Kesaniemi, W. Malbecq, C. A. Nienaber, S. Ray, T. Skjaerpe, K. Wachtell and R. Willenheimer (2008). "Intensive lipid lowering with simvastatin and ezetimibe in aortic stenosis." N Engl J Med **359**(13): 1343-1356.

Sacks, M. S. (2003). "Incorporation of experimentally-derived fiber orientation into a structural constitutive model for planar collagenous tissues." J Biomech Eng **125**(2): 280-287.

Sacks, M. S., W. David Merryman and D. E. Schmidt (2009). "On the biomechanics of heart valve function." J Biomech **42**(12): 1804-1824.

Sacks, M. S., Z. He, L. Baijens, S. Wanant, P. Shah, H. Sugimoto and A. P. Yoganathan (2002). "Surface strains in the anterior leaflet of the functioning mitral valve." Annals of Biomedical Engineering **30**(10): 1281-1290.

Sacks, M. S., D. B. Smith and E. D. Hiester (1998). "The aortic valve microstructure: effects of transvalvular pressure." Journal of Biomedical Materials Research **41**(1): 131-141.

Sacks, M. S. and A. P. Yoganathan (2007). "Heart valve function: a biomechanical perspective." Philos Trans R Soc Lond B Biol Sci **362**(1484): 1369-1391.

Sakamoto, Y., R. M. Buchanan and M. S. Sacks (2016). "On intrinsic stress fiber contractile forces in semilunar heart valve interstitial cells using a continuum mixture model." J Mech Behav Biomed Mater **54**: 244-258.

Schneider, P. J. and J. D. Deck (1981). "Tissue and cell renewal in the natural aortic valve of rats: an autoradiographic study." Cardiovasc Res **15**(4): 181-189.

Schoen, F. and R. Levy (1999). "Tissue heart valves: Current challenges and future research perspectives." Journal of Biomedical Materials Research **47**: 439-465.

Scott, M. and I. Vesely (1995). "Aortic valve cusp microstructure: The role of elastin." Annals of Thoracic Surgery **60**: S391-S394.

Simmons, C. A., G. R. Grant, E. Manduchi and P. F. Davies (2005). "Spatial Heterogeneity of Endothelial Phenotypes Correlates With Side-Specific Vulnerability to Calcification in Normal Porcine Aortic Valves." Circ Res **96**(7): 792-799.

Skallerud, B., V. Prot and I. S. Nordrum (2011). "Modeling active muscle contraction in mitral valve leaflets during systole: a first approach." Biomech Model Mechanobiol **10**(1): 11-26.

Song, T., I. Vesely and D. Boughner (1990). "Effects of dynamic fixation on shear behaviour of porcine xenograft valves." Biomaterials **11**(3): 191-196.

Stamatas, G. N. and L. V. McIntire "Rapid flow-induced responses in endothelial cells." (8756-7938 (Print)).

Stella, J. A., J. Liao and M. S. Sacks (2007). "Time-dependent biaxial mechanical behavior of the aortic heart valve leaflet." J Biomech **40**(14): 3169-3177.

Stella, J. A. and M. S. Sacks (2007). "On the biaxial mechanical properties of the layers of the aortic valve leaflet." J Biomech Eng **129**(5): 757-766.

Stephens, E. H., C. A. Durst, J. C. Swanson, K. J. Grande-Allen, N. B. Ingels and D. C. Miller (2010). "Functional Coupling of Valvular Interstitial Cells and Collagen Via alpha(2)beta(1) Integrins in the Mitral Leaflet." Cellular and Molecular Bioengineering **3**(4): 428-437.

Stephens, E. H., C. A. Durst, J. L. West and K. J. Grande-Allen (2011). "Mitral valvular interstitial cell responses to substrate stiffness depend on age and anatomic region." Acta Biomaterialia **7**(1): 75-82.

Stephens, E. H., T. C. Nguyen, A. Itoh, N. B. Ingels, Jr., D. C. Miller and K. J. Grande-Allen (2008). "The effects of mitral regurgitation alone are sufficient for leaflet remodeling." Circulation **118**(14 Suppl): S243-249.

Stephens, E. H., J. G. Saltarrelli, L. S. Baggett, I. Nandi, J. J. Kuo, A. R. Davis, E. A. Olmsted-Davis, M. J. Reardon, J. D. Morrisett and K. J. Grande-Allen (2011). "Differential proteoglycan and hyaluronan distribution in calcified aortic valves." Cardiovasc Pathol **20**(6): 334-342.

Stephens, E. H., T. A. Timek, G. T. Daughters, J. J. Kuo, A. M. Patton, L. S. Baggett, N. B. Ingels, D. C. Miller and K. J. Grande-Allen (2009). "Significant changes in mitral valve leaflet matrix composition and turnover with tachycardia-induced cardiomyopathy." Circulation **120**(11 Suppl): S112-119.

Stevanella, M., F. Maffessanti, C. A. Conti, E. Votta, A. Arnoldi, M. Lombardi, O. Parodi, E. G. Caiani and A. Redaelli (2011). "Mitral valve patient-specific finite element modeling from cardiac MRI: application to an annuloplasty procedure." Cardiovas Eng Tech **2**(2): 66-76.

Stewart, B. F., D. Siscovick, B. K. Lind, J. M. Gardin, J. S. Gottdiener, V. E. Smith, D. W. Kitzman and C. M. Otto (1997). "Clinical factors associated with calcific aortic valve disease. Cardiovascular Health Study." J Am Coll Cardiol **29**(3): 630-634.

Sugimoto, B. and M. S. Sacks (2013). "EFFECTS OF LEAFLET STIFFNESS ON IN-VITRO DYNAMIC BIOPROSTHETIC HEART VALVE LEAFLET SHAPE." Cardiovascular Engineering and Technology **in-press**.

Taber, L. A. and J. D. Humphrey (2001). "Stress-modulated growth, residual stress, and vascular heterogeneity." J Biomech Eng **123**(6): 528-535.

Talman, E. A. and D. R. Boughner (1995). "Glutaraldehyde fixation alters the internal shear properties of porcine aortic heart valve tissue." Annals of Thoracic Surgery **60**: S369-S373.

Tanaka, K., M. Sata, D. Fukuda, Y. Suematsu, N. Motomura, S. Takamoto, Y. Hirata and R. Nagai (2005). "Age-associated aortic stenosis in apolipoprotein E-deficient mice." J Am Coll Cardiol **46**(1): 134-141.

Tao, G., J. D. Kotick and J. Lincoln (2012). "Heart valve development, maintenance, and disease: the role of endothelial cells." Curr Top Dev Biol **100**: 203-232.

Taylor, P. M., P. Batten, N. J. Brand, P. S. Thomas and M. H. Yacoub (2003). "The cardiac valve interstitial cell." Int J Biochem Cell Biol **35**(2): 113-118.

Thubrikar, M. (1990). The Aortic Valve. Boca Raton, CRC.

Thubrikar, M., W. C. Piepgrass, L. P. Bosher and S. P. Nolan (1980). "The elastic modulus of canine aortic valve leaflets in vivo and in vitro." Circ Res **47**(5): 792-800.

Thubrikar, M. J., J. Aouad and S. P. Nolan (1986). "Comparison of the in vivo and in vitro mechanical properties of aortic valve leaflets." J Thorac Cardiovasc Surg **92**(1): 29-36.

Thubrikar, M. J., J. Aouad and S. P. Nolan (1986). "Patterns of calcific deposits in operatively excised stenotic or purely regurgitant aortic valves and their relation to mechanical stress." Am J Cardiol **58**(3): 304-308.

Thubrikar, M. J., S. P. Nolan, J. Aouad and J. D. Deck (1986). "Stress sharing between the sinus and leaflets of canine aortic valve." Ann Thorac Surg **42**(4): 434-440.

Timoshenko, S. (1953). History of strength of materials, with a brief account of the history of theory of elasticity and theory of structures. New York,, McGraw-Hill.

Towler, D. A. (2013). "Molecular and cellular aspects of calcific aortic valve disease." Circ Res **113**(2): 198-208.

Tseng, H. and K. J. Grande-Allen (2012). "Elastic fibers in the aortic valve spongiosa: A fresh perspective on its structure and role in overall tissue function (vol 7, pg 2101, 2011)." Acta Biomaterialia **8**(2): 924-924.

Vesely, I. (1998). "The role of elastin in aortic valve mechanics." J Biomech **31**(2): 115-123.

Vesely, I. and D. Boughner (1989). "Analysis of the bending behaviour of porcine xenograft leaflets and of neutral aortic valve material: bending stiffness, neutral axis and shear measurements." J Biomech **22**(6-7): 655-671.

Vesely, I. and W. J. Mako (1998). "Comparison of the compressive buckling of porcine aortic valve cusps and bovine pericardium." J Heart Valve Dis **7**(1): 34-39.

Vesely, I. and R. Noseworthy (1992). "Micromechanics of the fibrosa and the ventricularis in aortic valve leaflets." J Biomech **25**(1): 101-113.

Votta, E., E. Caiani, F. Veronesi, M. Soncini, F. M. Montevecchi and A. Redaelli (2008). "Mitral valve finite-element modelling from ultrasound data: a pilot study for a new approach to understand mitral function and clinical scenarios." Philos Transact A Math Phys Eng Sci **366**(1879): 3411-3434.

Wang, J., R. Zohar and C. A. McCulloch (2006). "Multiple roles of alpha-smooth muscle actin in mechanotransduction." Exp Cell Res **312**(3): 205-214.

Wang, J. H. and J. S. Lin (2007). "Cell traction force and measurement methods." Biomech Model Mechanobiol **6**(6): 361-371.

Wang, Q. and W. Sun (2013). "Finite Element Modeling of Mitral Valve Dynamic Deformation Using Patient-Specific Multi-Slices Computed Tomography Scans." Ann Biomed Eng **41**(1): 142-153.

Weber, K. T., Y. Sun, L. C. Katwa, J. P. Cleutjens and G. Zhou (1995). "Connective tissue and repair in the heart. Potential regulatory mechanisms." Ann N Y Acad Sci **752**: 286-299.

Weinberg, E. J. and M. R. Kaazempur Mofrad (2007). "Transient, three-dimensional, multiscale simulations of the human aortic valve." Cardiovasc Eng **7**(4): 140-155.

Weinberg, E. J. and M. R. Kaazempur Mofrad (2008). "A multiscale computational comparison of the bicuspid and tricuspid aortic valves in relation to calcific aortic stenosis." J Biomech **41**(16): 3482-3487.

Weinberg, E. J., D. Shahmirzadi and M. R. Mofrad (2010). "On the multiscale modeling of heart valve biomechanics in health and disease." Biomech Model Mechanobiol **9**(4): 373-387.

Weiss, R. M., M. Ohashi, J. D. Miller, S. G. Young and D. D. Heistad (2006). "Calcific aortic valve stenosis in old hypercholesterolemic mice." Circulation **114**(19): 2065-2069.

Wenk, J. F., Z. Zhang, G. Cheng, D. Malhotra, G. Acevedo-Bolton, M. Burger, T. Suzuki, D. A. Saloner, A. W. Wallace, J. M. Guccione and M. B. Ratcliffe (2010). "First finite element model of the left ventricle with mitral valve: insights into ischemic mitral regurgitation." Ann Thorac Surg **89**(5): 1546-1553.

Willems, I. E., M. G. Havenith, J. F. Smits and M. J. Daemen (1994). "Structural alterations in heart valves during left ventricular pressure overload in the rat." Lab Invest **71**(1): 127-133.

Woo, S. L. Y. and Y. Seguchi (1989). Tissue Engineering - 1989. New York, Asme.

Wu, B., S. Elmariah, F. S. Kaplan, G. Cheng and E. R. Mohler, 3rd (2005). "Paradoxical effects of statins on aortic valve myofibroblasts and osteoblasts: implications for end-stage valvular heart disease." Arterioscler Thromb Vasc Biol **25**(3): 592-597.

Wyss, K., C. Y. Yip, Z. Mirzaei, X. Jin, J. H. Chen and C. A. Simmons (2012). "The elastic properties of valve interstitial cells undergoing pathological differentiation." J Biomech **45**(5): 882-887.

Ye, Q., G. Zünd, P. Benedikt, S. Jockenhoevel, S. P. Hoerstrup, S. Sakyama, J. A. Hubbell and M. Turina (2000). "Fibrin gel as a three dimensional matrix in cardiovascular tissue engineering." European Journal of Cardio-Thoracic Surgery **17**(5): 587-591.

Yip, C. Y., J. H. Chen, R. Zhao and C. A. Simmons (2009). "Calcification by valve interstitial cells is regulated by the stiffness of the extracellular matrix." Arterioscler Thromb Vasc Biol **29**(6): 936-942.

Zeng, Z., P. Nievelstein-Post, Y. Yin, K. M. Jan, J. S. Frank and D. S. Rumschitzki (2007). "Macromolecular transport in heart valves. III. Experiment and theory for the size distribution of extracellular liposomes in hyperlipidemic rabbits." American Journal of Physiology-Heart and Circulatory Physiology **292**(6): H2687-H2697.

Zeng, Z. Q., Y. Y. Yin, A. L. Huang, K. M. Jan and D. S. Rumschitzki (2007). "Macromolecular transport in heart valves. I. Studies of rat valves with horseradish peroxidase." American Journal of Physiology-Heart and Circulatory Physiology **292**(6): H2664-H2670.

Zeng, Z. Q., Y. Y. Yin, K. M. Jan and D. S. Rumschitzki (2007). "Macromolecular transport in heart valves. II. Theoretical models." American Journal of Physiology-Heart and Circulatory Physiology **292**(6): H2671-H2686.